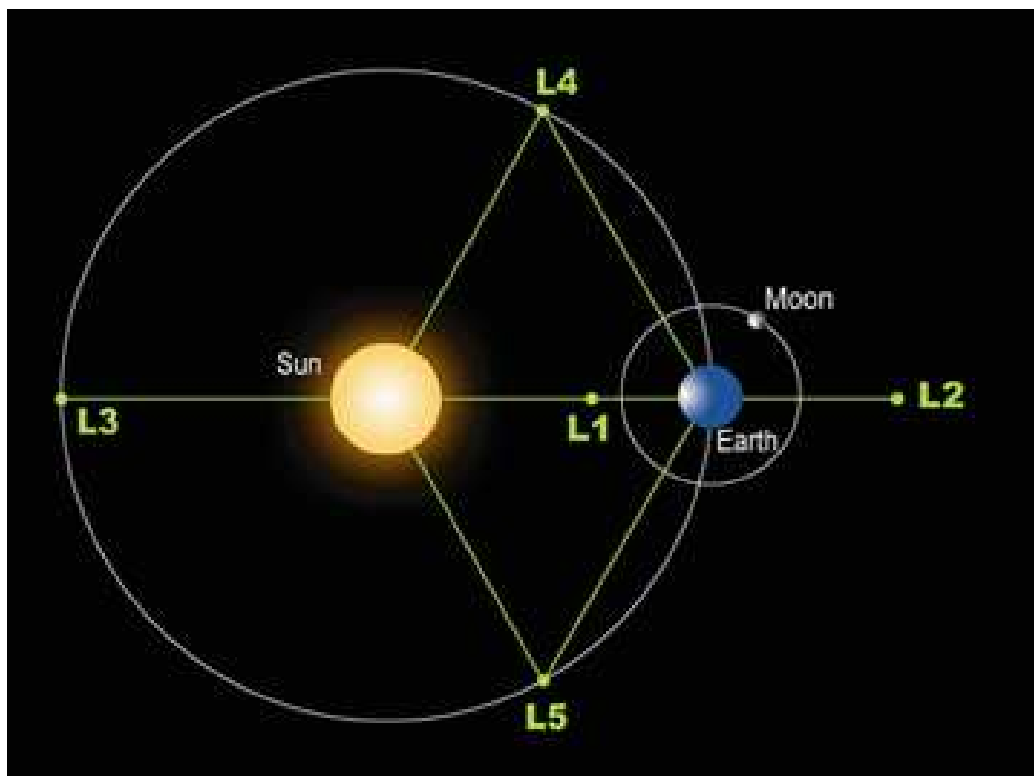

Transfer strategies to the L_3 libration point of the Sun-Earth system

MSc Thesis



Marco Tantardini

Delft, 20th November 2009

Transfer strategies to the L_3 libration point of the Sun-Earth system

MSc Thesis

Marco Tantardini

Delft, 20th November 2009

Ce jour-là, j'ai bien cru tenir quelque chose et que ma vie s'en trouverait changée.

Comme une eau, le monde vous traverse et pour un temps vous prête ses couleurs. Puis se retire, et vous place devant ce vide qu'on porte en soi, devant cette espèce d'insuffisance centrale de l'âme qu'il faut bien apprendre à côtoyer, à combattre, et qui, paradoxalement, est peut-être notre moteur le plus sûr.

[*Nicolas Bouvier, L'Usage du monde*]

Acknowledgement

Oh, well: the journey has been quite long, sometimes hard, sometimes exciting.

I still remember the day I was coming to Delft: last week of August, reading a book on the train, three bad years behind. I immediately fell in love with TU Delft and the teaching style I found. One week, and I extended my Erasmus into a full Master program. Definitely a turning moment.

A good year, but I wanted to see more: I have been lucky and persistent enough to live in California for ten months. Then thirty days travelling all over Tanzania, and finally back to old Europe. I found myself in Barcelona.

I want to thank Prof. Gerard Gomez and Prof. Josep Masdemont, my thesis supervisors in Barcelona, for letting me work with them and their research group.

I do want to thank Prof. Ron Noomen, my thesis advisor at TU Delft, for what he taught me, the interesting and informal discussions we had, and for letting me work on my thesis abroad.

Dr. Elena Fantino, my thesis co-supervisor, has been a friend and helped me at any time, weekdays and weekends: I have learnt much through her supervision.

Dr. Yuan Ren has given me many valuable advices, and much support especially for the L_1/L_2 Manifolds part and the Low Thrust study, while Ing. Pierpaolo Pergola helped me in the Gravity Assisted Transfers section.

I want to thank Prof. Antonella Geroldi, my Mathematics teacher in High School, for giving me a solid foundation, and Prof. Karel F. Wakker of TU Delft, for introducing me to the subject of Astrodynamics: his lecture notes have followed me all over the world.

When I was just a student with no experience, Ing. Antonio Carosi was the very first person who believed in me, giving me the opportunity to challenge myself and dream wider.

Thanks to Dr. Silvano Casini, who helped me reach California; and, when I returned, helped me get in touch with the Barcelona UB-UPC Dynamical

Systems Group. I hope I have fulfilled his trust.

When I was still in Europe, trying to find an internship in the United States, Dr. John M. Logsdon introduced me to The Planetary Society.

I do not have enough words to express my gratitude to Connie and Dr. Louis Friedman, Founder and Executive Director of The Planetary Society. They made me feel at home, and all those good memories will always be with me: from gardening on Sunday mornings, to discussing space exploration, from going to the Disney Hall or watching the opera live in HD, to studying the end of life of solar sail Cosmos 2. And I will not forget the staff of The Planetary Society.

Finally, I want to thank Dr. Simon Pete Worden, Director of the NASA Ames Research Center, for giving me the opportunity to work at the Mission Design Center of the NASA Ames.

My parents and my sister, my grandparents, my friends: they all know. *There's no need to say another word.*

Marco Tantardini

Contents

Acknowledgement	vii
List of Tables	xiii
List of Figures	xv
Nomenclature	xxiii
1 Introduction	1
1.1 Orbiting near Sun-Earth L_3 : Science	2
1.1.1 Space Weather and Monitoring the Sun	3
1.2 Missions to the Libration points, plus Stereo	6
1.2.1 ISEE-3: International Sun-Earth Explorer 3	7
1.2.2 WIND	9
1.2.3 SOHO: Solar Heliospheric Observatory	10
1.2.4 ACE: Advanced Composition Explorer	12
1.2.5 WMAP: Wilkinson Microwave Anisotropy Probe	13
1.2.6 GENESIS	15
1.2.7 HERSCHEL SPACE OBSERVATORY	16
1.2.8 PLANCK	18
1.2.9 GAIA	19
1.2.10 JWST: James Webb Space Telescope	21
1.2.11 DARWIN	22
1.2.12 TPF: Terrestrial Planet Finder	23
1.2.13 SAFIR: Single Aperture Far-Infrared Observatory	25
1.2.14 STEREO	26

2	Fundamental concepts of Astrodynamics	29
2.1	Fundamental Laws	29
2.1.1	Newton's Law of Motion	29
2.1.2	Newton's Law of Gravitation	30
2.2	n -body Problem	31
2.2.1	Integrals of motion	32
3	Circular Restricted 3-Body Problem	35
3.1	Equations of motion	35
3.2	Jacobi's integral	39
3.3	Surfaces of Hill	40
3.4	Lagrange libration points	42
3.5	Computation of the location of L_3	44
3.6	Stability in the Lagrange libration points	46
3.6.1	Collinear Lagrange points: stability	47
3.6.2	Equilateral Lagrange points: stability	48
3.7	Motion about the Lagrange libration points	49
3.7.1	Collinear Lagrange libration points	49
3.7.2	Equilateral Lagrange libration points	50
3.8	Hamiltonian formulation	50
3.9	Periodic orbits around the Libration points	53
3.9.1	Equations of motion	53
3.9.2	Lissajous orbits	56
3.9.3	Lyapunov orbits	59
3.9.4	Halo orbits and quasi-halo orbits	60
4	Transfers using High Thrust in the 2BP Sun-spacecraft	63
4.1	2-burn single-revolution tangential transfer	64
4.2	Bi-elliptic single-revolution transfer	67
4.3	Bi-elliptic one-tangent burn transfer	70
4.4	2-burn multi-revolution tangential transfer	72

5	Reaching Lyapunov orbits near L_3 through the manifolds	77
5.1	Finding symmetric periodic orbits: initial condition	78
5.2	Periodic orbits: definition	79
5.3	Variational equations: search of the initial condition and of the period	80
5.4	Lyapunov orbits near L_3 : results	82
5.5	Manifolds: theorems and procedure	84
5.5.1	Definition of invariant subspace	84
5.5.2	The Stable Manifold theorem	84
5.5.3	Floquet's theorem	85
5.5.4	The Stable Manifold theorem for a periodic orbit	87
5.5.5	Numerical method to compute the Manifolds	87
5.6	Numerical Results: manifolds of a family of Lyapunov orbits near L_3	89
5.7	Numerical Results: manifolds of Lyapunov orbits near L_1 and L_2 reaching Lyapunov orbits near L_3	91
6	Transfers using Low Thrust	101
6.1	Preliminary investigation: RTBP	102
6.2	Optimal heliocentric cruise segment in 2BP	112
6.2.1	Pontryagin minimum principle	113
6.2.2	Optimization model in cartesian coordinate system	114
6.2.3	Indirect Method	115
6.3	Numerical results: 2BP and constant acceleration	117
6.4	From the optimization in 2BP to RTBP	124
6.5	Optimization in 2BP and integration in RTBP, taking into account the mass flow	128
7	Gravity Assisted Transfers	133
7.1	Definition of the problem: assumptions and procedure	134
7.2	Equations for the Gravity Assist	135
7.2.1	Unpowered Swing-by	135
7.2.2	Powered Swing-by	136
7.3	Numerical results: Single and Multiple Gravity Assisted Transfers	139

8	Conclusions and possible future developments	145
	Bibliography	147
A	Family of Lyapunov Orbits near L_3	1
B	Runge-Kutta Methods for Integration	3

List of Tables

1.1	List of missions to the Libration points of the Sun-Earth system	6
3.1	μ , position of L_3 from the baricenter of the system, r_1 and r_2	45
4.1	r_b and ΔV_{Tot} for the cases of $n = 1, 3, 5, 7, 9$ for the 2-burn single-revolution tangential transfer ($1 AU = 149598000 km$)	66
4.2	r_b , ΔV_a , ΔV_c and ΔV_{Tot} for the cases of $n = 1, 3, 5, 7, 9$ for the bi-elliptic single-revolution transfer ($1 AU = 149598000 km$)	69
4.3	ΔV_b in [m/s] for the cases of $n = 1, 3, 5, 7, 9$ for the bi-elliptic single-revolution transfer	69
4.4	ΔV_{Tot} for different combinations of (r_b -Total time to reach L_3) for the bi-elliptic one-tangent burn transfer	70
4.5	r_b , ΔV_{Tot} and mass consumption for the cases of $n = 3, 5, 7, \dots, 23$ for the 2-burn multi-revolution transfer ($1 AU = 149598000 km$)	75
6.1	Transfer with Low Thrust: results of the optimization in 2BP, constant acceleration	117
7.1	Overview of the transfer trajectory to Sun-Earth L_3 through Gravity Assist with Mars: data found through global and local optimization	140
7.2	Overview of the transfer trajectory to Sun-Earth L_3 through multiple Gravity Assist with Venus-Venus-Earth: data found through global and local optimization	142
7.3	Overview of the transfer trajectory to Sun-Earth L_3 through Gravity Assist with Earth: data found through global and local optimization	144
7.4	Explored sequences of Gravity Assisted transfers trajectories to Sun-Earth L_3 : ΔV_{Tot} found through global and local optimization	144
A.1	Initial Condition (x_0 and \dot{y}_0), Period and Jacobi constant for the family of Lyapunov orbits generated near the libration point L_3 of the Sun-Earth system	2

List of Figures

1.1	Lagrange points, Sun-Earth system	1
1.2	Space Weather: scheme [http://sohowww.nascom.nasa.gov/]	3
1.3	Artist impression of Earth's Magnetosphere [http://sohowww.nascom.nasa.gov/]	4
1.4	Artist impression of Earth's Magnetosphere changed by CMEs [http://sohowww.nascom.nasa.gov/]	4
1.5	An image sequence showing the progress over eight hours of a clearly defined CME on 5-6 August 1999 [http://sohowww.nascom.nasa.gov/]	5
1.6	ISEE-3 trajectory [<i>Canalias et al., 2004</i>]	8
1.7	Wind orbit (Dec 17, 2007 - Jun 14, 2008) [<i>Official website</i>]	9
1.8	Picture of the Sun taken by SOHO on Sept 14, 1999 [<i>Official website</i>]	11
1.9	ACE Lissajous orbit near Sun-Earth L_1 [<i>Official website</i>]	12
1.10	WMAP trajectory [<i>Official website</i>]	14
1.11	Overview of Genesis trajectory [<i>Official website</i>]	16
1.12	3D model of Herschel spacecraft [<i>Official website</i>]	17
1.13	Planck orbit [<i>Official website</i>]	19
1.14	GAIA orbit [<i>Official website</i>]	20
1.15	Artist's impression of the JWST [<i>Official website</i>]	22
1.16	One of Darwin's telescopes [<i>Official website</i>]	23
1.17	Artist's impression of TPF-I [<i>Official website</i>]	24
1.18	Artist's impression of TPF-C [<i>Official website</i>]	24
1.19	A SAFIR concept based on the segmented-mirror technology to be employed for the JWST [<i>Official website</i>]	26
1.20	Stereo Orbit Description [http://stereo.jhuapl.edu]	27

1.21	Stereo Orbit. Left: Heliocentric Inertial Coordinates (Ecliptic Plane Projection); Right: Geocentric Solar Ecliptic Coordinates Fixed Earth-Sun Line (Ecliptic Plane Projection) [http://stereo.jhuapl.edu]	27
2.1	A system of n particles with respect to an inertial reference system [<i>Wakker, 2005</i>]	32
3.1	Reference frames in the CR3BP	36
3.2	Surfaces of Hill projected on XY-plane for decreasing values of C	41
3.3	Equilibrium points of the CR3BP problem in the xy -plane of the frame rotating with the mean motion of the orbit of m_1 and m_2	43
3.4	Location of the collinear equilibrium points and the primaries for $\mu \in [0, 0.5]$ [<i>Szebehely, 1967</i>]	44
3.5	Notation for the computation of $x = x(L_3)$ [<i>Szebehely, 1967</i>]	44
3.6	Richardson's reference system centered at the equilibrium point L_1 [<i>Richardson, 1980</i>]	54
3.7	Types of libration orbits. Top left: Halo orbit (xyz representation). Top right: Lissajous type orbit (xyz representation). Bottom left: planar Lyapunov orbit (xy projection). Bottom right: vertical Lyapunov orbit (yz projection) [<i>Canalias et al., 2004</i>]	62
3.8	Several types of orbits around L_1 . Upper left: vertical Lyapunov periodic orbit. Upper right: Quasi-periodic orbit around a vertical periodic orbit (Lissajous orbit). Lower left: halo periodic orbit. Lower right: quasi-halo orbit (quasi-periodic orbit around a halo orbit) [<i>Canalias et al., 2004</i>]	62
4.1	Scheme of the 2-burn single-revolution tangential transfer starting and ending at the same Sun distance (for two different values of aphelion distance)	64
4.2	ΔV_{Tot} for the 2-burn single-revolution tangential transfer for a range of orbital periods multiple of $\frac{T_{Earth}}{2}$ (with a phase difference of π), $n = [1, 3, 5, \dots, 99]$	65
4.3	Scheme of a bi-elliptic single-revolution transfer, from a circular orbit to a circular orbit with a bigger radius	67
4.4	ΔV_{Tot} for the bi-elliptic single-revolution transfer for a range of orbital periods multiple of $\frac{T_{Earth}}{2}$ (with a phase difference of π), $n = [1, 3, 5, \dots, 99]$	68
4.5	Scheme of the bi-elliptic one-tangent burn transfer, starting at distance from the Sun of 1 AU, and ending in L_3 at a distance r_1 , after $3/2 \pi$ of the revolution about the Sun	71
4.6	Scheme of the 2-burn multi-revolution transfer: applied ΔV s	72

4.7	Scheme of the 2-burn multi-revolution transfer: Earth and s/c dephased by angle φ	72
4.8	ΔV_{Tot} for the 2-burn multi-revolution transfer for a range of transfer periods multiple of $\frac{T_{Earth}}{2}$ (with a phase difference of π) , $n = [3, 5, 7, \dots, 99]$	74
4.9	Mean motion for the 2-burn multi-revolution transfer for a range of transfer periods multiple of $\frac{T_{Earth}}{2}$ (with a phase difference of π) , $n = [3, 5, 7, \dots, 150]$	75
5.1	Family of Lyapunov orbits near Sun-Earth L_3 in the RTBP reference frame: Earth (left), Sun (center) and Lyapunov orbits near L_3 (right)	82
5.2	Family of Lyapunov orbits near Sun-Earth L_3 in the RTBP reference frame	83
5.3	Behaviour of stable manifold of the smallest Lyapunov orbit of the family integrated for a long time span, RTBP reference frame . . .	89
5.4	Behaviour of stable manifold of the biggest Lyapunov orbit of the family integrated for a long time span, RTBP reference frame . . .	90
5.5	Horseshoe orbit of Asteroid 2002 AA29 [NASA www.neo.jpl.nasa.gov]	90
5.6	Plot of the unstable manifolds of Lyapunov orbits near L_1 (blue) and L_2 (red) reaching Lyapunov orbits near L_3 , RTBP reference frame	91
5.7	Plot of the chosen Lyapunov orbits near L_1 (blue) and L_2 (red) and the departing unstable manifolds, RTBP reference frame	92
5.8	Intersection of the unstable manifolds of Lyapunov orbits near L_1 (blue) and L_2 (red) with the family of Lyapunov orbits near L_3 , RTBP reference frame: Zoom	92
5.9	Plot of the ΔV required to insert the manifolds of Lyapunov orbits near L_1 into the intersecting Lyapunov orbits near L_3	93
5.10	Plot of the ΔV required to insert the manifolds of Lyapunov orbits near L_2 into the intersecting Lyapunov orbits near L_3	94
5.11	Plot of the ΔV required to insert the manifolds of Lyapunov orbits near L_1 into the intersecting Lyapunov orbits near L_3 as a function of time on the progenitor Lyapunov orbit	95
5.12	Plot of the transfer time on the manifolds of Lyapunov orbits near L_1 to the intersecting Lyapunov orbits near L_3 as a function of time on the progenitor Lyapunov orbit	95
5.13	Plot of the ΔV required to insert the manifolds of Lyapunov orbits near L_2 into the intersecting Lyapunov orbits near L_3 as a function of time on the progenitor Lyapunov orbit	96

5.14	Plot of the transfer time on the manifolds of Lyapunov orbits near L_2 to the intersecting Lyapunov orbits near L_3 as a function of time on the progenitor Lyapunov orbit	96
5.15	Plot of the orbits on the manifold of the Lyapunov orbit near L_1 with the minimum and maximum TOF, RTBP reference frame . .	98
5.16	Plot of the orbits on the manifold of the Lyapunov orbit near L_1 with the minimum and maximum TOF, RTBP reference frame: Zoom	98
5.17	Plot of the orbits on the manifold of the Lyapunov orbit near L_2 with the minimum and maximum TOF, RTBP reference frame . .	99
5.18	Plot of the orbits on the manifold of the Lyapunov orbit near L_2 with the minimum and maximum TOF, RTBP reference frame: Zoom	99
6.1	Low Thrust, preliminary investigation. $M = 5 * 10^{-4} m/s^2$, $\theta = 0$, $T_{final} = 40 y$, Value of the Jacobi Constant (when the thrust is turned off) $C = 2.99933595$, Low Thrust ON within the SI of the Earth, RTBP reference frame	103
6.2	Low Thrust, preliminary investigation. Zoom: $M = 5 * 10^{-4} m/s^2$, $\theta = 0$, $T_{final} = 40 y$, Value of the Jacobi Constant (when the thrust is turned off) $C = 2.99933595$, Low Thrust ON within the SI of the Earth, RTBP reference frame	104
6.3	Low Thrust, preliminary investigation. $M = 5 * 10^{-4} m/s^2$, $\theta = \pi$, $T_{final} = 40 y$, Value of the Jacobi Constant (when the thrust is turned off) $C = 2.99934005$, Low Thrust ON within the SI of the Earth, RTBP reference frame	104
6.4	Low Thrust, preliminary investigation. Zoom: $M = 5 * 10^{-4} m/s^2$, $\theta = \pi$, $T_{final} = 40 y$, Value of the Jacobi Constant (when the thrust is turned off) $C = 2.99934005$, Low Thrust ON within the SI of the Earth, RTBP reference frame	105
6.5	Low Thrust, preliminary investigation. $M = 5 * 10^{-4} m/s^2$, $\theta = \frac{\pi}{2}$, $T_{final} = 10 y$, Value of the Jacobi Constant (when the thrust is turned off) $C = 2.99933524$, Low Thrust ON within the SI of the Earth, RTBP reference frame	105
6.6	Low Thrust, preliminary investigation. $M = 5 * 10^{-4} m/s^2$, $\theta = \frac{3\pi}{2}$, $T_{final} = 10 y$, Value of the Jacobi Constant (when the thrust is turned off) $C = 2.99933387$, Low Thrust ON within the SI of the Earth, RTBP reference frame	106
6.7	Low Thrust, preliminary investigation. $M = 1 * 10^{-3} m/s^2$, $\theta = 0$, $T_{final} = 10 y$, Value of the Jacobi Constant (when the thrust is turned off) $C = 2.99781043$, Low Thrust ON within the SI of the Earth, RTBP reference frame	106

-
- 6.8 Low Thrust, preliminary investigation. Zoom: $M = 1 * 10^{-3} m/s^2$, $\theta = 0$, $T_{final} = 10 y$, Value of the Jacobi Constant (when the thrust is turned off) $C = 2.99781043$, Low Thrust ON within the SI of the Earth, RTBP reference frame 107
- 6.9 Low Thrust, preliminary investigation. $M = 1 * 10^{-3} m/s^2$, $\theta = \pi$, $T_{final} = 10 y$, Value of the Jacobi Constant (when the thrust is turned off) $C = 2.99781362$, Low Thrust ON within the SI of the Earth, RTBP reference frame 107
- 6.10 Low Thrust, preliminary investigation. $M = 1 * 10^{-3} m/s^2$, $\theta = \frac{\pi}{2}$, $T_{final} = 10 y$, Value of the Jacobi Constant (when the thrust is turned off) $C = 2.99782615$, Low Thrust ON within the SI of the Earth, RTBP reference frame 108
- 6.11 Low Thrust, preliminary investigation. $M = 1 * 10^{-3} m/s^2$, $\theta = \frac{3\pi}{2}$, $T_{final} = 10 y$, Value of the Jacobi Constant (when the thrust is turned off) $C = 2.99782617$, Low Thrust ON within the SI of the Earth, RTBP reference frame 108
- 6.12 Low Thrust, preliminary investigation. Zoom: $M = 1 * 10^{-3} m/s^2$, $\theta = \frac{3\pi}{2}$, $T_{final} = 10 y$, Value of the Jacobi Constant (when the thrust is turned off) $C = 2.99782617$, Low Thrust ON within the SI of the Earth, RTBP reference frame 109
- 6.13 Low Thrust, preliminary investigation. $M = 5 * 10^{-3} m/s^2$, $\theta = 0$, $T_{final} = 5 y$, Value of the Jacobi Constant (when the thrust is turned off) $C = 2.98503654$, Low Thrust ON within the SI of the Earth, RTBP reference frame 109
- 6.14 Low Thrust, preliminary investigation. Zoom: $M = 5 * 10^{-3} m/s^2$, $\theta = 0$, $T_{final} = 5 y$, Value of the Jacobi Constant (when the thrust is turned off) $C = 2.98503654$, Low Thrust ON within the SI of the Earth, RTBP reference frame 110
- 6.15 Low Thrust, preliminary investigation. $M = 5 * 10^{-3} m/s^2$, $\theta = \pi$, $T_{final} = 5 y$, Value of the Jacobi Constant (when the thrust is turned off) $C = 2.98504074$, Low Thrust ON within the SI of the Earth, RTBP reference frame 110
- 6.16 Low Thrust, preliminary investigation. $M = 5 * 10^{-3} m/s^2$, $\theta = \frac{\pi}{2}$, $T_{final} = 5 y$, Value of the Jacobi Constant (when the thrust is turned off) $C = 2.98503310$, Low Thrust ON within the SI of the Earth, RTBP reference frame 111
- 6.17 Low Thrust, preliminary investigation. $M = 5 * 10^{-3} m/s^2$, $\theta = \frac{3\pi}{2}$, $T_{final} = 5 y$, Value of the Jacobi Constant (when the thrust is turned off) $C = 2.98503416$, Low Thrust ON within the SI of the Earth, RTBP reference frame 111
- 6.18 Optimization in 2BP, Trajectory: L_1 , $M = 5 * 10^{-4} m/s^2$, $T_{final} = 1 y 9 d$ 118
- 6.19 Optimization in 2BP, Angle: L_1 , $M = 5 * 10^{-4} m/s^2$, $T_{final} = 1 y 9 d$ 118

6.20 Optimization in 2BP, Trajectory: L_2 , $M = 5 * 10^{-4} m/s^2$, $T_{final} = 1 y 40 d$	119
6.21 Optimization in 2BP, Angle: L_2 , $M = 5 * 10^{-4} m/s^2$, $T_{final} = 1 y 40 d$	119
6.22 Optimization in 2BP, Trajectory: L_1 , $M = 1 * 10^{-3} m/s^2$, $T_{final} = 269 d$	120
6.23 Optimization in 2BP, Angle: L_1 , $M = 1 * 10^{-3} m/s^2$, $T_{final} = 269 d$	120
6.24 Optimization in 2BP, Trajectory: L_2 , $M = 1 * 10^{-3} m/s^2$, $T_{final} = 282 d$	121
6.25 Optimization in 2BP, Angle: L_2 , $M = 1 * 10^{-3} m/s^2$, $T_{final} = 282 d$	121
6.26 Optimization in 2BP, Trajectory: L_1 , $M = 5 * 10^{-3} m/s^2$, $T_{final} = 143 d$	122
6.27 Optimization in 2BP, Angle: L_1 , $M = 5 * 10^{-3} m/s^2$, $T_{final} = 143 d$	122
6.28 Optimization in 2BP, Trajectory: L_2 , $M = 5 * 10^{-3} m/s^2$, $T_{final} = 146 d$	123
6.29 Optimization in 2BP, Angle: L_2 , $M = 5 * 10^{-3} m/s^2$, $T_{final} = 146 d$	123
6.30 Integrating in RTBP the optimized results in 2BP, Trajectory: L_1 , integration in RTBP $M = 5 * 10^{-4} m/s^2$, $T_{final} = 1 y 9 d$	124
6.31 Integrating in RTBP the optimized results in 2BP, Trajectory: L_2 , integration in RTBP $M = 5 * 10^{-4} m/s^2$, $T_{final} = 1 y 40 d$	125
6.32 Integrating in RTBP the optimized results in 2BP, Trajectory: L_1 , integration in RTBP $M = 1 * 10^{-3} m/s^2$, $T_{final} = 269 d$	125
6.33 Integrating in RTBP the optimized results in 2BP, Trajectory: L_2 , integration in RTBP $M = 1 * 10^{-3} m/s^2$, $T_{final} = 282 d$	126
6.34 Integrating in RTBP the optimized results in 2BP, Trajectory: L_1 , integration in RTBP $M = 5 * 10^{-3} m/s^2$, $T_{final} = 143 d$	126
6.35 Integrating in RTBP the optimized results in 2BP, Trajectory: L_2 , integration in RTBP $M = 5 * 10^{-3} m/s^2$, $T_{final} = 146 d$	127
6.36 Optimization in 2BP, Trajectory: L_1 , $T = 90 mN$, $I_{sp} = 3100 s$, $m_0 = 500 kg$, $m_{final} = 355 kg$, $T_{final} = 1 y 201 d$	128
6.37 Optimization in 2BP, Angle: L_1 , $T = 90 mN$, $I_{sp} = 3100 s$, $m_0 = 500 kg$, $m_{final} = 355 kg$, $T_{final} = 1 y 201 d$	129
6.38 Integrating in RTBP the optimized results in 2BP, Trajectory: L_1 , integration in RTBP $T = 90 mN$, $I_{sp} = 3100 s$, $m_0 = 500 kg$, $m_{final} = 355 kg$, $T_{final} = 1 y 201 d$	129
6.39 Optimization in 2BP, Trajectory: L_2 , $T = 90 mN$, $I_{sp} = 3100 s$, $m_0 = 500 kg$, $m_{final} = 339 kg$, $T_{final} = 1 y 264 d$	130

6.40	Optimization in 2BP, Angle: L_2 , $T = 90 \text{ mN}$, $I_{sp} = 3100 \text{ s}$, $m_0 = 500 \text{ kg}$, $m_{final} = 339 \text{ kg}$, $T_{final} = 1 \text{ y } 264 \text{ d}$	130
6.41	Integrating in RTBP the optimized results in 2BP, Trajectory: L_2 , integration in RTBP $T = 90 \text{ mN}$, $I_{sp} = 3100 \text{ s}$, $m_0 = 500 \text{ kg}$, $m_{final} = 339 \text{ kg}$, $T_{final} = 1 \text{ y } 264 \text{ d}$	131
7.1	Scheme of the unpowered swing-by	136
7.2	Scheme of the powered swing-by	137
7.3	Results of direct transfer Earth-L_3	139
7.4	Results of the Gravity Assisted transfer trajectory Earth-Mars-L_3	140
7.5	Results of the Gravity Assisted transfer trajectory Earth-Venus-Venus-Earth-L_3	141
7.6	Results of the Gravity Assisted transfer trajectory Earth-Earth-L_3	143

Nomenclature

Roman Symbols

a	Semi-Major Axis	[m]
c	Constant	[-]
C	Jacobi constant	[AU ² TU ⁻²]
e	Eccentricity	[-]
E	Subspace	[-]
g	Gravitational Acceleration	[m s ⁻²]
G	Gravitational Constant: $6.67259 \cdot 10^{-11}$	[m ³ kg ⁻¹ s ⁻²]
H	Angular Momentum	[m ² s ⁻¹]
I_{sp}	Specific Impulse	[s]
k	Constant	[-]
L	Lagrangian function	[-]
m	Mass	[kg]
M	Constant acceleration	[m s ⁻²]
M	Monodromy matrix	[-]
P_n	Legendre Function	
r	Radius	[m]
S	Angular coordinate	[°]
t	Time	[s]
T	Revolution Period	[s]
T	Thrust	[N]
U	Gravity Potential	[m ² s ⁻²]
V	Velocity	[m s ⁻¹]
W	Manifold	[-]

Greek Symbols

Δ	Change	[-]
ζ	Coordinate in (pseudo)-inertial reference frame	[m]
η	Coordinate in (pseudo)-inertial reference frame	[m]
ϕ	Phase Angle	[°]
Φ	State transition matrix	[-]
Γ	Periodic orbit	[-]
λ	Constant	[-]
λ	Eigenvalue	[-]
μ	Gravitational Parameter	[m ³ s ⁻²]
ν	Constant	[-]
ξ	Coordinate in (pseudo)-inertial reference frame	[m]

ω	Angular velocity	[rad s ⁻¹]
ω	Constant	[-]
ψ	Phase Angle	[°]

Subscripts

<i>a</i>	Arrival
<i>d</i>	Departure
<i>f</i>	Final
<i>i</i>	Initial
<i>i, j, k</i>	Identifiers for Different Bodies
<i>k</i>	Kinetic
<i>max</i>	Maximum
<i>min</i>	Minimum
<i>n</i>	Degree of Legendre Function
<i>p</i>	Potential
<i>Per</i>	Pericenter
<i>sid</i>	Sideral
<i>sp</i>	Specific
<i>Tot</i>	Total
<i>tr</i>	Transfer

Acronyms

3BP	3-Body Problem
ACE	Advanced Composition Explorer
CME	Coronal Mass Ejection
CR3BP	Circular Restricted 3-Body Problem
CSA ASC	Canadian Space Agency
DLS	Double Lunar Swingby
EP	Electric Propulsion
ESA	European Space Agency
EVA	Extra-Vehicular Activity
GA	Gravity Assist
GEO	Geostationary Earth Orbit
GTO	Geostationary Transfer Orbit
ISEE-3	International Sun-Earth Explorer 3
ISS	International Space Station
ISTP	International Solar Terrestrial Physics
JWST	James Webb Space Telescope
L1	Lagrange Point 1
L2	Lagrange Point 2
L3	Lagrange Point 3
L4	Lagrange Point 4
L5	Lagrange Point 5
LEO	Low Earth Orbit
NASA	National Aeronautics and Space Administration
NEO	Near Earth Object
NOAA	National Oceanic and Atmospheric Administration
S/C	Spacecraft

SAFIR	Single Aperture Far-Infrared Observatory
SEP	Solar Energetic Protons
SI	Sphere of Influence
SOHO	Solar Heliospheric Observatory
TOF	Time of Flight
TPF	Terrestrial Planet Finder
WMAPS	Wilkinson Microwave Anisotropy Probe

Chapter 1

Introduction

The aim of the present research is to study possible ways to transfer from the vicinity of the Earth to the vicinity of the Lagrange collinear point L_3 of the Sun-Earth system (Figure (1.1)). Such a study aims at performing an investigation into an area that is so far little explored: the vicinity of L_3 has never been the destination of a space mission due to its far distance from the Earth and to the serious communication problems involved. In particular, this research will focus on the transfer trajectory in order to obtain ΔV s and transfer times for different initial conditions and approaches to the problem, since in literature there is a big gap about transfers to Sun-Earth L_3 .

First, possible reasons to plan a mission to L_3 will be discussed, and in particular we will focus on Space Weather and Monitoring the Sun. A gallery of missions to the the Libration points, plus Stereo, will follow, and in *Chapter 2* and *Chapter 3* Fundamental concepts of Astrodynamics and the Circular Restricted 3-Body Problem (CR3BP) will be treated. Then, we will consider four different approaches to reach L_3 (or orbits near the libration point): *Chapter 4* will focus on High Thrust transfers in the 2-Body Problem (2BP) Sun-spacecraft, in *Chapter 5* a family of Lyapunov orbits near L_3 will be studied, as the transfer through the manifolds of either these Lyapunov orbits or of Lyapunov orbits near L_1/L_2 (in the framework of the CR3BP). In *Chapter 6* transfer trajectories with Low Thrust will be considered, and in *Chapter 7* we will analyse Gravity-Assisted Transfers using High Thrust. In *Chapter 8* the conclusions will be drawn.

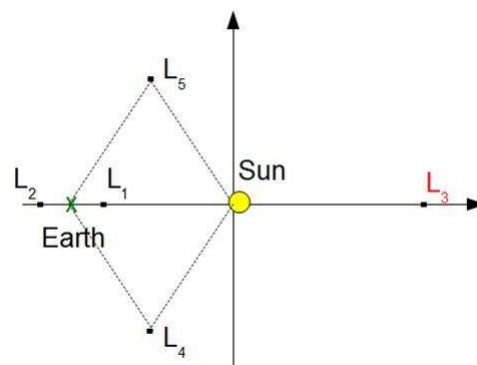


Figure 1.1 Lagrange points, Sun-Earth system

1.1 Orbiting near Sun-Earth L_3 : Science

The aim of this research is to explore transfers to the Sun-Earth Libration point L_3 with a range of techniques as wide as possible, in order to obtain values in terms of ΔV and flight time for each approach. Therefore, since this investigation does not want to be a mission proposal but a study about Celestial Mechanics, giving a reason to reach L_3 is not the primary concern of the research. The philosophy is: let's study how to go there, then in the future, with the technology of the time, a reason to put a spacecraft near L_3 will be found. However, here we would like to mention few possible reasons to design a mission to this libration point.

Before proceeding, it is important to remind that so far no missions have been planned to L_3 (when SOHO was designed there was the idea of having a second spacecraft near L_3 , but then this secondary mission was not developed) since this region presents some challenges which are hard to be overcome, especially concerning communications: a direct communication spacecraft-Earth is not possible if the probe is put in L_3 (there is the Sun in between). This could be solved in two ways: designing a big orbit (Lyapunov, in our research) near L_3 , in such a way that at some parts of the orbit the spacecraft can communicate with the Earth (as we will see, this leads to a Lyapunov orbit with a semi-amplitude in the y -direction of order 0.1 AU), or bounce the signal to other spacecraft that, at the time of the possible mission, would be visible (for example, near the equilateral point L_4 and/or L_5). Moreover a spacecraft near L_3 suffers of big perturbations due to Venus, which comes within 0.3 AU of L_3 every 20 months.

Three possible reasons to do science orbiting near L_3 are the following:

- Perform some kind of relativity experiments
- Near Earth Objects (NEOs) tracking
- Monitor the Sun

As for the first one, L_3 may offer a privileged site to perform relativity experiments, such as measuring the gravitational bending of light on behalf of the Sun. However, this should be explored more in detail, and probably such relativity testing has already been done when Cassini was near superior conjunction [*Bertotti, 2003*].

Concerning NEOs tracking [*Stokes, 2003*], the idea would be to monitor in real time regions of the sky that at a given time are not visible from the Earth or the satellites used to track NEOs, because of the presence of the Sun. However, it is true that there is a sort of blind spot at superior conjunction, and an observing platform near L_3 would help to solve that problem, but from a discovery perspective a superior observing location would be on an interior orbit, with a period of 6-9 months, what is usually called a Venus-trailing orbit. This puts the spacecraft interior to Earth, so it can find objects 1 AU from the Sun at full phase, something that does not happen so much at Earth or L_3 . More

importantly, the spacecraft circulates faster than Earth, and so it easily sweeps up objects that would lurk in Earth's blind spot for decades at a time. Therefore, while an L_3 NEO mission might be useful, it does not look as the most attractive choice.

Monitoring the Sun, and especially the evolution of its active regions, at the moment looks the best reason to plan a scientific mission near the Sun-Earth L_3 point.

In the following section *space weather* will be briefly addressed [www.swpc.noaa.gov]. The "philosophy" of the possible mission will be also briefly outlined.

1.1.1 Space Weather and Monitoring the Sun

The Sun's activity causes large changes in the Sun's plasma and energetic par-

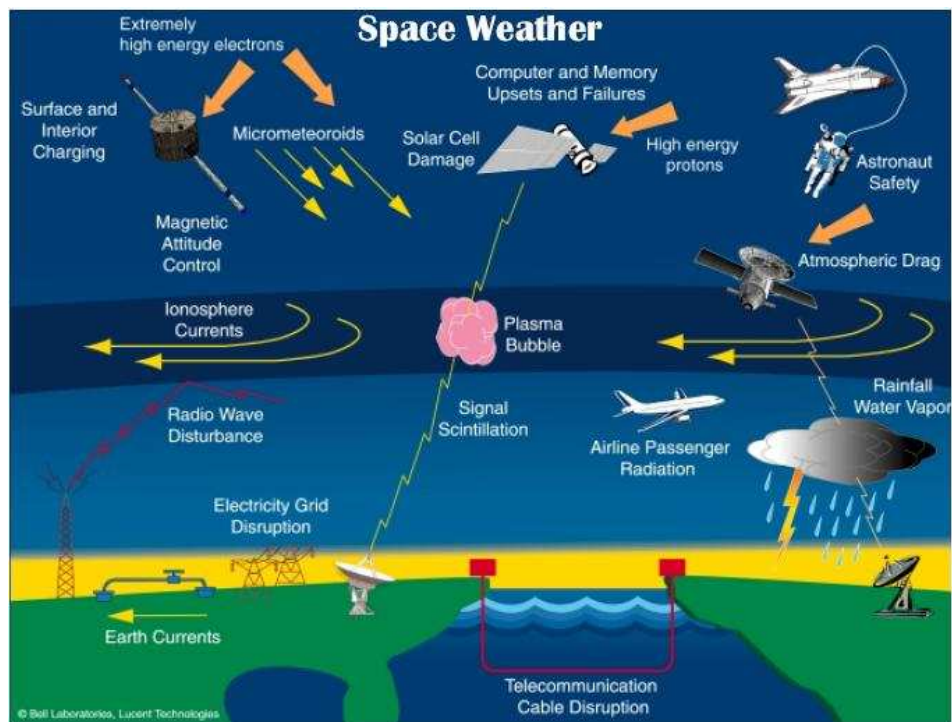


Figure 1.2 Space Weather: scheme [http://sohowww.nascom.nasa.gov/]

ticle populations, and these changes are responsible for the *space weather* that affects Earth. Space weather can impact the upper atmosphere and may influence long-term climate trends. The effects are related to Coronal Mass Ejections (CMEs), Solar Energetic Protons (SEPs), and coronal holes, the source of high-speed streams. CMEs are powerful eruptions that can eject a small part of the Sun's atmosphere into interplanetary space, and despite their importance at the moment scientist do not fully understand their origin and evolution.

The Sun has an 11-year cycle of activity determined by the reversal of its magnetic poles. During the solar minimum, the Sun may churn out a strong CME every two or three days; that's approximately 180 CMEs per year, though

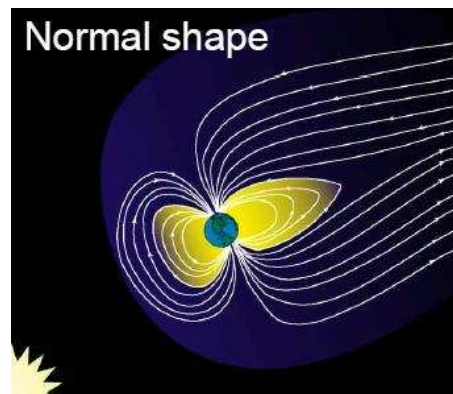


Figure 1.3 Artist impression of Earth's Magnetosphere [<http://sohowww.nascom.nasa.gov/>]

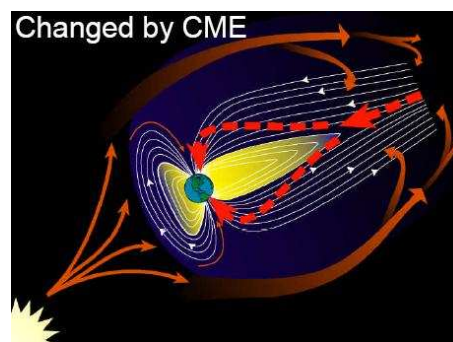


Figure 1.4 Artist impression of Earth's Magnetosphere changed by CMEs [<http://sohowww.nascom.nasa.gov/>]

only about 10-15 CMEs are directed at Earth. During solar maximum, the Sun averages five CMEs daily, and sends about 100 Earthward per year. The last solar maximum took place approximately 2000-2001. The largest storms occur when a fast CME hits Earth shortly after its shock arrives. Geomagnetic storms, which are magnetic storms on Earth due to solar activity (see Figures (1.3) and (1.4)), produce aurora borealis and aurora australis. However, they can also cause a variety of highly undesirable consequences, as summed up in Figure (1.2). "Killer" electrons accelerated in the magnetosphere during geomagnetic storms can cause communications satellites to fail. Electrical current surges in power lines, interference in the broadcast of radio, television, and telephone signals, and problems with defense communications are all associated with magnetic storms. In 1989, near a solar maximum, a very strong solar storm impacted the Earth's magnetosphere: Quebec, Canada, lost power for 9 hours. Odd behavior in air and marine navigation instruments has been observed, and a compass anywhere on Earth is certainly affected. These storms are known to alter the atmospheric ozone layer. Even increased pipeline corrosion has been attributed to them. Major solar activity is a very serious concern in space flight. Communications may be disrupted. Large solar disturbances heat the upper atmosphere, causing it to expand and create increased drag on spacecraft in low orbits, shortening their orbital lifetime. Spacecraft could potentially tumble and burn up in the atmosphere. Intense SEP events contain very high levels of radiation, more than a million times the normal daily dose for a human on Earth. Radiation sickness can result when humans are outside the protective magnetosphere of the Earth, as in missions to the Moon and to Mars. High-energy solar protons can produce

increased radiation in the atmosphere at altitudes where supersonic aircraft fly. This is especially true for flights over the north and south magnetic poles, areas unprotected by the Earth's magnetic field, where the radiation has direct access to the atmosphere. To reduce the risk to aircraft crews and passengers, and reduce risk to the aircraft, routine forecasts and alerts are sent through the Federal Aviation Administration so that a flight in potential danger can consider what course of action to take to minimize radiation exposure.

The National Oceanic and Atmospheric Administration (NOAA) forecasts high-speed solar wind and solar particle events from the Space Environment Center. The broadcast of solar wind, magnetic field, and SEP data from the scientific satellites SOHO, ACE, Wind and Stereo (key information about these missions can be found in the next chapter) allow forecasts of major activity up to one hour beforehand. However, this data is still not enough, and some of these satellites are coming close to the end of their lifetime.

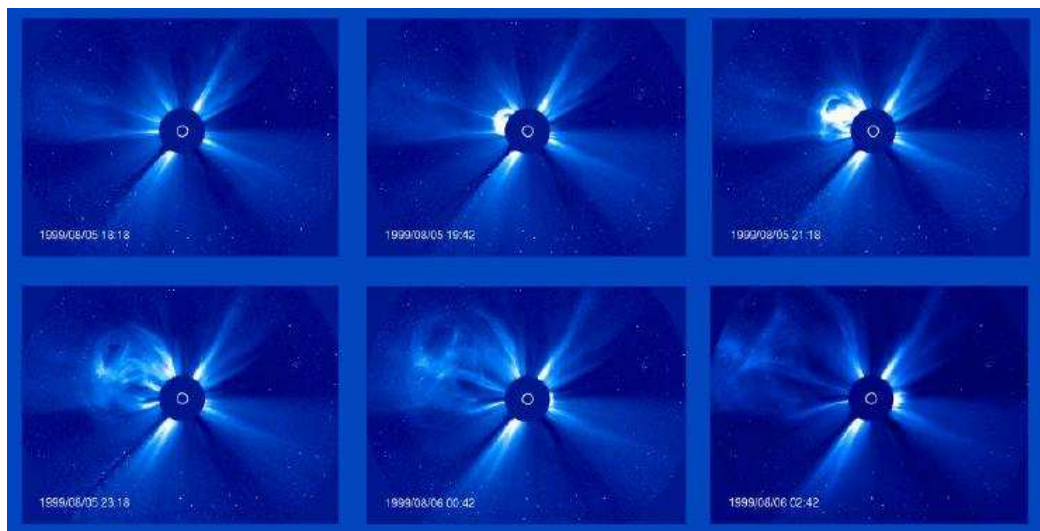


Figure 1.5 An image sequence showing the progress over eight hours of a clearly defined CME on 5-6 August 1999 [<http://sohowww.nascom.nasa.gov/>]

The Sun's rotational period is about 25 days at the equator, 27 days at 35 degrees latitude, 33 days at 75 degrees latitude, and about 35 days near the poles. Forecasts of the order of the Sun's rotational period are based primarily on the persistence of patterns of solar and/or geophysical activity from one solar rotation to the next: solar-terrestrial predictions on time scales of 27 days to several years (medium term) are less developed than short-term (days) or long-term solar cycle scale predictions. This could be done having many (small and low cost) satellites spread around the Sun, the spacecraft orbiting near L_3 being part of this constellation. Moreover, the spacecraft near L_3 would monitor the evolution of the Sun's activity on the side opposite to the Earth: precise forecasts of the order of the solar rotation would allow a better planning of the operations that are influenced by space weather, for example Extra-Vehicular Activities (EVAs) at the International Space Station (ISS), or, apart from those already mentioned above, Earth-based business like assembling microchips (which is sometimes stopped during magnetic storms).

1.2 Missions to the Libration points, plus Stereo

As shown in Table (1.1), several spacecraft have already reached the vicinity of L_1 and L_2 and, thus, design and analysis capabilities are clearly available for such missions. In fact, the design strategies used for some spacecraft launched in the past few years have been very successful, but much more challenging trajectory goals are already being suggested for the next few decades. The structure of the phase space in the vicinity of the collinear points has been examined and the fundamental motions (both planar and three-dimensional) are under investigation. Families of periodic and quasi-periodic orbits have been determined. These include the periodic halo orbits, as well as Lissajous trajectories and quasi-halos. The capability to numerically produce these types of motion is an ongoing development. The local behaviour near these orbits is also of critical importance in any effort to develop general methodologies for mission analysis and design, and has been the focus of the efforts of a number of researchers. These studies have been directly responsible for the application of invariant manifolds to ultimately produce viable transfer trajectories for several missions currently being planned.

Here an overview of the past and future missions to the Lagrange points will be given, and a brief description of each one (note that these missions are to L_1 and L_2 only, as there is no one planned to Sun-Earth L_3). Considering what has been written in the Science section, information about the Stereo mission will also be included, even if this mission is not to a libration point.

Data and pictures have been collected either from the websites of those space missions (when available), or from [*Canalias et al., 2004*].

ISEE-3 (NASA)	L_1	1978	Solar wind, cosmic rays
WIND (NASA)	L_1	1994	Solar wind, Earth magneto-sphere
SOHO (ESA-NASA)	L_1	1996	Solar observatory
ACE (NASA)	L_1	1997	Solar wind, particles
WMAP (NASA)	L_2	2001	Background cosmic radiation
GENESIS (NASA)	L_1, L_2	2001	Solar wind composition
HERSCHEL (ESA)	L_2	2009	Infrared astronomy
PLANK (ESA)	L_2	2009	Cosmic microwave background
GAIA (ESA)	L_2	2011	Astrometry
JWST (NASA)	L_2	2013	Space telescope
DARWIN (ESA)	L_2	2015	Planetary systems
TPF (NASA)	L_2	2014-2020	Planetary systems
SAFIR (NASA)	L_2	2015-2020	Infrared telescope

Table 1.1 List of missions to the Libration points of the Sun-Earth system

1.2.1 ISEE-3: International Sun-Earth Explorer 3

Mission Overview

- **Orbit** Halo orbit around the Earth-Sun libration point L_1
 $A_x = 175000 \text{ km}$, $A_y = 666670 \text{ km}$, $A_z = 1200 \text{ km}$
- **Transfer** Direct Transfer, 100 days
- **Launch** August 12, 1978
- **Launcher** Delta
- **Mission** Investigate Solar-Terrestrial relationships, solar wind, magnetosphere, and cosmic rays
- **Operational Lifetime** Planned for 4 years, extended in 1981 and renamed ICE. Still active
- **Manoeuvres** 3 trajectory manoeuvres at the transfer (57 m/s), 15 station keeping manoeuvres (30 m/s), attitude and spin control and an anomalous jet firing (32 m/s)
- **Agency** NASA
- **Website** n.a.

Spacecraft

- **Mass** 479 kg (includes 89 kg fuel at launch)
- **Propulsion** Hydrazine fuel for orbit and attitude control
- **Power** 173 W
- **Communication Subsystem** The tower structure supports the medium-gain S-band antenna. This antenna has a flat, disk-like pattern that is perpendicular to the spin axis and has an effective beam-width of 12 deg. Its gain is roughly 7 dB over an isotropic antenna

The International Sun Earth Explorer 3 (ISEE-3) spacecraft was part of a three spacecraft mission (ISEE 1,2 and 3) whose purpose was to study the solar wind and the solar terrestrial relationship at the boundaries of the Earth's magnetosphere. After a series of manoeuvres and lunar flybys, ISEE-3 (renamed to International Comet Explorer: ICE) encountered Comet Giacobini-Zinner in 1985 and provided distance observations of Comet Halley in 1986.

Launched on August 12, 1978, ISEE-3 was placed into a large amplitude class-I halo orbit around the Sun-Earth L_1 libration point. This orbit was selected for two reasons:

- the orbit passes slightly above and below the ecliptic plane, and easily clears the zone of solar interference

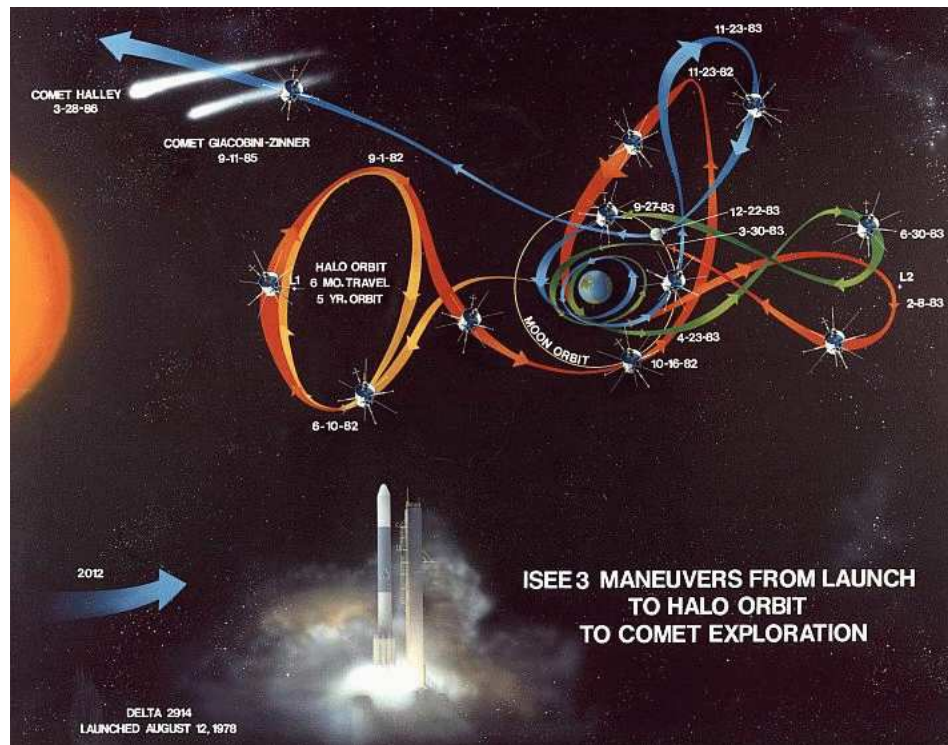


Figure 1.6 ISEE-3 trajectory [Canalias et al., 2004]

- for a large-amplitude halo orbit the ΔV requirement for orbit insertion is significantly lower (the ΔV cost decreases linearly as the amplitude increases)

In 1981, it was proposed that ISEE-3 be manoeuvred into Earth's magneto-tail, and then later towards a comet. On June 10, 1982 the first of these manoeuvres was started which moved the spacecraft out of its halo orbit where it has orbited for nearly 4 years. Fifteen manoeuvres were required through the magneto-tail, along with the five lunar flybys to get the spacecraft out of the Earth-Moon system and on its way towards comet Giacobini-Zinner. The fifth and final lunar flyby on December 22, 1983, passed only 119.4 km above the Moon's surface near the Apollo 11 landing site. At this point, the spacecraft was renamed ICE.

On June 5, 1985, the spacecraft was manoeuvred 26550 km behind comet Giacobini-Zinner so that its fields and particles instruments could sample the comets tail. ICE approached the comet at a distance of 7862 km at its closest approach on September 11, 1985, with a flyby velocity of 20.7 km/s. Because the spacecraft did not carry any dust protection equipment, it was expected to suffer some damage during the encounter. However, the spacecraft survived relatively unscathed.

In 1986, ICE made distant observations of comet Halley on the sun-ward side of the comet. It flew by at a distance of 31 million km from the comet on March 28, 1986, and provided upstream solar wind data.

In 1995 NASA ended the ICE mission, and ordered the probe shut down, with only a carrier signal left operating. However, in 2008 NASA successfully located and reactivated ICE using the Deep Space Network.

In 2014, ICE will return to the vicinity of Earth where it could possibly be captured for analysis of its exterior dust impacts.

1.2.2 WIND

Mission Overview

- **Orbit** Lissajous orbit around Sun-Earth libration point L_1
 $A_x = 10000 \text{ km}$, $A_y = 350000 \text{ km}$, $A_z = 25000 \text{ km}$
- **Transfer** Multiple Lunar Gravity Assist
- **Launch** November 1, 1994
- **Launcher** Delta II
- **Mission** Study the solar wind and its interaction with the Earth's magnetosphere
- **Operational Lifetime** 3 years. Extended mission since 1997 continues to evolve
- **Manoeuvres** 685 m/s (allocation cost). During WIND's nominal mission phase, sixty-two manoeuvres were executed with a total Δv of 307 m/s
- **Agency** NASA
- **Website** <http://www-istp.gsfc.nasa.gov/istp/wind/>

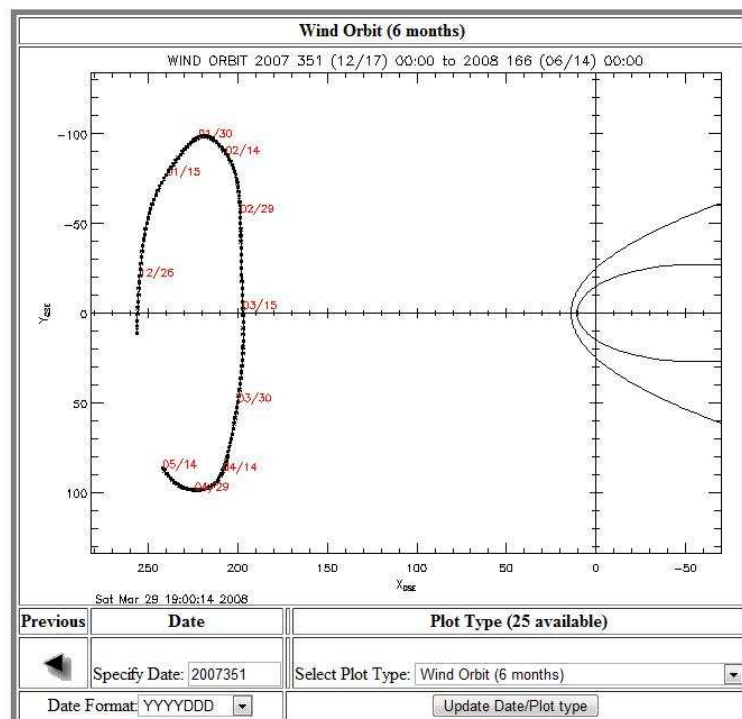


Figure 1.7 Wind orbit (Dec 17, 2007 - Jun 14, 2008) [Official website]

Spacecraft

- **Mass** 1195 kg (includes 300 kg fuel at launch)
- **Propulsion** Hydrazine propellant for orbit and attitude control

- **Power** n.a.
- **Communication Subsystem** n.a.

The Interplanetary Physics Laboratory spacecraft, better known as Wind, was launched on November 1, 1994, on a mission to study the solar wind and its interactions with the Earth's magnetosphere. Wind is a component of NASA's Global Geospace Science initiative, an element of the International Solar Terrestrial Physics (ISTP) Program. Wind's nominal mission comprised 3 years in a Double Lunar Swingby (DLS) trajectory, in which pairs of lunar flybys alternately raise and lower apogee and maintain orbital alignment near the Sun-Earth line. The DLS trajectory allowed Wind to study different regions of the magnetosphere and the upstream solar wind with a minimum of propellant.

Upon completion of its 3-year nominal mission, Wind embarked on an ambitious extended mission in October 1997, and has been at L_1 continuously since 2004. It is still operating.

1.2.3 SOHO: Solar Heliospheric Observatory

Mission Overview

- **Orbit** L_1 Halo orbit
 $A_x = 206448 \text{ km}$, $A_y = 666672 \text{ km}$, $A_z = 120000 \text{ km}$
- **Transfer** Direct
- **Launch** December, 2 1995
- **Launcher** Atlas II-AS
- **Mission** Study the Sun, from its deep core to the outer corona, the solar wind and cosmic rays
- **Operational Lifetime** Planned for 2 years, extended in 1997, still operating
- **Manoeuvres** 275 m/s (allocation cost). Total capability 318 m/s
- **Agency** ESA-NASA
- **Website** <http://sohowww.nascom.nasa.gov/home.html>

Spacecraft

- **Mass** 1853 kg (launch mass), including 610 kg of payload and 251 kg of fuel
- **Propulsion** On board hydrazine thrusters
- **Power** 1150 W, solar cell array panels

- **Communication Subsystem** S-band, Earth-pointing high gain antenna, 200 kbps during real time operation, 40 kbps during on-board storage mode transmitting continuously to the DSN ground stations

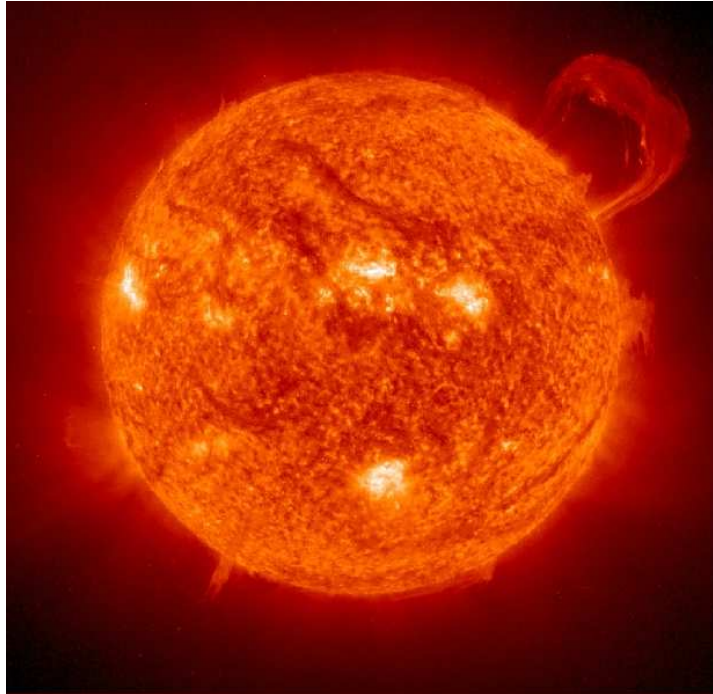


Figure 1.8 Picture of the Sun taken by SOHO on Sept 14, 1999 [Official website]

This joint ESA and NASA mission has been very successful. Its almost perfect orbit transfer and insertion have led to a low fuel consumption. In addition to all solar data gathered by the Observatory, since the beginning of the observations around L_1 SOHO has found more than 620 comets.

The primary mission constraints for the halo orbit was that the minimum Sun-Earth-Vehicle (SEV) angle never be less than 4.5 degrees (solar exclusion zone, where strong solar interference would make communication impossible). The selected Halo orbit fulfilled this requirement.

SOHO had to face some important problems in its operational life. In June, 24-25 1998 it suffered a loss of communication with the Earth. SOHO's roll rate began increasing, and the attitude control failed as it rolled into a tumble while still thrusting. Fortunately at the time of the loss there was still 206 kg of fuel remaining in SOHO's tanks, representing a ΔV capability of 225 m/s to perform correcting manoeuvres. After some weak radio contacts from SOHO and gradually longer contacts during early August, its position was guessed and attitude control reestablished. Two recovery manoeuvres were performed on September 1 and 25, with a total moderate cost of 7 m/s. Nevertheless, two of the three roll control gyros were now useless. Another correcting manoeuvre was necessary in October, and by the last half of November the situation for SOHO was rapidly improving. A small orbit correcting manoeuvre (10 cm/s) was planned for December 21 1998, when the only remaining gyroscope failed irretrievably.

SOHO currently continues to operate after having been in space for over ten years. In addition to its scientific mission, it is currently the main source of near-real time solar data for space weather prediction.

1.2.4 ACE: Advanced Composition Explorer

Mission Overview

- **Orbit** Lissajous orbit around the Earth-Sun libration point L_1
 $A_x = 81755 \text{ km}$, $A_y = 264071 \text{ km}$, $A_z = 157406 \text{ km}$
- **Transfer** Direct (Constrained), 109 days
- **Launch** August 25, 1997
- **Launcher** Delta II
- **Mission** Measure the composition of energetic particles from the Sun, the heliosphere and the Galaxy
- **Operational Lifetime** The spacecraft has enough propellant on board to maintain an orbit at L_1 until 2024
- **Manoeuvres** For the launch/transfer trajectory: Transfer trajectory insertion, Orbit Shaping Manoeuvres, Lissajous Orbit Insertion Manoeuvre; Maintenance manoeuvres: Station Keeping manoeuvres (once every 8 weeks), Orbit Shaping manoeuvres (once every 3-6 months or as necessary to maintain Sun-Earth-Vehicle angle requirements), Attitude reorientation manoeuvres (once every 5-7 days), Spin rate adjustment manoeuvres (as required)
- **Agency** NASA
- **Website** <http://www.srl.caltech.edu/ACE/>

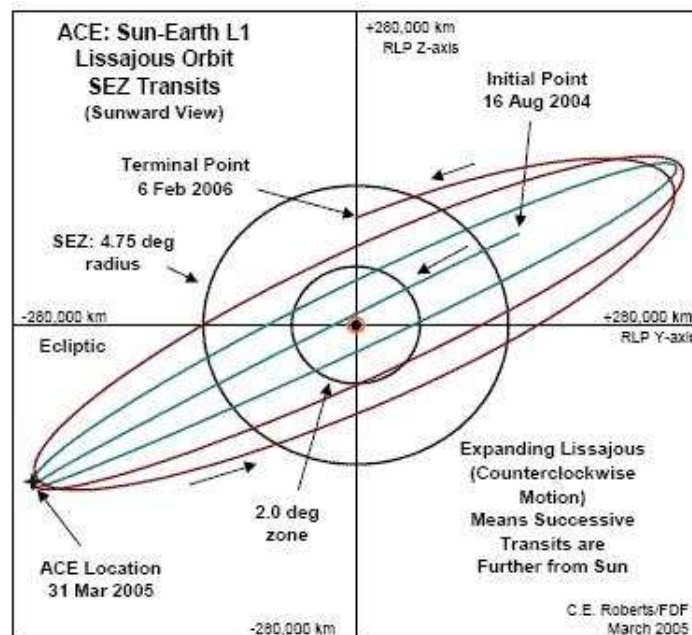


Figure 1.9 ACE Lissajous orbit near Sun-Earth L_1 [Official website]

Spacecraft

- **Mass** 785 kg (includes 195 kg fuel at launch)
- **Propulsion** Hydrazine fuel for insertion and maintenance in orbit
- **Power** 443 W, four fixed solar arrays
- **Communication Subsystem** S-band, 7 kbps (real time), 2 Gbit (total) solid state recorders

Launched on August 25, 1997, ACE was placed in a modified halo orbit around the Sun-Earth L_1 libration point. This orbit is a "broken Lissajous" approximation to a true halo orbit providing Sun-Earth-ACE angles of ten and five degrees respectively. The period of this orbit is about 178 days.

ACE was launched during solar minimum conditions and then observed the transition to solar maximum. During this period the number of solar flares and coronal mass ejections increased dramatically, including some of the largest solar particle events observed since the dawn of the space age. Studies of solar wind, solar particles, and cosmic rays by ACE, in combination with other spacecraft such as Ulysses and Voyager, provided new insight into the bubble of solar wind that envelops our solar system, and the nature of its interactions with the Galaxy.

The instruments on the ACE spacecraft are designed to sample the matter that comes near the Earth from the Sun, from the apparently (but not actually) empty space between the planets, and from the Milky Way galaxy beyond the solar system. They do so with a collecting power 10 to 1000 times greater than previous experiments. Particles are identified by their type (which atom they are), by their mass (which isotope they are), by their electric charge or ionic state, and by their energy. Even very rare isotopes can be studied. The information gathered by ACE is compared with that from other missions, past and present, for a better understanding of the interaction between the Sun, the Earth, and the Galaxy.

1.2.5 WMAP: Wilkinson Microwave Anisotropy Probe

Mission Overview

- **Orbit** L_2 Lissajous
 $A_y = 264000 \text{ km}$, $A_z = 264000 \text{ km}$
- **Transfer** 3 Earth-moon phasing loops, lunar gravity assist to L_2
- **Launch** June, 30 2001
- **Launcher** Delta II
- **Mission** Produce an accurate full-sky map of the cosmic microwave background temperature fluctuations (anisotropy), the oldest light in the universe
- **Operational Lifetime** 27 months: 3 months trajectory to orbit insertion + 2 years at L_2 ; Fuel limit over 3 years; still operating

- **Manoeuvres** Station keeping trim manoeuvres approximately every 3 months
- **Agency** NASA
- **Website** <http://map.gsfc.nasa.gov/>

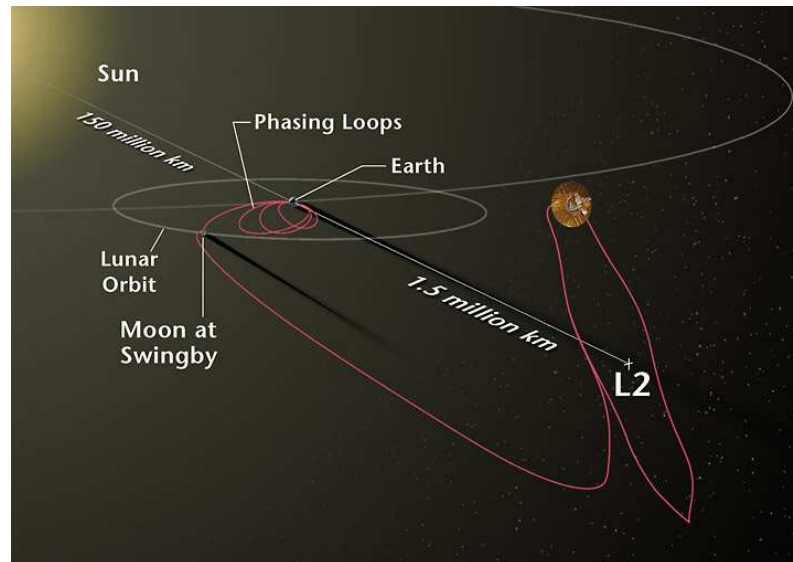


Figure 1.10 WMAP trajectory [*Official website*]

Spacecraft

- **Mass** 836 kg
- **Propulsion** Blow-down hydrazine with 8 thrusters
- **Power** 419 W (solar arrays + battery)
- **Communication Subsystem** Two S-band transponders (2 GHz), one prime and the other redundant. Two omni-directional antennas and two medium gain antennas for high speed data transmission to Earth

WMAP has been the first mission to use L_2 as a permanent observing station. An orbit about the Sun-Earth L_2 libration point provides for a very stable thermal environment and near 100% observing efficiency since the Sun, Earth, and Moon are always behind the instruments field of view. Moreover, WMAP's large distance from Earth protects it from near-Earth emission and other disturbances.

WMAP measures the temperature differences in the Cosmic Microwave Background radiation, and from its orbit near L_2 it covers the entire sky every six months.

1.2.6 GENESIS

Mission Overview

- **Orbit** Lissajous Orbit around Sun-Earth libration point Point L_1
 $A_x = 25000 \text{ km}$, $A_y = 800000 \text{ km}$, $A_z = 250000 \text{ km}$
- **Transfer** Direct, 83 days
- **Launch** August 28, 2001
- **Launcher** Delta 7326
- **Mission** Collect and return solar wind samples to Earth
- **Operational Lifetime** The sample return capsule crash-landed on September 8, 2004
- **Manoeuvres** ΔV budget: Launch Error Corrections 93 m/s, Lunar Orbit Insertion 636 m/s, Station Keeping 24 m/s, Return Station Keeping 45 m/s, Primary Entry Target 4 m/s, Deboost Spacecraft 20 m/s, Attitude Control and Stabilization 71 m/s, Backup Entry 87 m/s, Margin 70 m/s
- **Agency** NASA
- **Website** <http://genesission.jpl.nasa.gov/>

Spacecraft

- **Mass** 636 kg (includes 142 kg fuel at launch)
- **Propulsion** Hydrazine mono-propellant thruster using a helium pressurant
- **Power** 254 W
- **Communication Subsystem** S-band telemetry reception at 15 kilobits per second during the halo orbit phase, and 120 bits per second during the cruise and return phases

Genesis had three operational phases: launch segment, acquisition and return leg. The techniques used to design the pieces represented an innovative approach to trajectory design so Genesis has been the first mission designed using modern Dynamical Systems Theory. The near-optimal Genesis trajectory launch segment was obtained using the stable manifold of the nominal Lissajous orbit and the return leg by using the unstable manifold, in fact, exploiting the homoclinic behaviour of the L_1 and L_2 regions (homoclinic and heteroclinic chains).

Genesis was placed in a Lissajous orbit around the Sun-Earth libration point L_1 on November 16, 2001, with solar-wind collection starting shortly thereafter, on December 3. The spacecraft completed five orbits by April, 2004, making approximately two orbits per year.

In April, 2004, it departed from the Lissajous orbit, swing-past the Earth (there

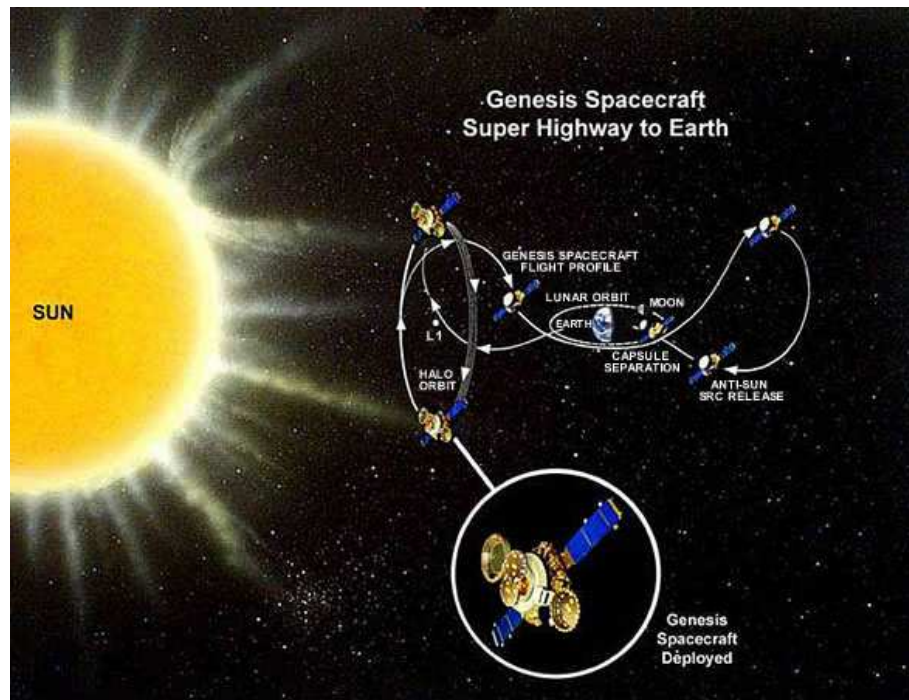


Figure 1.11 Overview of Genesis trajectory [Official website]

was no lunar flyby), and passed close to the L_2 point. This trajectory put the spacecraft in position for a daylight re-entry. The sample return capsule crash-landed on September 8, 2004.

1.2.7 HERSCHEL SPACE OBSERVATORY

Mission Overview

- **Orbit** L_2 large amplitude Lissajous
 $A_x \approx 800000 \text{ km}$, $A_y \approx 500000 \text{ km}$, $A_z \approx 500000 \text{ km}$
- **Transfer** Stable manifold transfer from Ariane launch
- **Launch** May 2009
- **Launcher** Ariane 5
- **Mission** Far-infrared astronomy. To investigate the history of how stars and galaxies formed and to study how they continue to form in our own and other galaxies
- **Operational Lifetime** Nominal mission: 3 years
- **Manoeuvres** Once it is inserted in the Lissajous, not more than 1 m/s per year of station keeping ΔV . A manoeuvre once per month
- **Agency** ESA
- **Website** <http://herschel.esac.esa.int/>

Spacecraft

- **Mass** 3300 kg
- **Propulsion** n.a.
- **Power** 1450 W (solar panels)
- **Communication Subsystem** n.a.

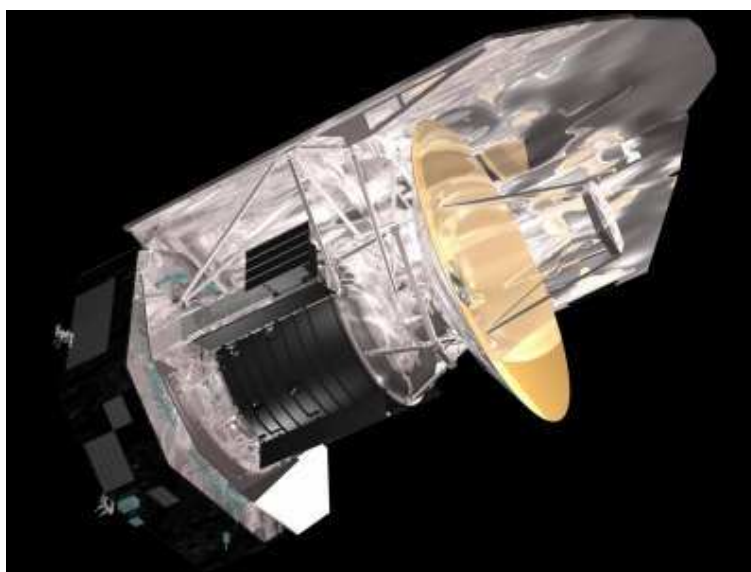


Figure 1.12 3D model of Herschel spacecraft [*Official website*]

The design of the Herschel orbit was constrained in several ways. It had to be an orbit which could be reached from a maximum mass Ariane launch, taking into account the Sun aspect angle during the Ariane powered ascent and the duration of the eclipse in the transfer. This led to the class of large-size Lissajous orbits. The insertion in the orbit used Dynamical Systems Theory to minimise fuel consumption, by choosing suitable launch windows. Ariane was launched sometime inside these windows, reaching the stable manifolds of large Lissajous orbits, so that Herschel could approach its planned orbit with near zero cost by travelling along these manifolds towards its observing location.

1.2.8 PLANCK

Mission Overview

- **Orbit** L_2 Lissajous, maximum elongation from L_2 of 280000 km, Sun-Earth-spacecraft angle never exceeding 10 degrees; 6 months period
- **Transfer** With Herschel. Lissajous amplitude reduction manoeuvre 3 months after launch
- **Launch** May 2009
- **Launcher** Ariane 5
- **Mission** Cosmic microwave background: image the anisotropies of the Cosmic Background Radiation Field over the whole sky, with unprecedented sensitivity and angular resolution
- **Operational Lifetime** 21 months (15 months orbiting L_2 and collecting data after 6 months transfer)
- **Manoeuvres** To maintain the spin-axis along the Sun-spacecraft line, approximately 1 manoeuvre/hour of 2.5 arc-minutes along the ecliptic plane
- **Agency** ESA
- **Website** planck.esa.int/

Spacecraft

- **Mass** 1800 kg at launch
- **Propulsion** n.a.
- **Power** 1655 W
- **Communication Subsystem** Collects data in a solid-state recorder and down-links it to ground station 3 hours/day. The spacecraft is not reoriented towards the Earth, thus the telemetry antenna is designed to have an adequate gain within a 10 degrees half-cone from the spin axis to achieve full band width even in the extremes of the orbit

Planck has been delivered by Ariane into the stable manifold of a Lissajous orbit of large size, together with Herschel (during the launch Planck took the place of the lower passenger, inside the launcher adapter). It had to be manoeuvred from there to an orbit with a smaller size.

Planck Surveyor will observe the whole sky at least twice at all nine frequencies over two separate six-months periods, and after about 18 months in orbit the data will be combined into maps of the microwave sky at the various data processing centres situated around Europe.

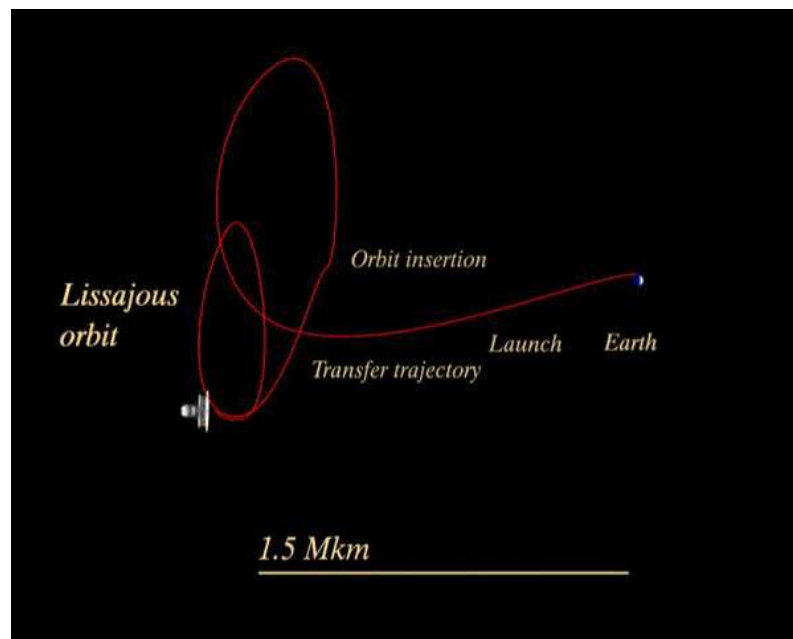


Figure 1.13 Planck orbit [Official website]

1.2.9 GAIA

Mission Overview

- **Orbit** L_2 Lissajous
 $A_y = 340000 \text{ km}$, $A_z = 90000 \text{ km}$
- **Transfer** First inserted in a circular orbit of 51.8 degrees inclination, 190 km altitude. A second burn, with or without lunar gravity assist (which could save about 50 m/s), will insert GAIA to its orbit around L_2
- **Launch** Fall 2011
- **Launcher** Soyuz-Fregat
- **Mission** Galactic structure, astrometry: measure the positions of an extremely large number of stars with unprecedented accuracy. Clarify the origin and history of our Galaxy, by providing tests of the various formation theories, and of star formation and evolution
- **Operational Lifetime** Operational lifetime of 5 years, might be extended until 2020
- **Manoeuvres** 180 m/s (for a 6 months launch window)
- **Agency** ESA
- **Website** <http://gaia.esa.int/>

Spacecraft

- **Mass** 2030 kg at launch
- **Propulsion** Field Emission Electric Propulsion once in orbit near L_2
- **Power** 2910 W (solar panels)
- **Communication Subsystem** Continuous payload data rate of about 1 Mbps. Down-link to Earth stations 8 hours a day, X-band 3 Mbps capacity

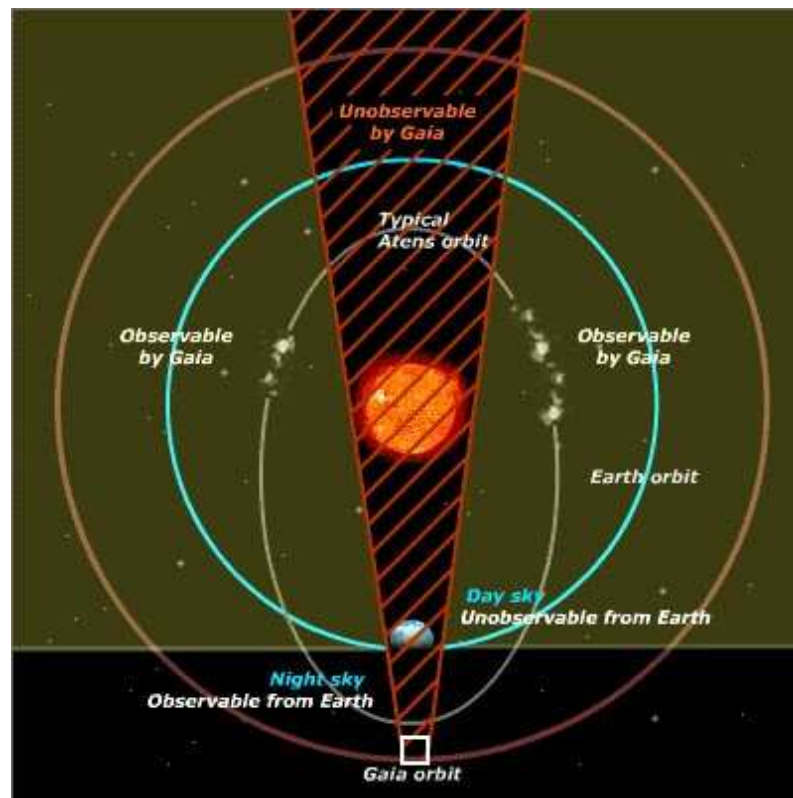


Figure 1.14 GAIA orbit [*Official website*]

The selection of the orbit arises from a trade-off between communication, operations, cost, thermal environment, and accessibility with current rockets.

GAIA will be a continuously scanning spacecraft, accurately measuring one-dimensional coordinates along great circles, and in two simultaneous fields of view, separated by a well-defined and well-known angle (these one-dimensional coordinates are then converted into the astrometric parameters in a global data analysis). GAIA will allow astronomers to compile the most detailed 3-D model of the distribution of stars in our Galaxy ever obtained.

1.2.10 JWST: James Webb Space Telescope

Mission Overview

- **Orbit** Lissajous orbit around the Earth-Sun libration point L_2
 $A_x \approx 290000 \text{ km}$, $A_y \approx 800000 \text{ km}$, $A_z \approx 131000 \text{ km}$
- **Transfer** Direct
- **Launch** 2013
- **Launcher** Ariane 5
- **Mission** Determine the shape of the Universe, explain galaxy evolution, understand the birth and formation of stars, determine how planetary systems form and interact, determine how the Universe built up its present chemical/elemental composition and probe the nature and abundance of Dark Matter
- **Operational Lifetime** 5 to 10 years
- **Manoeuvres** 150 m/s (allocation cost)
- **Agency** NASA, ESA , CSA ASC
- **Website** <http://ngst.gsfc.nasa.gov/>

Spacecraft

- **Mass** 6200 kg
- **Propulsion** Hydrazine thrusters for gyro despin
- **Power** n.a.
- **Communication Subsystem** X-band 1.6 Mbps down-link

The JWST will be bigger and much more powerful than the Hubble Space Telescope, yet also cheaper to build and operate. The powerful observatory's design features a 6.5 meter aperture primary mirror, comprised of 18 hexagonal-shaped segments. The large-size mirror, which could fit seven Hubble Space Telescope mirrors within its surface area, gives it the light-collecting sensitivity to see objects 400 times fainter than those currently observed by ground and space-based telescopes.

The telescope's five-layer Sun-shield will shield the telescope from sunlight and keep it at a cold temperature: only 30 degrees above absolute zero. The extreme cold enables JWST to see light in infrared wavelengths, allowing it to detect light through dense, dusty clouds where star and planet formation takes place.

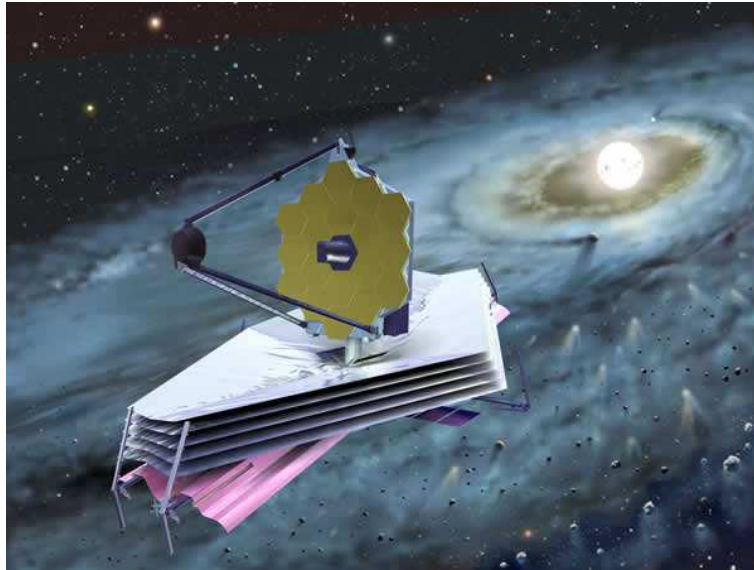


Figure 1.15 Artist's impression of the JWST [*Official website*]

1.2.11 DARWIN

Mission Overview

- **Orbit** L_2 halo orbit
- **Transfer** Direct
- **Launch** 2015 or later
- **Launcher** Ariane 5
- **Mission** To look for Earth-like planets and signs of life on them, and to provide imaging of space in the 5 to 28 micron band
- **Operational Lifetime** 5 years
- **Manoeuvres** n.a.
- **Agency** ESA
- **Website** www.esa.int/science/darwin

Spacecraft

- **Mass** 4240 kg
- **Propulsion** Ion engines or squirting cold gas out of the thrusters
- **Power** n.a.
- **Communication Subsystem** n.a

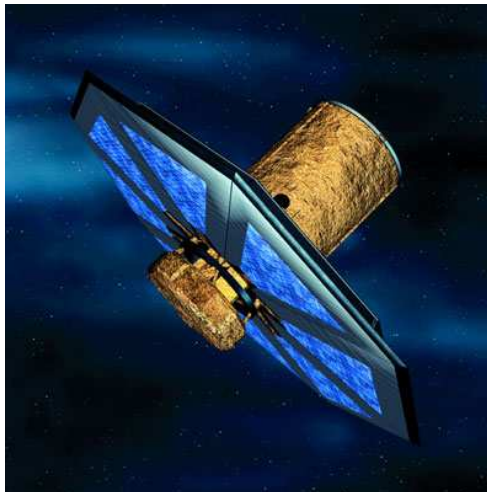


Figure 1.16 One of Darwin's telescopes [Official website]

Darwin will observe in the mid-infrared. Life on Earth leaves its mark at these wavelengths, so they are good places to look for fingerprints of Earth-like planets and life. In addition to searching for planets, it is designed to provide images with 10 - 100 times more detail than can be achieved now.

1.2.12 TPF: Terrestrial Planet Finder

Mission Overview

- **Orbit** Lissajous Orbit around the Sun-Earth libration point L_2
- **Transfer** n.a.
- **Launch** 2014-2020 (as of June 2008, actual funding has not materialized, and TPF remains without a launch date)
- **Launcher** Ariane 5, EELV, or Delta IV Heavy
- **Mission** To search for Earth-like planets that might harbour life. TPF will take family portraits of stars and their orbiting planets and determine which planets may have the right chemistry to sustain life
- **Operational Lifetime** 5 years
- **Manoeuvres** n.a.
- **Agency** NASA
- **Website** <http://tpf.jpl.nasa.gov>

Spacecraft

- **Mass** t.b.d , in the range 3700-4900 kg
- **Propulsion** Electric propulsion
- **Power** n.a.
- **Communication Subsystem** n.a.

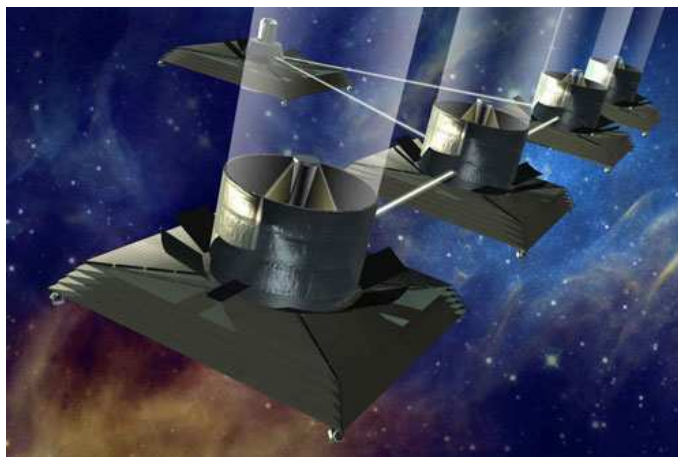


Figure 1.17 Artist's impression of TPF-I [*Official website*]

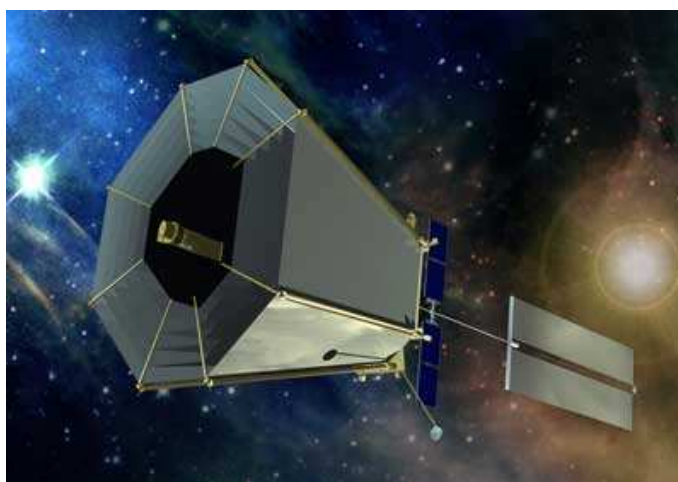


Figure 1.18 Artist's impression of TPF-C [*Official website*]

The Terrestrial Planet Finder (TPF) is a spacecraft-based infrared interferometer that will combine high sensitivity and spatial resolution to detect and characterise approximately 150 planetary systems within 15 parsec of our Sun. In a five-years mission, TPF will look for the atmospheric signatures of life using the methods of planetary spectroscopy and long-baseline stellar interferometry.

NASA has chosen on May, 2004 to fly two separate missions with distinct and complementary architectures to achieve the goal of the Terrestrial Planet Finder. The two missions are:

- **Terrestrial Planet Finder-C** a moderate-sized visible-light telescope, similar to the 4-by 6-meter version currently under study, to be launched around 2014. Onboard coronagraph instrumentation will use a central disc and other specialised techniques to block the glare of a star, allowing detection and characterisation of dimmer planets around it
- **Terrestrial Planet Finder-I** multiple spacecraft carrying 3 to 4 meter infrared telescopes flying in precise formation, to be launched before 2020, and to be conducted jointly with ESA. Combining the infrared, or heat radiation gathered by the multiple telescopes, using a technique called interferometry, will simulate a much larger telescope. This will enable the mission to detect and study individual planets orbiting a parent star observed by TPF-C and also new ones beyond the reach of TPF-C

1.2.13 SAFIR: Single Aperture Far-Infrared Observatory

Mission Overview

- **Orbit** Sun-Earth L_2 point
- **Transfer** n.a.
- **Launch** 2015-2020
- **Launcher** n.a.
- **Mission** Probe the epoch of re-ionization due to the first stars when the Universe was less than 1/20 its present age, trace the formation and evolution of star-forming and active galaxies since their inception, explore the connection between black holes and their host galaxies, reveal the details of star and planet formation in nearby debris-disk systems, search for and quantify prebiotic molecules in the interstellar medium
- **Operational Lifetime** 5 years
- **Manoeuvres** n.a.
- **Agency** NASA
- **Website** <http://safir.jpl.nasa.gov/>

Spacecraft

- **Mass** n.a.
- **Propulsion** n.a.
- **Power** n.a.
- **Communication Subsystem** While the communication segment baseline for Safir is the set of DSN antennas, a dedicated ground station would also meet Safirs modest down-link needs if a larger antenna and/or higher transmitting power were implemented on the spacecraft



Figure 1.19 A SAFIR concept based on the segmented-mirror technology to be employed for the JWST [Official website]

Safir is a large (10 m-class), cold (4-10 K) space telescope for wavelengths between $20\ \mu\text{m}$ and 1 mm. It will provide sensitivity of a factor of a hundred or more over that of Spitzer telescope and Herschel, leveraging their capabilities and building on their scientific legacies.

1.2.14 STEREO

Mission Overview

- **Orbit** One observatory is placed ahead of Earth in its orbit ("A") and the other behind ("B"), nearly in Earth's orbit
- **Transfer** Lunar Gravity Assist
- **Launch** October 26, 2006
- **Launcher** Delta II
- **Mission** Provide stereoscopic measurements of the Sun and Coronal Mass Ejections (CMEs)
- **Operational Lifetime** 2 years minimum, already extended
- **Agency** NASA
- **Website** <http://stereo.jhuapl.edu> and <http://stereo.gsfc.nasa.gov>

Spacecraft

- **Mass** 620 kg each (547 kg dry mass)

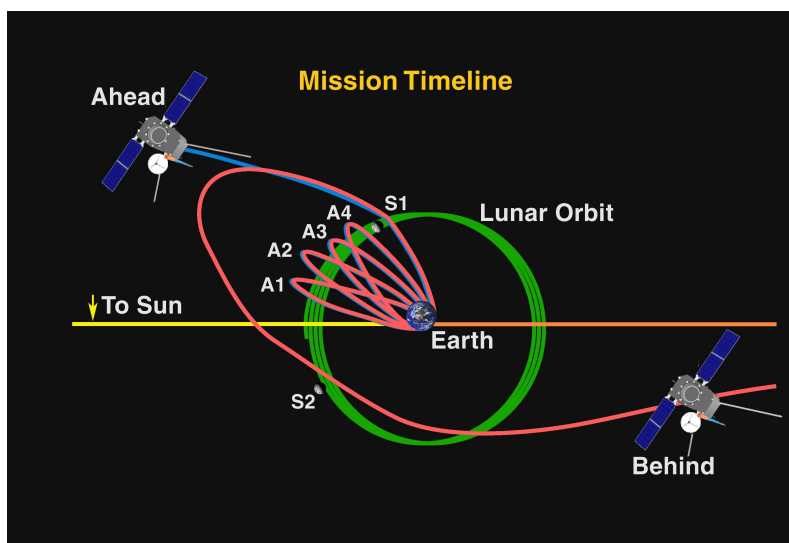


Figure 1.20 Stereo Orbit Description [http://stereo.jhuapl.edu]

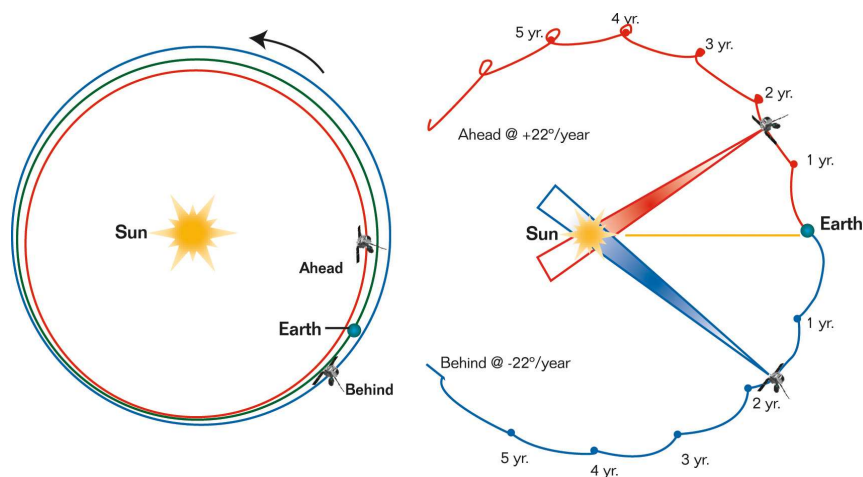


Figure 1.21 Stereo Orbit. Left: Heliocentric Inertial Coordinates (Ecliptic Plane Projection); Right: Geocentric Solar Ecliptic Coordinates Fixed Earth-Sun Line (Ecliptic Plane Projection) [http://stereo.jhuapl.edu]

- **Propulsion** Three sets of four hydrazine thrusters, each thruster is 4.4 N
- **Power** 596 watts (average)
- **Communication Subsystem** Data Downlink: 720 kilobits per second; Memory: 1 gigabyte

On December 15, 2006, the twin spacecraft encountered the moon (S1) and completed the mission’s first lunar swingby. The "A" spacecraft passed only 7340 km from the moon’s surface; then lunar gravity was used to hurl the spacecraft away from Earth, placing the observatory slightly "ahead" of Earth. During the initial lunar gravitational assist, the "B" spacecraft flew higher above the moon at a distance of 11776 km above the moon’s surface where the lunar gravity was slightly weaker. Although the moon’s gravity slightly boosted the

"B" observatory's orbit, the spacecraft re-encountered the moon on January 21, 2007, at S2. The "B" spacecraft came within 8818 km from the moon's surface, swinging past the lunar body in the opposite direction of the "A" spacecraft and into an orbit "behind" Earth.

Spacecraft "A" orbits the Sun every 346 days while "B" orbits every 388 days.

The Stereo spacecraft achieved 90 degrees separation on January 24, 2009, a condition known as quadrature. This is of interest because the mass ejections seen from the side on the limb by one spacecraft can potentially be observed by the in situ particle experiments of the other spacecraft. As they pass through Earth's Lagrangian points L_4 and L_5 (in late 2009), they will search for Lagrangian (Trojan) asteroids. On February 6, 2011, the two spacecraft will be exactly 180 degrees apart from each other, allowing the entire Sun to be seen for the first time. In 2015, contact will be lost for several months when the spacecraft pass behind the Sun. After this, they can continue to be operated after rolling by 180 degrees to point the high gain antenna at Earth. They will then start to approach Earth again, with closest approach sometime in 2023. They will not be recaptured into Earth orbit.

Fundamental concepts of Astrodynamics

Astrodynamics is an application of the classical theories of Celestial Mechanics, which in turn may be considered part of the broad field of Astronomy. Celestial Mechanics, and thus Astrodynamics, is based upon four laws: Newton's three *laws of motions* and Newton's *law of gravitation*. In this chapter we will especially refer to [Wakker, 2005].

2.1 Fundamental Laws

2.1.1 Newton's Law of Motion

The three laws of motion, which were formulated in 1687 by Sir Isaac Newton in his *Philosophiae Naturalis Principia Mathematica*, usually abbreviated to *Principia*, are the following:

First law: Every particle continues in its state of rest or uniform motion in a straight line relative to an inertial reference frame, unless it is compelled to change that state by forces acting upon it.

Second law: The time rate of change of linear momentum of a particle relative to an inertial reference frame is proportional to the resultant of all forces acting upon that particle and is collinear with and in the direction of the resultant force.

Third law: If two particles exert forces on each other, these forces are equal in magnitude and opposite in direction.

In Astrodynamics the very fact that satellites and spacecraft are always extremely small with respect to the Earth and other celestial bodies is used, and that the planets and their moons are very small relative to the Sun. This means that for all practical cases, in which the translational dynamics (non rotational) of these bodies is analyzed, they can be considered as point masses or particles.

The first two of Newton's laws are sufficient for the determination of the motion of one particle subject to any number of known forces; but another

principle is needed when the investigation concerns the motion of a system of two or more particles subject to their mutual interactions. The third law of motion expresses precisely this principle. It is that if one body presses against another the second resists the action of the first with the same force. And also, though it is not so easy to conceive it, if one body acts upon another through any distance, the second reacts upon the first one with an equal and oppositely directed force.

Newton's second law can be formulated as follows:

$$\bar{F} = m \frac{d\bar{v}}{dt} \quad (2.1)$$

Equation (2.1) is only valid for bodies of constant mass and when their motion is considered with respect to an inertial reference frame.

2.1.2 Newton's Law of Gravitation

Partially based on the observed motions of the planets around the Sun, Newton formulated his law of gravitation and published it also in his *Principia*:

Two particles attract each other with a force directly proportional to their masses and inversely proportional to the square of the distance between them.

Mathematically, this law can be expressed as follows:

$$\bar{F}_{ij} = G \frac{m_i m_j}{r_{ij}^3} \bar{r}_{ij} \quad (2.2)$$

where \bar{F}_{ij} is the gravitational force exerted by body j on body i , m_i and m_j are the masses of the two particles respectively, \bar{r}_{ij} is the position vector from i to j , and the proportionality constant G known as the Universal Gravitational Constant has a value of $6.66810^{-11} Nm^2 kg^{-2}$ (it was first measured by Cavendish). This law gives the force body j exerts on body i with the outward direction from body i being positive (see Figure (2.1)).

The universal law of gravitation can be rewritten by introducing a scalar potential

$$U_i = -G \frac{m_j}{r_{ij}} + U_{i0} \quad (2.3)$$

where U_{i0} is an arbitrary constant. U_i is therefore the potential of the force field generated by m_j at the location of m_i per unit mass of m_i . Then it follows that:

$$\frac{\bar{F}_{ij}}{m_i} = -\nabla_i U_i = -\frac{\partial U_i}{\partial \bar{r}_i} \quad (2.4)$$

2.2 *n*-body Problem

Let us consider a system composed of n bodies (particles) (Figure (2.1)), where the body i with mass m_i has coordinates x_i, y_i, z_i with respect to an inertial reference frame. For any other body j the corresponding parameters are m_j, x_j, y_j, z_j . The position of body j relative to body i can be expressed as:

$$\bar{r}_{ij} = \bar{r}_j - \bar{r}_i \quad (2.5)$$

where the magnitude of vector \bar{r}_{ij} is:

$$r_{ij} = \sqrt{(x_j - x_i)^2 + (y_j - y_i)^2 + (z_j - z_i)^2} \quad (2.6)$$

When it is assumed that outside the system of n bodies no other bodies exist and that within the system of n bodies only gravitational forces occur, then, applying Newton's second law of motion and Newton's law of gravitation, the motion of body i with respect to the inertial reference frame can be written as:

$$m_i \frac{d^2 \bar{r}_i}{dt^2} = \sum_j^* G \frac{m_i m_j}{r_{ij}^3} \bar{r}_{ij} \quad (2.7)$$

The notation * indicates that the summation is taken from $j = 1$ to $j = n$, excluding $j = i$. This equation shows that the motion of body i is governed largely by those bodies j for which the ratio m_j/r_{ij}^2 is large, i.e. bodies that have large masses and that are located near body i . The equation of motion of body i may be written as three scalar second-order differential equations. Similarly, for the motion of n bodies $3n$ second-order differential equations can be written. Generally, this set cannot be solved analytically and one has to rely on numerical integration techniques as well as perturbation theories to determine the motion of the bodies. However, some general characteristics of the many-body problem can be derived. These characteristics are known as the *ten integrals of motion*.

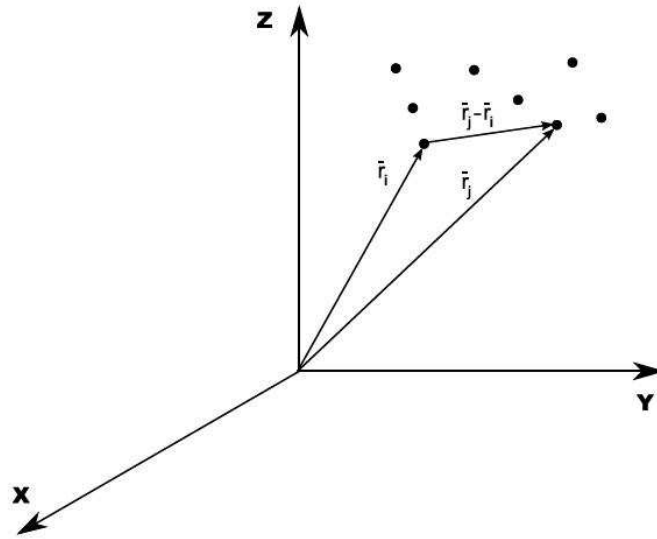


Figure 2.1 A system of n particles with respect to an inertial reference system [Wakker, 2005]

2.2.1 Integrals of motion

Ten independent algebraic integrals of motion for the n -body problem have been shown to exist. Six of these integrals are derived from considerations of the linear momentum of the system. A further three integrals are derived from considerations of the total angular momentum of the system. The last integral is derived from energy considerations.

As they can be found in any book about astrodynamics, the ten integrals are briefly derived here.

Linear momentum: Summing Equation (2.7) over all i :

$$\sum_i m_i \frac{d^2 \bar{r}_i}{dt^2} = G \sum_i \sum_j^* \frac{m_i m_j}{r_{ij}^3} \bar{r}_{ij} \quad (2.8)$$

The right-hand side of Equation (2.8) is equal to zero as the double summation means all contributions come in anti-symmetric pairs, e.g. $\bar{r}_{13} = -\bar{r}_{31}$

Hence:

$$\sum_i m_i \frac{d^2 \bar{r}_i}{dt^2} = \frac{d^2}{dt^2} \left(\sum_i m_i \bar{r}_i \right) = 0 \quad (2.9)$$

The position vector of the centre of mass of the n bodies is given by:

$$\bar{r}_{cm} = \frac{\sum_i m_i \bar{r}_i}{\sum_i m_i} \quad (2.10)$$

Using Equation (2.10) and integrating Equation (2.9), we obtain:

$$\frac{d}{dt} \bar{r}_{cm} = \bar{a} \qquad \bar{r}_{cm} = \bar{a}t + \bar{b} \qquad (2.11)$$

Equations (2.11) in scalar form give six integrals of motion relating to the linear momentum and initial (at $t = 0$) position of the centre of mass with respect to an inertial reference frame.

Angular momentum: Three more integrals of motion can be found by taking the vector product of Equation (2.7) and \bar{r}_i and subsequently applying a summation for all i :

$$\sum_i \bar{r}_i \times \left(m_i \frac{d^2 \bar{r}_i}{dt^2} \right) = \sum_i \bar{r}_i \times \left(\sum_j^* G \frac{m_i m_j}{r_{ij}^3} \bar{r}_{ij} \right) \qquad (2.12)$$

Due to its anti-symmetric properties, the right-hand side of this equation is equal to zero and we may write:

$$\frac{d}{dt} \left(\sum_i m_i \bar{r}_i \times \frac{d\bar{r}_i}{dt} \right) = 0 \qquad (2.13)$$

Integrating:

$$\sum_i m_i \bar{r}_i \times \frac{d\bar{r}_i}{dt} = \bar{H} \qquad (2.14)$$

where \bar{H} denotes the total angular momentum of the n -body system. This vector quantity is normal to the invariable plane defined by Laplace that contains the center of mass. In scalar form this introduces three more integrals of motion.

Energy: Taking the scalar product of Equation (2.7) and $\frac{d\bar{r}_i}{dt}$ and summing over all i :

$$\sum_i m_i \frac{d\bar{r}_i}{dt} \cdot \frac{d^2 \bar{r}_i}{dt^2} = G \sum_i \sum_j^* \frac{m_i m_j}{r_{ij}^3} \frac{d\bar{r}_i}{dt} \cdot \bar{r}_{ij} \qquad (2.15)$$

that can be rewritten as:

$$\frac{d}{dt} \left(\frac{1}{2} \sum_i m_i \frac{d\bar{r}_i}{dt} \cdot \frac{d\bar{r}_i}{dt} \right) = G \sum_i \sum_j^* \frac{m_i m_j}{r_{ij}^3} \frac{d\bar{r}_i}{dt} \cdot (\bar{r}_j - \bar{r}_i) \qquad (2.16)$$

Algebraic manipulation yields to:

$$\frac{d}{dt} \left(\sum_i \frac{1}{2} m_i V_i^2 \right) = \frac{d}{dt} \left(\frac{1}{2} G \sum_i \sum_j^* \frac{m_i m_j}{r_{ij}} \right) \quad (2.17)$$

or, after integration:

$$\sum_i \frac{1}{2} m_i V_i^2 - \frac{1}{2} G \sum_i \sum_j^* \frac{m_i m_j}{r_{ij}} = C \quad (2.18)$$

The first term in this equation represents the *total kinetic energy* E_k of the system of n bodies. The second term (including the minus sign), which actually expresses some kind of internal energy of the system, is called the *potential energy* E_p of the system. Thus, Equation (2.18) may be written as:

$$E_k + E_p = C \quad (2.19)$$

Equation (2.19) is the tenth and last integral of motion and shows that the sum of the total kinetic and potential energy of the system remains constant.

In 1887, H. Burns showed that these first integrals are the only algebraic first integrals which can be obtained. As well, in 1899, H. Poincaré stated that, besides these first integrals, one cannot obtain other uniform and analytic first integrals, while Painlevé showed that there does not exist other algebraic first integrals only with respect to the components of the velocity vectors [Teodorescu, 2008].

Circular Restricted 3-Body Problem

The 3-body problem (3BP) can be defined as the problem of calculating the motions of three bodies in space moving under the influence of only their mutual gravitational attraction.

As written in [Wakker, 2005], throughout the last three centuries, the 3BP has played a major role in the development of natural sciences. It has triggered many mathematical studies, methods and theories by Euler, Laplace, Lagrange, Jacobi, Newton, Hamilton and many others. The difficulties experienced in finding solutions for the 3BP were the reason for the introduction of new qualitative analysis methods by Poincaré, Birkhoff and others; methods which have since then been extended to many other branches of science.

Most of the theory is taken from [Wakker, 2005], unless otherwise indicated. However, the Circular Restricted 3-Body Problem (CR3BP) reference frame we define is rotated of π around the z -axis respect to the one used in [Wakker, 2005].

3.1 Equations of motion

Let's assume that the forces on three bodies P_1, P_2, P_3 , with masses m_1, m_2, m_3 are solely due to the gravitational attractions between the bodies and that the bodies may be considered as point masses. Moreover, in the CR3BP it is assumed that the mass of two bodies is much larger than the mass of the third body. Therefore, the third body moves in the gravitational field of the two massive bodies, and the gravitational attraction by the third body on these massive bodies can be neglected. Moreover, the two massive bodies move in circular orbits about the center of mass of the system.

The orbits of the two massive bodies being known, the problem is to determine the motion of the third body. The general 3BP is thus reduced from nine second-order differential equations to three second-order ones. This means a reduction from order eighteen to order six.

Since the mass of the third body is assumed to be negligible, the two main bodies move as if they form a 2-body system: both the bodies move in a single plane and the two bodies are always positioned diametrically opposite to each other.

In order to write down the equations of motion for the CR3BP, an inertial reference frame $\xi\eta\zeta$ is then defined, with its origin at the center of mass of the system and with the ζ -axis perpendicular to the plane in which the two bodies are moving (see Fig. 3.1). The coordinates of the main bodies P_1 and P_2 are $\xi_1, \eta_1, 0$ and $\xi_2, \eta_2, 0$. The coordinates of the third body are ξ, η, ζ . The motion of the third body P does not have to occur in the $\xi\eta$ -plane and the equation of motion with respect to the inertial reference frame may be written as :

$$\frac{d^2\bar{r}}{dt^2} = -G\frac{m_1}{r_1^3}\bar{r}_1 - G\frac{m_2}{r_2^3}\bar{r}_2 \quad (3.1)$$

where

$$r_1^2 = (\xi - \xi_1)^2 + (\eta - \eta_1)^2 + \zeta^2 \quad (3.2)$$

$$r_2^2 = (\xi - \xi_2)^2 + (\eta - \eta_2)^2 + \zeta^2 \quad (3.3)$$

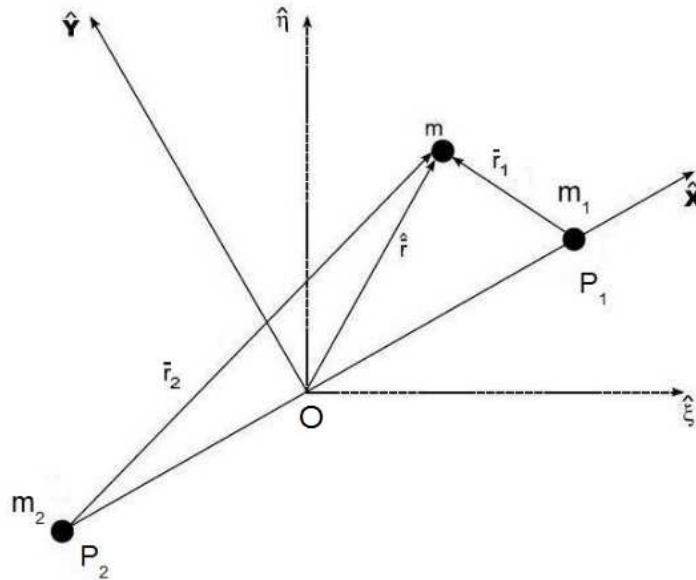


Figure 3.1 Reference frames in the CR3BP

Since the two main bodies move in circular orbits about the center of mass O , the distances OP_1 and OP_2 are constant, and the line segment P_1P_2 rotates about O with constant angular velocity ω .

We now define a new reference frame XYZ which again has its origin at O and of which the X -axis coincides with the line P_1P_2 (see Figure (3.1)). Moreover, the XY -plane coincides with the $\xi\eta$ -plane. This reference frame rotates about the

ζ -axis with a constant angular velocity ω .

When the velocity of P with respect to the inertial reference frame is indicated by $d\bar{r}/dt$ and with respect to the rotating reference frame by $\delta\bar{r}/dt$, we can write:

$$\frac{d\bar{r}}{dt} = \frac{\delta\bar{r}}{dt} + \bar{\omega} \times \bar{r} \quad (3.4)$$

We may also write:

$$\frac{d}{dt} \left(\frac{\delta\bar{r}}{dt} \right) = \frac{\delta^2\bar{r}}{\delta t^2} + \bar{\omega} \times \frac{\delta\bar{r}}{dt} \quad (3.5)$$

Differentiation of Equation (3.4) yields for the acceleration with respect to the inertial reference frame:

$$\frac{d^2\bar{r}}{dt^2} = \frac{d}{dt} \left(\frac{\delta\bar{r}}{dt} \right) + \bar{\omega} \times \frac{d\bar{r}}{dt} \quad (3.6)$$

where we have used the fact that $\bar{\omega}$ is constant. Substitution of Equations (3.4) and (3.5) into Equation (3.6) yields:

$$\frac{d^2\bar{r}}{dt^2} = \frac{\delta^2\bar{r}}{\delta t^2} + 2\bar{\omega} \times \frac{\delta\bar{r}}{dt} + \bar{\omega} \times (\bar{\omega} \times \bar{r}) \quad (3.7)$$

Substitution of Equation (3.7) into Equation (3.1) yields for the equation of motion of P with respect to the rotating reference frame:

$$\frac{\delta^2\bar{r}}{\delta t^2} = -G \left(\frac{m_1}{r_1^3} \bar{r}_1 + \frac{m_2}{r_2^3} \bar{r}_2 \right) - 2\bar{\omega} \times \frac{\delta\bar{r}}{dt} - \bar{\omega} \times (\bar{\omega} \times \bar{r}) \quad (3.8)$$

To simplify Equation (3.8) we now introduce new units.

We define:

$$m_1 = 1 - \mu \qquad m_2 = \mu \quad (3.9)$$

We require that $\mu \leq 1/2$, which means that if the masses of both bodies are not equal, body P_1 has the larger mass.

Since O is the center of mass of the system:

$$\frac{OP_1}{OP_2} = \frac{m_2}{m_1} = \frac{\mu}{1-\mu} \quad (3.10)$$

Moreover, we consider the distance $OP_1 + OP_2$ equal to the value 1, thus:

$$OP_1 = \mu \quad (3.11)$$

$$OP_2 = 1 - \mu \quad (3.12)$$

Considering $1/\omega$ as the unit of time, and using:

$$\bar{r}_1 = (x - \mu)\bar{e}_x + y\bar{e}_y + z\bar{e}_z \quad (3.13)$$

$$\bar{r}_2 = -(x - \mu + 1)\bar{e}_x + y\bar{e}_y + z\bar{e}_z \quad (3.14)$$

$$\bar{r} = x\bar{e}_x + y\bar{e}_y + z\bar{e}_z \quad (3.15)$$

$$\frac{\delta\bar{r}}{\delta t} = \dot{x}\bar{e}_x + \dot{y}\bar{e}_y + \dot{z}\bar{e}_z \quad (3.16)$$

$$\bar{e}_z \times \frac{\delta\bar{r}}{\delta t} = \dot{x}\bar{e}_y - \dot{y}\bar{e}_x \quad (3.17)$$

Equation (3.8) becomes:

$$\begin{aligned} \ddot{x} - 2\dot{y} &= x - \frac{1-\mu}{r_1^3}(x-\mu) - \frac{\mu}{r_2^3}(x-\mu+1) \\ \ddot{y} + 2\dot{x} &= y - \frac{1-\mu}{r_1^3}y - \frac{\mu}{r_2^3}y \\ \ddot{z} &= -\frac{1-\mu}{r_1^3}z - \frac{\mu}{r_2^3}z \end{aligned} \quad (3.18)$$

where:

$$r_1^2 = (x - \mu)^2 + y^2 + z^2 \quad r_2^2 = (x - \mu + 1)^2 + y^2 + z^2 \quad (3.19)$$

Introducing a scalar function U :

$$U = \frac{1}{2}(x^2 + y^2) + \frac{1 - \mu}{r_1} + \frac{\mu}{r_2} \quad (3.20)$$

System (3.18) becomes:

$$\begin{aligned} \ddot{x} - 2\dot{y} &= \frac{\partial U}{\partial x} \\ \ddot{y} + 2\dot{x} &= \frac{\partial U}{\partial y} \\ \ddot{z} &= \frac{\partial U}{\partial z} \end{aligned} \quad (3.21)$$

System (3.21) represents the equations of motions for the CR3BP.

3.2 Jacobi's integral

Multiplication of Equation (3.21-1) with \dot{x} , of Equation (3.21-2) with \dot{y} , and of Equation (3.21-3) with \dot{z} , and summation, yields:

$$\dot{x}\ddot{x} + \dot{y}\ddot{y} + \dot{z}\ddot{z} = \dot{x}\frac{\partial U}{\partial x} + \dot{y}\frac{\partial U}{\partial y} + \dot{z}\frac{\partial U}{\partial z} \quad (3.22)$$

Since U is only a function of the spatial coordinates x, y, z and not explicitly of time, we may write:

$$\frac{dU}{dt} = \frac{\partial U}{\partial x}\dot{x} + \frac{\partial U}{\partial y}\dot{y} + \frac{\partial U}{\partial z}\dot{z} \quad (3.23)$$

Combining Equations (3.22) and (3.23) yields, after integration:

$$\dot{x}^2 + \dot{y}^2 + \dot{z}^2 = 2U - C \quad (3.24)$$

Or

$$V^2 = 2U - C \quad (3.25)$$

where the value of the integration constant C is determined by the position and velocity of body P at time $t = 0$.

The constant C is referred to as the *Jacobian constant*, and may be expressed as:

$$C = x^2 + y^2 + \frac{2(1-\mu)}{r_1} + \frac{2\mu}{r_2} - V^2 \quad (3.26)$$

3.3 Surfaces of Hill

If the velocity of the small body P is zero, Equation (3.25) becomes:

$$2U = C \quad (3.27)$$

This equation describes the Surfaces of Hill, which are surfaces in XYZ space on which the velocity of P is zero.

Since for any real body $V^2 \geq 0$, the regions around both main bodies where the third body can move are given by:

$$x^2 + y^2 + \frac{2(1-\mu)}{r_1} + \frac{2\mu}{r_2} \geq C \quad (3.28)$$

So, although the orbit of the third body cannot be determined, with Equation (3.28) it is possible to determine which part of the XYZ -space is accessible to the third body for a given value of C .

Contour plots of the effective potential give the five cases of Hill's region. The white areas in Figure (3.2) are the Hill's regions and the shaded areas are the forbidden realm.

Case 1, $C > C_1$: If the Jacobi constant of the particle is larger than C_1 , the particle cannot move between the realms around m_1 and m_2 .

Case 2, $C_1 > C > C_2$: If the Jacobi constant is just smaller than C_1 , a neck between the realms around m_1 and m_2 opens up, permitting the particle to move between the two realms. The L_1 point is in this neck.

case 3, $C_2 > C > C_3$: When the Jacobi constant is just smaller than C_2 , the particle can move between the vicinity of m_1 and m_2 and the exterior realm via a neck around L_2 .

Case 4, $C_3 > C > 3 = C_4 = C_5$: In this case the Jacobi constant is smaller than C_3 but larger than C_4 and C_5 , which is always 3. The particle can pass directly from the vicinity of m_1 to the exterior realm via a neck around L_3 .

Case 5, $C < 3 = C_4 = C_5$: If the Jacobi constant is smaller than $C_4 = C_5 = 3$,

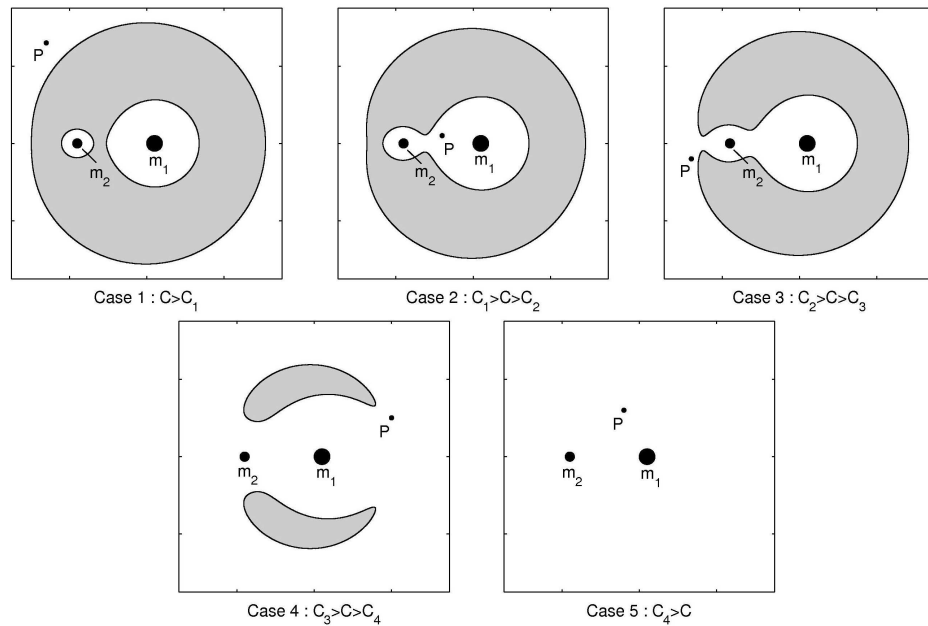


Figure 3.2 Surfaces of Hill projected on XY -plane for decreasing values of C

the forbidden realm disappears. Case 5 is where the particle is free to move in the entire XY -plane.

The critical values of C which separate these five cases are the values C_i , $i = 1, 2, 3, 4$, corresponding to the equilibrium points L_i , $i = 1, 2, 3, 4, 5$, where C_4 is the same for libration points L_4 and L_5 . For instance, for case 3, the Jacobi constant value lies between C_2 and C_3 which are the Jacobi constant values of the libration points L_2 and L_3 , respectively.

A glance at Figure (3.2) reveals that, beginning in case 1, there are three main realms of possible motion, or simply realms. Considering, for example, Figure (3.2)(a), the white region surrounding m_1 is referred to as the m_1 realm, sometimes referred to as the interior realm. The small region surrounding m_2 is the m_2 realm. The realm which lies outside both the m_1 and m_2 realms, and extends to infinity, is the exterior realm. For case 1, the realms are separated. Moving up in energy to case 2, a neck around L_1 opens up between the m_1 and m_2 realms, permitting the particle to transfer between the two. An additional neck opens up around L_2 when we move up in energy to case 3, permitting travel between all three realms.

3.4 Lagrange libration points

To determine and locate these equilibrium points we assume:

$$\ddot{x} = \ddot{y} = \ddot{z} = \dot{x} = \dot{y} = \dot{z} = 0 \quad (3.29)$$

from Equations (3.21) it follows that:

$$\frac{\partial U}{\partial x} = \frac{\partial U}{\partial y} = \frac{\partial U}{\partial z} = 0 \quad (3.30)$$

That implies:

$$\begin{aligned} x - \frac{1-\mu}{r_1^3}(x-\mu) - \frac{\mu}{r_2^3}(x-\mu+1) &= 0 \\ y \left(1 - \frac{1-\mu}{r_1^3} - \frac{\mu}{r_2^3} \right) &= 0 \\ z &= 0 \end{aligned} \quad (3.31)$$

The third equation of (3.31) implies that the five points L_1 to L_5 are all located in the XY -plane.

Combination of Equation (3.19) and (3.31) yields as a first solution:

$$\begin{aligned} y &= 0 \\ x - (1-\mu) \frac{x-\mu}{|x-\mu|^3} - \mu \frac{x-\mu+1}{|x-\mu+1|^3} &= 0 \end{aligned} \quad (3.32)$$

The second equation of System (3.32) is a fifth-degree equation, and it can be shown that it has three real roots, corresponding to the points L_1, L_2, L_3 . Thus, these points are located on the x -axis. Point L_2 is located to the left of P_2 , L_3 is located to the right of P_1 . For point L_1 $r_2 \leq r_1$, whereby L_1 is located closer to P_2 when μ is smaller.

The second solution can be found from System (3.31) by solving the two

equations:

$$\begin{aligned} x - \frac{1-\mu}{r_1^3}(x-\mu) - \frac{\mu}{r_2^3}(x-\mu+1) &= 0 \\ 1 - \frac{1-\mu}{r_1^3} - \frac{\mu}{r_2^3} &= 0 \end{aligned} \quad (3.33)$$

Reworking both equations of System (3.33), it can be shown that the second solution is obtained, which is:

$$r_1 = r_2 = 1 \quad (3.34)$$

This solution corresponds to the points L_4 and L_5 . Thus, these points form an equilateral triangle with the two main bodies. The coordinates of the points L_4 and L_5 are:

$$x = -\frac{1}{2} + \mu \quad y = \pm \frac{1}{2}\sqrt{3} \quad (3.35)$$

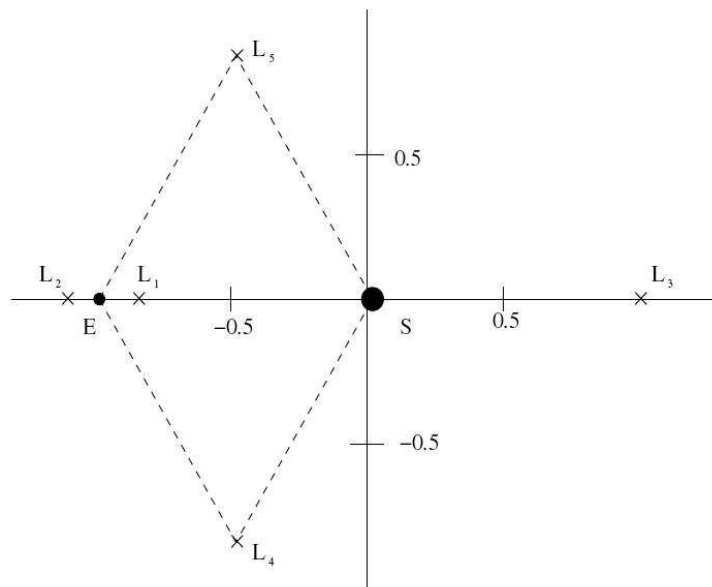


Figure 3.3 Equilibrium points of the CR3BP problem in the xy -plane of the frame rotating with the mean motion of the orbit of m_1 and m_2

3.5 Computation of the location of L_3

Here we will show how to compute the location of L_3 (and in particular L_3 of the Sun-Earth System), according to [Szebehely, 1967].

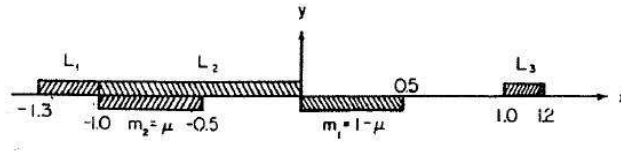


Figure 3.4 Location of the collinear equilibrium points and the primaries for $\mu \in [0, 0.5]$ [Szebehely, 1967]

According to the equations of the CR3BP, to compute the location of the collinear Lagrange points requires the solution of:

$$x - \frac{(1 - \mu)(x - \mu)}{r_1^3} - \frac{\mu(x + 1 - \mu)}{r_2^3} = 0 \quad (3.36)$$

since $y = 0$ and where $r_1 = (x - \mu)$, $r_2 = (x + 1 - \mu)$, $\mu = \frac{m_2}{m_1 + m_2}$, being, in this case, m_2 the mass of the Earth and m_1 the mass of the Sun. Computation of the values of the abscissas of the collinear points requires the solution of Euler's quintic equations.

Equation (3.36) can be rewritten as:

$$x + \frac{A}{(x - \mu)^2} + \frac{B}{(x + 1 - \mu)^2} = 0 \quad (3.37)$$

Let's define a reference frame as in Figure (3.5):

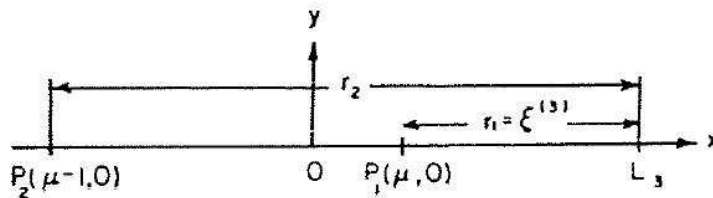


Figure 3.5 Notation for the computation of $x = x(L_3)$ [Szebehely, 1967]

This is the reference frame used only for the L_3 case, otherwise other reference

frames are usually defined. Then $r_1 = x - \mu$ and $r_2 = 1 + x - \mu$, which substituted in Equation (3.36) gives:

$$x - \frac{1 - \mu}{(x - \mu)^2} - \frac{\mu}{(1 + x - \mu)^2} = 0 \quad (3.38)$$

thus, $[A = \mu - 1, B = -\mu]$.

Writing $r_1 = \xi = x - \mu$, $r_2 = 1 + \xi$, then $x = \mu + \xi$, and we have:

$$\xi + \mu - \frac{1 - \mu}{\xi^2} - \frac{\mu}{(1 + \xi)^2} = 0 \quad (3.39)$$

or

$$\xi^3 = \frac{(1 - \mu)(1 + \xi)^2}{1 + 2\mu + \xi(2 + \mu + \xi)} \quad (3.40)$$

The quintic equation becomes:

$$\xi^5 + (2 + \mu)\xi^4 + (1 + 2\mu)\xi^3 - (1 - \mu)\xi^2 - 2(1 - \mu)\xi - (1 - \mu) = 0 \quad (3.41)$$

which, because of the single sign-change present, indicates one and only one positive root. Since this root is near +1 it is advantageous to introduce $\eta = \xi - 1$, which gives:

$$\eta^5 + (7 + \mu)\eta^4 + (19 + 6\mu)\eta^3 + (24 + 13\mu)\eta^2 + 2(6 + 7\mu)\eta + 7\mu = 0 \quad (3.42)$$

Equation (3.42) can be solved using, for example, the Newton's Method, taking as initial approximation $\eta_0 = -7/12 \mu$. Thus r_1 and r_2 are found.

μ	$3.0404234 \cdot 10^{-6}$
$x(L_3)$	1.00000126684308
r_1	0.99999822641968
r_2	1.99999822641968

Table 3.1 μ , position of L_3 from the baricenter of the system, r_1 and r_2

As shown in Table (3.1), for the Sun-Earth system the distance Sun- L_3 has the value of 0.99999824799915, in the normalized reference frame introduce above.

3.6 Stability in the Lagrange libration points

One may wonder whether the equilibrium in the libration points is stable or not. Here, we define the motion to be stable if a body under the influence of a small perturbation does not move away from the libration point unboundedly. So, this definition means that we consider a motion stable, if the motion of the body does not diverge from the libration point.

Stability in these five Lagrange points can be investigated through linearisation of the equations of motion in their neighbourhood. Linearisation of the first two equations of System (3.21) leads to the following system of equations:

$$\begin{bmatrix} \dot{x} \\ \dot{v}_x \\ \dot{y} \\ \dot{v}_y \end{bmatrix} = \begin{bmatrix} 0 & 1 & 0 & 0 \\ \frac{\partial^2 U}{\partial x^2} & 0 & \frac{\partial^2 U}{\partial x \partial y} & 2 \\ 0 & 0 & 0 & 1 \\ \frac{\partial^2 U}{\partial x \partial y} & -2 & \frac{\partial^2 U}{\partial y^2} & 0 \end{bmatrix}_{(x,y)=L_j(x,y)} \begin{bmatrix} x \\ v_x \\ y \\ v_y \end{bmatrix} \quad (3.43)$$

where $v_x = \dot{x}$, $v_y = \dot{y}$ and $j = 1, \dots, 5$.

Linearizing the third equation of System (3.21) we have:

$$\ddot{z} - z \left. \frac{\partial^2 U}{\partial z^2} \right|_{(x,y)=L_j(x,y)} = 0 \quad (3.44)$$

we note that the motion in z -direction is completely decoupled from the motion in the x -direction and y -direction. Because $U_{zz} < 0$, the solution for the motion in the z -direction is:

$$z = C_1 \cos \left(\sqrt{\left| \frac{\partial^2 U}{\partial z^2} \right|} t \right) + C_2 \sin \left(\sqrt{\left| \frac{\partial^2 U}{\partial z^2} \right|} t \right) \quad (3.45)$$

Hence, for all libration points the motion in the z -direction is purely periodic, therefore stable. The period of this motion is independent of the motion in the x -direction and y -direction.

The characteristic equation for System (3.43) is obtained by evaluating the following determinant:

$$\begin{vmatrix} -\lambda & 1 & 0 & 0 \\ \frac{\partial^2 U}{\partial x^2} & -\lambda & \frac{\partial^2 U}{\partial x \partial y} & 2 \\ 0 & 0 & -\lambda & 1 \\ \frac{\partial^2 U}{\partial x \partial y} & -2 & \frac{\partial^2 U}{\partial y^2} & -\lambda \end{vmatrix} \quad (3.46)$$

which leads to:

$$\lambda^4 + (4 - U_{xx} - U_{yy})\lambda^2 + U_{xx}U_{yy} - U_{xy}^2 \quad (3.47)$$

where U_{ij} means $\frac{\partial U}{\partial i \partial j}$

The solution of Equation (3.47) will consist of four values of λ that will, generally, have complex values. However, the equation is quadratic in λ^2 and thus the values of λ will consist of opposite pairs. For example: $\lambda_2 = -\lambda_1$, $\lambda_4 = -\lambda_3$. If the four roots are all different, the motion of a body with respect to the libration point can be written as:

$$\begin{aligned} x(t) &= A_1 e^{\lambda_1 t} + A_2 e^{-\lambda_1 t} + A_3 e^{\lambda_3 t} + A_4 e^{-\lambda_3 t} \\ y(t) &= B_1 e^{\lambda_1 t} + B_2 e^{-\lambda_1 t} + B_3 e^{\lambda_3 t} + B_4 e^{-\lambda_3 t} \end{aligned} \quad (3.48)$$

If λ_2 and λ_4 , and hence λ_1 and λ_3 , are equal ($\lambda_1 = \lambda_2 = \lambda_3 = \lambda_4$), the solution is:

$$\begin{aligned} x(t) &= A_1 e^{\lambda_1 t} + A_2 e^{-\lambda_1 t} + A_3 t e^{\lambda_1 t} + A_4 t e^{-\lambda_1 t} \\ y(t) &= B_1 e^{\lambda_1 t} + B_2 e^{-\lambda_1 t} + B_3 t e^{\lambda_1 t} + B_4 t e^{-\lambda_1 t} \end{aligned} \quad (3.49)$$

From Equations (3.48) and (3.49) we may conclude that the motion is stable if all λ are different and their real part is smaller or equal to zero. The last requirement can be expressed as follows. In general, we may write: $\lambda = \alpha + i\beta$, where α and β are real values. So, we may write: $e^{\lambda t} = e^{\alpha t} \cdot e^{i\beta t}$. The term $e^{i\beta t}$ is associated with the *sine* and *cosine* functions. We therefore may conclude that if $\alpha = 0$ the term $e^{\lambda t}$ will lead to pure sinusoidal oscillations, if $\alpha < 0$ to damped oscillations, and if $\alpha > 0$ to diverging oscillations. So, if $\alpha \leq 0$, $x(t)$ and $y(t)$ cannot increase arbitrarily. Since the λ 's occur in opposite pairs, the requirement for stability reduces to λ_i 's different and pure imaginary, which results in λ_i^2 being real and $\lambda_i^2 < 0$. In that case the motion is non-damped pure oscillation.

3.6.1 Collinear Lagrange points: stability

For collinear points L_1 , L_2 and L_3 we may write:

$$y_{L_i} = z_{L_i} = 0 \quad r_1^2 = (x_{L_i} - \mu)^2 \quad r_2^2 = (x_{L_i} - \mu + 1)^2 \quad (3.50)$$

where $i = 1, 2, 3$. Therefore it follows by substitution that:

$$U_{xx} = 1 + 2K \quad U_{xy} = 0 \quad U_{yy} = 1 - K \quad (3.51)$$

where:

$$K = \frac{1 - \mu}{r_1^3} + \frac{\mu}{r_2^3} \quad (3.52)$$

Substitution of Equation (3.51) into (3.47) yields:

$$\lambda^4 + (2 - K)\lambda^2 + (1 + 2K)(1 - K) = 0 \quad (3.53)$$

Then, the eigenvalues are:

$$\lambda^2 = \frac{(K - 2) \pm \sqrt{K(9K - 8)}}{2} \quad (3.54)$$

As we have found earlier, for a stable equilibrium, this equation should have two real negative roots of λ^2 . Then, the product of these roots is positive, which, since $K > 0$, requires:

$$1 - K > 0 \quad (3.55)$$

The location of points L_1 , L_2 , L_3 is described by the first equation of System (3.31), which can be also rewritten as:

$$x \left(1 - \frac{1 - \mu}{r_1^3} - \frac{\mu}{r_2^3} \right) - \frac{\mu(1 - \mu)}{r_1^3} + \frac{\mu(1 - \mu)}{r_2^3} = 0 \quad (3.56)$$

or, with Equation (3.52):

$$1 - K = \frac{\mu(1 - \mu)}{x} \left(\frac{1}{r_2^3} - \frac{1}{r_1^3} \right) \quad (3.57)$$

It is clear from this equation that if x is positive, which implies that $r_1 < r_2$, it follows that:

$$1 - K < 0 \quad (3.58)$$

From Equations (3.55) and (3.58) it follows that the equilibrium at the points L_1 , L_2 and L_3 is *unstable*.

3.6.2 Equilateral Lagrange points: stability

If $\mu \leq 0.03852$, a body located at the equilibrium points L_4 or L_5 will perform, after a small perturbation, a *non-damped oscillation* about these points. For $\mu > 0.03852$, the motion of the body will diverge with respect to the libration points L_4 or L_5 .

3.7 Motion about the Lagrange libration points

We have already found with Equation (3.45) that for all five libration points the motion in the z -direction is an undamped oscillation and is uncoupled from the motion in the x -direction and y -direction.

3.7.1 Collinear Lagrange libration points

According to the results found in the previous section, for the collinear Lagrange points:

$$U_{xx} = 1 + 2K > 3 \quad U_{xy} = 0 \quad U_{yy} = 1 - K < 0 \quad (3.59)$$

The characteristic equation of the linearised system is given by Equation (3.53).

Defining

$$\alpha = 1 - \frac{1}{2}K < \frac{1}{2} \quad \beta^2 = (2K + 1)(K - 1) > 0 \quad (3.60)$$

the solution of Equation (3.53) becomes:

$$\lambda^2 = -\alpha \pm \sqrt{\alpha^2 + \beta^2} \quad (3.61)$$

So, two roots (λ_1 and λ_2) are real, while the other two roots (λ_3 and λ_4) are pure imaginary. The real roots give rise to an exponential increase of the distances x and y , while the imaginary roots result in a periodic motion.

It has already been shown that the four roots λ_i are two by two of the opposite sign, resulting in the equations of motion (3.48). The coefficients A_i , B_i in these equations are not independent. In fact:

$$B_i = \frac{\lambda_i^2 - 2K - 1}{2\lambda_i} A_i = \gamma_i A_i \quad (3.62)$$

where $i = 1, 2, 3, 4$. Consequently, the four initial conditions x_0 , y_0 , \dot{x}_0 , \dot{y}_0 will completely determine the eight coefficients A_i , B_i .

Thus, the equations of motion (3.48) become:

$$\begin{aligned} x(t) &= A_1 e^{\lambda_1 t} + A_2 e^{-\lambda_1 t} + A_3 e^{\lambda_3 t} + A_4 e^{-\lambda_3 t} \\ y(t) &= \gamma_1 A_1 e^{\lambda_1 t} + \gamma_2 A_2 e^{-\lambda_1 t} + \gamma_3 A_3 e^{\lambda_3 t} + \gamma_4 A_4 e^{-\lambda_3 t} \end{aligned} \quad (3.63)$$

3.7.2 Equilateral Lagrange libration points

Since we are not interested in the motion of the third body in the vicinity of L_4 or L_5 , here we will not go into detail. However, the procedure to investigate it is similar to the analysis done for the collinear Lagrange libration points. The general solution has the same structure of Equations (3.48), but, of course, it has different eigenvalues.

A detailed analysis can be found in any book about astrodynamics, for example in [Wakker, 2005].

3.8 Hamiltonian formulation

The equations of motion for the CR3BP can also be derived through the use of a Hamiltonian function.

Here we will follow [Koon *et al.*, 2006].

Consider the Euler-Lagrange equations:

$$\frac{d}{dt} \frac{\partial L}{\partial \dot{q}_i} - \frac{\partial L}{\partial q_i} = 0 \quad (3.64)$$

where q_i are generalised coordinates, $i = 1, \dots, n$.

In the inertial reference frame, the Lagrangian \mathbf{L} is:

$$\mathbf{L}(\xi, \eta, \zeta, \dot{\xi}, \dot{\eta}, \dot{\zeta}, t) = \frac{1}{2}(\dot{\xi}^2 + \dot{\eta}^2 + \dot{\zeta}^2) - \mathbf{U}(\xi, \eta, \zeta, t) \quad (3.65)$$

In the rotating frame, the Lagrangian L is given by:

$$L(x, y, z, \dot{x}, \dot{y}, \dot{z}) = \frac{1}{2}((\dot{x} - y)^2 + (\dot{y} + x)^2 + \dot{z}^2) - U(x, y, z) \quad (3.66)$$

It is now *time independent*, simplifying the analysis of the solutions.

Since both the distances r_1 and r_2 are invariant under rotation, the gravitational potential is:

$$U(x, y, z) = -\frac{1-\mu}{r_1} - \frac{\mu}{r_2} \quad (3.67)$$

where r_1 and r_2 are expressed in rotating coordinates as:

$$r_1^2 = (x - \mu)^2 + y^2 + z^2 \quad (3.68)$$

$$r_2^2 = (x - \mu + 1)^2 + y^2 + z^2 \quad (3.69)$$

The theory of moving systems says that one can simply write down the Euler-Lagrange equations in the rotating frame and one will get the correct equations. It is a very efficient generic method for deriving equations for either moving systems or for systems seen from moving frames.

In this case, the Euler-Lagrange equations are:

$$\begin{aligned} \frac{d}{dt}(\dot{x} - y) &= \dot{y} + x - U_x \\ \frac{d}{dt}(\dot{y} + x) &= -(\dot{x} - y) - U_y \\ \frac{d}{dt}\dot{z} &= -U_z \end{aligned} \quad (3.70)$$

and, after simplification:

$$\begin{aligned} \ddot{x} - 2\dot{y} &= -\bar{U}_x \\ \ddot{y} + 2\dot{x} &= -\bar{U}_y \\ \ddot{z} &= -\bar{U}_z \end{aligned} \quad (3.71)$$

where:

$$\bar{U}(x, y, z) = -\frac{1}{2}(x^2 + y^2) + U(x, y, z) \quad (3.72)$$

is the augmented or effective potential.

Whenever one has a Lagrangian system, one can transform it to Hamiltonian form by means of the Legendre transformation:

$$p_i = \frac{\partial L}{\partial \dot{q}_i} \quad H(q_i, p_i) = \sum_{i=1}^n p_i \dot{q}_i - L(q_i, p_i)$$

to get the equations in Hamiltonian form:

$$\dot{q}_i = \frac{\partial H}{\partial p_i} \quad \dot{p}_i = -\frac{\partial H}{\partial q_i} \quad (3.73)$$

In our case, the Legendre transformation is given by:

$$\begin{aligned} p_x &= \frac{\partial L}{\partial \dot{x}} = \dot{x} - y \\ p_y &= \frac{\partial L}{\partial \dot{y}} = \dot{y} + x \\ p_z &= \frac{\partial L}{\partial \dot{z}} = \dot{z} \end{aligned} \tag{3.74}$$

and so we obtain the Hamiltonian function:

$$\begin{aligned} H(x, y, z, p_x, p_y, p_z) &= p_x \dot{x} + p_y \dot{y} + p_z \dot{z} - L \\ &= \frac{1}{2}((p_x + y)^2 + (p_y - x)^2) + p_z^2 + \bar{U} \end{aligned} \tag{3.75}$$

where p_x , p_y and p_z are the the momenta conjugate to x , y , and z respectively. Hence the Hamiltonian equations are given by:

$$\begin{aligned} \dot{x} &= \frac{\partial H}{\partial p_x} = p_x + y \\ \dot{y} &= \frac{\partial H}{\partial p_y} = p_y - x \\ \dot{z} &= \frac{\partial H}{\partial p_z} = p_z \\ \dot{p}_x &= -\frac{\partial H}{\partial x} = p_y - x - \bar{U}_x \\ \dot{p}_y &= -\frac{\partial H}{\partial y} = -p_x - y - \bar{U}_y \\ \dot{p}_z &= -\frac{\partial H}{\partial z} = -\bar{U}_z \end{aligned} \tag{3.76}$$

Substituting the first three equations in the other three, we find the equations of motion for the CR3BP, which are the same as those found before in System (3.21):

$$\begin{aligned} \ddot{x} - 2\dot{y} &= -\bar{U}_x \\ \ddot{y} + 2\dot{x} &= -\bar{U}_y \\ \ddot{z} &= -\bar{U}_z \end{aligned} \tag{3.77}$$

Note that $C = -2H$

3.9 Periodic orbits around the Libration points

We have already found the equations of motion of a particle (body) around the collinear libration points for the CR3BP. In this section we will rewrite those equations, and analyse them in more detail. In particular, we will see Lissajous, Lyapunov, Halo and quasi-Halo orbits (illustrations can be found at the end of the chapter).

We will especially refer to [Richardson, 1980] and [Gomez and Masdemont, 1998].

3.9.1 Equations of motion

In a reference system, centered at any of the three collinear equilibria ($L_{1,2,3}$, and with the x-axis, in all cases, oriented with r_{12} , as in Figure (3.6)), the Lagrangian can be written in the form:

$$\begin{aligned} L &= \frac{1}{2}(\dot{\rho}, \dot{\rho}) + \frac{r_1 \rho}{r_{12}^3} - \dot{r}_1 \dot{\rho} + \mu \left[\frac{1}{|r_1 - \rho|} - \frac{r_1 \rho}{r_1^3} \right] + (1 - \mu) \left[\frac{1}{|r_2 - \rho|} - \frac{r_2 \rho}{r_2^3} \right] \\ &= \frac{1}{2}(\dot{\rho}, \dot{\rho}) + \frac{d}{dt}(\dot{r}_1 \rho) + \mu \left[\frac{1}{|r_1 - \rho|} - \frac{r_1 \rho}{r_1^3} \right] + (1 - \mu) \left[\frac{1}{|r_2 - \rho|} - \frac{r_2 \rho}{r_2^3} \right] \end{aligned}$$

The terms involving the factors μ and $(1-\mu)$ have the form of a third-body perturbing potential. Using power series developments in terms of Legendre polynomials, the Lagrangian can be rewritten as:

$$L = \frac{1}{2}(\dot{\rho}, \dot{\rho}) + \frac{d}{dt}(\dot{r}_1 \rho) + \frac{\mu}{r_1} \sum_{n=2}^{\infty} \left(\frac{\rho}{r_1} \right)^n P_n(\cos S_1) + \frac{1-\mu}{r_2} \sum_{n=2}^{\infty} \left(\frac{\rho}{r_2} \right)^n P_n(\cos S_2)$$

Taking the unit of distance as:

$$\begin{aligned} r_1 &= 1, \text{ for the motion about } L_1 \text{ or } L_2 \\ r_2 &= 1, \text{ for the motion about } L_3 \end{aligned}$$

where r_1 is the distance libration point-smaller primary and r_2 is the distance libration point-bigger primary, the Lagrangian can be written in the form:

$$L = \frac{1}{2}(\rho', \rho') + \sum_{n=2}^{\infty} c_n \rho^n P_n \left(\frac{x}{\rho} \right) \quad (3.78)$$

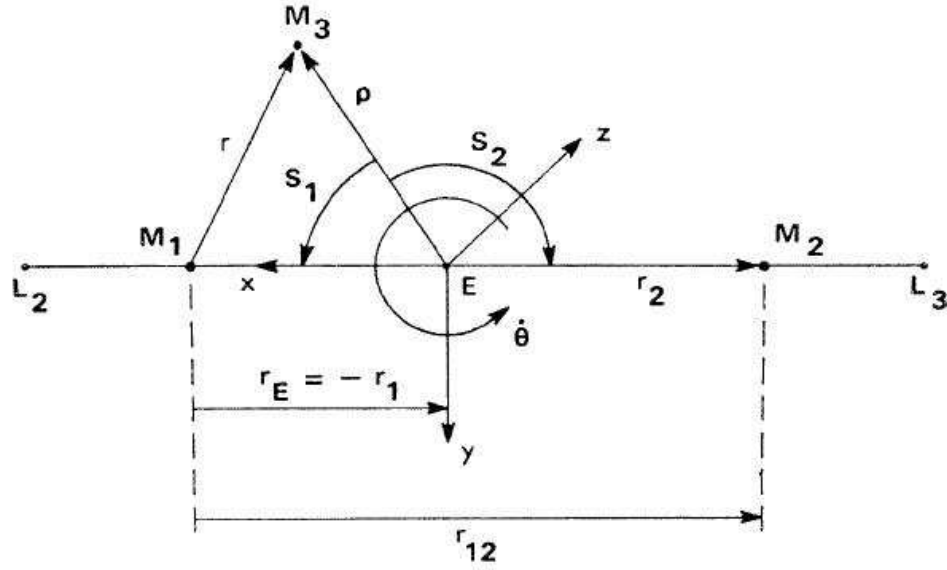


Figure 3.6 Richardson's reference system centered at the equilibrium point L_1 [Richardson, 1980]

where primes denote derivatives with respect to the variable $s = \gamma_L^{3/2}t$, P_n the Legendre polynomials, and where

$$\gamma_L = \begin{cases} r_1/r_{12} & \text{for } L_1, L_2 \\ r_2/r_{12} & \text{for } L_3 \end{cases}$$

The constants c_n are given by the expressions:

$$c_n = \frac{1}{\gamma_L^3} \left((\pm 1)^n \mu + (-1)^n \frac{(1-\mu)\gamma_L^{n+1}}{(1 \mp \gamma_L)^{n+1}} \right) \quad (3.79)$$

with the upper sign for L_1 and the lower one for L_2 , and

$$c_n = \frac{1}{\gamma_L^3} \left(1 - \mu + \frac{\mu\gamma_L^{n+1}}{(1 + \gamma_L)^{n+1}} \right) \quad (3.80)$$

for L_3 .

The equations of motion have the following compact expressions:

$$\begin{aligned}
x'' - 2y' - (1 + 2c_2)x &= \sum_{n=2}^{\infty} (n+1)c_{n+1}\rho^n P_n\left(\frac{x}{\rho}\right) \\
y'' + 2x' + (c_2 - 1)y &= \sum_{n=3}^{\infty} c_n y \rho^{n-2} \bar{P}_n\left(\frac{x}{\rho}\right) \\
z'' + c_2 z &= \sum_{n=3}^{\infty} c_n z \rho^{n-2} \bar{P}_n\left(\frac{x}{\rho}\right)
\end{aligned} \tag{3.81}$$

where:

$$\bar{P}_n = \sum_{k=0}^{[(n-2)/2]} (3 + 4k - 2n) P_{n-2k-2}\left(\frac{x}{\rho}\right)$$

The equations of System (3.81) represent, once again, the equations of motion for the CR3BP.

In literature, System (3.81) is usually written in a different form, and x'' , x' are expressed as \ddot{x} , \dot{x} , even if the derivatives are with respect to S and not to t (the same for the other two coordinates, y and z).

Thus, System (3.81) becomes:

$$\begin{aligned}
\ddot{x} - 2\dot{y} - (1 + 2c_2)x &= \frac{\partial}{\partial x} \sum_{n \geq 3} c_n \rho^n P_n\left(\frac{x}{\rho}\right) \\
\ddot{y} + 2\dot{x} + (c_2 - 1)y &= \frac{\partial}{\partial y} \sum_{n \geq 3} c_n \rho^n P_n\left(\frac{x}{\rho}\right) \\
\ddot{z} + c_2 z &= \frac{\partial}{\partial z} \sum_{n \geq 3} c_n \rho^n P_n\left(\frac{x}{\rho}\right)
\end{aligned} \tag{3.82}$$

3.9.2 Lissajous orbits

The linearization of System (3.82) can be written as:

$$\begin{aligned}\ddot{x} - 2\dot{y} - (1 + 2c_2)x &= 0 \\ \dot{y} + 2\dot{x} + (c_2 - 1)y &= 0 \\ \ddot{z} + c_2z &= 0\end{aligned}\tag{3.83}$$

where the value of c_2 depends on the mass parameter and the L_i we are studying.

The solution of this linearised system is:

$$\begin{aligned}x(t) &= A_1e^{\lambda t} + A_2e^{-\lambda t} + A_3 \cos \omega t + A_4 \sin \omega t \\ y(t) &= cA_1e^{\lambda t} - cA_2e^{-\lambda t} - kA_4 \cos \omega t + kA_3 \sin \omega t \\ z(t) &= A_5 \cos \nu t + A_6 \sin \nu t\end{aligned}\tag{3.84}$$

where A_i are arbitrary constants and c, k, λ, ω and ν are constants depending on c_2 only:

$$\begin{aligned}\omega &= \sqrt{\frac{2 - c_2 + \sqrt{9c_2^2 - 8c_2}}{2}} \\ \nu &= \sqrt{c_2} \\ c &= \frac{\lambda^2 - 1 - 2c_2}{2\lambda} \\ \lambda &= \sqrt{\frac{c_2 - 2 + \sqrt{9c_2^2 - 8c_2}}{2}} \\ k &= \frac{-(\omega^2 + 1 + 2c_2)}{2\omega}\end{aligned}$$

As already briefly addressed, we can see in System (3.84) that A_1 and A_2 are the coefficients of the exponential part. A_1 is called the unstable hyperbolic amplitude, because it accompanies the part corresponding to the eigenvalue which is responsible for instability. On the other hand, A_2 is the stable hyperbolic amplitude as it corresponds to an eigenvalue with negative real part. For instance, the relation $A_1 = 0 ; A_2 \neq 0$, defines a stable manifold. Any orbit verifying this condition will tend forward in time to the Lissajous orbit defined by A_3, A_4, A_5 and A_6 , since the term containing the A_2 -component will die out. A similar fact happens when $A_1 \neq 0 ; A_2 = 0$. The term with A_1 will increase in forward time, but die out backwards in time. Therefore, solutions having $A_1 \neq 0$ go away from

the oscillating or central part exponentially fast in forward time, and form the so-called unstable manifold.

Solutions with $A_1 = A_2 = 0$ belong to the so-called centre manifold, as they only have bounded terms (oscillating) as they only contain the part of the solution corresponding to pure imaginary eigenvalues. Furthermore, it is convenient to look at the central solutions as having an amplitude and a phase in the xy plane (A_x and ϕ) as well as an amplitude and a phase in the z direction (A_z and ψ).

Therefore, we use the following relations:

$$\begin{aligned} A_3 &= A_x \cos \phi \\ A_4 &= -A_x \sin \phi \\ A_5 &= A_z \cos \psi \\ A_6 &= -A_z \sin \psi \end{aligned}$$

Finally, the expression of the linearised solutions on the center manifold takes the form:

$$\begin{aligned} x(t) &= A_x \cos(\omega t + \phi) \\ y(t) &= k A_x \sin(\omega t + \phi) \\ z(t) &= A_z \cos(\nu t + \psi) \end{aligned} \tag{3.85}$$

where ω and ν are the planar and vertical characteristic frequencies and k is a constant. The parameters A_x and A_z are the in-plane and out-of-plane amplitudes of the orbit and ϕ , ψ are the phases. These linear solutions are already Lissajous trajectories.

Getting back to System (3.84), in this linear approximation the in-plane and out-of-plane motions are decoupled and we get the following relations between the coordinates of the trajectory and the constants A_1, A_2, \dots, A_6 , (which are in fact first integrals of motion):

$$\begin{pmatrix} x \\ y \\ \dot{x} \\ \dot{y} \end{pmatrix} = \begin{pmatrix} e^{\lambda t} & e^{-\lambda t} & \cos \omega t & \sin \omega t \\ c e^{\lambda t} & -c e^{-\lambda t} & k \sin \omega t & -k \cos \omega t \\ \lambda e^{\lambda t} & -\lambda e^{-\lambda t} & -\omega \sin \omega t & \omega \cos \omega t \\ c \lambda e^{\lambda t} & c \lambda e^{-\lambda t} & k \omega \cos \omega t & k \omega \sin \omega t \end{pmatrix} \begin{pmatrix} A_1 \\ A_2 \\ A_3 \\ A_4 \end{pmatrix}$$

$$\begin{pmatrix} z \\ \dot{z} \end{pmatrix} = \begin{pmatrix} \cos \nu t & \sin \nu t \\ -\nu \sin \nu t & \nu \cos \nu t \end{pmatrix} \begin{pmatrix} A_5 \\ A_6 \end{pmatrix}$$

Inverting the system, the first integrals of System (3.84) are found, in terms of a given state vector at time t , $(x(t), y(t), z(t), \dot{x}(t), \dot{y}(t), \dot{z}(t))$:

$$\begin{pmatrix} A_1 \\ A_2 \\ A_3 \\ A_4 \end{pmatrix} = \begin{pmatrix} \frac{-k\omega}{2d_1}e^{-\lambda t} & \frac{\omega}{2d_2}e^{-\lambda t} & \frac{k}{2d_2}e^{-\lambda t} & \frac{1}{2d_1}e^{-\lambda t} \\ \frac{-k\omega}{2d_1}e^{\lambda t} & \frac{-\omega}{2d_2}e^{\lambda t} & \frac{-k}{2d_2}e^{\lambda t} & \frac{1}{2d_1}e^{\lambda t} \\ \frac{c\lambda}{d_1}\cos\omega t & \frac{\lambda}{d_2}\sin\omega t & \frac{-c}{d_2}\sin\omega t & \frac{-1}{d_1}\cos\omega t \\ \frac{c\lambda}{d_1}\sin\omega t & \frac{-\lambda}{d_2}\cos\omega t & \frac{c}{d_2}\cos\omega t & \frac{-1}{d_1}\sin\omega t \end{pmatrix} \begin{pmatrix} x \\ y \\ \dot{x} \\ \dot{y} \end{pmatrix}$$

$$\begin{pmatrix} A_5 \\ A_6 \end{pmatrix} = \begin{pmatrix} \cos\nu t & \frac{-1}{\nu}\sin\nu t \\ -\sin\nu t & \frac{1}{\nu}\cos\nu t \end{pmatrix} \begin{pmatrix} z \\ \dot{z} \end{pmatrix}$$

where $d_1 = c\lambda - k\omega$ and $d_2 = c\omega + k\lambda$

When we consider the nonlinear terms of System (3.82), we look for formal series solutions in powers of the amplitudes A_x and A_z of the type:

$$\begin{pmatrix} x \\ y \\ z \end{pmatrix} = \sum_{i,j=1}^{\infty} \left(\sum_{|k|\leq i, |m|\leq j} \begin{pmatrix} x \\ y \\ z \end{pmatrix}_{ijkm} \begin{pmatrix} \cos \\ \sin \\ \cos \end{pmatrix} (k\theta_1 + m\theta_2) \right) A_x^i A_z^j \quad (3.86)$$

where $\theta_1 = \Omega t + \phi$ and $\theta_2 = Nt + \psi$. Here the exponential terms are taken equal to zero. Due to the presence of nonlinear terms, the frequencies Ω and N cannot be kept equal to ω and ν , and they must be expanded in powers of the amplitudes:

$$\Omega = \omega + \sum_{i,j=1}^{\infty} \omega_{ij} A_x^i A_z^j \quad N = \nu + \sum_{i,j=1}^{\infty} \nu_{ij} A_x^i A_z^j$$

The goal is to compute the coefficients x_{ijkm} , y_{ijkm} , z_{ijkm} , ω_{ij} , and ν_{ij} recurrently up to a finite order $N = i + j$. Identifying the coefficients of the general solution (3.86) with the ones obtained from the solution of the linear part (3.85), in literature we see that the non-zero values are $x_{1010} = 1$, $y_{1010} = k$, $z_{1010} = 1$, $\omega_{00} = \omega$ and $\nu_{00} = \nu$. Inserting the linear solution (3.85) in the equations of motion, we get a remainder for each equation, which is a series in A_x and A_z beginning with terms of order $i + j = 2$. In order to get the coefficients of order 2, this known order 2 terms must be equated to the unknown order 2 terms of the left-hand side of the equations. The general step is similar. It assumes that the solution has been computed up to a certain order $n - 1$. Then it is substituted in the right-hand side of the CR3BP equations, producing terms of order n in A_x and A_z . This known order n terms must be equated with the unknown terms of order n of the left-hand side.

3.9.3 Lyapunov orbits

In the planar restricted three body problem, there exists only one planar periodic motion around L_i ($i = 1, 2, 3$) for each given energy level: the planar Lyapunov orbit. The use of planar Lyapunov orbits is convenient for several reasons. Obviously, the complexity of the problem is reduced when using the planar approximation, because the order of the system, as well as the dimension of the manifolds and their intersections is smaller than for the spatial problem. In addition, planar Lyapunov orbits exist also in the 3D restricted three body problem, and they surround the rest of types of orbits in the Poincaré maps. In fact, the xy projection of hyperbolic manifolds belonging to other libration orbits (Lissajous or Halo orbits, for instance) is actually contained in the manifolds of the Lyapunov orbits of the corresponding energy level. Therefore, using these planar orbits is a natural way of studying the 3D channels in the libration regions. Furthermore, planar Lyapunov orbits and their hyperbolic manifolds can be computed using Lindstedt-Poincaré procedures.

System (3.82) is reduced to:

$$\begin{aligned}\ddot{x} - 2\dot{y} - (1 + 2c_2)x &= \frac{\partial}{\partial x} \sum_{n \geq 3} c_n \rho^n P_n \left(\frac{x}{\rho} \right) \\ \ddot{y} + 2\dot{x} + (c_2 - 1)y &= \frac{\partial}{\partial y} \sum_{n \geq 3} c_n \rho^n P_n \left(\frac{x}{\rho} \right)\end{aligned}\quad (3.87)$$

The solution of the linear part of equations (3.87) is:

$$\begin{aligned}x(t) &= A_1 e^{\lambda t} + A_2 e^{-\lambda t} + A_x \cos(\omega t + \phi) \\ y(t) &= c A_1 e^{\lambda t} - c A_2 e^{-\lambda t} + k A_x \sin(\omega t + \phi)\end{aligned}\quad (3.88)$$

where k , c , ω and λ are the same constants defined in the previous section, *Lissajous orbits*.

As for Lissajous orbits, A_1 and A_2 are the amplitudes associated with the hyperbolic manifolds. If $A_1 = A_2 = 0$, the linear part of the Lyapunov orbit with amplitude A_x are found. When $A_1 = 0$ and $A_2 \neq 0$, orbits tend to the Lyapunov orbit of amplitude A_x when time tends to infinity (stable manifold). On the contrary, when $A_x = 0$ and $A_1 \neq 0$, orbits leave the vicinity of the Lyapunov exponentially fast in forward time (unstable manifold).

When the non-linear terms of (3.87) are also considered, solutions are obtained by means of formal series in powers of the amplitudes of the form:

$$\begin{aligned}
x(t) &= \sum e^{(i-j)\theta_2} [x_{ijk}^p \cos(p\theta) + \bar{x}_{ijk}^p \sin(p\theta)] A_1^i A_2^j A_x^k \\
y(t) &= \sum e^{(i-j)\theta_2} [y_{ijk}^p \cos(p\theta) + \bar{y}_{ijk}^p \sin(p\theta)] A_1^i A_2^j A_x^k
\end{aligned} \tag{3.89}$$

where $\theta = \omega t + \phi$, $\theta_2 = \lambda t$, and:

$$\omega = \sum \omega_{ijk} A_1^i A_2^j A_x^k, \quad \lambda = \sum \lambda_{ijk} A_1^i A_2^j A_x^k$$

Summation is extended over all i, j, k and p . However, due to symmetries, many of the coefficients $x_{ijk}^p, \bar{x}_{ijk}^p, y_{ijk}^p, \bar{y}_{ijk}^p, \omega_{ijk}, \lambda_{ijk}$ are zero. Moreover the series are truncated at a certain (high) order.

3.9.4 Halo orbits and quasi-halo orbits

Halo orbits are periodic orbits which bifurcate from the planar Lyapunov periodic orbits when the in-plane and out-of-plane frequencies are equal. This is a 1:1 resonance that appears as a consequence of the nonlinear terms of the equations and, in contrast with the Lissajous orbits, they do not appear as a solution of the linearised equations.

In order to apply the Lindstedt-Poincaré procedure, following [Richardson, 1980] the equations of motion (3.82) are modified by adding to the third equation a term like $\Delta \cdot z$, where Δ is a frequency type series:

$$\Delta = \sum_{i,j=0}^{\infty} d_{ij} A_x^i A_z^j$$

that must satisfy the condition $\Delta = 0$.

Starting looking for the (non-trivial) librating solutions with frequency ω :

$$\begin{aligned}
x(t) &= A_x \cos(\omega t + \phi) \\
y(t) &= k A_x \sin(\omega t + \phi) \\
z(t) &= A_z \cos(\omega t + \psi)
\end{aligned} \tag{3.90}$$

After this step, halo orbits are determined up to order 1, and $\Delta = 0$ is read as $d_{00} = 0$. Halo orbits depend only on one frequency or one amplitude since they are 1-D invariant tori, so we have not two independent amplitudes A_x and A_z . The relation between A_x and A_z is contained in the condition $\Delta = 0$ which implicitly defines $A_x = A_x(A_z)$.

When the full equations are considered, one has to look for formal expansions in powers of the amplitudes A_x and A_z of the type:

$$\begin{pmatrix} x \\ y \\ z \end{pmatrix} = \sum_{i,j=1}^{\infty} \left(\sum_{|k| \leq i+j} \begin{pmatrix} x \\ y \\ z \end{pmatrix}_{ijk} \begin{pmatrix} \cos \\ \sin \\ \cos \end{pmatrix}(k\theta) \right) A_x^i A_z^j \quad (3.91)$$

where $\theta = \Omega t + \phi$, and, as for the Lissajous orbits, the frequency Ω must be expanded as:

$$\Omega = \sum_{i,j=1}^{\infty} \omega_{ij} A_x^i A_z^j$$

The procedure for the computation of the unknown coefficients x_{ijk} , y_{ijk} , z_{ijk} , ω_{ij} and d_{ij} is similar to the one described for the Lissajous trajectories.

Quasi-halo orbits are quasi-periodic orbits (depending on two basic frequencies) on two-dimensional tori around a halo orbit. Given a halo orbit of frequency ω , the series expansions for the coordinates of the quasi-halo orbits around it will be of the form:

$$\begin{pmatrix} x \\ y \\ z \end{pmatrix} = \sum_{i=1}^{\infty} \left(\sum_{|k| \leq i, |m| \leq i} \begin{pmatrix} x \\ y \\ z \end{pmatrix}_{ikm} \begin{pmatrix} \cos \\ \sin \\ \cos \end{pmatrix}(k(\omega t + \phi_1) + m(\nu t + \phi_2)) \right) A_\gamma^i$$

These expansions depend on two frequencies (ω, ν) and one amplitude A_γ (related to the size of the torus around the halo orbit). The frequency ν is the second natural frequency of the torus, and it is close to the normal frequency around the base halo orbit. The amplitude A_γ is related to the size of the torus around the "base" halo orbit which is taken as backbone.

In order to apply the Lindstedt-Poincaré method to compute the quasi-halo orbits, it is convenient to perform a change of variables transforming the halo orbit to an equilibrium point of the equations of motion. Then, orbits librating around the equilibrium point in the new coordinates correspond to orbits librating around the halo orbit in the original ones.

In Figures (3.7) and (3.8) some examples of libration orbits are shown.

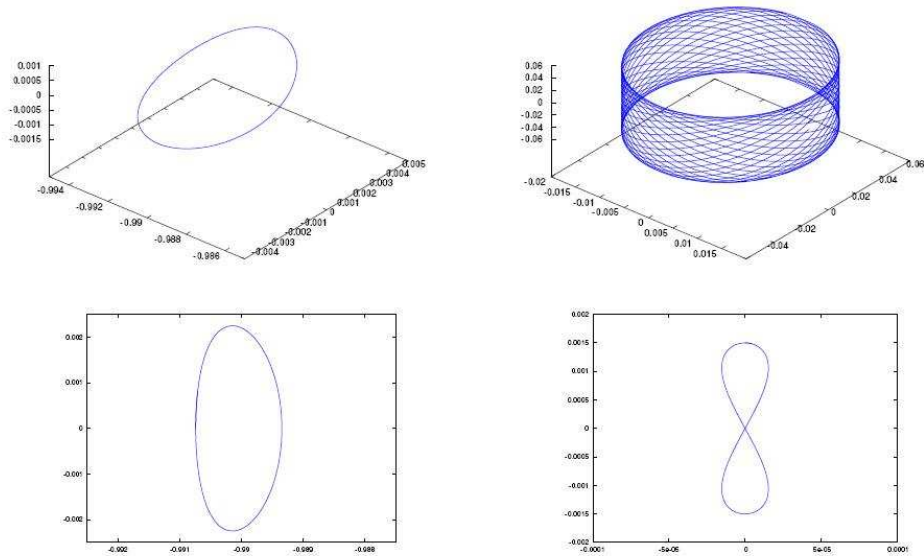


Figure 3.7 Types of libration orbits. Top left: Halo orbit (xyz representation). Top right: Lissajous type orbit (xyz representation). Bottom left: planar Lyapunov orbit (xy projection). Bottom right: vertical Lyapunov orbit (yz projection) [Canalias et al., 2004]

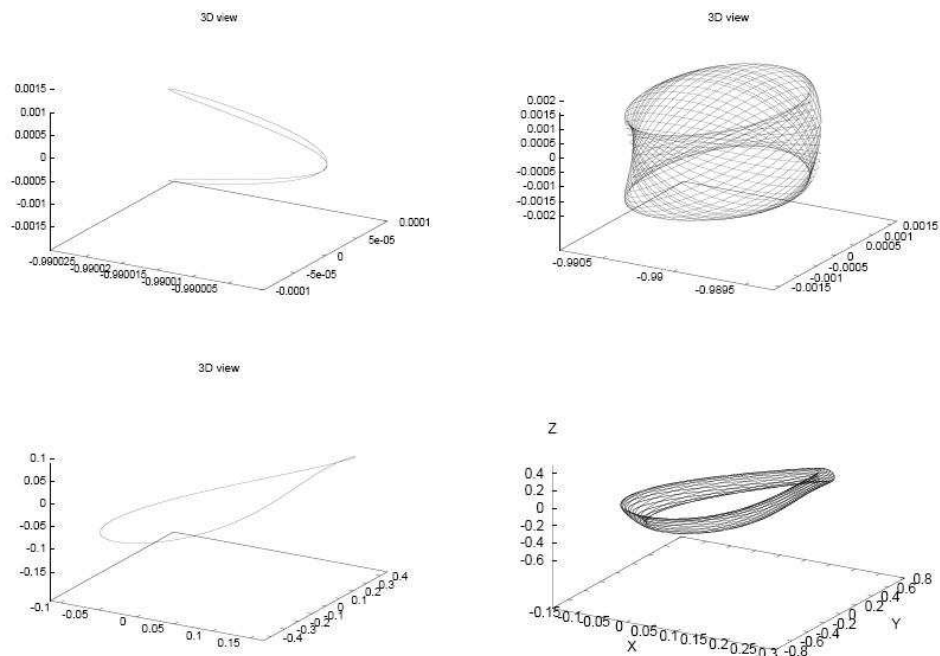


Figure 3.8 Several types of orbits around L_1 . Upper left: vertical Lyapunov periodic orbit. Upper right: Quasi-periodic orbit around a vertical periodic orbit (Lissajous orbit). Lower left: halo periodic orbit. Lower right: quasi-halo orbit (quasi-periodic orbit around a halo orbit) [Canalias et al., 2004]

Transfers using High Thrust in the 2BP Sun-spacecraft

In this chapter we will study the transfer from the Earth to the L_3 libration point of the Sun-Earth system using High Thrust propulsion (impulsive shots) in the 2BP Sun-s/c.

In particular, we will use standard and well-known manoeuvres such as *2-burn* single-revolution tangential transfer, *bi-elliptic* single-revolution transfer, a third case that can be called a *bi-elliptic one-tangent burn* transfer and a fourth one which is a *2-burn* multi-revolution tangential transfer.

Since the Sun- L_3 distance is very close to the value of the distance Sun-Earth (as we have shown in *Section 3.5*, Sun- L_3 is a bit smaller than Sun-Earth, and equal to 0.999998 AU), thus the transfer problem can be modeled just as a phase problem: the bi-elliptic transfer results will confirm this fact.

Exploring the third case (bi-elliptic one-tangent burn transfer), we will have an idea of the ΔV required when the final phase of the s/c is not an integer multiple of π -times the period of the Earth.

Finally, the 2-burn multi-revolution case will turn to be very interesting, cheaper than the 2-burn single-revolution strategy in terms of ΔV (for the same transfer time).

As a starting orbit, we decided to consider the Earth orbit (and not a LEO or GEO or GTO), and the same for the target point: L_3 , and not an orbit near it. Orbits near the libration point L_3 will be considered in the following chapters, when studying the CR3BP and different approaches to the transfer problem, as the use of the manifolds.

4.1 2-burn single-revolution tangential transfer

Since the normalized distance Sun- L_3 is very close to one (which is the distance Sun-Earth), at this simplified step of the study we can model the transfer as a phase problem, thus starting from a distance from the Sun equal to 1 AU (149598000 km) and ending at the same point, but dephased by π with respect to the Earth.

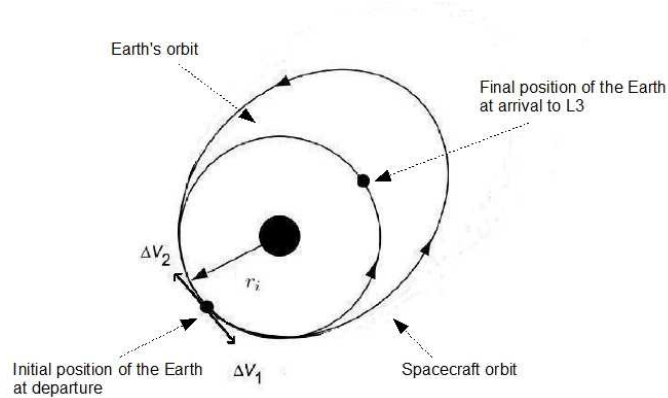


Figure 4.1 Scheme of the 2-burn single-revolution tangential transfer starting and ending at the same Sun distance (for two different values of aphelion distance)

The scheme is the one shown in Figure (4.1), where ΔV_1 and ΔV_2 are tangent to the orbit, and, since the starting and ending orbits are the same one, equal in magnitude (but have opposite direction).

A parameter n has been defined as:

$$T_{(transfer\ ellipse)} \triangleq t = \frac{n}{2} T_{(Earth)} \quad (4.1)$$

where n is 1, 3, 5, 7, 9, ..., 99 . Thus, $n = 1$ would mean that the period of the transfer ellipse is half of the period of the Earth, $n = 5$ that the period of the transfer ellipse is twice plus a half ($5/2$) the period of the Earth, and so on.

Calling r_i the initial distance (Sun-Earth, which is also the perihelion of the transfer ellipse) and r_b the aphelion distance, the velocities are the following:

$$|\bar{V}_i| = \sqrt{\frac{\mu}{r_i}} = |\bar{V}_f| \quad (4.2)$$

$$|\bar{V}_{tr1}| = \sqrt{\frac{2\mu}{r_i} - \frac{\mu}{a_{tr}}} \quad (4.3)$$

$$|\bar{V}_{tr2}| = \sqrt{\frac{2\mu}{r_i} - \frac{\mu}{a_{tr}}} \quad (4.4)$$

where μ is not the same as the one defined before, but $\mu = GM_{Sun}$ (with $G = 6.67428 \cdot 10^{-11} m^3 kg^{-1} s^{-2}$ the gravitational constant), and $a_{tr} = \frac{r_i + r_b}{2}$ the semi-major axis of the transfer ellipse.

V_{tr1} is the velocity that the s/c must have at Sun distance r_i to reach r_b and V_{tr2} is the velocity of the s/c at Sun distance r_i when in a elliptic orbit of semi-major axis a_{tr} .

$$\Delta V_1 = |\bar{V}_{tr1} - \bar{V}_i| \quad (4.5)$$

$$\Delta V_2 = |\bar{V}_i - \bar{V}_{tr2}| \quad (4.6)$$

Since $\Delta V_1 = \Delta V_2$, then:

$$\Delta V_{Tot} = 2\Delta V_1 \quad (4.7)$$

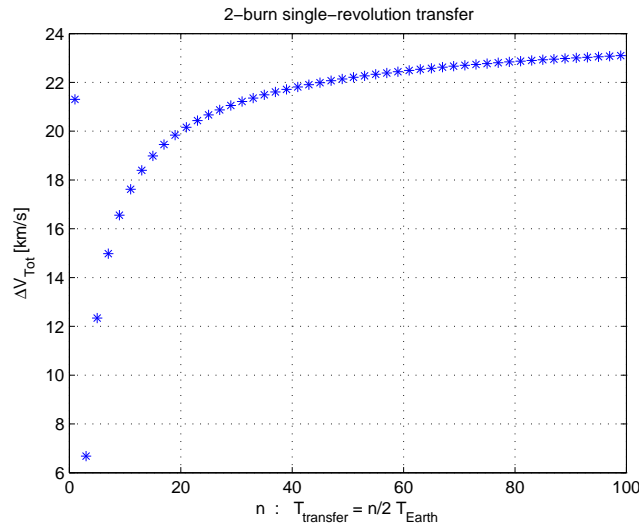


Figure 4.2 ΔV_{Tot} for the 2-burn single-revolution tangential transfer for a range of orbital periods multiple of $\frac{T_{Earth}}{2}$ (with a phase difference of π), $n = [1, 3, 5, \dots, 99]$

The radius r_b has been computed as follows: t has been found using Equation (4.1), for the same range of n . Moreover, the transfer period t can be computed as:

$$t = 2\pi \sqrt{\frac{a_{tr}^3}{\mu}} \quad (4.8)$$

where the value of a_{tr} depends on r_b . Thus, r_b for each n -step has been computed

combining Equation (4.1) and Equation (4.8).

Analysing the results shown in Figure (4.2), it is easy to see that when the transfer period is half of the Earth period, then ΔV_{Tot} is very big, since this is the only case in which r_i is not the perihelion but the aphelion.

A transfer period of one year and a half ($n = 3$) is the cheapest solution. For bigger r_b (thus, for longer transfer times) ΔV_{Tot} increases, and becomes bigger than $\Delta V_{Tot}(n = 1)$ when $n = 33$.

Table (4.1) gives the values of r_b (normalized respect to 1 AU) for the first 5 cases ($n = 1, 3, 5, 7, 9$) and ΔV_{Tot} .

n	r_b [AU]	ΔV_{Tot} [km/s]
1	0.259904	21.306
3	1.620706	6.679
5	2.683981	12.337
7	3.610374	14.980
9	4.451288	16.556

Table 4.1 r_b and ΔV_{Tot} for the cases of $n = 1, 3, 5, 7, 9$ for the 2-burn single-revolution tangential transfer ($1 AU = 149598000 km$)

4.2 Bi-elliptic single-revolution transfer

In this section we will consider a bi-elliptic single-revolution transfer, starting at the same Sun distance as in the 2-burn single-revolution tangential transfer (1 AU), but arriving at a Sun distance $r_f = 0.999998$ AU after a whole revolution (which is, as we have seen before, the actual distance of L_3 from the Sun).

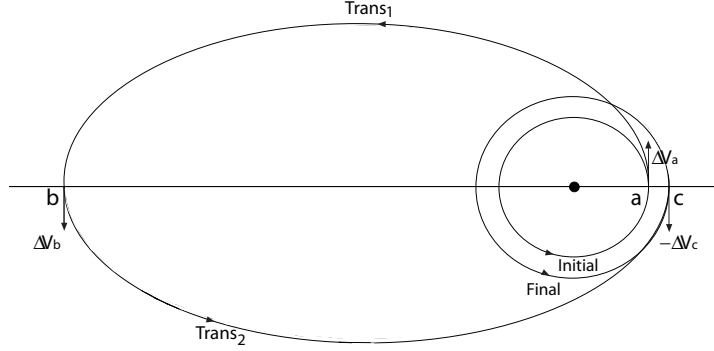


Figure 4.3 Scheme of a bi-elliptic single-revolution transfer, from a circular orbit to a circular orbit with a bigger radius

The scheme is the same as the one shown in Figure (4.3), with the difference that for our case the final orbit has a smaller radius than the initial one, thus with ΔV_b having opposite direction. However, as we have already mentioned, since the difference between the two circular orbits is so small, ΔV_b will be very close to zero, confirming that for this phasing study the 2-burn tangential model is enough.

Calling r_i the initial distance from the Sun, r_f the final one and r_b the apohelion distance, the velocities are the following:

$$|\bar{V}_i| = \sqrt{\frac{\mu}{r_i}} \quad (4.9)$$

$$|\bar{V}_{tr1a}| = \sqrt{\frac{2\mu}{r_i} - \frac{\mu}{a_1}} \quad (4.10)$$

$$|\bar{V}_{tr1b}| = \sqrt{\frac{2\mu}{r_b} - \frac{\mu}{a_1}} \quad (4.11)$$

$$|\bar{V}_{tr2b}| = \sqrt{\frac{2\mu}{r_b} - \frac{\mu}{a_2}} \quad (4.12)$$

$$|\bar{V}_{tr2c}| = \sqrt{\frac{2\mu}{r_f} - \frac{\mu}{a_2}} \quad (4.13)$$

$$|\bar{V}_f| = \sqrt{\frac{\mu}{r_f}} \quad (4.14)$$

with $a_1 = \frac{r_i+r_b}{2}$ the semi-major axis of the first transfer ellipse ($Trans_1$) and $a_2 = \frac{r_f+r_b}{2}$ the semi-major axis of the second transfer ellipse ($Trans_2$).

$$\Delta V_a = |\bar{V}_{tr1a} - \bar{V}_i| \quad (4.15)$$

$$\Delta V_b = |\bar{V}_{tr2b} - \bar{V}_{tr1b}| \quad (4.16)$$

$$\Delta V_c = |\bar{V}_f - \bar{V}_{tr2c}| \quad (4.17)$$

Then:

$$\Delta V_{Tot} = \Delta V_a + \Delta V_b + \Delta V_c \quad (4.18)$$

The radius r_b has been computed as follows: t has been found as for the 2-burn single-revolution tangential transfer using Equation (4.1), for the same range of n . Moreover, the transfer period t can be computed as:

$$t = \pi \sqrt{\frac{a_1^3}{\mu}} + \pi \sqrt{\frac{a_2^3}{\mu}} \quad (4.19)$$

where the values of a_1 and a_2 depend on r_b . Thus, using for example the Newton's method, r_b for each value of n has been computed combining Equations (4.1) and (4.19).

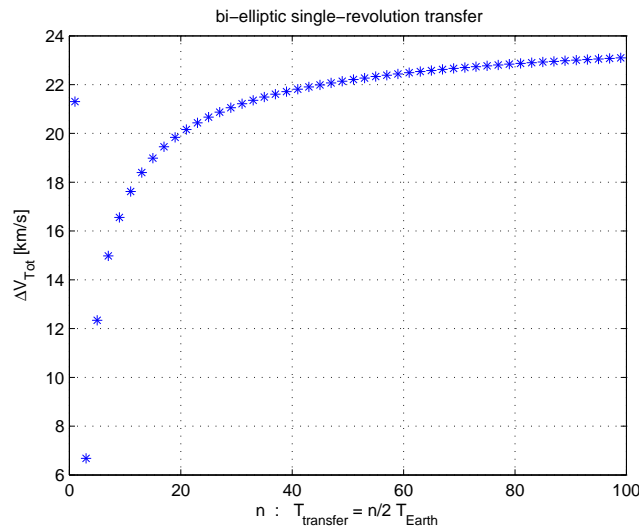


Figure 4.4 ΔV_{Tot} for the bi-elliptic single-revolution transfer for a range of orbital periods multiple of $\frac{T_{Earth}}{2}$ (with a phase difference of π), $n = [1, 3, 5, \dots, 99]$

n	r_b [AU]	ΔV_a [km/s]	ΔV_c [km/s]	ΔV_{Tot} [km/s]
1	0.259904	10.653	10.653	21.306
3	1.620707	3.339	3.339	6.679
5	2.683982	6.168	6.168	12.337
7	3.610375	7.490	7.490	14.980
9	4.451289	8.278	8.278	16.556

Table 4.2 r_b , ΔV_a , ΔV_c and ΔV_{Tot} for the cases of $n = 1, 3, 5, 7, 9$ for the bi-elliptic single-revolution transfer ($1 AU = 149598000 km$)

In Figure (4.4) the results for the bi-elliptic single-revolution transfer are given.

In Table (4.2) the values of r_b and ΔV_a , ΔV_c and ΔV_{Tot} for the first 5 cases ($n = 1, 3, 5, 7, 9$) are shown: note that the values of r_b are very close to those obtained using a 2-burn single-revolution transfer model.

Moreover, comparing Tables (4.1) and (4.2), the difference for ΔV_{Tot} taking three digits after the decimal point is zero: since the value of r_f is very close to the value of r_i , the transfer problem can be modeled just as a phase problem, using the 2-burn transfer strategy.

Indeed, the values of ΔV_b are very small: here in Table (4.3) ΔV_b in [m/s] for the cases of $n = 1, 3, 5, 7, 9$.

n	ΔV_b [m/s]
1	0.013465
3	0.011208
5	0.008654
7	0.007169
9	0.006191

Table 4.3 ΔV_b in [m/s] for the cases of $n = 1, 3, 5, 7, 9$ for the bi-elliptic single-revolution transfer

4.3 Bi-elliptic one-tangent burn transfer

Here we will investigate a different transfer strategy, reaching L_3 when the phase is not a multiple of π . As for an example, a phase of $3/2 \pi$ the revolution about the Sun has been chosen. Moreover, also considering the results analysed in the previous section, the distance Sun- L_3 will be considered equal to 1 AU (as for the starting point), and not equal to r_1 (however, the model we made is flexible enough to have r_1 or any other value as the target final Sun-distance).

Before making any computation it is easy to predict that this transfer strategy is more expensive than the previous two ones: however, we want to have an idea of the orders of magnitude, and see if for some particular cases ΔV_{Tot} is comparable with those obtained in the 2-burn tangential transfer for some values of n , or much bigger.

In Figure (4.5) the scheme is shown: r_b , the aphelion distance, is the "input" parameter. Thus, for any given r_b , a ΔV_a to leave the circular orbit and insert the s/c into the elliptic orbit is computed, and so the transfer time to reach point b . Then a ΔV_b is required in order to insert the s/c into a trajectory that connects points b and c and makes the s/c reach c from b in a prescribed time. In c a third burn (ΔV_c) circularizes the orbit. The problem of going from b to c in a prescribed time is the classic Lambert's problem [Vallado, 2007]: thus for each value of r_b the Lambert's problem had to be solved.

Considering a phase of $3/2 \pi$ the revolution about the Sun, the total transfer time has to be an integer plus one quarter of the year.

Details of the computations will not be given here.

In Table (4.4) the results for the cases that have been considered are shown.

r_b [AU]	Total time to reach L_3 [years]	ΔV_{Tot} [km/s]
0.7	1/4	111.6
0.7	1+1/4	59.1
1	1+1/4	45.2
1.3	1+1/4	33.3
1.3	2+1/4	56.4
1.5	1/4	72.7
1.5	1+1/4	23.5
1.5	2+1/4	52.5
1.5	3+1/4	59.8
1.7	1+1/4	16.9
1.8	1+1/4	19.2

Table 4.4 ΔV_{Tot} for different combinations of (r_b -Total time to reach L_3) for the bi-elliptic one-tangent burn transfer

The value of ΔV_{Tot} is always high, and clearly depends on the combination (r_b -Total time to reach L_3).

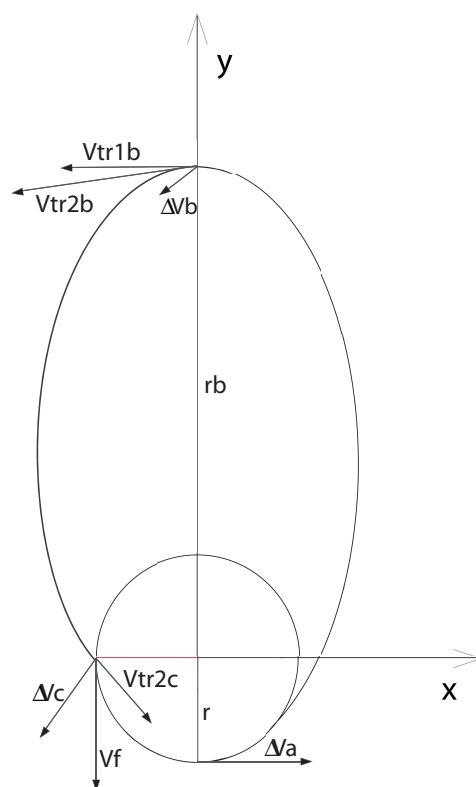


Figure 4.5 Scheme of the bi-elliptic one-tangent burn transfer, starting at distance from the Sun of 1 AU, and ending in L_3 at a distance r_1 , after $3/2 \pi$ of the revolution about the Sun

A minimum has been found near $r_b = 1.7 \text{ AU}$ for a total transfer time of a year and a quarter.

4.4 2-burn multi-revolution tangential transfer

In this section a strategy that can be called 2-burn multi-revolution tangential transfer will be considered, and is shown in Figure (4.6) and (4.7).

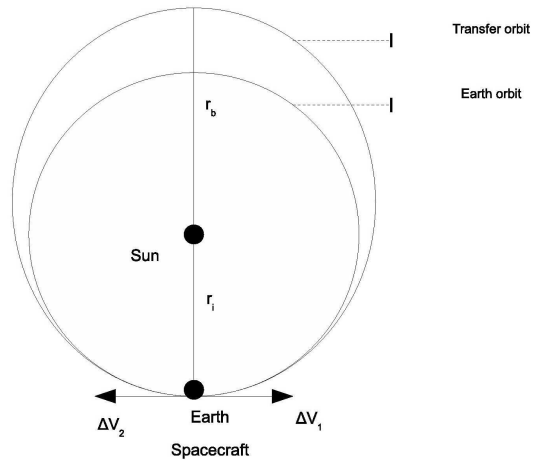


Figure 4.6 Scheme of the 2-burn multi-revolution transfer: applied ΔV s

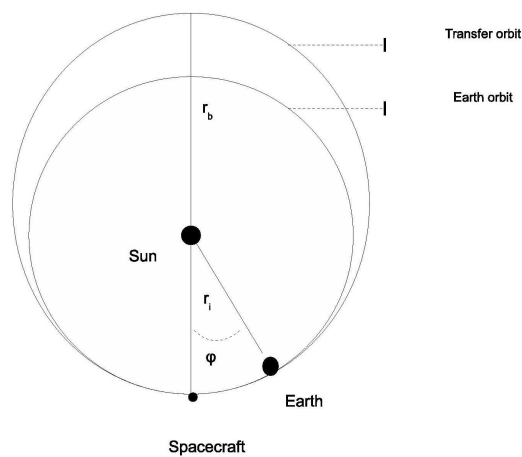


Figure 4.7 Scheme of the 2-burn multi-revolution transfer: Earth and s/c dephased by angle φ

The period of the transfer ellipse has been defined as:

$$T_{(transfer\ ellipse)} \triangleq t = T_{(Earth)} + T_{(Diff)} \quad (4.20)$$

where $T_{(Diff)} = T_{(Earth)}/(ny \cdot 2)$ and ny is $1, 2, 3, \dots, 49$. This means that the spacecraft reaches L_3 after ny -years and a half. The transfer ellipse has a period which leads, after one revolution about the Sun, to have a phase difference between the Earth and the spacecraft of $\varphi = \pi/ny$ (as shown in Figure (4.7)), being the Earth heading the spacecraft.

The total transfer time can be written as:

$$T_{(total\ transfer)} = \frac{n}{2} T_{(Earth)} = \frac{2ny + 1}{2} T_{(Earth)} \quad (4.21)$$

where n is $3, 5, 7, 9, \dots, 99$. Thus, $n = 3$ would mean that the total transfer period is one and a half of the period of the Earth, $n = 5$ that the total transfer period is twice plus a half ($5/2$) the period of the Earth, and so on.

The parameter n can not be taken equal to 1 since that would not lead to any multi-revolution transfer.

Calling r_i the initial distance (Sun-Earth, which is also the perihelion of the transfer ellipse) and r_b the aphelion distance, the velocities are the following:

$$|\bar{V}_i| = \sqrt{\frac{\mu}{r_i}} = |\bar{V}_f| \quad (4.22)$$

$$|\bar{V}_{tr1}| = \sqrt{\frac{2\mu}{r_i} - \frac{\mu}{a_{tr}}} \quad (4.23)$$

$$|\bar{V}_{tr2}| = \sqrt{\frac{2\mu}{r_i} - \frac{\mu}{a_{tr}}} \quad (4.24)$$

V_{tr1} is the velocity that the s/c must have at Sun distance r_i to reach r_b and V_{tr2} is the velocity of the s/c at Sun distance r_i when in a elliptic orbit of semi-major axis a_{tr} .

$$\Delta V_1 = |\bar{V}_{tr1} - \bar{V}_i| \quad (4.25)$$

$$\Delta V_2 = |\bar{V}_i - \bar{V}_{tr2}| \quad (4.26)$$

Since $\Delta V_1 = \Delta V_2$, then:

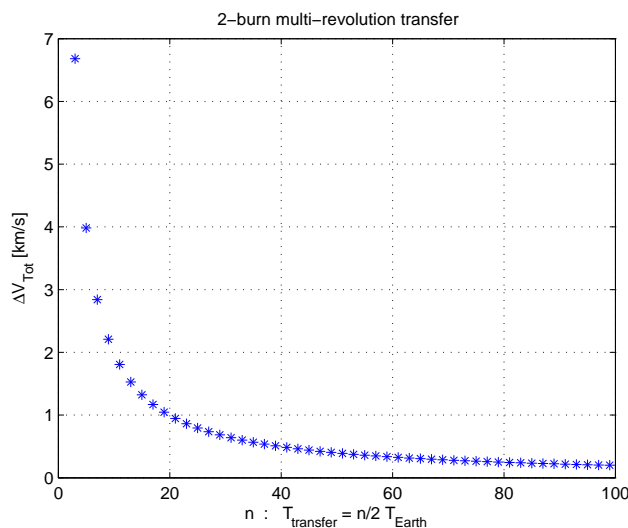


Figure 4.8 ΔV_{Tot} for the 2-burn multi-revolution transfer for a range of transfer periods multiple of $\frac{T_{Earth}}{2}$ (with a phase difference of π), $n = [3, 5, 7, \dots, 99]$

$$\Delta V_{Tot} = 2\Delta V_1 \quad (4.27)$$

The radius r_b is computed combining Equations (4.8) and (4.20).

The results shown in Figure (4.8) look quite interesting, much cheaper (at a given flight time) than the other strategies considered so far.

This case can be considered complementary to the one we called 2-burn single-revolution transfer: in fact $n = 3$ of the 2-burn single-revolution transfer represents the same orbit of $n = 3$ of the 2-burn multi-revolution strategy.

In the 2-burn multi-revolution transfer, except for the case just mentioned, the ΔV_{Tot} is always smaller than for the 2-burn single-revolution transfer. The reason is that, instead of inserting the s/c into a bigger orbit that after a revolution intercepts L_3 (for n increasing, r_b becomes bigger and bigger), in the multi-revolution strategy r_b becomes closer and closer to the value of 1 AU with n increasing (and the mean motion $\sqrt{\frac{\mu}{a_{tr}^3}}$ becomes closer and closer to 1, as shown in Figure (4.9), which is the value of the mean motion for the Earth).

In Table (4.5) the values of r_b for the first 11 cases ($n = 3, 5, 7, \dots, 23$), ΔV_{Tot} and the mass consumption are given.

The (fuel) mass consumption has been computed from the rocket equation:

$$\frac{m_0}{m_f} = e^{\frac{\Delta V_{Tot}}{I_{sp} g_0}} \quad (4.28)$$

where m_0 is the initial total mass of the s/c (including propellant), m_f is the final total mass, $m_{fuel} = m_0 - m_f$, I_{sp} is the specific impulse of the rocket, and $g_0 = 9.81 \text{ m/s}^2$. $I_{sp} = 300 \text{ s}$ has been chosen.

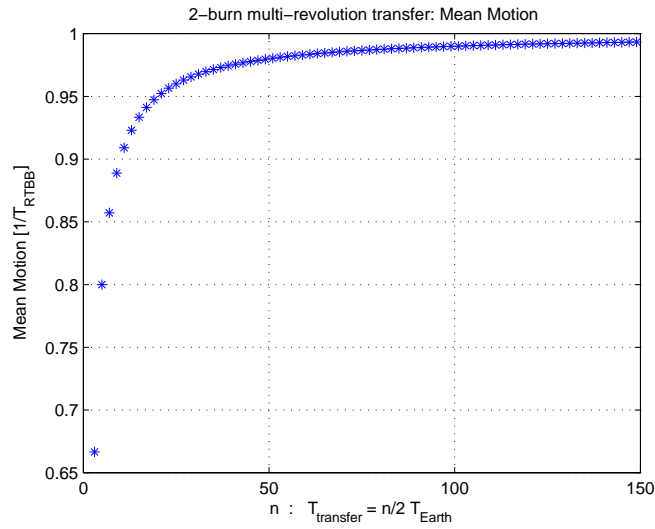


Figure 4.9 Mean motion for the 2-burn multi-revolution transfer for a range of transfer periods multiple of $\frac{T_{Earth}}{2}$ (with a phase difference of π), $n = [3, 5, 7, \dots, 150]$

n	r_b [AU]	ΔV_{Tot} [km/s]	m_{fuel}/m_0 [%]
3	1.620706	6.679	89.6
5	1.320763	3.983	74.1
7	1.216436	2.840	61.9
9	1.163345	2.207	52.7
11	1.131175	1.805	45.8
13	1.109594	1.527	40.4
15	1.094110	1.323	36.2
17	1.082460	1.167	32.7
19	1.073376	1.044	29.8
21	1.066095	0.945	27.4
23	1.060128	0.863	25.4

Table 4.5 r_b , ΔV_{Tot} and mass consumption for the cases of $n = 3, 5, 7, \dots, 23$ for the 2-burn multi-revolution transfer ($1 AU = 149598000 km$)

The mass consumption, that is given by $m_{fuel}/m_0 = 1 - m_f/m_0$ and is expressed as a fraction of the total initial mass, has been computed in such a way that the results of the 2-burn multi-revolution transfer can be compared with those in *Chapter 6* (Low Thrust, with varying acceleration).

Reaching Lyapunov orbits near L_3 through the manifolds

In this chapter we will focus on transfers to Lyapunov orbits near the L_3 libration point of the Sun-Earth system using the manifolds.

First, a family of Lyapunov orbits near L_3 and their manifolds will be studied. The procedure to compute a symmetric planar (Lyapunov) orbit will be shown, as well as the method to compute the manifolds.

Even if a Halo orbit might look the better target (considering, for example, the purpose of monitoring the surface of the Sun that is hidden from the Earth), we chose planar Lyapunov orbits near L_3 as the target orbit. In fact, the transfer to L_3 through the manifolds is in practice fully described in the planar approximation, thus with the manifolds of a Lyapunov orbit. However, the extension to the three-dimensional Halo case can be easily done.

Results on transfer times moving inside the stable manifolds of these Lyapunov orbits will be given. Unfortunately the flight time will look too long for a mission, therefore another strategy had to be found.

As a second strategy to reach Lyapunov orbits near L_3 , we decided to use the unstable manifolds departing from Lyapunov orbits near L_1 and L_2 . In this case a ΔV will be needed, in order to open the forbidden region and match the Jacobi constant of the target Lyapunov orbit. The results in terms of transfer time and ΔV s will be shown: the cheapest solution to reach the target Lyapunov orbit near L_3 will have a ΔV of about 0.5 km/s.

5.1 Finding symmetric periodic orbits: initial condition

In this section the procedure to compute the initial condition (IC) for the smallest Lyapunov orbit of the family will be explained. Then, a continuation method will be used, taking the initial state of the previous orbit to the IC of the next one of the family.

As introduced before, changing coordinates in order to center the equations at the equilibrium point, the RTBP equations become (System (3.82)):

$$\begin{aligned}\ddot{x} - 2\dot{y} - (1 + 2c_2)x &= \frac{\partial}{\partial x} \sum_{n \geq 3} c_n \rho^n P_n \left(\frac{x}{\rho} \right) \\ \ddot{y} + 2\dot{x} + (c_2 - 1)y &= \frac{\partial}{\partial y} \sum_{n \geq 3} c_n \rho^n P_n \left(\frac{x}{\rho} \right) \\ \ddot{z} + c_2 z &= \frac{\partial}{\partial z} \sum_{n \geq 3} c_n \rho^n P_n \left(\frac{x}{\rho} \right)\end{aligned}\tag{5.1}$$

where the value of c_2 depends on the mass parameter and the Lagrange point we are studying.

The linearization of System (5.1) can be written as:

$$\begin{aligned}\ddot{x} - 2\dot{y} - (1 + 2c_2)x &= 0 \\ \ddot{y} + 2\dot{x} + (c_2 - 1)y &= 0 \\ \ddot{z} + c_2 z &= 0\end{aligned}\tag{5.2}$$

which has, as a planar solution:

$$\begin{aligned}x(t) &= A_x \cos(\omega t + \phi) \\ y(t) &= k A_x \sin(\omega t + \phi)\end{aligned}\tag{5.3}$$

As we are trying to find a good approximation of a planar symmetric periodic orbit near L_3 , we choose the IC as $t = \phi = 0$ and

$$\begin{aligned}x_i &= A_x \\ y_i &= 0 \\ z_i &= 0 \\ \dot{x}_i &= 0 \\ \dot{y}_i &= \omega k A_x \\ \dot{z}_i &= 0\end{aligned}$$

and then, transform coordinates in order to have again RTBP coordinates.

Once we have this good approximation of an IC of a symmetric periodic orbit, we refine it in order to make the orbit cut the x-axis orthogonally again, and have the appropriate initial condition of the orbit. The initial condition $(x_i, y_i, \dot{x}_i, \dot{y}_i)$ is integrated in the RTBP (we used a Runge-KuttaFeldberg 7-8 integrator) until it cuts $y = 0$ at the point $(x_f, 0, \dot{x}_f, \dot{y}_f)$. When the section $y = 0$ is cut, if $\dot{x}_f = 0$, then the trajectory cuts the x-axis orthogonally, but if $\dot{x}_f \neq 0$ then the IC has to be changed (refined) using a Newton method until the x-axis is cut orthogonally.

In the following sections the mathematical definition of a periodic orbit and a method to refine the IC will be will be given.

5.2 Periodic orbits: definition

Let's assume that the behaviour of a dynamical system is described by the system of differential equations:

$$\dot{X} = F(X) \tag{5.4}$$

with $X \in \mathbb{R}^n$ and $X(0) = X_0$. X is the state vector of the system, defined as:

$$X = \begin{pmatrix} r \\ v \end{pmatrix} \tag{5.5}$$

with

$$\dot{X} = \begin{pmatrix} v \\ a \end{pmatrix} = F(X) \tag{5.6}$$

where r , v and a define position, velocity and acceleration of the particle.

The solution of System (5.4) passing through X_0 at $t = 0$ is denoted by:

$$\phi_t(X_0) \tag{5.7}$$

A solution of System (5.4) is defined periodic if there exists a constant $T > 0$ such that

$$X(t) = X(t + T) \tag{5.8}$$

for all t . The period of this solution is defined to be the minimum such T .

5.3 Variational equations: search of the initial condition and of the period

The variational equations express the variation of the final state X of a system as a function of the variation of its initial state X_0 .

As mentioned before, to compute the Lyapunov orbits we have not used the Lindstedt-Poincaré procedures, but we have exploited the fact that a planar Lyapunov orbit is a periodic orbit with symmetry with respect to the x-axis. The initial state vector X_0 and the period T are found using a differential correction procedure that involves the state transition matrix Φ . The state transition matrix is a square matrix of dimension 6, and it is defined as:

$$\Phi = \frac{\partial X}{\partial X_0} = \begin{pmatrix} \frac{\partial r}{\partial r_0} & \frac{\partial r}{\partial v_0} \\ \frac{\partial v}{\partial r_0} & \frac{\partial v}{\partial v_0} \end{pmatrix} = \begin{pmatrix} \Phi_{11} & \Phi_{12} \\ \Phi_{21} & \Phi_{22} \end{pmatrix} \quad (5.9)$$

Φ satisfies the matricial differential equation

$$\frac{d\Phi}{dt} = A\Phi \quad (5.10)$$

where

$$A = \frac{\partial F}{\partial X} = \begin{pmatrix} \frac{\partial v}{\partial r} & \frac{\partial v}{\partial v} \\ \frac{\partial a}{\partial r} & \frac{\partial a}{\partial v} \end{pmatrix} = \begin{pmatrix} A_{11} & A_{12} \\ A_{21} & A_{22} \end{pmatrix} \quad (5.11)$$

and the submatrices A_{11} and A_{12} are respectively the 3×3 null matrix and the 3×3 identity matrix, whereas the matrix A_{21} is a symmetric matrix

$$A_{21} = \frac{\partial a}{\partial r} = \begin{pmatrix} \frac{\partial \ddot{x}}{\partial x} & \frac{\partial \ddot{x}}{\partial y} & \frac{\partial \ddot{x}}{\partial z} \\ \frac{\partial \ddot{y}}{\partial x} & \frac{\partial \ddot{y}}{\partial y} & \frac{\partial \ddot{y}}{\partial z} \\ \frac{\partial \ddot{z}}{\partial x} & \frac{\partial \ddot{z}}{\partial y} & \frac{\partial \ddot{z}}{\partial z} \end{pmatrix} \quad (5.12)$$

and the matrix A_{22} is

$$A_{22} = \begin{pmatrix} 0 & 2 & 0 \\ -2 & 0 & 0 \\ 0 & 0 & 0 \end{pmatrix} \quad (5.13)$$

Equation (5.10) represents a system of 36 differential equations that can be summarized in the following way:

$$\dot{\Phi}_{11} = \Phi_{21} \quad (5.14)$$

$$\dot{\Phi}_{12} = \Phi_{22} \quad (5.15)$$

$$\dot{\Phi}_{21} = A_{21}\Phi_{11} + A_{22}\Phi_{21} \quad (5.16)$$

$$\dot{\Phi}_{22} = A_{21}\Phi_{12} + A_{22}\Phi_{22} \quad (5.17)$$

The system has initial conditions:

$$\left(\frac{\partial X}{\partial X_0} \right)_{t=t_0} = I \quad (5.18)$$

Since the state X at a given time $t = \frac{T}{2}$ depends on the initial state X_0 and on the instant $\frac{T}{2}$ it is computed, its variation δX is:

$$\delta X = \frac{\partial X}{\partial X_0} \delta X_0 + \left(\frac{\partial X}{\partial t} \right) \delta t = \Phi \delta X_0 + \left(\frac{\partial X}{\partial t} \right) \delta t \quad (5.19)$$

where $\delta t = \delta \frac{T}{2}$ and $\frac{\partial X}{\partial t}$ is the vector field f .

Since $\delta X = (\delta x, \delta y, 0, \delta \dot{x}, \delta \dot{y}, 0)$ and $\delta X_0 = (\delta x_0, 0, 0, 0, \delta \dot{y}_0, 0)$, then:

$$\begin{bmatrix} \delta x \\ \delta y \\ 0 \\ \delta \dot{x} \\ \delta \dot{y} \\ 0 \end{bmatrix} = \begin{bmatrix} \Phi_{11} \delta x_0 + \Phi_{15} \delta \dot{y}_0 + f_1 \delta t \\ \Phi_{21} \delta x_0 + \Phi_{25} \delta \dot{y}_0 + f_2 \delta t \\ \Phi_{31} \delta x_0 + \Phi_{35} \delta \dot{y}_0 + f_3 \delta t \\ \Phi_{41} \delta x_0 + \Phi_{45} \delta \dot{y}_0 + f_4 \delta t \\ \Phi_{51} \delta x_0 + \Phi_{55} \delta \dot{y}_0 + f_5 \delta t \\ \Phi_{61} \delta x_0 + \Phi_{65} \delta \dot{y}_0 + f_6 \delta t \end{bmatrix} \quad (5.20)$$

We are interested in the second and fourth equations of the system, since we want:

$$\begin{aligned} \delta y &= 0 \\ \delta \dot{x} &= -\dot{x} \end{aligned} \quad (5.21)$$

For a given Lyapunov orbit, $\delta x_0 = 0$, then:

$$\begin{aligned} \delta t &= -\frac{\Phi_{25}}{f_2} \delta \dot{y}_0 \\ \delta \dot{y}_0 &= -\frac{\dot{x} f_2}{(f_2 \Phi_{45} - f_4 \Phi_{25})} \end{aligned} \quad (5.22)$$

The second equation of System (5.22) gives the correction on the \dot{y} element of the initial state X . A Newton method is used and the initial state of the Lyapunov orbit is found.

Then, once the initial state of the first Lyapunov orbit is obtained, the whole family of Lyapunov orbits is generated with a continuation method.

5.4 Lyapunov orbits near L_3 : results

The range of amplitudes of the family has been defined as follows.

In order to have direct communication with the Earth at some points of the orbit near L_3 , the s/c needs to have a semi-amplitude in the y-direction of order 0.1 AU. Therefore, the initial states on the x-axis have been chosen in the range of orders 10^{-4} AU to 10^{-1} AU. As can be seen from the following plots, this leads to orbits that have a semi-amplitude in the y-direction of up to 0.25 AU. Note that some orbits of the family do not allow direct communication with the Earth. However, these smaller orbits have been taken into account, since the communication with the Earth might also be done by bouncing the signal to other spacecraft that, at the time of the possible mission, would be visible (as mentioned in *Section 1.1*).

The initial states of each Lyapunov orbits have been integrated in the RTBP, using a Runge-KuttaFeldberg 7-8 integrator, and the results are shown in Figures (5.1) and (5.2).

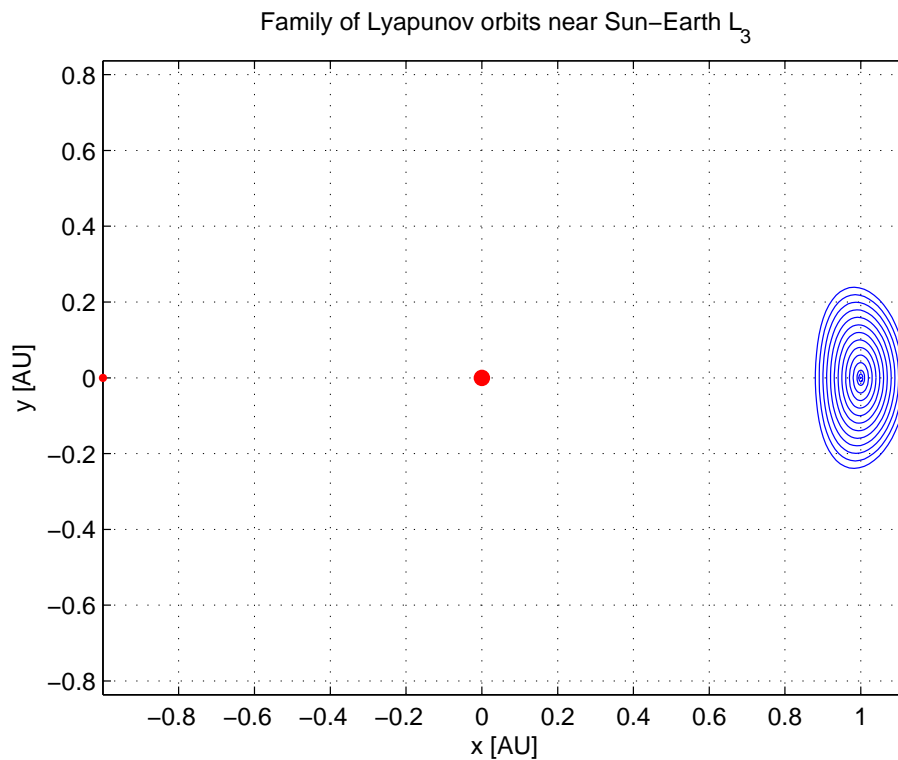


Figure 5.1 Family of Lyapunov orbits near Sun–Earth L_3 in the RTBP reference frame: Earth (left), Sun (center) and Lyapunov orbits near L_3 (right)

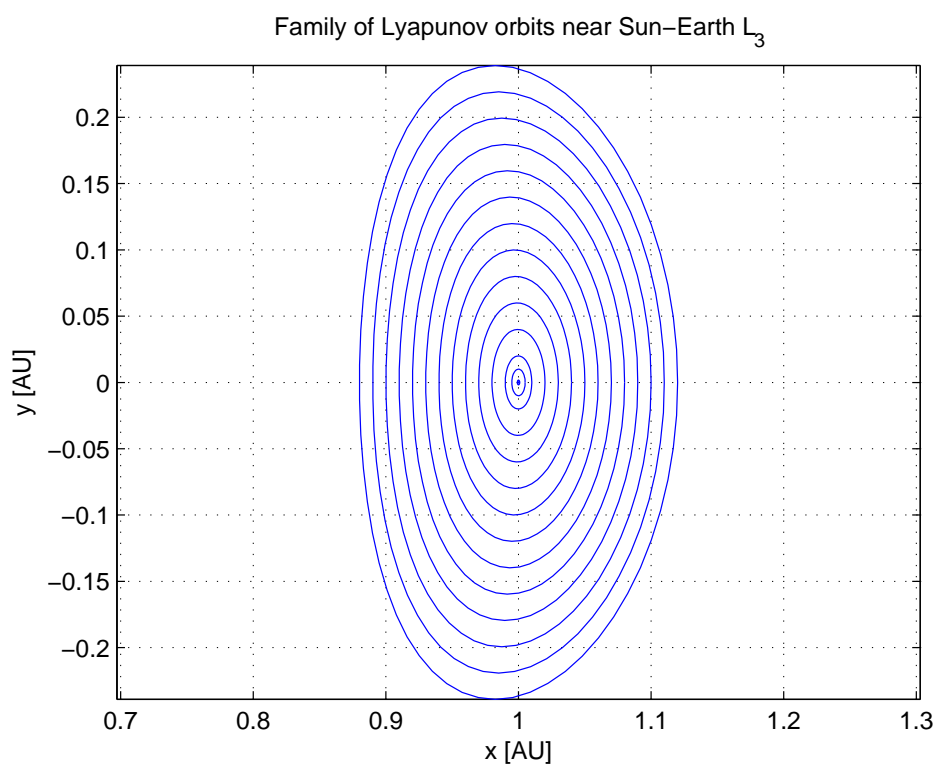


Figure 5.2 Family of Lyapunov orbits near Sun-Earth L_3 in the RTBP reference frame

The database of the family of Lyapunov orbits is much denser than in Figures (5.1) and (5.2): we chose not to plot all Lyapunov orbits of the family to have a clearer figure (however, the range is the same: the smallest and the biggest orbits of the family are given in the plots).

The initial state vector of each Lyapunov orbit (and the corresponding Jacobi constant) can be found in the *Appendix A*.

5.5 Manifolds: theorems and procedure

In this section the theory of Stable and Unstable Manifolds will be given.

First, the invariant subspaces will be defined, then the Stable Manifold theorem and the Floquet's Theorem will be given. We will conclude with the Stable Manifold theorem for a periodic orbit and the numerical method to compute the manifolds.

We will refer to [Parker and Chua, 1991] and [Perko, 2006].

5.5.1 Definition of invariant subspace

Let $w_j = u_j + iv_j$ be a generalized eigenvector for the real matrix A defined in Equation (5.11) and computed in the equilibrium point $X = \bar{X}$, corresponding to the eigenvalue $\lambda_j = a_j + ib_j$.

The *stable subspace* of \mathbb{R}^n is defined as:

$$E^s = \{u_j, v_j | a_j < 0\} \quad (5.23)$$

The *unstable subspace* of \mathbb{R}^n is defined as:

$$E^u = \{u_j, v_j | a_j > 0\} \quad (5.24)$$

The *central subspace* of \mathbb{R}^n is defined as:

$$E^c = \{u_j, v_j | a_j = 0\} \quad (5.25)$$

E^s , E^u and E^c are the subspaces generated by the generalized eigenvector w_j corresponding to the eigenvalues λ_j with negative, positive and null real part respectively.

E^s , E^u and E^c are invariant respect to the flux e^{At} , which means that every solution that has its origin respectively in E^s , E^u and E^c at $t = 0$ is contained respectively in E^s , E^u and E^c for every $t \in \mathbb{R}$.

5.5.2 The Stable Manifold theorem

Let's consider the nonlinear System (5.4). The linearization of System (5.4) near the equilibrium point \bar{X} is defined as the linear system:

$$\dot{X} = AX \quad (5.26)$$

$X \in \mathbb{R}^n$, where A is the matrix defined in Equation (5.11) computed in the equilibrium point $X = \bar{X}$.

The invariant subspaces are generated from the linear System (5.26). Their properties can be extended to the solution of the nonlinear System (5.4) through the Stable Manifold theorem.

The Stable Manifold theorem states that near a hyperbolic equilibrium point \bar{X} the nonlinear System (5.26) has stable and unstable manifolds S and U tangent at \bar{X} to the stable and unstable subspaces E^s and E^u of the linearized System (5.26).

Furthermore, S and U have the same dimension of E^s and E^u , and if ϕ_t is the flow of the nonlinear System (5.26), then S and U are positively and negatively invariant under ϕ_t respectively and satisfy:

$$\lim_{t \rightarrow \infty} \phi_t(c) = \bar{X} \quad (5.27)$$

for all $c \in S$, and:

$$\lim_{t \rightarrow -\infty} \phi_t(c) = \bar{X} \quad (5.28)$$

for all $c \in U$.

The global stable manifold $W^s(\bar{X})$ is defined as:

$$W^s(\bar{X}) = \bigcup_{t \leq 0} \phi_t(S) \quad (5.29)$$

and the global unstable manifold $W^u(\bar{X})$:

$$W^u(\bar{X}) = \bigcup_{t \geq 0} \phi_t(U) \quad (5.30)$$

The existence and uniqueness of solutions of the System (5.4) ensures that two stable (respectively unstable) manifolds of two distinct equilibrium points never intersect each other.

5.5.3 Floquet's theorem

A manifold can be associated with a point or an orbit depending on whether the solution of the system converges to a point or an orbit.

Let's assume that for the autonomous System (5.4) a periodic orbit Γ with period T exists

$$\Gamma : X = \gamma(t) \quad (5.31)$$

for $t \leq 0 \leq T$. As before, the linearization of System (5.4) near Γ is defined by the non-autonomous linear system:

$$\dot{X} = A(t)X \quad (5.32)$$

with

$$A(t) = \frac{dF(\gamma(t))}{dX} \quad (5.33)$$

square matrix, continuous and periodic with period T .

Given the periodic nature of A , it is possible to apply the Floquet's theorem to Equation (5.32).

Let's consider the system:

$$\dot{X} = P(t)X \quad (5.34)$$

where P is a square matrix continuous and periodic with period T

$$P(T + t) = P(t) \quad (5.35)$$

Floquet's theorem states that any fundamental matrix $\Phi(t)$ being the solution of System (5.34) can be represented in the following form:

$$\Phi(t) = Z(t)e^{Rt} \quad (5.36)$$

where R and Z are two square matrices of the same size of P , R is constant and Z is nonsingular, differentiable and periodic with period T . Moreover, if $\Phi(0) = I$, then $Z(0) = I$. The eigenvalues of matrix R are called characteristic exponents of $\gamma(t)$ and the eigenvalues of the matrix e^{Rt} are called characteristic multipliers of $\gamma(t)$.

Recalling now that a fundamental matrix being the solution of System (5.32) is the state transition matrix Φ defined in Equation (5.9)

$$\Phi(X_0, t) = \frac{\partial X}{\partial X_0} \quad (5.37)$$

6×6 nonsingular that satisfies:

$$\dot{\Phi}(X_0, t) = A(t)\Phi(X_0, t) \quad (5.38)$$

and

$$\Phi(X_0, 0) = I \quad (5.39)$$

the monodromy matrix is defined as the fundamental matrix evaluated after a period of the orbit:

$$M = \Phi(X_0, T) \quad (5.40)$$

Although this definition depends on the choice of the initial and final point (the final is the initial after a period T) along the orbit, all monodromy matrices are related by relations of similarity and hence their eigenvalues are invariant quantities and therefore independent of the choice of the point at which they are calculated.

Floquet's theorem can obviously be applied to the matrix M and this leads to:

$$M = \Phi(X_0, T) = Z(T)e^{RT} = Z(0)e^{RT} = e^{RT} \quad (5.41)$$

Therefore, diagonalizing the state transition matrix Φ at time T we obtain the characteristic multipliers $e^{\lambda_i t}$ with $\lambda_i = a_i + ib_i$ the characteristic exponent corresponding to the generalized eigenvector $w_i = u_i + iv_i$ for $\Phi(T)$. If the real part of the characteristic exponents is different from zero, the periodic orbit is called hyperbolic.

The determinant of M is equal to 1.

5.5.4 The Stable Manifold theorem for a periodic orbit

The invariant stable subspace and the invariant unstable subspace of a periodic orbit Γ of System (5.4) associated to the point $0 \in \Gamma$ (the initial state vector X_0 translated to the origin) can be defined as:

$$E^s(\Gamma) = \{u_j, v_j | a_j < 0\} \quad (5.42)$$

$$E^u(\Gamma) = \{u_j, v_j | a_j > 0\} \quad (5.43)$$

The local stable manifold $W_{loc}^s(\Gamma)$ and the local unstable manifold $W_{loc}^u(\Gamma)$ are defined as:

$$W_{loc}^s(\Gamma) = \{x \in U | \phi_t(x) \rightarrow \Gamma \quad t \rightarrow +\infty \quad \phi_t(x) \in U \quad \forall t \geq 0\} \quad (5.44)$$

$$W_{loc}^u(\Gamma) = \{x \in U | \phi_t(x) \rightarrow \Gamma \quad t \rightarrow -\infty \quad \phi_t(x) \in U \quad \forall t \leq 0\} \quad (5.45)$$

where U is some neighborhood of Γ and ϕ_t is the flux of System (5.4).

The local manifolds can be extended to the global manifolds as follows:

$$W^s(\Gamma) = \bigcup_{t \leq 0} \phi_t(W_{loc}^s(\Gamma)) \quad (5.46)$$

$$W^u(\Gamma) = \bigcup_{t \geq 0} \phi_t(W_{loc}^u(\Gamma)) \quad (5.47)$$

The stable manifold theorem guarantees the existence of these objects and states that the stable manifold W_{loc}^s of Γ and the unstable manifold W_{loc}^u of Γ are tangent respectively to the subspaces E^s and E^u at point $0 \in \Gamma$.

5.5.5 Numerical method to compute the Manifolds

The stable and unstable manifolds associated to a periodic orbit Γ are tangent respectively to the subspaces E^s and E^u , namely to the spaces of eigenvectors of the monodromy matrix whose eigenvalues have the modulus respectively less and greater than 1.

The eigenvector associated to the eigenvalue greater than 1 in modulus defines the direction of greater expansion, due to the unstable nature of the orbit. The eigenvector corresponding to the eigenvalue less than 1 in modulus defines the stable manifold.

To generate numerically the manifold of a periodic orbit, first the eigenvalues of the monodromy matrix M at $t = T$ and the normalized eigenvectors $Y^s(X(T))$ and $Y^u(X(T))$ corresponding respectively to the eigenvalue less and greater than 1 are computed.

A small shift in the direction of the right eigenvector gives the approximation of a point on the stable or unstable manifold.

Integrating backward in time starting from:

$$X^s(X(T)) = X^s(X_0) = X_0 + \epsilon Y^s(X_0) \quad (5.48)$$

the stable manifold that forward in time reaches $X(T) = X_0$ is found.

Integrating forward in time starting from:

$$X^u(X(T)) = X^u(X_0) = X_0 + \epsilon Y^u(X_0) \quad (5.49)$$

the unstable manifold that leaves from $X(T) = X_0$ is found.

Each point of the periodic orbit Γ has different eigenvectors and different initial conditions.

Therefore, the procedure to compute the stable and unstable manifold can be summed up as follows:

$$X(t) = \Phi(t)X(0) \quad (5.50)$$

$$Y^s(X(t)) = \Phi(t)Y^s(X_0) \quad (5.51)$$

$$Y^u(X(t)) = \Phi(t)Y^u(X_0) \quad (5.52)$$

$$X^s(X(t)) = X(t) + \epsilon Y^s(X(t)) \quad (5.53)$$

$$X^u(X(t)) = X(t) + \epsilon Y^u(X(t)) \quad (5.54)$$

The reason of normalizing the eigenvectors corresponding respectively to the eigenvalue less and greater than 1 ($Y^s(X_0)$ and $Y^u(X_0)$) is due to the fact that if these eigenvectors are normalized, then ϵ is the distance from the periodic orbit. If the eigenvectors are not normalized, then each trajectory has a phase difference with respect to the others.

In our computation we took $\epsilon = 10^{-5}$.

5.6 Numerical Results: manifolds of a family of Lyapunov orbits near L_3

We first started computing the manifolds of the family of Lyapunov orbits generated before.

The stable manifold of the smallest orbit of the family is shown in Figure (5.3), and the stable manifold of the biggest orbit of the family is given in Figure (5.4).

As can be seen, these manifolds have a horseshoe shape and do not reach the smaller primary (here, the Earth). Moreover, the motion in these manifolds is very slow, and in particular the slower the bigger the Lyapunov orbit is. Here, for the smallest orbit it takes about 700 years from the closest point to the Earth to the target Lyapunov orbit near L_3 (that becomes roughly 200 years if the target is a box near L_3 with a semi-amplitude in the y-direction of order 0.1 AU, due to the fact the stable manifolds tend asymptotically to the orbits they are generated from). For the biggest Lyapunov orbit the transfer time has the value of about 800 years.

Therefore, it is obvious that the stable manifolds of the Lyapunov orbits near L_3 can not be used for the transfer Earth- L_3 , but can be only studied for astronomical purposes. Indeed in the past few years some asteroids that fly in the region of these manifolds have been discovered and observed, as for example asteroid 2002 AA29 [Connors et al., 2002]. This asteroid moves in a 3D horseshoe orbit in the Sun-Earth system (see Figure (5.5)). The horseshoe

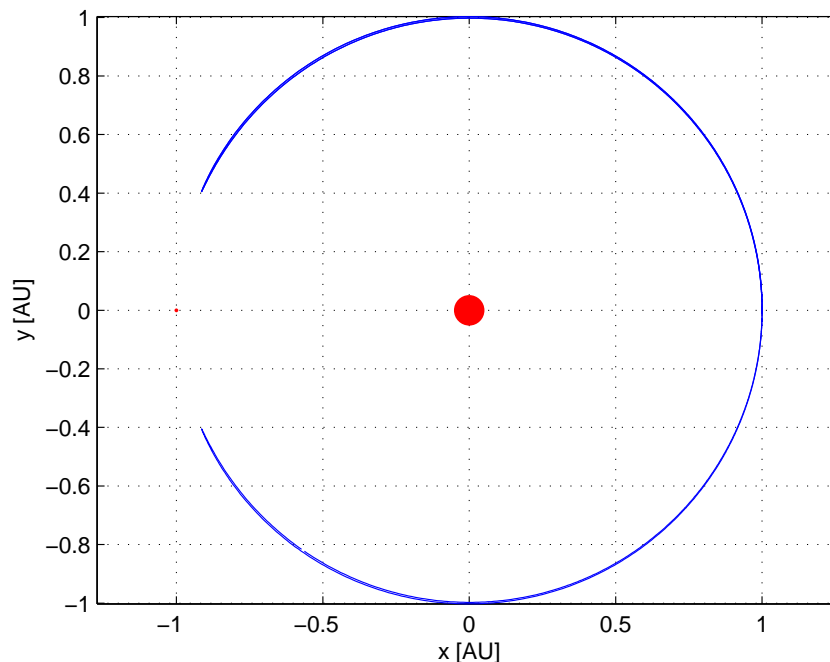


Figure 5.3 Behaviour of stable manifold of the smallest Lyapunov orbit of the family integrated for a long time span, RTBP reference frame

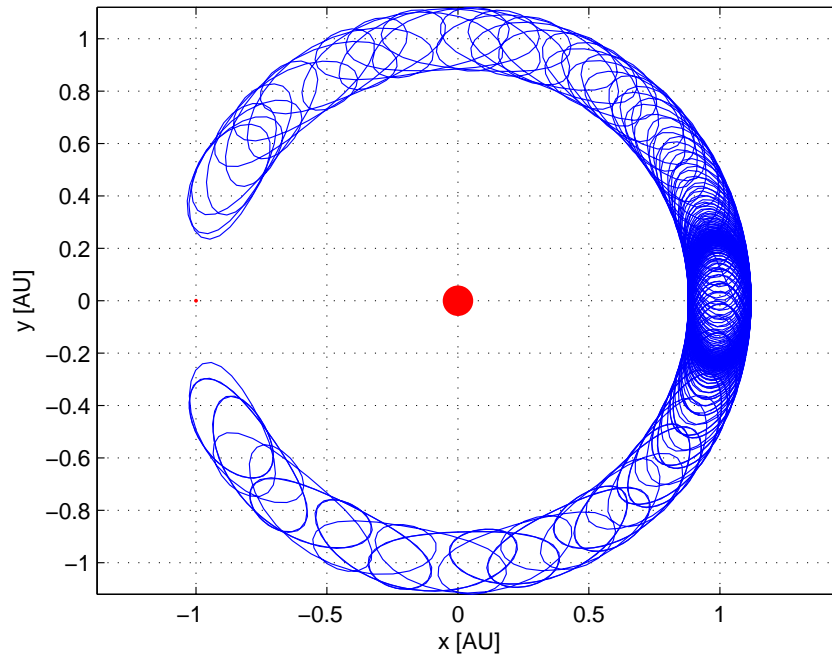


Figure 5.4 Behaviour of stable manifold of the biggest Lyapunov orbit of the family integrated for a long time span, RTBP reference frame

shape of the manifold can be explained taking into account the mass of the two primaries of the system. According to [Barrabés and Ollé, 2006], when $0 < \mu \leq 0.01174$ the invariant manifold associated with each value of μ has a horseshoe shape (as we have already seen, for the Sun-Earth system $\mu \approx 0.3 \cdot 10^{-5}$).

Moreover, the very slow motion of the manifolds of orbits near L_3 can be justified as follows. When μ is small (as in our case) the mean distance of the manifold of libration point L_3 from the zero-velocity curve (Hill's surface) is of order $\mu^{1/2}$, while for the manifold of L_1/L_2 it is $\mu^{1/3}$ [Font, 1990]. It is clear that the closer to the zero-velocity curve, the slower the motion.

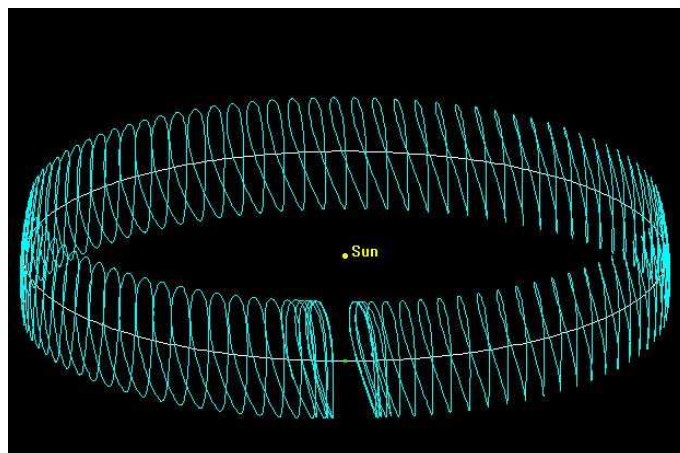


Figure 5.5 Horseshoe orbit of Asteroid 2002 AA29 [NASA www.neo.jpl.nasa.gov]

5.7 Numerical Results: manifolds of Lyapunov orbits near L_1 and L_2 reaching Lyapunov orbits near L_3

Since the study of the manifolds of Lyapunov orbits near L_3 did not lead to any results that could be flown by a s/c, we decided to consider another strategy, and in particular the manifolds of L_1 and L_2 .

It is commonly known that the manifolds of L_1 and L_2 (or orbits near these points) are much faster, and can reach the region "nearby" L_3 in few years. However, due to the value of the Jacobi constant, the manifolds of L_1 and L_2 can not reach neither L_3 nor periodic orbits near this point: a ΔV is required to open the forbidden region and match the Jacobi constant of either L_3 or the target orbit near it.

As can be seen in Figure (5.6), the manifold of L_1 remains inside the forbidden region, while the manifold of L_2 is outside.

We proceeded as follows. A Lyapunov orbit near L_1 (blue color) and a Lyapunov orbit near L_2 (red color) have been defined. For our simulation, as can be seen in Figure (5.7), we chose Lyapunov orbits with a semi-amplitude in the x-direction of order 0.003 AU, leading to a semi-amplitude in the y-direction of order 0.008 AU ($C = 3.000689736839$ for the Lyapunov orbit near L_1 , $C = 3.000686749335$ for the Lyapunov orbit near L_2). Then, the unstable manifolds leaving from some (we took 200) points on the Lyapunov orbit have been generated, integrating forward in time until each orbit contained in the manifolds crosses the x-axis in the region nearby L_3 . Since a wide family of Lyapunov orbits near L_3 has been previously generated, at $y = 0$ some of them overlap with the manifolds departing from the two Lyapunov orbits near L_1 and L_2 .

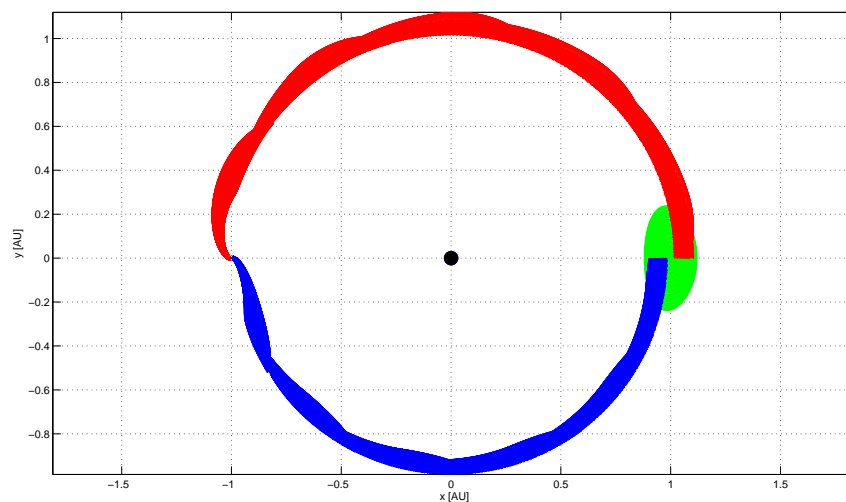


Figure 5.6 Plot of the unstable manifolds of Lyapunov orbits near L_1 (blue) and L_2 (red) reaching Lyapunov orbits near L_3 , RTBP reference frame

In Figure (5.8) the intersection of the manifolds departing from the two chosen

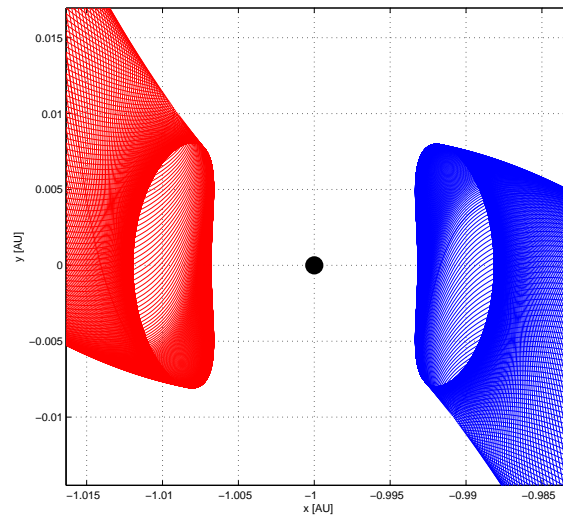


Figure 5.7 Plot of the chosen Lyapunov orbits near L_1 (blue) and L_2 (red) and the departing unstable manifolds, RTBP reference frame

Lyapunov orbits near L_1 and L_2 with the family of Lyapunov orbits near L_3 is shown. Once the range of intersecting orbits has been defined, we computed the

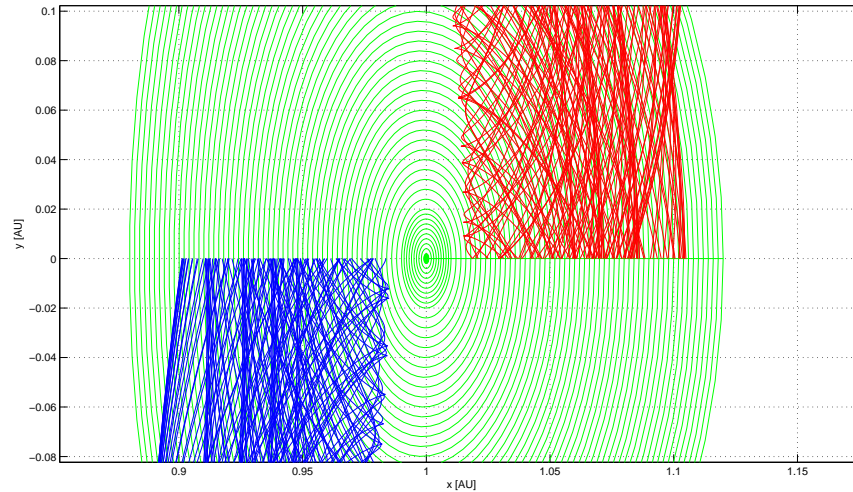


Figure 5.8 Intersection of the unstable manifolds of Lyapunov orbits near L_1 (blue) and L_2 (red) with the family of Lyapunov orbits near L_3 , RTBP reference frame: Zoom

ΔV required to match the Jacobi constant and insert the s/c into the Lyapunov orbit that passes through the same point on the x-axis. Note that the ΔV could be applied at any point where the manifolds and the target orbits overlap, but we decided to have this velocity change at $y = 0$.

Since periodic Lyapunov orbits near L_3 are symmetric with respect to the x-axis, then in $y = 0$ the velocity component in the x-direction is equal to zero.

Therefore, the velocity change that has to be applied is equal to:

$$\Delta V = \sqrt{(\dot{x}_{trMan})^2 + (\dot{y}_{LyapL3} - \dot{y}_{trMan})^2} \quad (5.55)$$

where \dot{x}_{trMan} is the velocity in the x-direction of the transfer manifold departing from the Lyapunov orbit near L_1 or L_2 when crossing $y = 0$, \dot{y}_{trMan} is the velocity in the y-direction of the transfer manifold departing from the Lyapunov orbit near L_1 or L_2 when crossing $y = 0$, and \dot{y}_{LyapL3} is the velocity that has to be matched, being the velocity of the Lyapunov orbit near L_3 in $y = 0$.

The plots of the ΔV required for orbit insertion are given in Figures (5.9) and (5.10). For a given point on the x-axis, there are more ΔV s: this is right, due to the fact that at a given x the magnitude of the velocity of the orbit in the transfer manifold is only one (all the orbits contained in the manifold have the same Jacobi constant), but the direction can vary in a range ($V_{trMan} = \sqrt{\dot{x}_{trMan}^2 + \dot{y}_{trMan}^2}$ is defined by the position, with different combinations of \dot{x}_{trMan} and \dot{y}_{trMan}).

Therefore Figures (5.9) and (5.10) should be read as ranges of ΔV for orbit insertion.

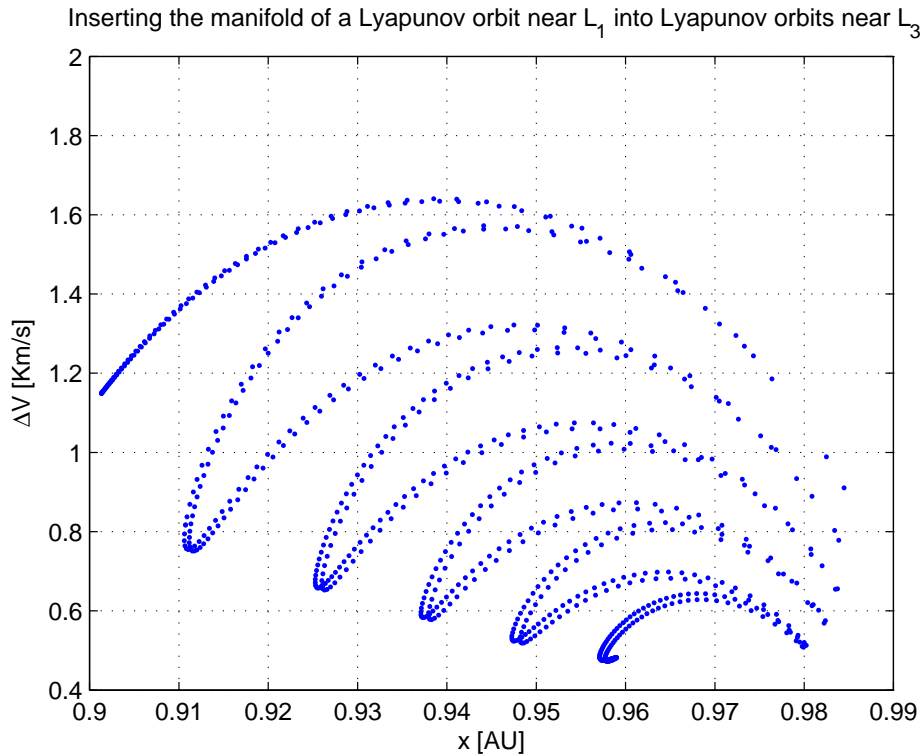


Figure 5.9 Plot of the ΔV required to insert the manifolds of Lyapunov orbits near L_1 into the intersecting Lyapunov orbits near L_3

The plots show that the closer to L_3 the arrival Lyapunov orbit is, the lower the minimum ΔV . Moreover, the range are almost the same for the manifolds departing from near L_1 and those departing from near L_2 (the maximum ΔV for L_2 is a bit bigger), and in particular [0.5 km/s - 1.5 km/s].

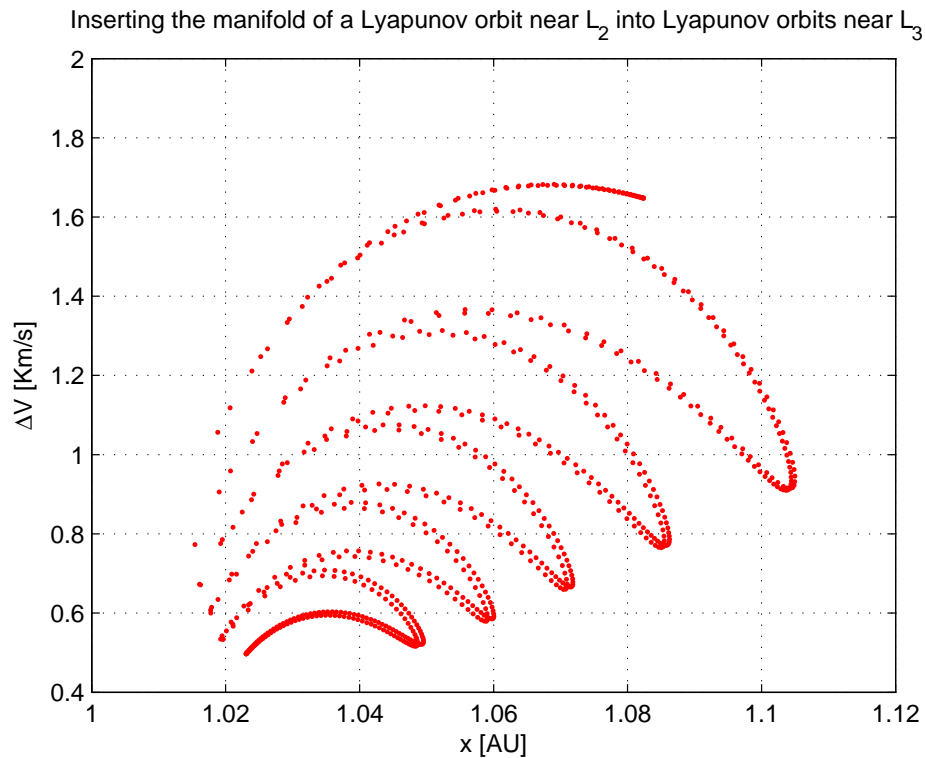


Figure 5.10 Plot of the ΔV required to insert the manifolds of Lyapunov orbits near L_2 into the intersecting Lyapunov orbits near L_3

As for ESA missions Herschel and Planck [Hechler, 2008], if the launcher injects the s/c directly into the stable manifold of the Lyapunov orbit near L_1 or L_2 , then this is the only ΔV required for the s/c to reach the target Lyapunov orbit near L_3 .

Once the s/c is released from the launcher and put into the stable manifold, L_1 or L_2 are reached in about 60 days. Then, through the unstable manifold, from L_1 to the region nearby L_3 it takes 5.5 – 10.5 years, depending on the departing point on the Lyapunov orbit, and 6–11 years leaving from L_2 .

In Figures (5.11) and (5.13) we give the plots of ΔV as a function of the departing time on the Lyapunov orbit near L_1 or L_2 .

The zero is defined at the point on the Lyapunov orbit near L_1 or L_2 at $y = 0$ and on the left side of the libration point, increasing clockwise.

In Figures (5.12) and (5.14) the transfer time is reported.

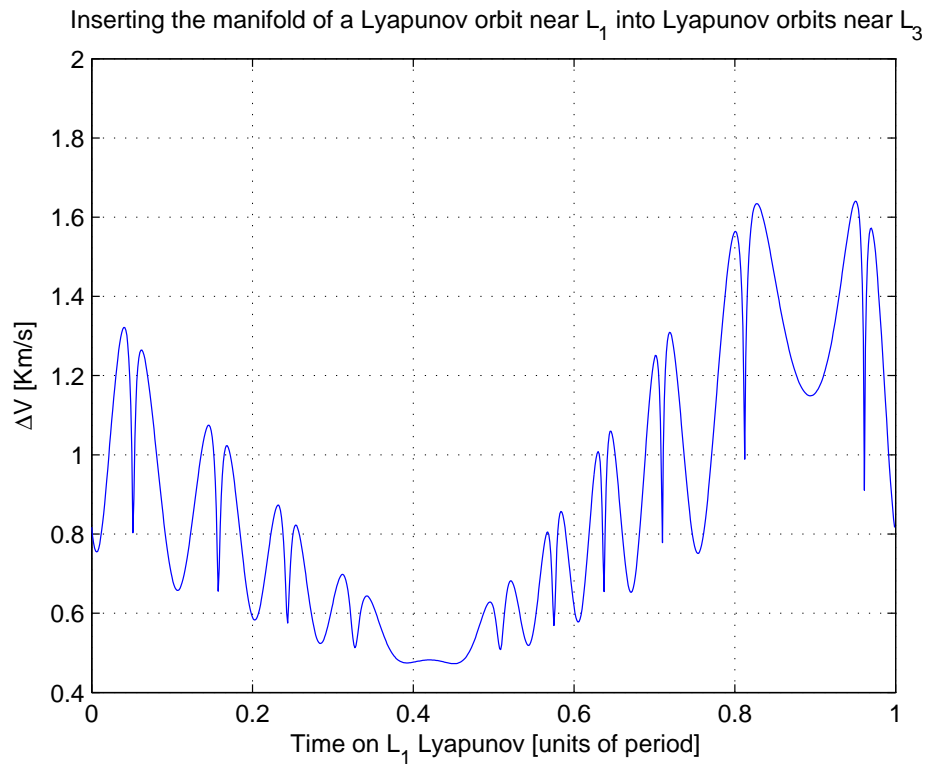


Figure 5.11 Plot of the ΔV required to insert the manifolds of Lyapunov orbits near L_1 into the intersecting Lyapunov orbits near L_3 as a function of time on the progenitor Lyapunov orbit

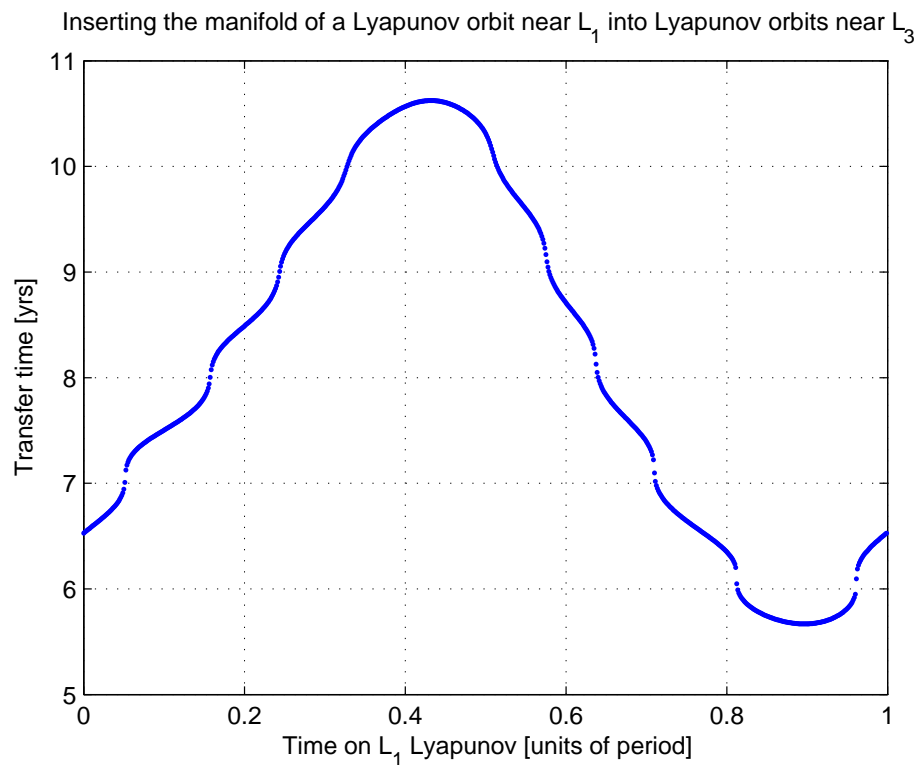


Figure 5.12 Plot of the transfer time on the manifolds of Lyapunov orbits near L_1 to the intersecting Lyapunov orbits near L_3 as a function of time on the progenitor Lyapunov orbit

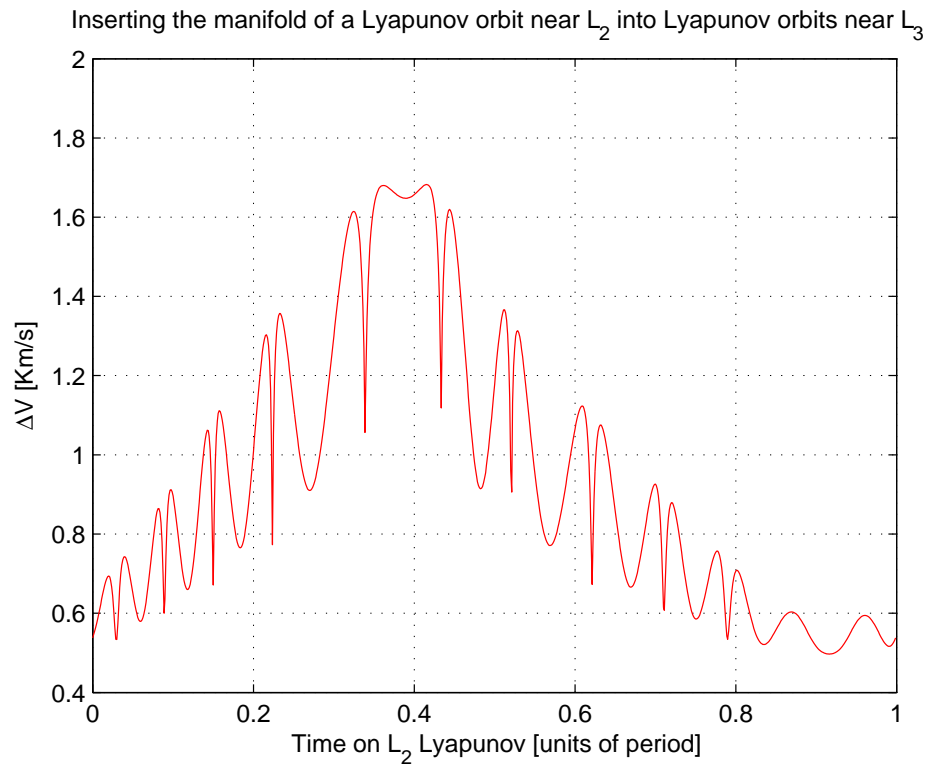


Figure 5.13 Plot of the ΔV required to insert the manifolds of Lyapunov orbits near L_2 into the intersecting Lyapunov orbits near L_3 as a function of time on the progenitor Lyapunov orbit

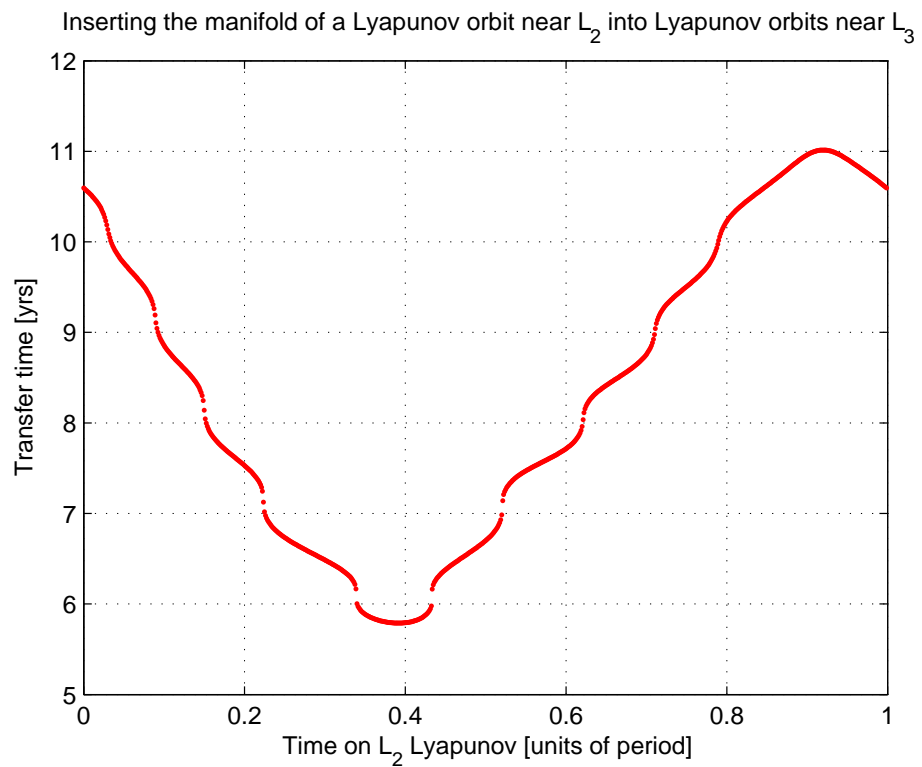


Figure 5.14 Plot of the transfer time on the manifolds of Lyapunov orbits near L_2 to the intersecting Lyapunov orbits near L_3 as a function of time on the progenitor Lyapunov orbit

Looking at the results, we can conclude that in case the manifolds of Lyapunov orbits near L_1 and L_2 are used for the transfer, the departing orbits should be left at the right phase angle, depending on the chosen ΔV or time of flight.

It seems that the minimum for L_1 has a phase difference of π respect to the minimum for L_2 (difference of half the period on the departing orbit), and vice versa. In both the cases, the minimum ΔV is reached when the departing point is on the side of the Lyapunov orbit that is farther from the Earth.

The local oscillation of the ΔV is due to the oscillating value of x for increasing time on the progenitor Lyapunov orbit and the direction of the velocity vector on the manifold when crossing $y = 0$.

Moreover, it seems that the minimum ΔV corresponds to the maximum time of flight, and vice versa. This fact can be explained as follows. As shown in Figures (5.15) and (5.17), the trajectory on the manifold that has the maximum transfer time (also called Time of Flight, TOF) is closer to the zero-velocity curve (Hill's surface) and so travels slower and at the same time reaches L_3 at a lower speed. Then the insertion manevuer is smaller since L_3 and the Lyapounov orbits near the libration point have essentially zero velocity.

The transfer time depends on the number of bounces that the trajectory on the manifold does on the zero-velocity curve. The closer to the zero-velocity curve, the higher the number of bounces and the longer the transfer time. The TOF on each arc from a bounce to the next one depends on the period of the Lyapunov orbit that generates the manifold.

Inserting the manifold of a Lyapunov orbit near L_1 into Lyapunov orbits near L_3 --- RTBP r.f

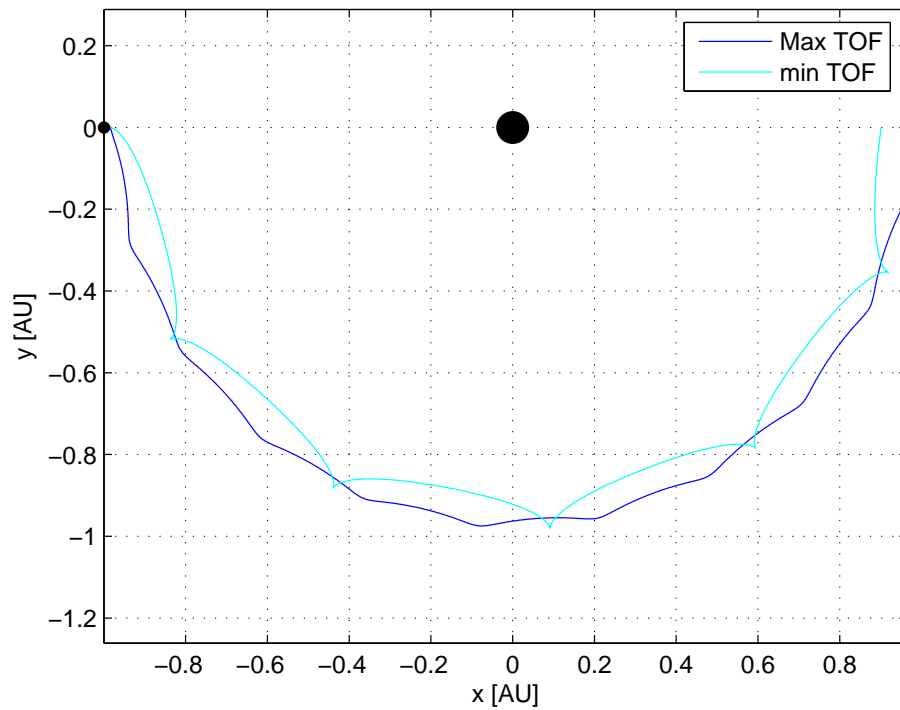


Figure 5.15 Plot of the orbits on the manifold of the Lyapunov orbit near L_1 with the minimum and maximum TOF, RTBP reference frame

Inserting the manifold of a Lyapunov orbit near L_1 into Lyapunov orbits near L_3 --- RTBP r.f

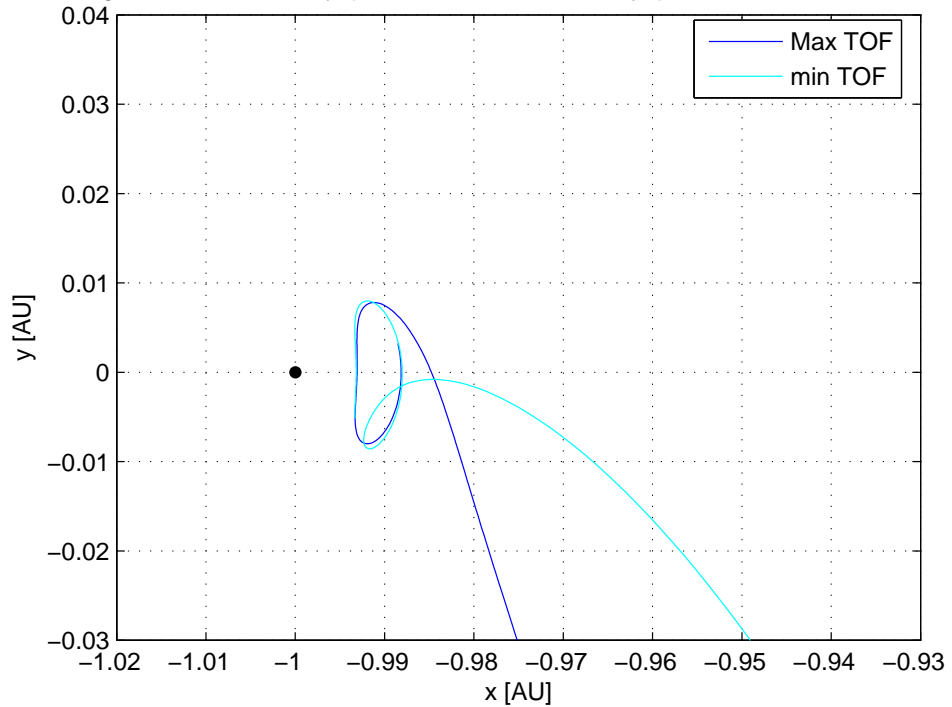


Figure 5.16 Plot of the orbits on the manifold of the Lyapunov orbit near L_1 with the minimum and maximum TOF, RTBP reference frame: Zoom

Inserting the manifold of a Lyapunov orbit near L_2 into Lyapunov orbits near L_3 --- RTBP r.f

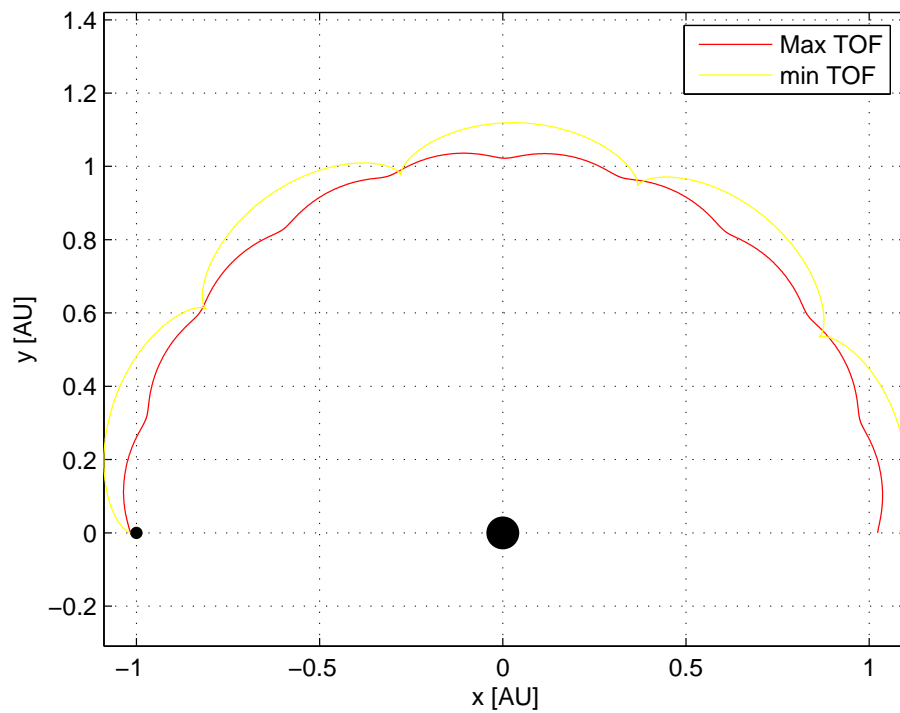


Figure 5.17 Plot of the orbits on the manifold of the Lyapunov orbit near L_2 with the minimum and maximum TOF, RTBP reference frame

Inserting the manifold of a Lyapunov orbit near L_2 into Lyapunov orbits near L_3 --- RTBP r.f

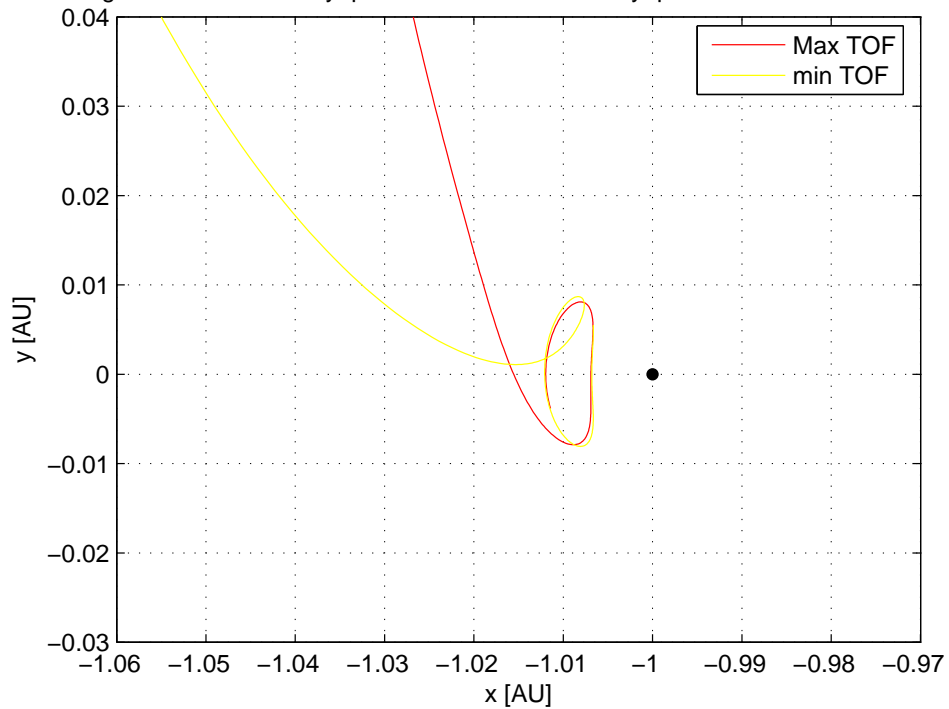


Figure 5.18 Plot of the orbits on the manifold of the Lyapunov orbit near L_2 with the minimum and maximum TOF, RTBP reference frame: Zoom

Transfers using Low Thrust

In this chapter we will focus on transfers to the L_3 libration point of the Sun-Earth system using Low Thrust.

At the beginning of the study the thrust will be considered constant in magnitude, and three different values will be taken. As it is commonly known and can be found in literature [*Wakker, 2005*], Electric Propulsion (EP) typically provides accelerations in the range 10^{-4} - 10^{-2} m/s^2 . We chose $5 \cdot 10^{-4}$, $1 \cdot 10^{-3}$ and $5 \cdot 10^{-3}$ m/s^2 .

We will first consider RTBP, with the thrust ON while the s/c is within the Sphere of Influence (SI) of the Earth, and then turned OFF. Plots in the RTBP will be provided.

Since this strategy will not look succesful (and too sensitive to the initial condition), we moved to 2BP, still considering a constant acceleration. First, finding the optimal control of the heliocentric cruise segment (out of the SI) by using the Pontryagin minimum principle.

Then, the transfer trajectory has been propagated in RTBP, using the optimal control history obtained from the 2BP. The results showed that out of the SI, the optimal trajectories in 2BP and RTBP are (almost) the same as long as the chosen constant acceleration is big enough (in our case, for all the three accelerations that have been taken), because the influence of the gravity of the Earth is quite small.

Finally, the same approach has been used considering the mass flow, and therefore an acceleration that varies linearly with time. We chose the same EP parameters of the Dawn spacecraft flown by NASA. In this case, in the 2BP optimization the results will not look very different from those obtained having an acceleration constant in magnitude. However, due to the low value of the varying acceleration, in the RTBP model the s/c ends in the region "nearby" L_3 , but does not reach the target point.

6.1 Preliminary investigation: RTBP

As a preliminary investigation we decided to consider RTBP and the thrust ON only when the s/c is within the SI of the Earth.

As initial states, a Geostationary Earth Orbit (GEO) has been taken (altitude equal to 35700 km), varying the phase angle. We considered such a big orbit because in the RTBP model we used, if the third body comes too close to one of the primaries, either it hits the primary, or the integration is not precise anymore. However, even if this parking orbit might look quite big, for this preliminary investigation it is not a problem. On the parking orbit, the phase angle θ has been defined as follows: equal to zero when the s/c is on the line connecting the two primaries and on the side of L_1 , increasing anticlockwise.

The direction of the thrust has been taken equal to the direction of the velocity of the s/c with respect to an inertial reference frame centered on the Earth (V_{sid}). The RTBP equations have been modified including the accelerations due to the thrust:

$$\begin{aligned}\ddot{x} &= +2\dot{y} + x - \frac{1-\mu}{r_1^3}(x-\mu) - \frac{\mu}{r_2^3}(x-\mu+1) + T_x \\ \ddot{y} &= -2\dot{x} + y - \frac{1-\mu}{r_1^3}y - \frac{\mu}{r_2^3}y + T_y \\ \ddot{z} &= -\frac{1-\mu}{r_1^3}z - \frac{\mu}{r_2^3}z + T_z\end{aligned}\tag{6.1}$$

where

$$\begin{aligned}T_x &= \frac{\dot{x}_{sid}}{\|V_{sid}\|}M \\ T_y &= \frac{\dot{y}_{sid}}{\|V_{sid}\|}M \\ T_z &= \frac{\dot{z}_{sid}}{\|V_{sid}\|}M\end{aligned}\tag{6.2}$$

where M is the constant acceleration. Since we only considered planar transfers and parking orbits in the xy-plane, \ddot{z} and T_z are always equal to zero.

The thrust is then turned OFF when the s/c leaves the SI of the Earth. In literature the SI of the Earth is defined in two ways: either considering the Hill's Sphere (radius of 925000 km) or taking the distance of L_1 (1.5 million km). We have chosen to turn OFF the thrust when the s/c reaches a distance from the center of the Earth equal to 1.5 million km.

We ran the simulations taking three values of constant acceleration M ($5 \cdot 10^{-4}$, $1 \cdot 10^{-3}$ and $5 \cdot 10^{-3} \text{ m/s}^2$) and different values of θ . The results are on the following pages, shown in Figures (6.1)-(6.17).

As can be seen, while the thrust is ON within the SI of the Earth, the s/c

spirals about the Earth increasing its semi-major axis. Then the thrust is turned OFF and the s/c (which is the third body of the RTBP) moves in the space delimited by the forbidden region defined by the gained energy level. The energy level of the s/c is described by its Jacobi constant, and for each case it can be found in the caption of the figure.

Note that in all these simulations the s/c never reaches L_3 and its trajectory is very sensitive to the initial state. Moreover, the value of the Jacobi constant of the s/c is always too far from the one of the target, that is the value of the Jacobi constant for L_3 ($C = 3.00000608083736$): the difference, when passing "close" to L_3 , should be smaller than about order 10^{-8} if s/c is required to remain nearby L_3 . As shown taking different values for the final time (T_{final}), in this preliminary study the s/c never matches the velocity of L_3 , thus, once it becomes close, it overtakes the target.

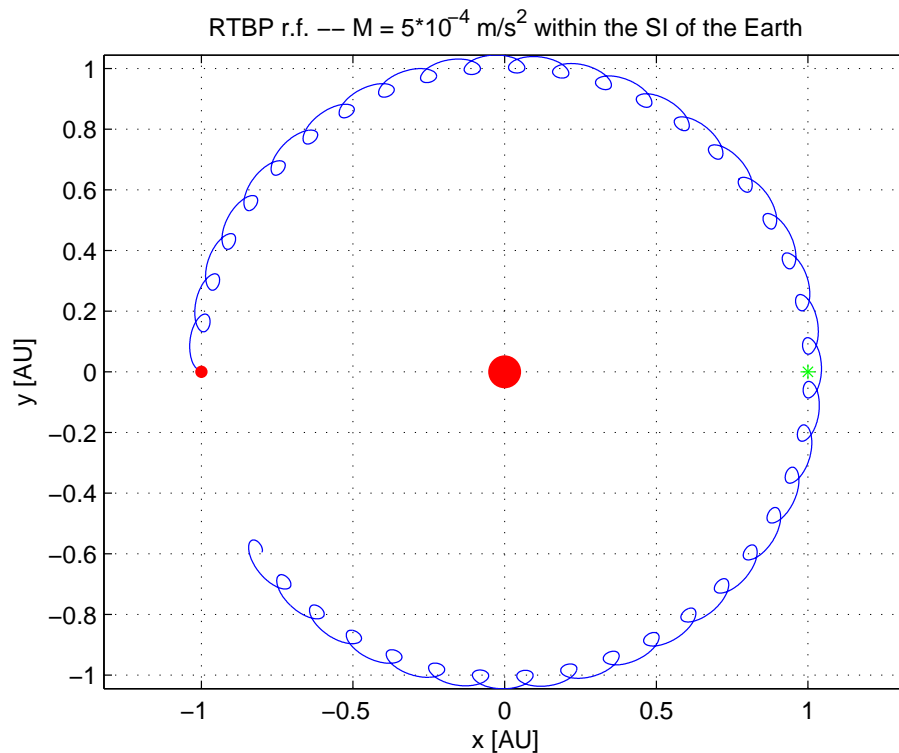


Figure 6.1 Low Thrust, preliminary investigation. $M = 5 * 10^{-4} m/s^2$, $\theta = 0$, $T_{final} = 40 y$, Value of the Jacobi Constant (when the thrust is turned off) $C = 2.99933595$, Low Thrust ON within the SI of the Earth, RTBP reference frame

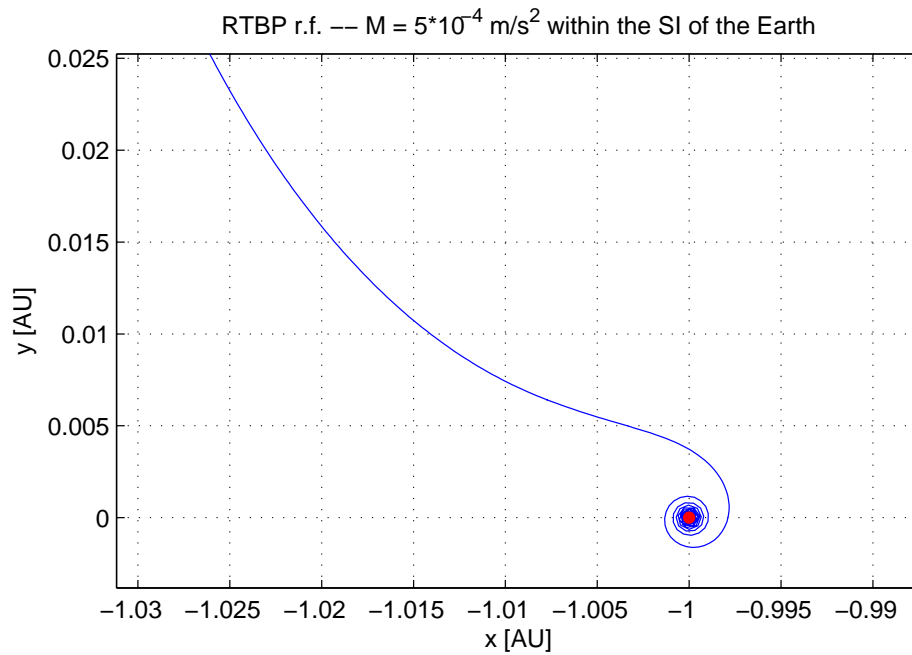


Figure 6.2 Low Thrust, preliminary investigation. Zoom: $M = 5 * 10^{-4} m/s^2$, $\theta = 0$, $T_{final} = 40 y$, Value of the Jacobi Constant (when the thrust is turned off) $C = 2.99933595$, Low Thrust ON within the SI of the Earth, RTBP reference frame

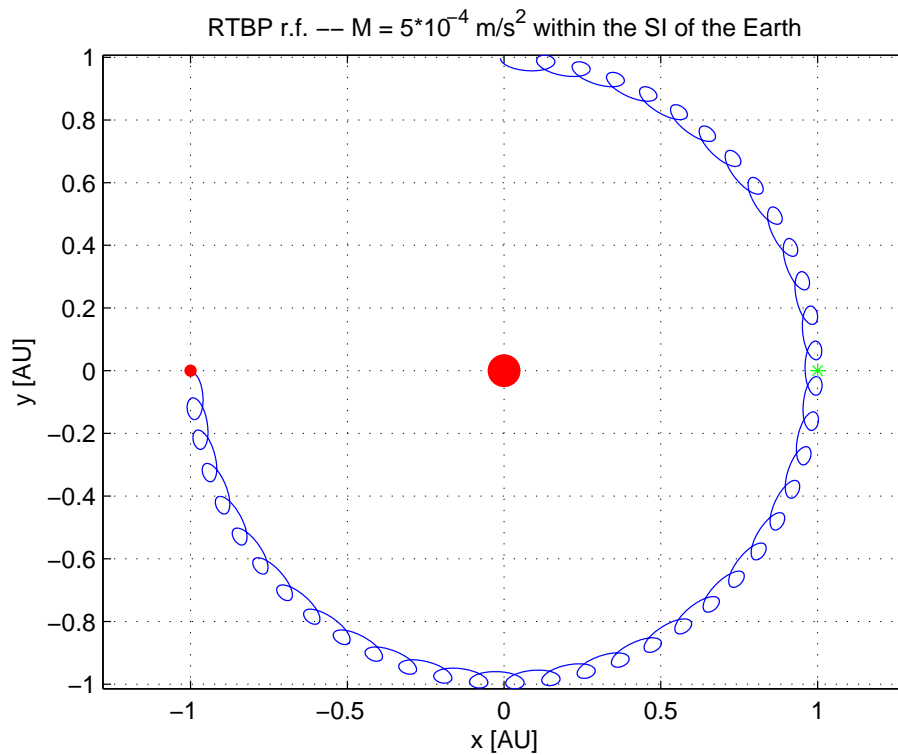


Figure 6.3 Low Thrust, preliminary investigation. $M = 5 * 10^{-4} m/s^2$, $\theta = \pi$, $T_{final} = 40 y$, Value of the Jacobi Constant (when the thrust is turned off) $C = 2.99934005$, Low Thrust ON within the SI of the Earth, RTBP reference frame

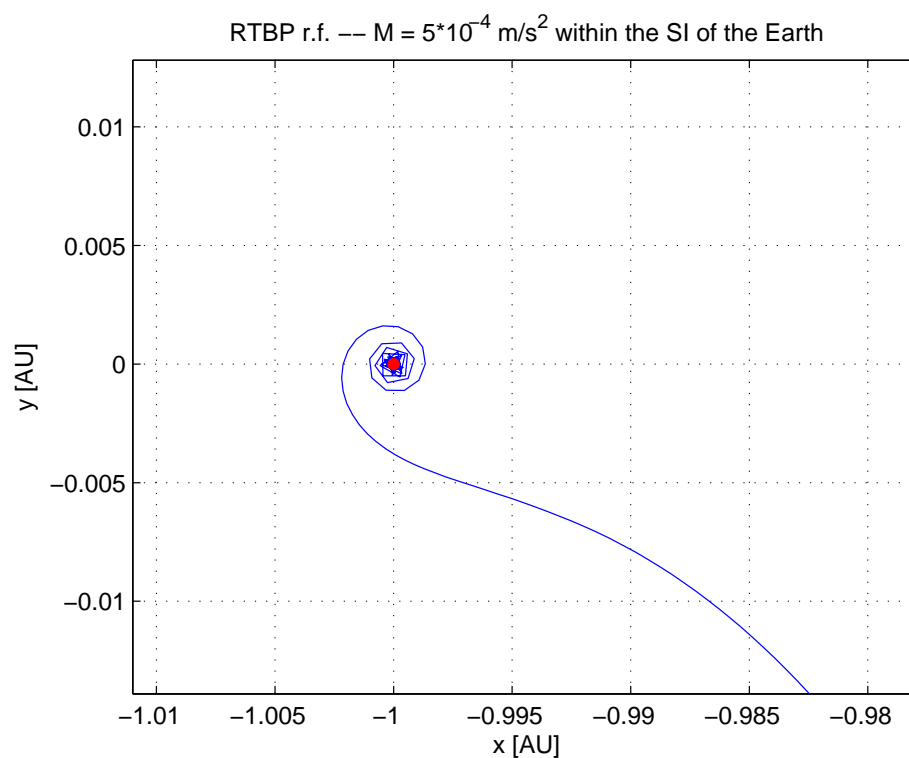


Figure 6.4 Low Thrust, preliminary investigation. Zoom: $M = 5 * 10^{-4} m/s^2$, $\theta = \pi$, $T_{final} = 40 y$, Value of the Jacobi Constant (when the thrust is turned off) $C = 2.99934005$, Low Thrust ON within the SI of the Earth, RTBP reference frame

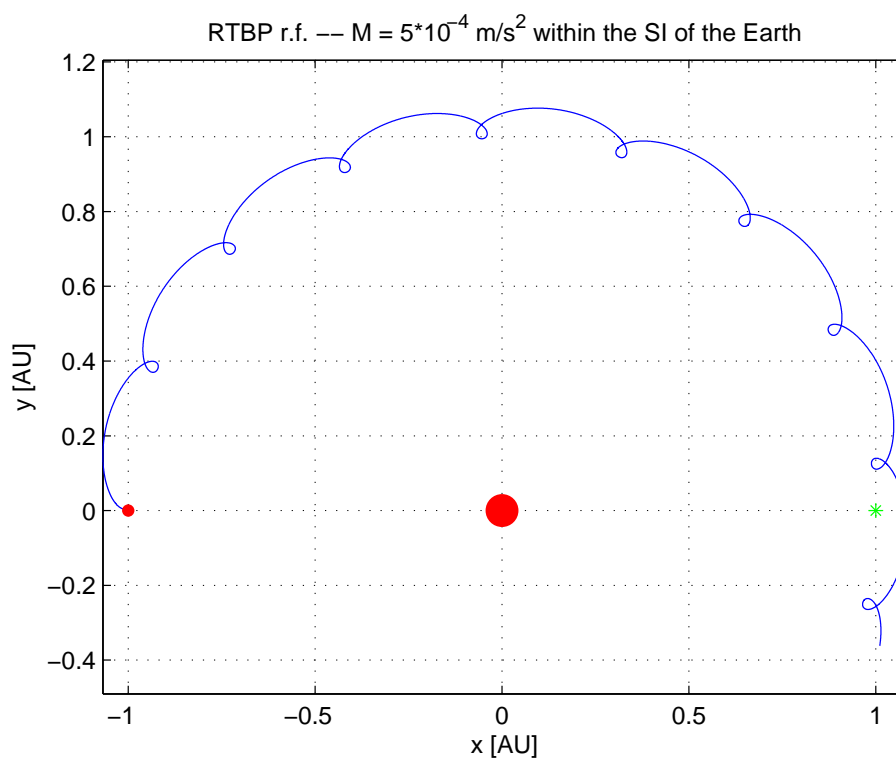


Figure 6.5 Low Thrust, preliminary investigation. $M = 5 * 10^{-4} m/s^2$, $\theta = \frac{\pi}{2}$, $T_{final} = 10 y$, Value of the Jacobi Constant (when the thrust is turned off) $C = 2.99933524$, Low Thrust ON within the SI of the Earth, RTBP reference frame

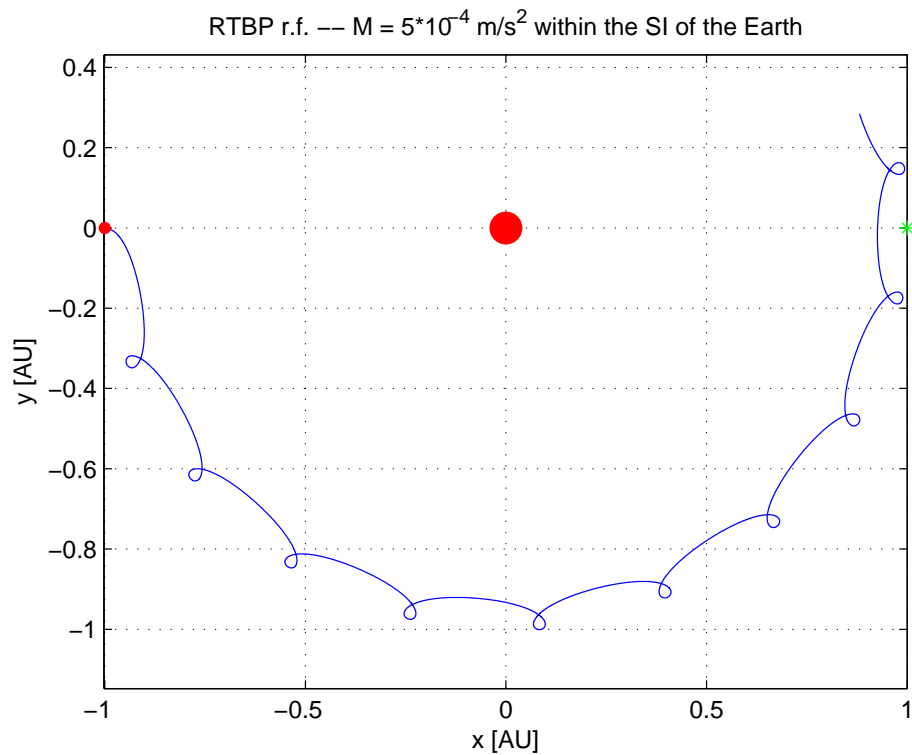


Figure 6.6 Low Thrust, preliminary investigation. $M = 5 \cdot 10^{-4} \text{ m/s}^2$, $\theta = \frac{3\pi}{2}$, $T_{final} = 10 \text{ y}$, Value of the Jacobi Constant (when the thrust is turned off) $C = 2.99933387$, Low Thrust ON within the SI of the Earth, RTBP reference frame

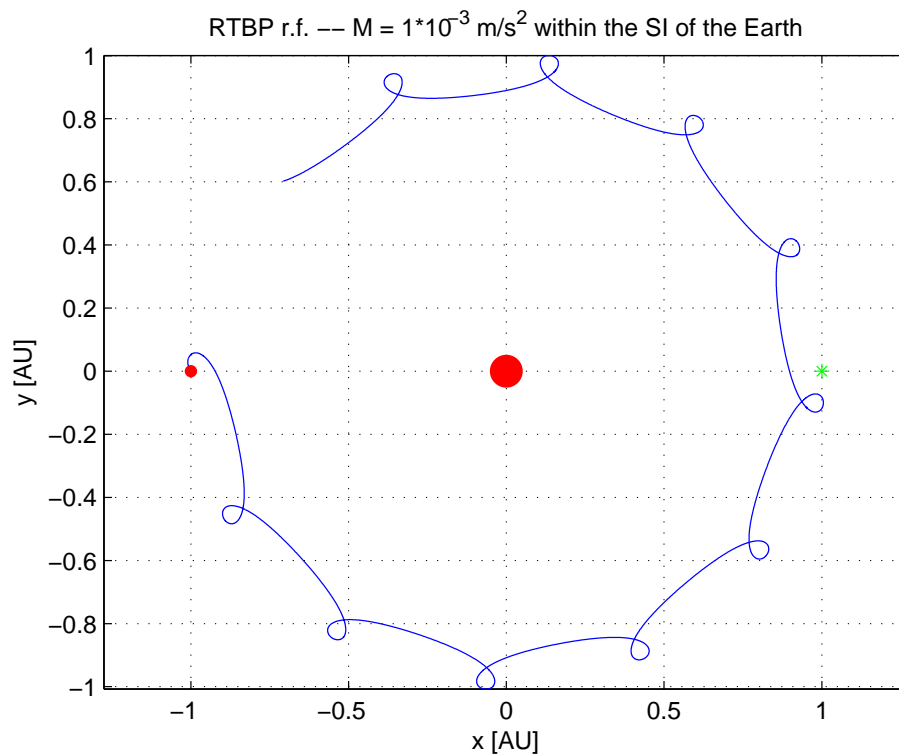


Figure 6.7 Low Thrust, preliminary investigation. $M = 1 \cdot 10^{-3} \text{ m/s}^2$, $\theta = 0$, $T_{final} = 10 \text{ y}$, Value of the Jacobi Constant (when the thrust is turned off) $C = 2.99781043$, Low Thrust ON within the SI of the Earth, RTBP reference frame

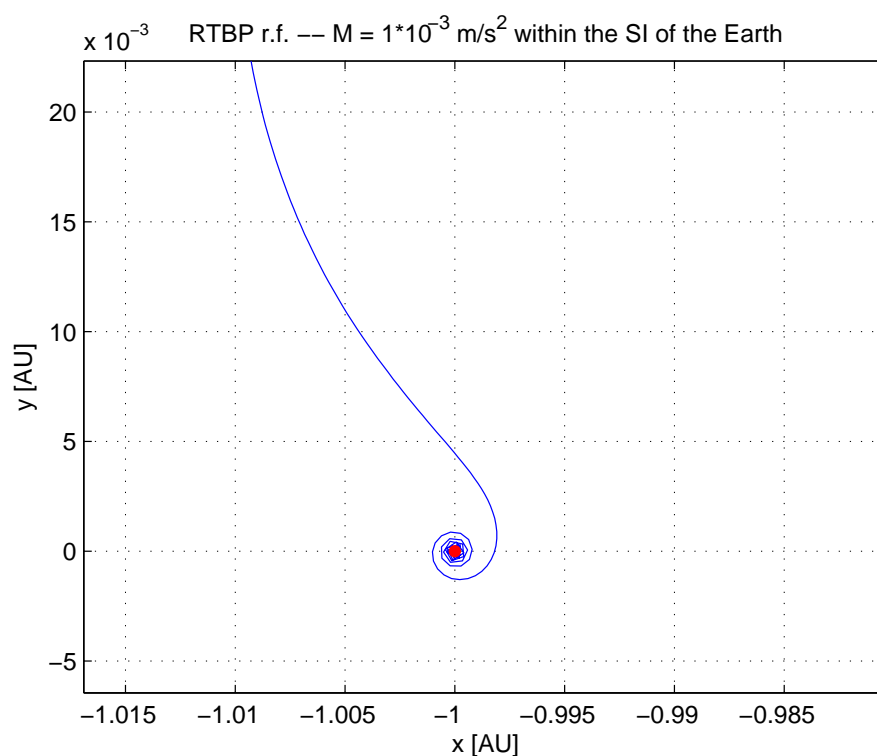


Figure 6.8 Low Thrust, preliminary investigation. Zoom: $M = 1 * 10^{-3} m/s^2$, $\theta = 0$, $T_{final} = 10 y$, Value of the Jacobi Constant (when the thrust is turned off) $C = 2.99781043$, Low Thrust ON within the SI of the Earth, RTBP reference frame

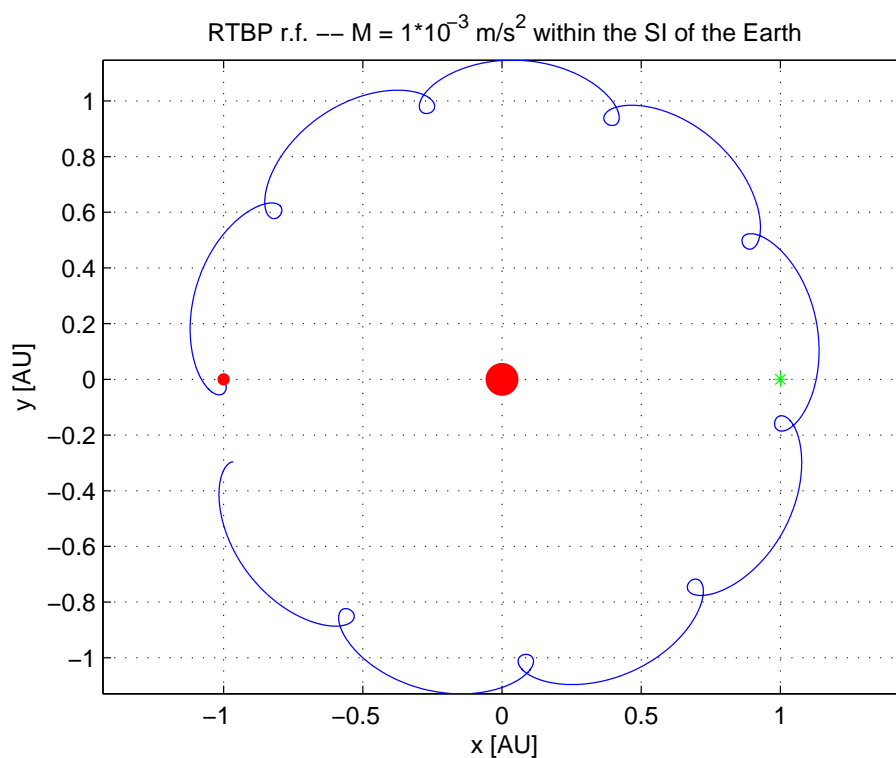


Figure 6.9 Low Thrust, preliminary investigation. $M = 1 * 10^{-3} m/s^2$, $\theta = \pi$, $T_{final} = 10 y$, Value of the Jacobi Constant (when the thrust is turned off) $C = 2.99781362$, Low Thrust ON within the SI of the Earth, RTBP reference frame

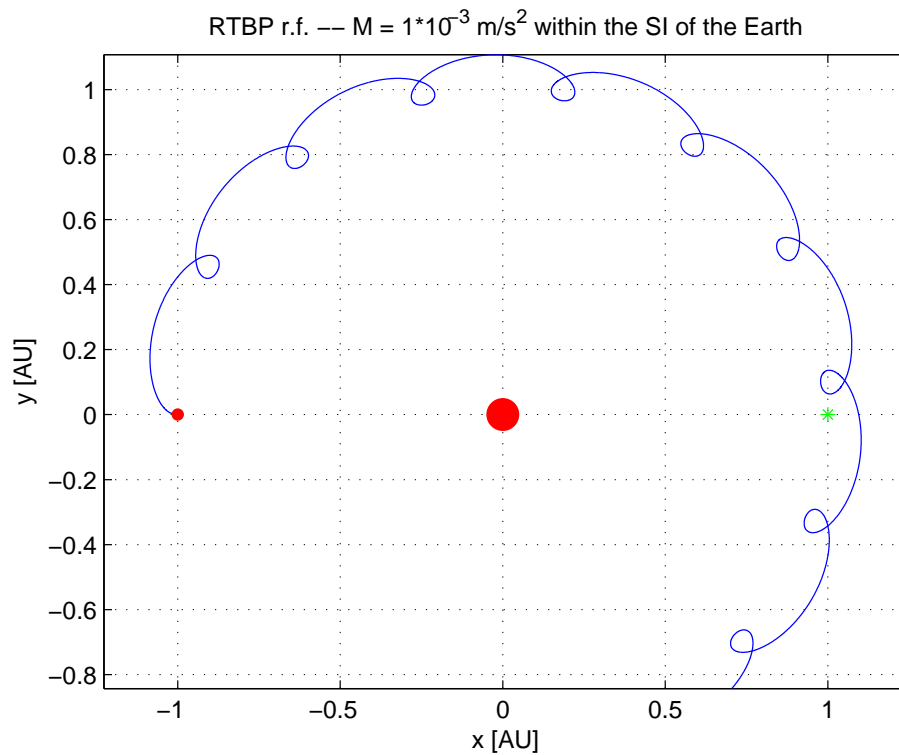


Figure 6.10 Low Thrust, preliminary investigation. $M = 1 \cdot 10^{-3} \text{ m/s}^2$, $\theta = \frac{\pi}{2}$, $T_{final} = 10 \text{ y}$, Value of the Jacobi Constant (when the thrust is turned off) $C = 2.99782615$, Low Thrust ON within the SI of the Earth, RTBP reference frame

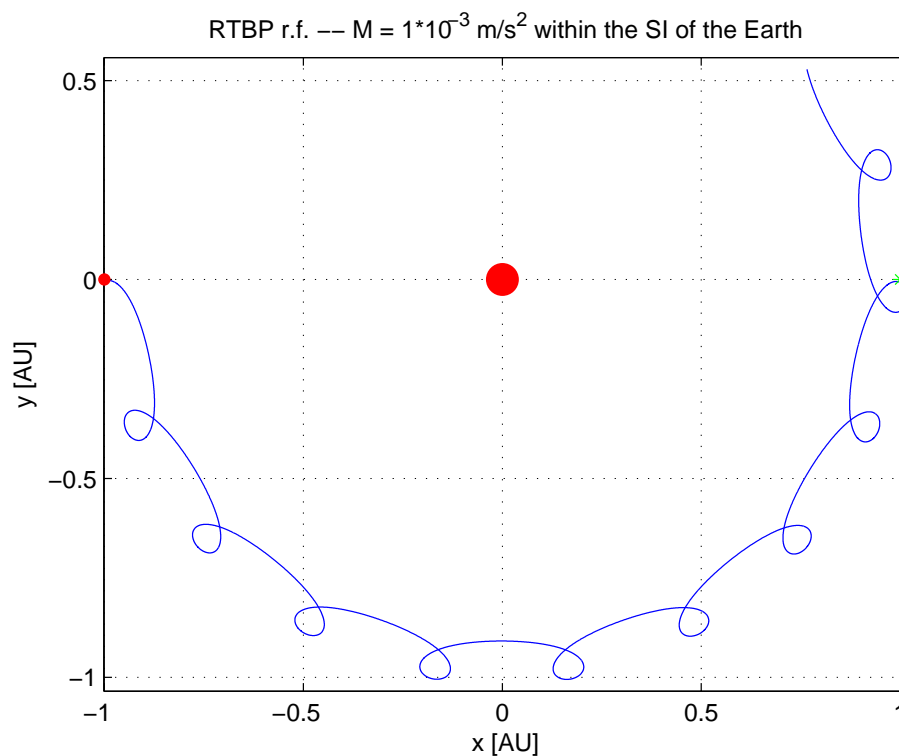


Figure 6.11 Low Thrust, preliminary investigation. $M = 1 \cdot 10^{-3} \text{ m/s}^2$, $\theta = \frac{3\pi}{2}$, $T_{final} = 10 \text{ y}$, Value of the Jacobi Constant (when the thrust is turned off) $C = 2.99782617$, Low Thrust ON within the SI of the Earth, RTBP reference frame

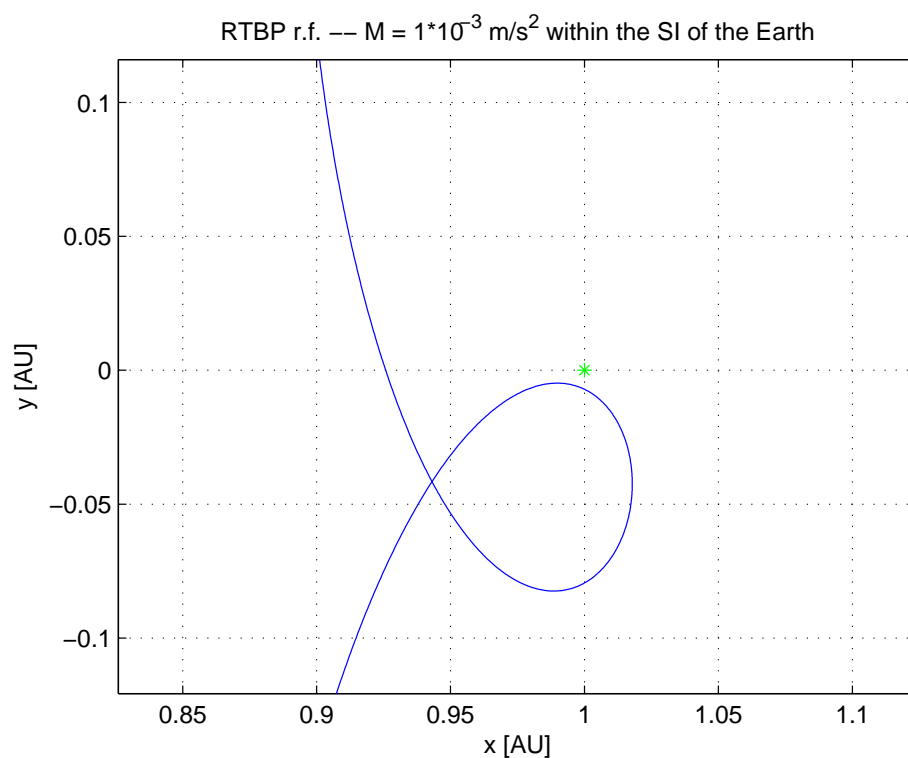


Figure 6.12 Low Thrust, preliminary investigation. Zoom: $M = 1 \cdot 10^{-3} \text{ m/s}^2$, $\theta = \frac{3\pi}{2}$, $T_{final} = 10 \text{ y}$, Value of the Jacobi Constant (when the thrust is turned off) $C = 2.99782617$, Low Thrust ON within the SI of the Earth, RTBP reference frame

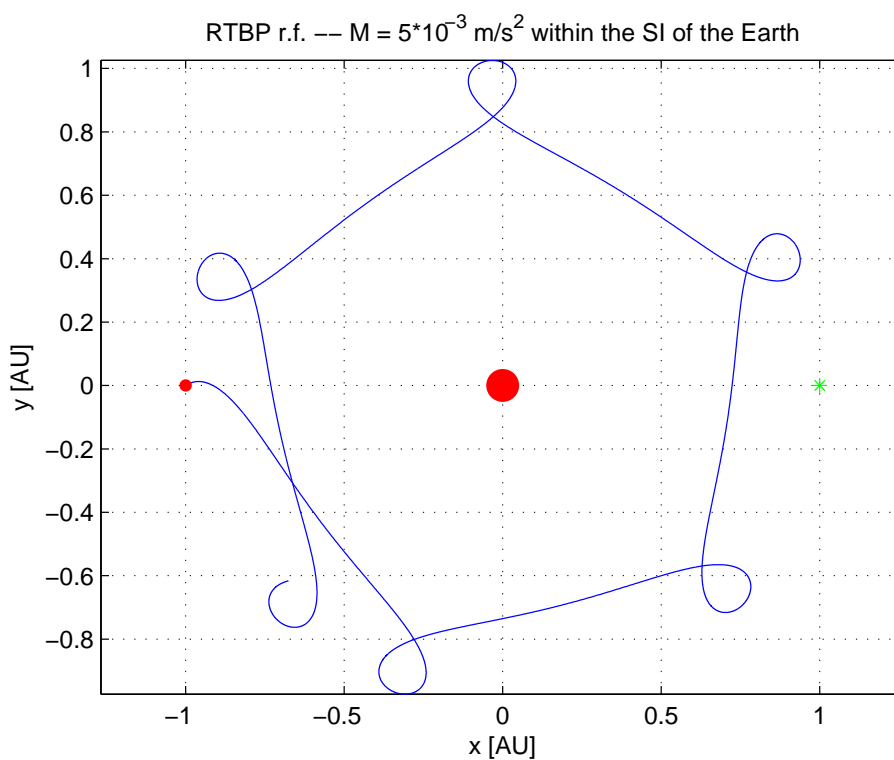


Figure 6.13 Low Thrust, preliminary investigation. $M = 5 \cdot 10^{-3} \text{ m/s}^2$, $\theta = 0$, $T_{final} = 5 \text{ y}$, Value of the Jacobi Constant (when the thrust is turned off) $C = 2.98503654$, Low Thrust ON within the SI of the Earth, RTBP reference frame

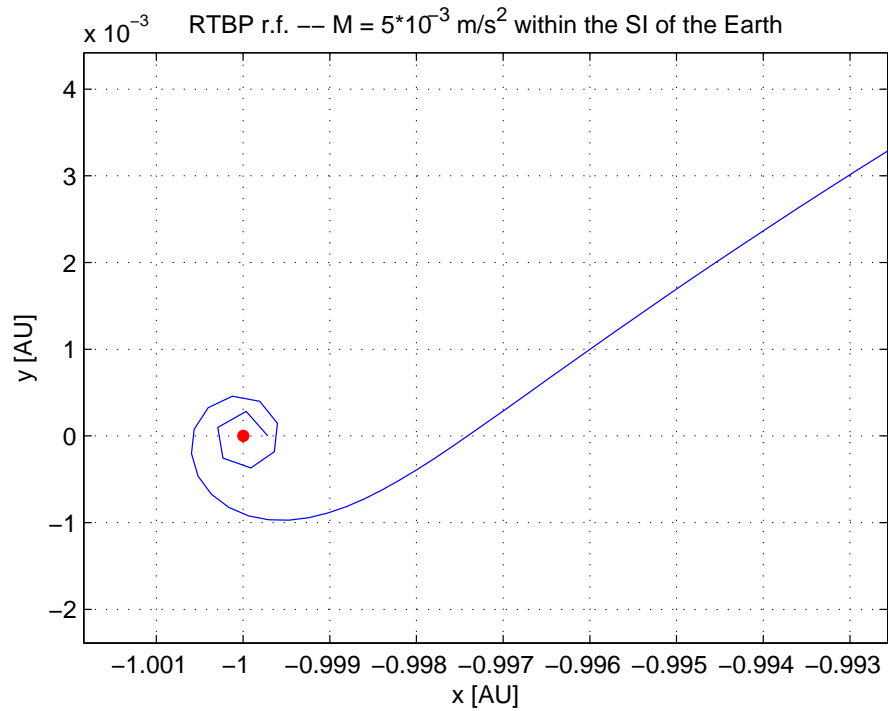


Figure 6.14 Low Thrust, preliminary investigation. Zoom: $M = 5 \times 10^{-3} \text{ m/s}^2$, $\theta = 0$, $T_{final} = 5 \text{ y}$, Value of the Jacobi Constant (when the thrust is turned off) $C = 2.98503654$, Low Thrust ON within the SI of the Earth, RTBP reference frame

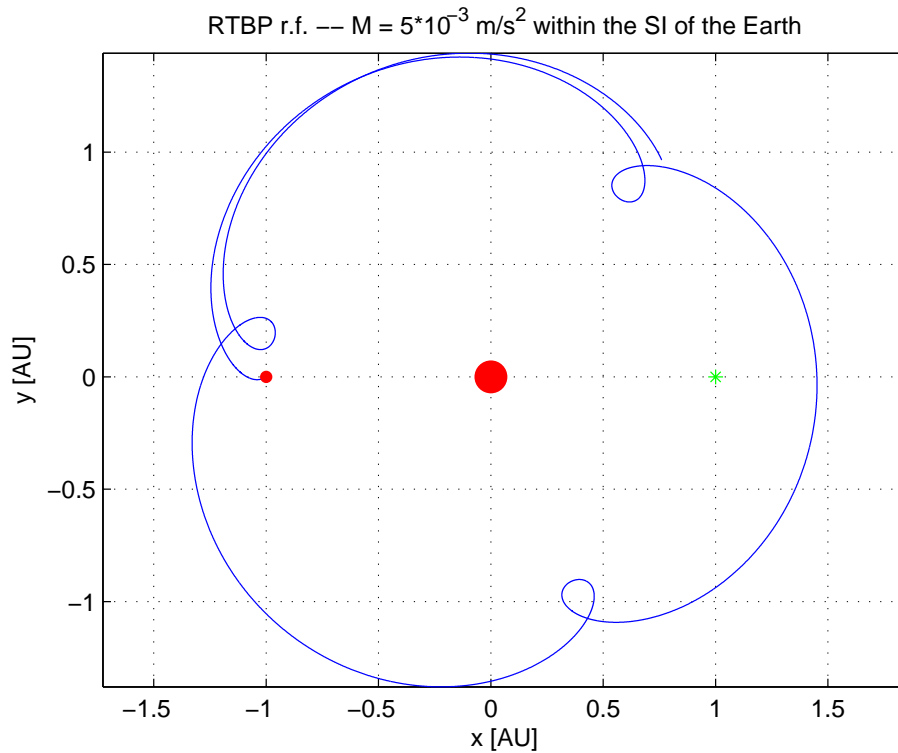


Figure 6.15 Low Thrust, preliminary investigation. $M = 5 \times 10^{-3} \text{ m/s}^2$, $\theta = \pi$, $T_{final} = 5 \text{ y}$, Value of the Jacobi Constant (when the thrust is turned off) $C = 2.98504074$, Low Thrust ON within the SI of the Earth, RTBP reference frame

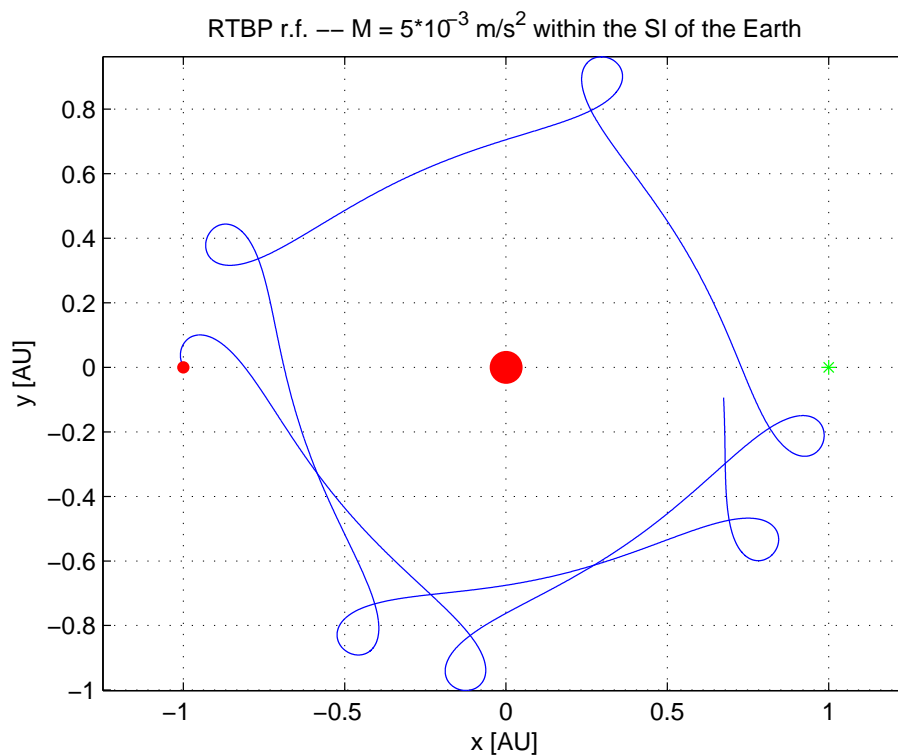


Figure 6.16 Low Thrust, preliminary investigation. $M = 5 \times 10^{-3} \text{ m/s}^2$, $\theta = \frac{\pi}{2}$, $T_{final} = 5 \text{ y}$, Value of the Jacobi Constant (when the thrust is turned off) $C = 2.98503310$, Low Thrust ON within the SI of the Earth, RTBP reference frame

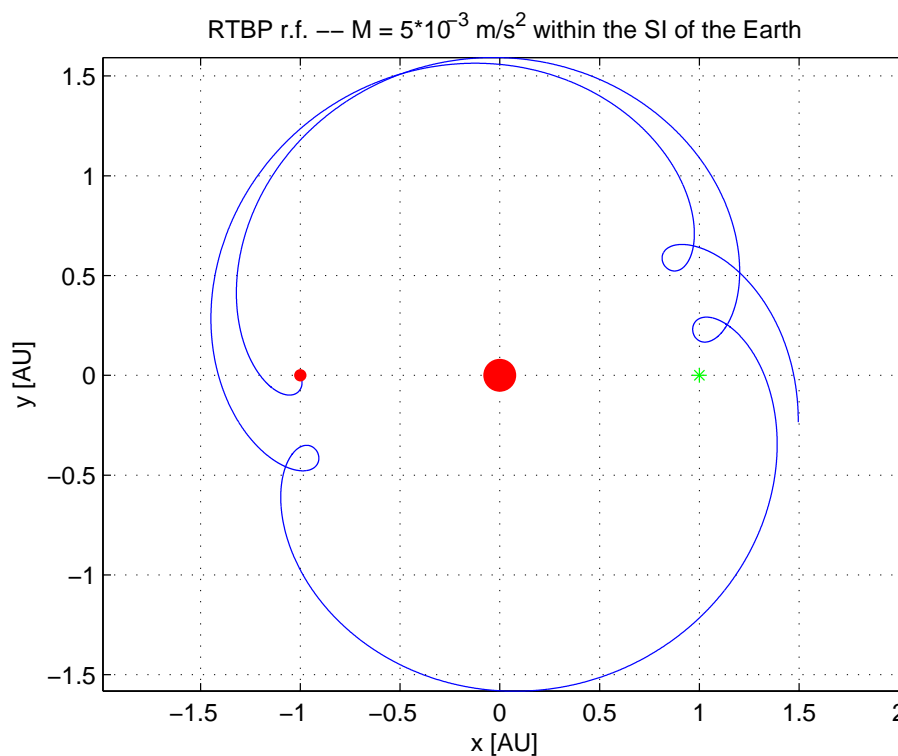


Figure 6.17 Low Thrust, preliminary investigation. $M = 5 \times 10^{-3} \text{ m/s}^2$, $\theta = \frac{3\pi}{2}$, $T_{final} = 5 \text{ y}$, Value of the Jacobi Constant (when the thrust is turned off) $C = 2.98503416$, Low Thrust ON within the SI of the Earth, RTBP reference frame

6.2 Optimal heliocentric cruise segment in 2BP

Since the preliminary study did not lead to any reasonable results, we decided to tackle the problem optimizing the transfer not in RTBP but in the 2BP. Indeed, the heliocentric cruise segment is always far from the Earth, and the optimal model in 2BP is easier and less sensitive than the RTBP.

In the 2BP, the transfer from the Earth to the Sun-Earth L_3 applying Low Thrust can be considered as a Two-Point Boundary-Value Problem (TPBVP), and we will especially refer to [Gao, 2003].

The 2BP equations have been modified including the accelerations due to the thrust:

$$\begin{aligned}\ddot{x} &= -\frac{GM_{Sun}}{\|r\|^3}x + T_x \\ \ddot{y} &= -\frac{GM_{Sun}}{\|r\|^3}y + T_y \\ \ddot{z} &= -\frac{GM_{Sun}}{\|r\|^3}z + T_z\end{aligned}\tag{6.3}$$

where

$$\begin{aligned}T_x &= \frac{T}{m}\alpha_x \\ T_y &= \frac{T}{m}\alpha_y \\ T_z &= \frac{T}{m}\alpha_z\end{aligned}\tag{6.4}$$

and

$$\dot{m} = \frac{T}{g_0 \cdot I_{sp}}\tag{6.5}$$

$$m = m_0 - \dot{m} \cdot t\tag{6.6}$$

G is the gravitational constant, M_{Sun} is the mass of the Sun, and $GM_{Sun} \approx 1.3271 * 10^{11} km^3/s^2$.

T is the force applied on the spacecraft, m the mass of the spacecraft, \dot{m} the mass flow, I_{sp} the specific impulse, g_0 the gravity acceleration at zero-altitude, $\frac{T}{m}$ the acceleration due to the thrust (equal to M when the mass flow is taken equal to zero) and α the thrust acceleration direction unit vector.

The direction of vector α will be varied by the optimizer in such a way that the target L_3 is reached minimizing the transfer time (when Equations (6.5) and (6.6) are taken into account, since the mass flow is constant, minimizing the transfer time the total propellant mass is also minimized).

As before, since we only considered planar transfers and parking orbits in the xy-plane, \ddot{z} and T_z are always equal to zero.

6.2.1 Pontryagin minimum principle

The TPBVP is based on calculus of variations, which is widely utilized to obtain optimal control of continuous-time systems. Detailed explanations can be found in [Bryson, Ho, 1969].

TPBVP results from the necessity condition that the first-order variation of performance index (involving constraints using Lagrangian multipliers) be zero. The second-order variation of performance index is typically not investigated.

TBPVP is briefly stated as follows.

The general expression of a system dynamic model can be written as:

$$\dot{X} = F(X, u, t) \quad (6.7)$$

with $t > t_0$ and t_0 fixed, where X is the system state vector, u is the system input vector and t_0 is the fixed initial time. The general performance index is defined as:

$$J = \phi[X(t_f), t_f] + \int_{t_0}^{t_f} L(X, u, t) dt \quad (6.8)$$

where t_f is the final time and $t < t_f$. Also, for many optimal control problems, there exists terminal state constraints, which are generally denoted as:

$$\psi[X(t_f), t_f] = 0 \quad (6.9)$$

The problem statement is usually composed of Equations (6.7), (6.8) and (6.9). Obtaining the optimal solution starts with the scalar Hamiltonian function, which is formed as:

$$H(X, u, t) = L(X, u, t) + \lambda^T F(X, u, t) \quad (6.10)$$

The derivative of the Hamiltonian with respect to the Lagrangian multiplier λ (costate) provides the state equations of motion.

$$\dot{X} = \frac{\partial H}{\partial \lambda} = F(X, u, t) \quad (6.11)$$

The costate equation is the derivative of the Hamiltonian with respect to the states.

$$\dot{\lambda} = -\frac{\partial H}{\partial X} = -\frac{\partial F^T}{\partial X} \lambda - \frac{\partial L}{\partial X} \quad (6.12)$$

with $t \leq t_f$. The optimality condition is computed by taking partial derivative of the Hamiltonian with respect to the control vector:

$$\frac{\partial H}{\partial u} = \frac{\partial F^T}{\partial u} \lambda + \frac{\partial L}{\partial u} = 0 \quad (6.13)$$

Boundary conditions are evaluated at both initial and final time.

$X(t_0)$ is given at the initial time, and boundary conditions at the final time are as follows:

$$\left(\frac{\partial \phi}{\partial X} + \frac{\partial \psi^T}{\partial X} \nu - \lambda \right)^T \Big|_{t_f} dX(t_f) + \left(\frac{\partial \phi}{\partial t} + \frac{\partial \psi^T}{\partial t} \nu + H \right) \Big|_{t_f} dt_f = 0 \quad (6.14)$$

Furthermore, if the control input $u(t)$ is constrained, a more general stationary condition must be added to strengthen the stationary condition given in Equation (6.13):

$$H(X^*, u^*, \lambda^*, t) \leq H(X^*, u^* + \delta u, \lambda^*, t) \quad (6.15)$$

for all admissible δu , where "*" denotes the optimal solution. This is also called Pontryagin's minimum principle.

6.2.2 Optimization model in cartesian coordinate system

The equation of motion of the spacecraft can be expressed by position and velocity vectors, which are Equations (6.3) and $\dot{r} = v$. A general performance index is given in terms of the terminal states and final time. The integral term is taken out from the general performance index because in our case only variables at the terminal time are considered. Therefore, the performance index is:

$$J = \phi[r(t_f), v(t_f), t_f] \quad (6.16)$$

According to the calculus of variations, the necessary condition of optimal control problem can be obtained from the Hamiltonian, which is formed as:

$$H = \lambda_r^T v + \lambda_v^T \left(-\frac{GM_{Sun}}{\|r\|^3} r + \frac{T}{m} \alpha \right) \quad (6.17)$$

where λ_r^T and λ_v^T are Lagrangian multipliers (costates) associated with the states r and v , respectively.

The optimal thrust vector can be obtained by setting $\frac{\partial H}{\partial \alpha}$ with the constraint $\alpha^T \alpha = 1$. A simple expression for the optimal control is as follows, which only involves the costates associated with the velocity vector:

$$\alpha^* = -\frac{\lambda_v}{\|\lambda_v\|} \quad (6.18)$$

Taking partial derivative of the Hamiltonian with respect to the states, the costate equations are:

$$\dot{\lambda}_r = -\frac{\partial H}{\partial r} = \lambda_v \frac{GM_{Sun}}{\|r\|^3} - \frac{3GM_{Sun}\lambda_v^T r}{\|r\|^5} \quad (6.19)$$

$$\dot{\lambda}_v = -\frac{\partial H}{\partial v} = \lambda_r \quad (6.20)$$

For a bounded thrust problem, Pontryagin's minimum principle states that the Hamiltonian must be minimized with respect to all admissible controls at all time. The Hamiltonian is linear in the thrust T , therefore the switching function is:

$$H_T = \frac{\partial H}{\partial T} = \lambda_v^T \frac{1}{m} \alpha^* \quad (6.21)$$

$$T = 0 \text{ if } H_T > 0$$

$$T = T_{max} \text{ if } H_T < 0$$

$$0 < T < T_{max} \text{ if } H_T = 0$$

A general expression of equality constraints is:

$$\psi[r(t_f), v(t_f)] = 0 \quad (6.22)$$

where t_f represents the final time of orbit transfer. The function $\psi(\cdot)$ denotes the terminal constraints. The transversality conditions for the costates are:

$$\lambda_r(t_f) = \left. \frac{\partial \phi}{\partial r} \right|_{t=t_f} + \nu_r^T \left. \frac{\partial \psi}{\partial r} \right|_{t=t_f} \quad (6.23)$$

$$\lambda_v(t_f) = \left. \frac{\partial \phi}{\partial v} \right|_{t=t_f} + \nu_v^T \left. \frac{\partial \psi}{\partial v} \right|_{t=t_f} \quad (6.24)$$

For the free-transfer time, the variable-time condition exists:

$$\left[\frac{\partial \phi}{\partial t} + \left(\frac{\partial \psi^T}{\partial t} \right) \nu + H \right]_{t=t_f} = 0 \quad (6.25)$$

where $\nu = [\nu_r, \nu_v]^T$.

Equation (6.18) is the control steering which is governed by the costate dynamic Equations (6.19) and (6.20). Equation (6.22) represents constraints for the mission, which must be satisfied for any feasible solution. Equations (6.23), (6.24) and (6.25) are the necessary conditions for optimal control theory.

6.2.3 Indirect Method

By using the Pontryagin minimum principle, the optimal control problem can be transformed into a TPBVP, which consists in the dynamical equations, conjugate equations, initial states, final states and transversality conditions shown in the previous section. In the TPBVP, the number of equations and the number of boundary conditions are the same. If the solution of the TPBVP (initial states and initial conjugate states) is found, it is possible to propagate forward and obtain the history of the states and the conjugate states. Then, with the control equation, the history of the optimal control can be computed.

Unfortunately, finding an effective computing method to solve directly the TPBVP transformed from the optimal control problem is very hard. Shooting method and parallel shooting method are the common methods, which are always used to solve the TPBVP. However, the convergence of these methods depends on the initial guesses. Without a good initial guess the iteration can not converge at all. In our problem the initial guesses of the conjugate states do not have any physical meaning, and giving a good initial guesses of them is quite difficult.

An indirect (hybrid) method is used. The basic idea of the indirect (hybrid) method is to increase the degree of freedom of the system. Some of the boundary conditions are ignored, such as the final value of the Hamiltonian and the transversality conditions. Now the system has many solutions, and we do not know which is the optimal. The parameter optimization method has to be used to find the optimal solution.

For our problem, the transversality conditions (6.23) and (6.24), the final

value of the Hamiltonian (6.25) are ignored. The parameter optimization problem can be described as:

Optimization parameters: $z = [\lambda_r(t_0), \lambda_v(t_0), t_f]$

Constraints: $\psi[r(t_f), v(t_f)] = 0$

Performance index: $J = \phi[r(t_f), v(t_f), t_f] = t_f$

This is a nonlinear constrained optimization. We need to minimize the performance index subject to the constraints, and some of the optimization parameters are bounded variables. These parameters only could be adjusted between their lower and upper bounds.

The sequential quadratic programming algorithm (SQP) is an effective method to solve this kind of problem. The SNOPT (that has SQP inside) is widely used in trajectory optimization and other areas [*Gill et al., 2002*].

6.3 Numerical results: 2BP and constant acceleration

Here the results of the optimization in the 2BP are given, considering constant accelerations ($\frac{T}{m} = M$ and thus not taking into account Equations (6.5) and (6.6)). We have taken L_1 or L_2 of the Sun-Earth system as initial states, since these two libration points define the limit of the SI of the Earth, which is at $t = 0$ at coordinates $(-1, 0)$. The Sun is at $(0, 0)$ and remains still, while the Earth moves about it, and thus the target, L_3 . The transfer trajectory of the s/c is drawn in blue, and the instant direction of the thrust is also given.

Two angles have been defined, and their evolution is given in the plots.

One angle is counted anticlockwise from the thrust vector to the velocity vector (of the s/c). The other angle is counted anticlockwise from the thrust vector to the vector perpendicular to the one that defines the position of the spacecraft respect to the Sun. The cross-product of the position vector and the perpendicular to the position gives a vector with the same direction and sense of the z-axis of the RTBP reference frame.

Table (6.1) gives an overview of the plots given below. The target L_3 is always reached, and in all the simulations the transfer time is always reasonable.

Initial state	M [m/s^2]	Transfer time
L_1	$5 * 10^{-4}$	1 y 9 d
L_2	$5 * 10^{-4}$	1 y 40 d
L_1	$1 * 10^{-3}$	269 d
L_2	$1 * 10^{-3}$	282 d
L_1	$5 * 10^{-3}$	143 d
L_2	$5 * 10^{-3}$	146 d

Table 6.1 Transfer with Low Thrust: results of the optimization in 2BP, constant acceleration

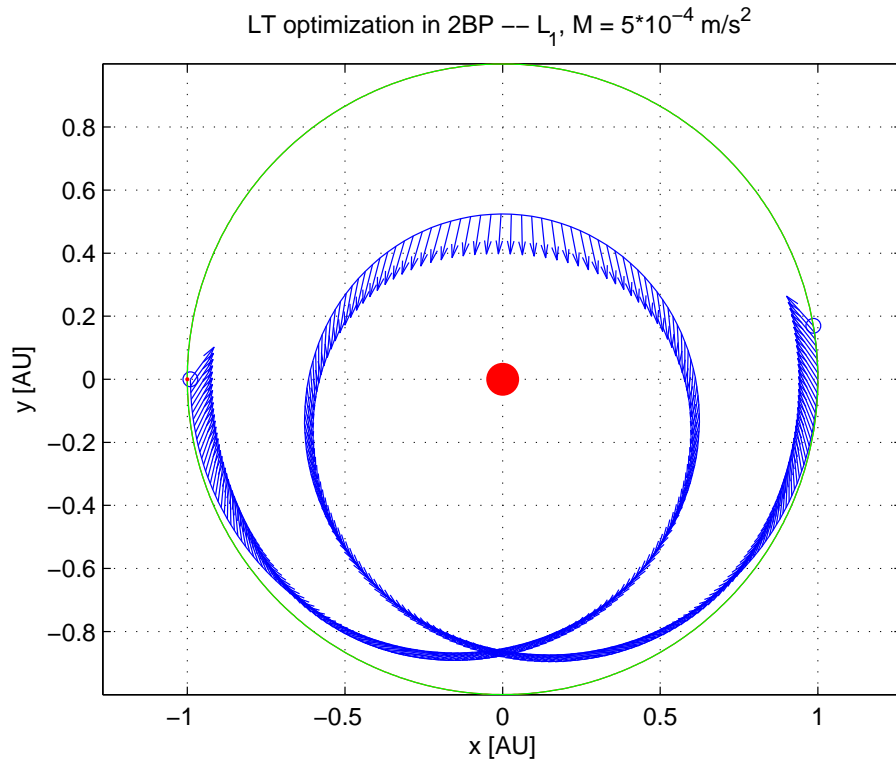


Figure 6.18 Optimization in 2BP, Trajectory: $L_1, M = 5 \cdot 10^{-4} \text{ m/s}^2, T_{final} = 1 \text{ y } 9 \text{ d}$

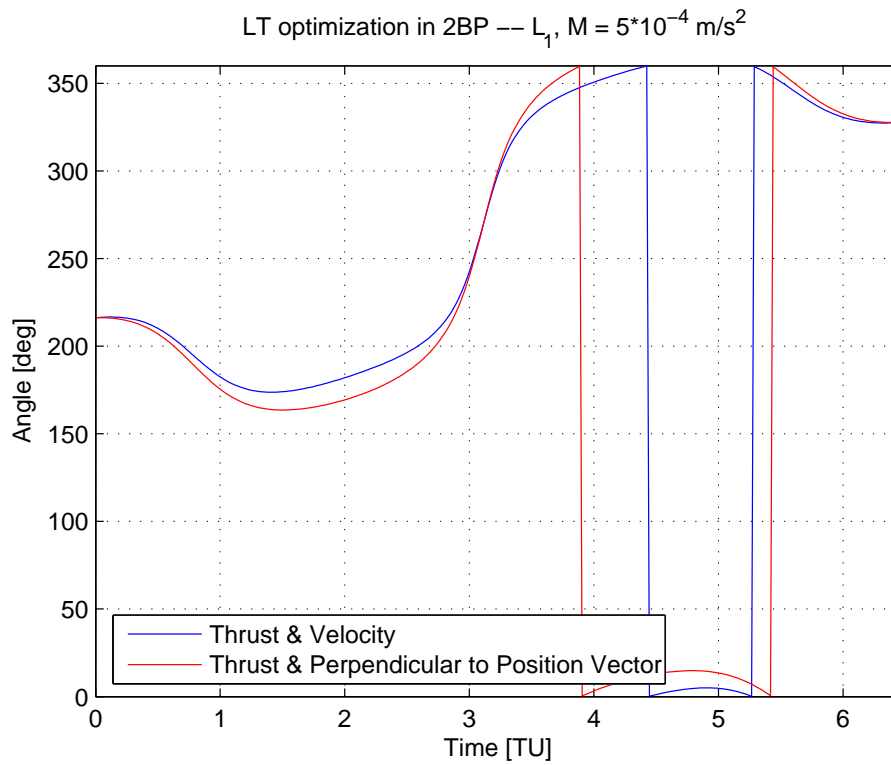


Figure 6.19 Optimization in 2BP, Angle: $L_1, M = 5 \cdot 10^{-4} \text{ m/s}^2, T_{final} = 1 \text{ y } 9 \text{ d}$

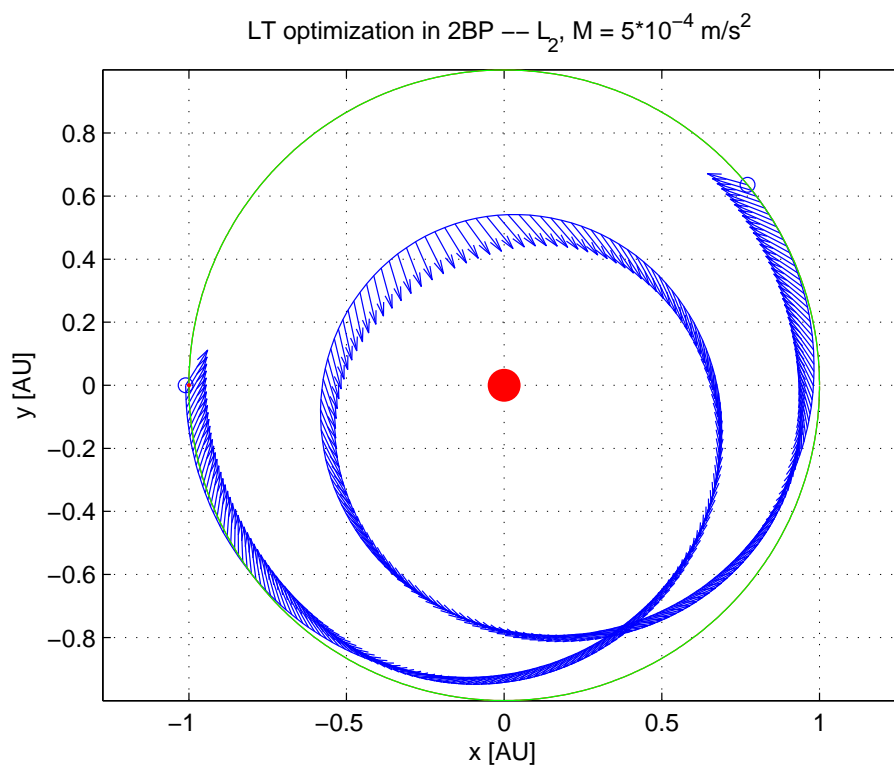


Figure 6.20 Optimization in 2BP, Trajectory: L_2 , $M = 5 \cdot 10^{-4} \text{ m/s}^2$, $T_{final} = 1 \text{ y } 40 \text{ d}$

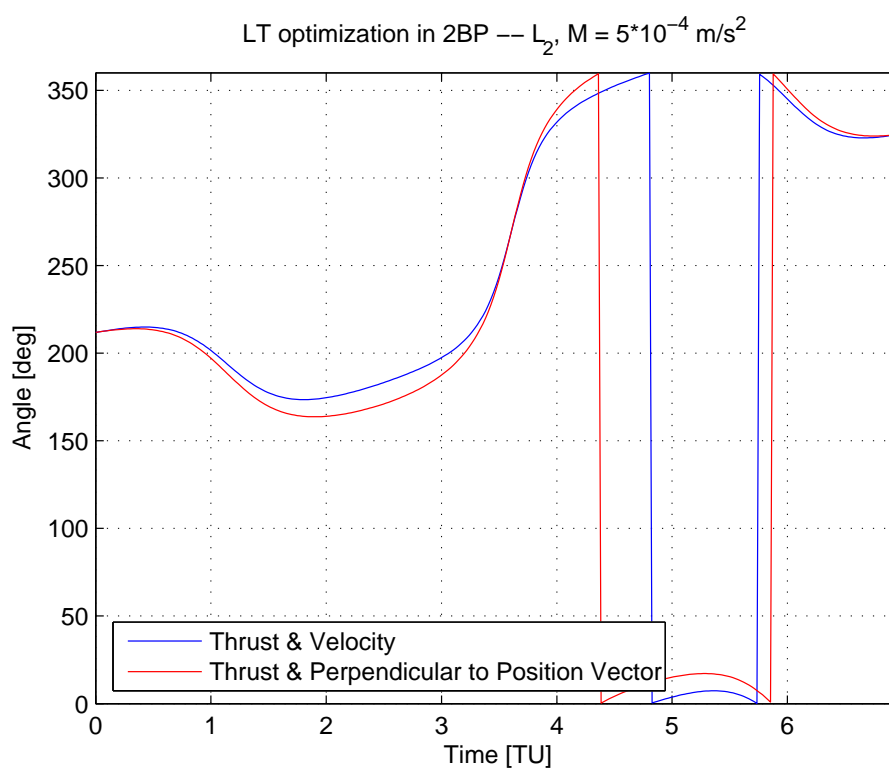


Figure 6.21 Optimization in 2BP, Angle: L_2 , $M = 5 \cdot 10^{-4} \text{ m/s}^2$, $T_{final} = 1 \text{ y } 40 \text{ d}$

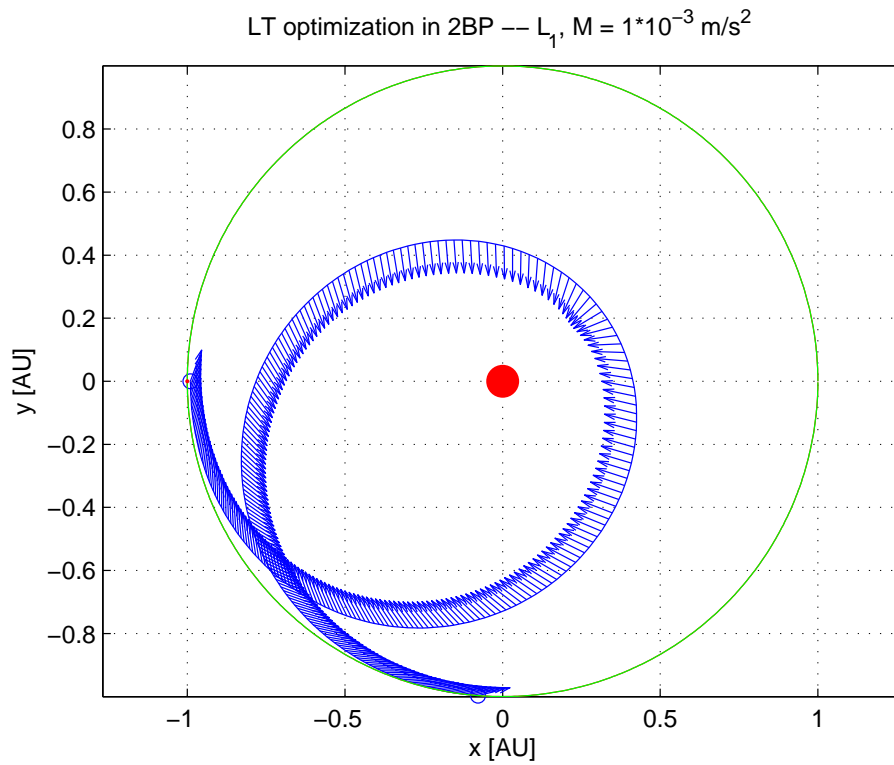


Figure 6.22 Optimization in 2BP, Trajectory: L_1 , $M = 1 \cdot 10^{-3} \text{ m/s}^2$, $T_{final} = 269 \text{ d}$

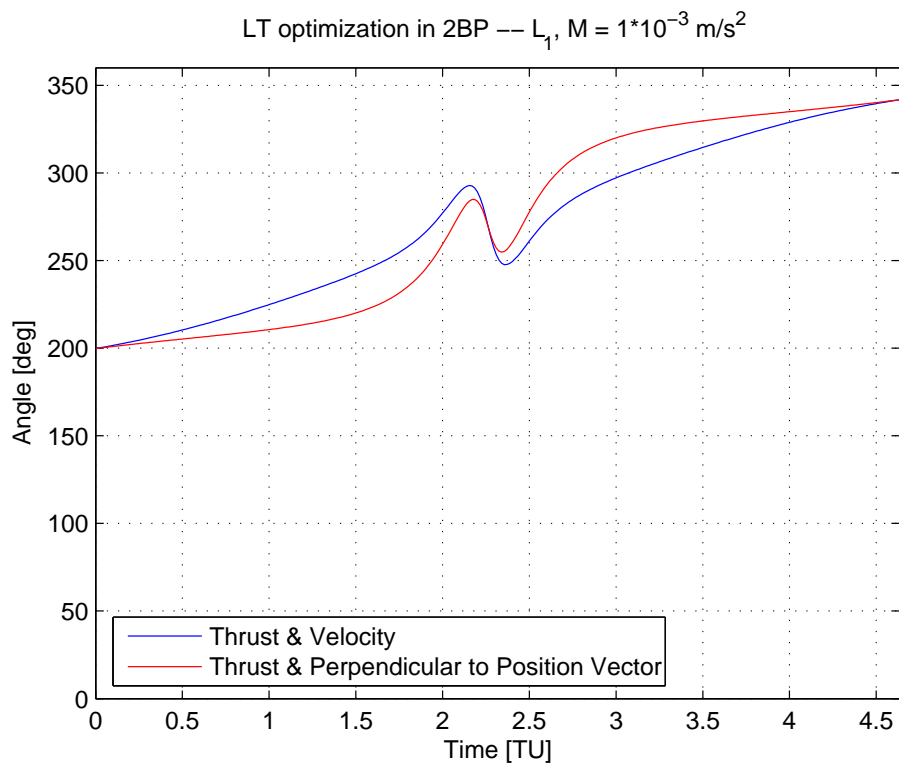


Figure 6.23 Optimization in 2BP, Angle: L_1 , $M = 1 \cdot 10^{-3} \text{ m/s}^2$, $T_{final} = 269 \text{ d}$

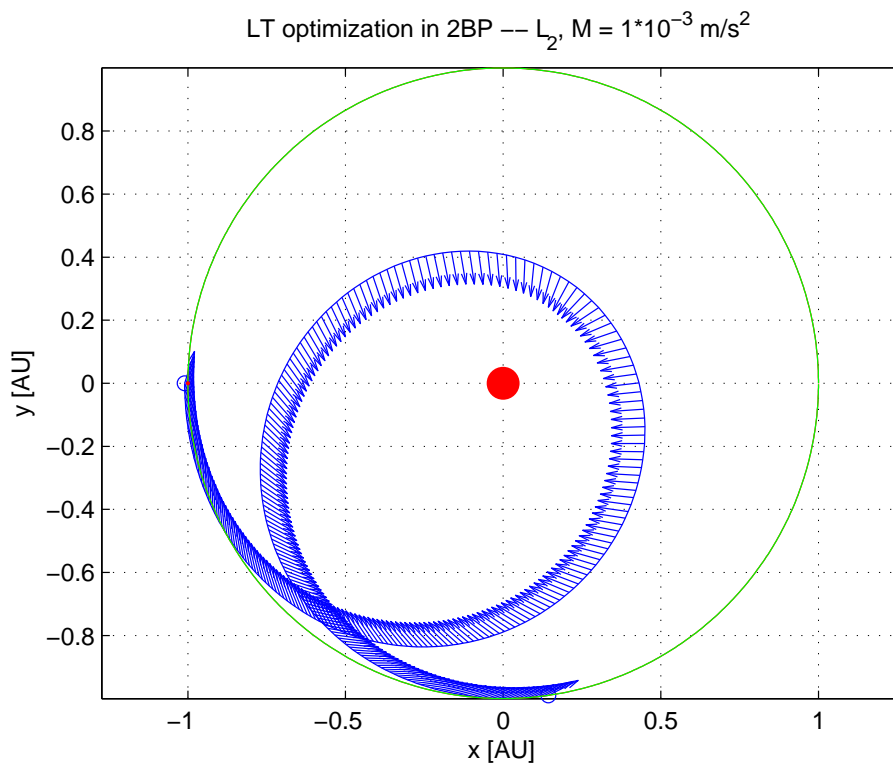


Figure 6.24 Optimization in 2BP, Trajectory: L_2 , $M = 1 \cdot 10^{-3} \text{ m/s}^2$, $T_{final} = 282 \text{ d}$

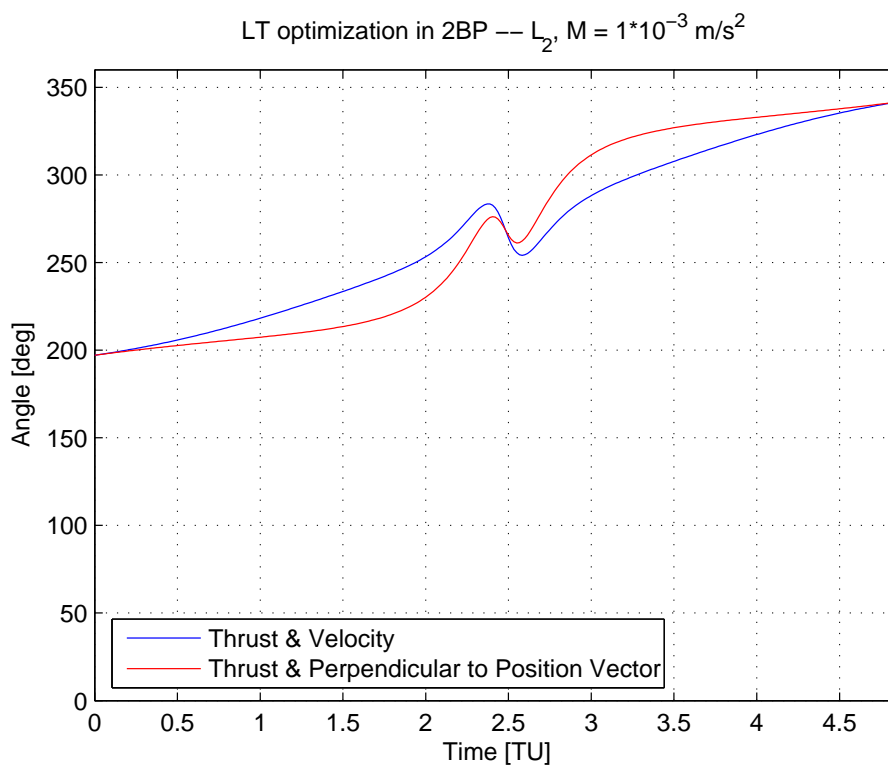


Figure 6.25 Optimization in 2BP, Angle: L_2 , $M = 1 \cdot 10^{-3} \text{ m/s}^2$, $T_{final} = 282 \text{ d}$

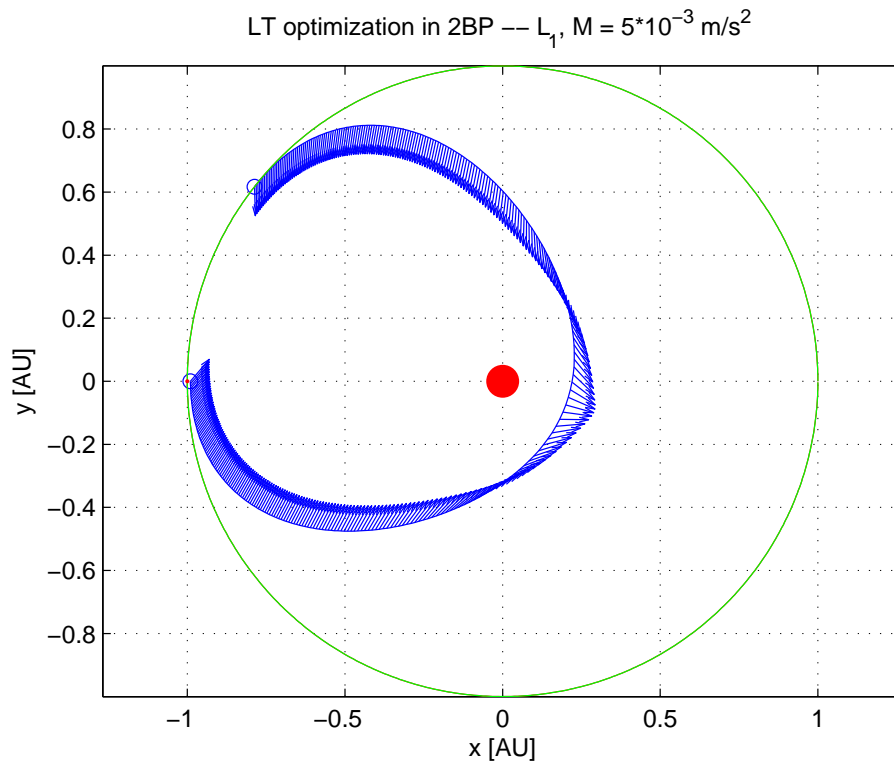


Figure 6.26 Optimization in 2BP, Trajectory: L_1 , $M = 5 \cdot 10^{-3} \text{ m/s}^2$, $T_{final} = 143 \text{ d}$

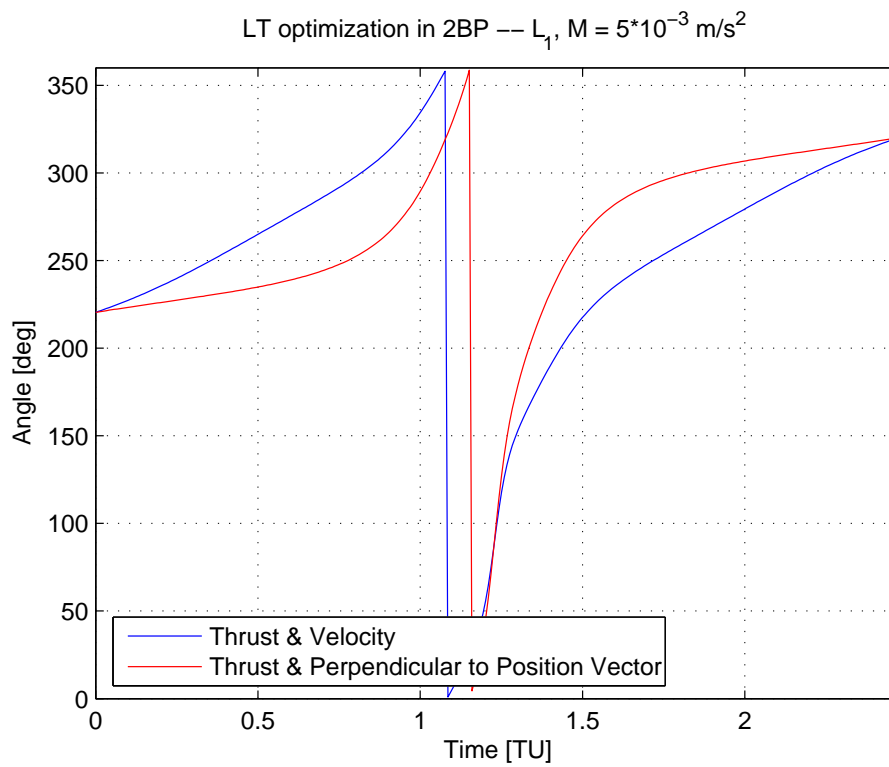


Figure 6.27 Optimization in 2BP, Angle: L_1 , $M = 5 \cdot 10^{-3} \text{ m/s}^2$, $T_{final} = 143 \text{ d}$

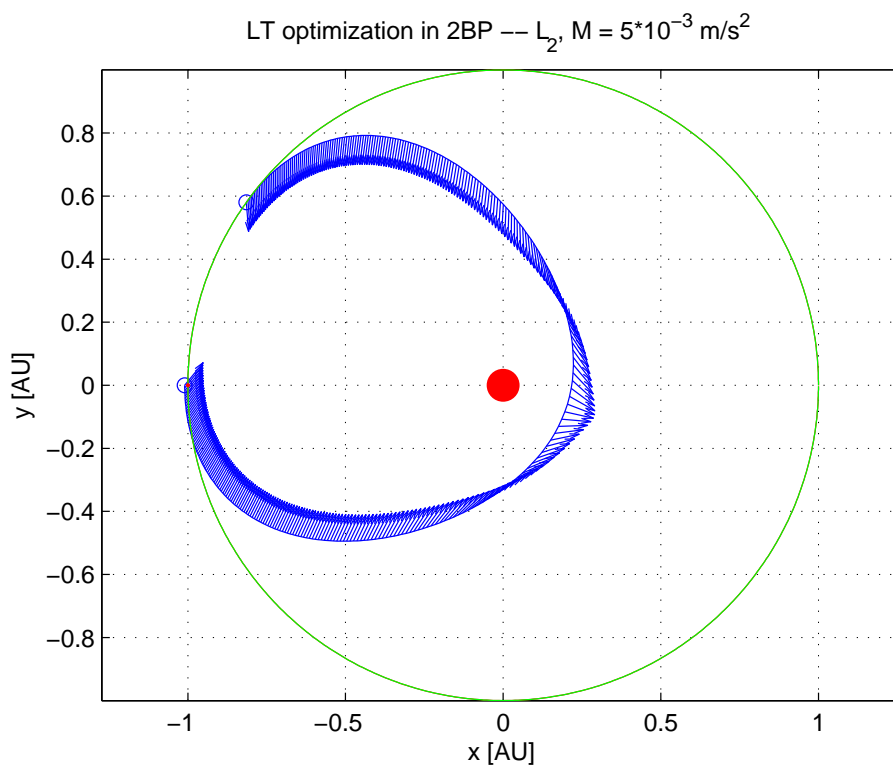


Figure 6.28 Optimization in 2BP, Trajectory: L_2 , $M = 5 \cdot 10^{-3} \text{ m/s}^2$, $T_{final} = 146 \text{ d}$

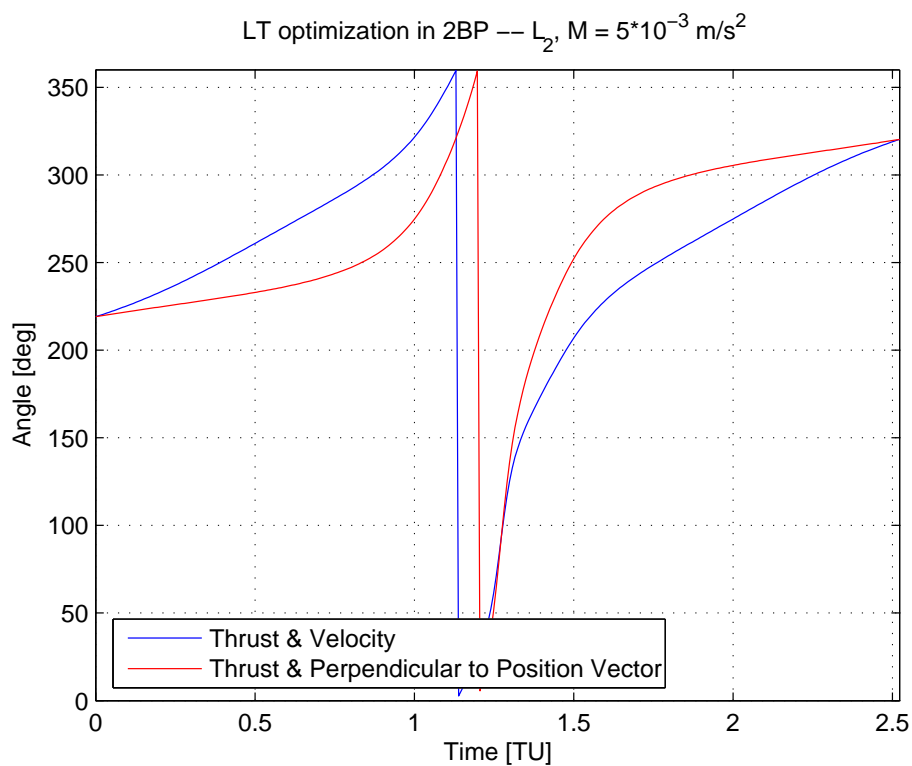


Figure 6.29 Optimization in 2BP, Angle: L_2 , $M = 5 \cdot 10^{-3} \text{ m/s}^2$, $T_{final} = 146 \text{ d}$

6.4 From the optimization in 2BP to RTBP

In this section the transfer trajectories propagated in RTBP are given, using the optimal control history obtained from the 2BP.

The results show that, for the values of constant acceleration M that we have taken, the optimal trajectories in 2BP and RTBP are (almost) the same.

Indeed, in the following plots the s/c always reaches the target L_3 (which has x-coordinate 1.00000126684308 AU in the RTBP reference frame, as shown in Section 3.5).

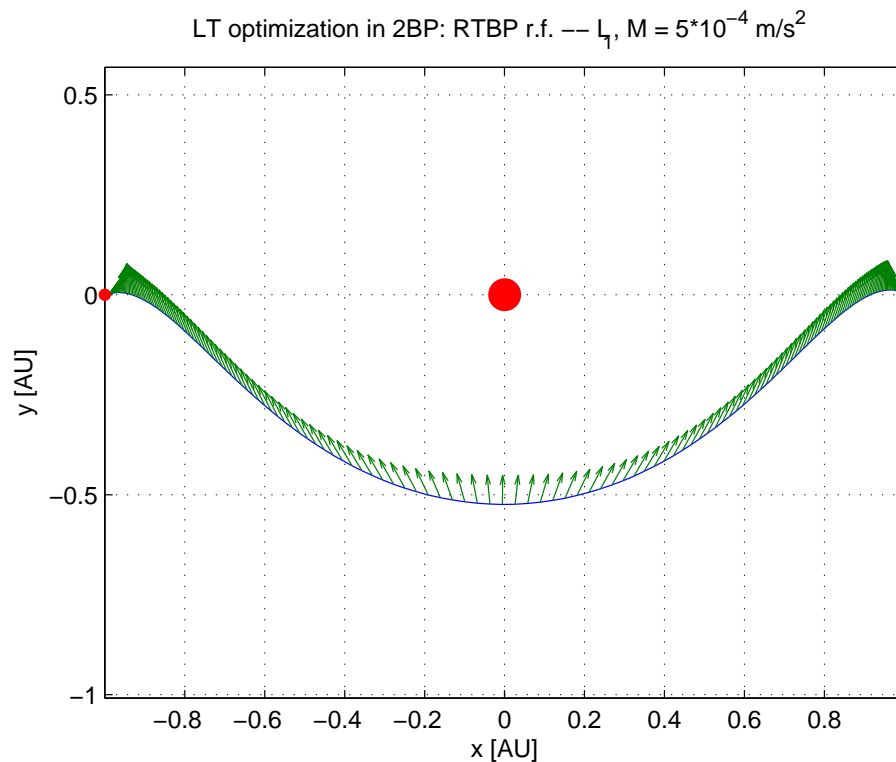


Figure 6.30 Integrating in RTBP the optimized results in 2BP, Trajectory: L_1 , integration in RTBP $M = 5 \cdot 10^{-4} \text{ m/s}^2$, $T_{final} = 1 \text{ y } 9 \text{ d}$

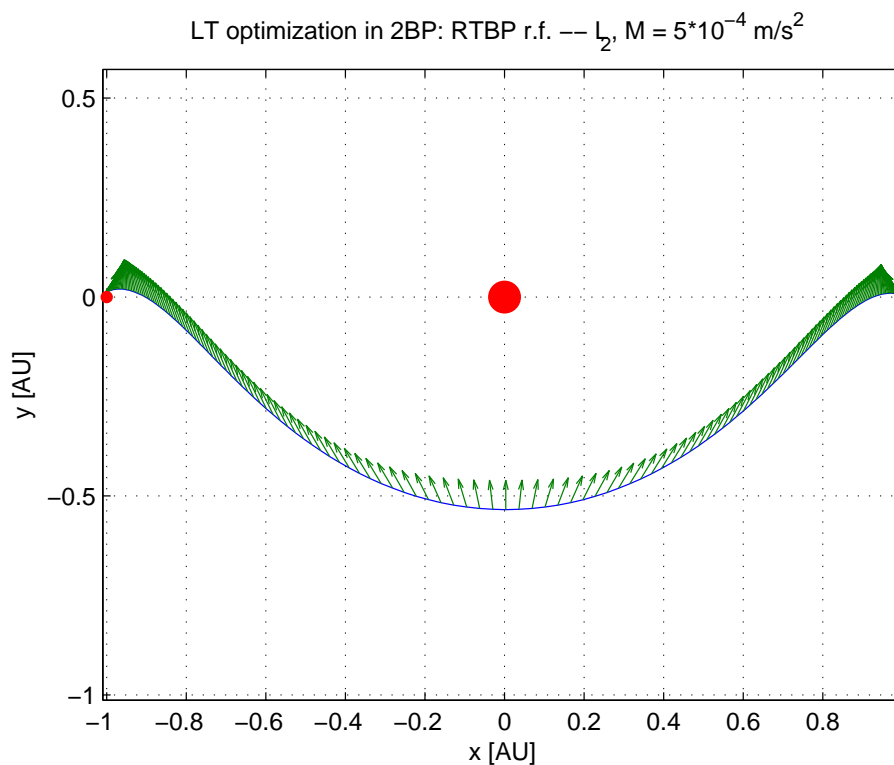


Figure 6.31 Integrating in RTBP the optimized results in 2BP, Trajectory: L_2 , integration in RTBP $M = 5 \cdot 10^{-4} \text{ m/s}^2$, $T_{final} = 1 \text{ y } 40 \text{ d}$

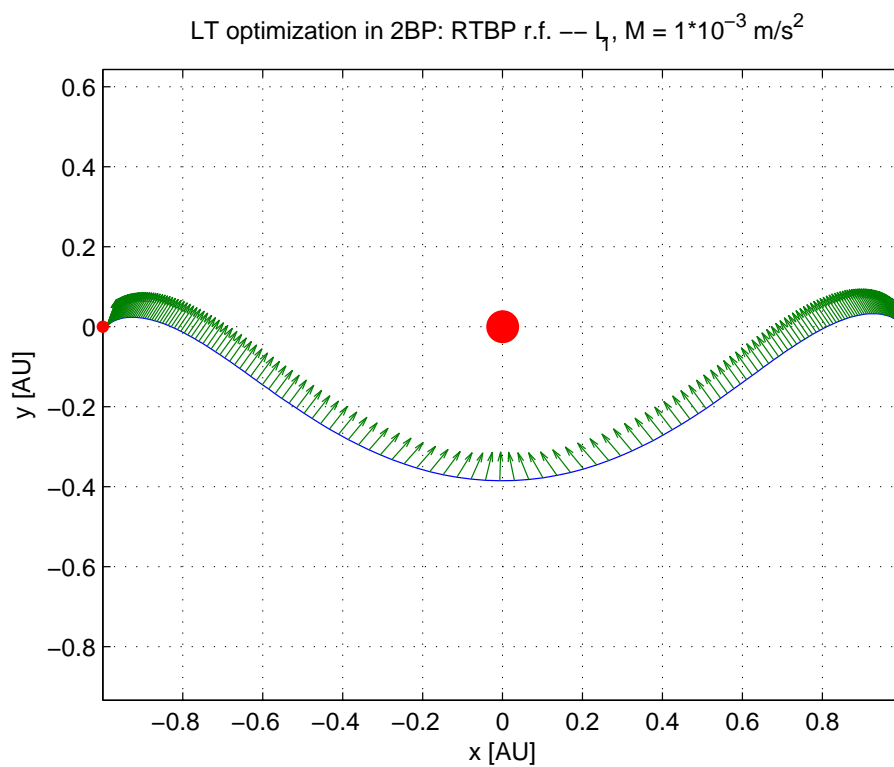


Figure 6.32 Integrating in RTBP the optimized results in 2BP, Trajectory: L_1 , integration in RTBP $M = 1 \cdot 10^{-3} \text{ m/s}^2$, $T_{final} = 269 \text{ d}$

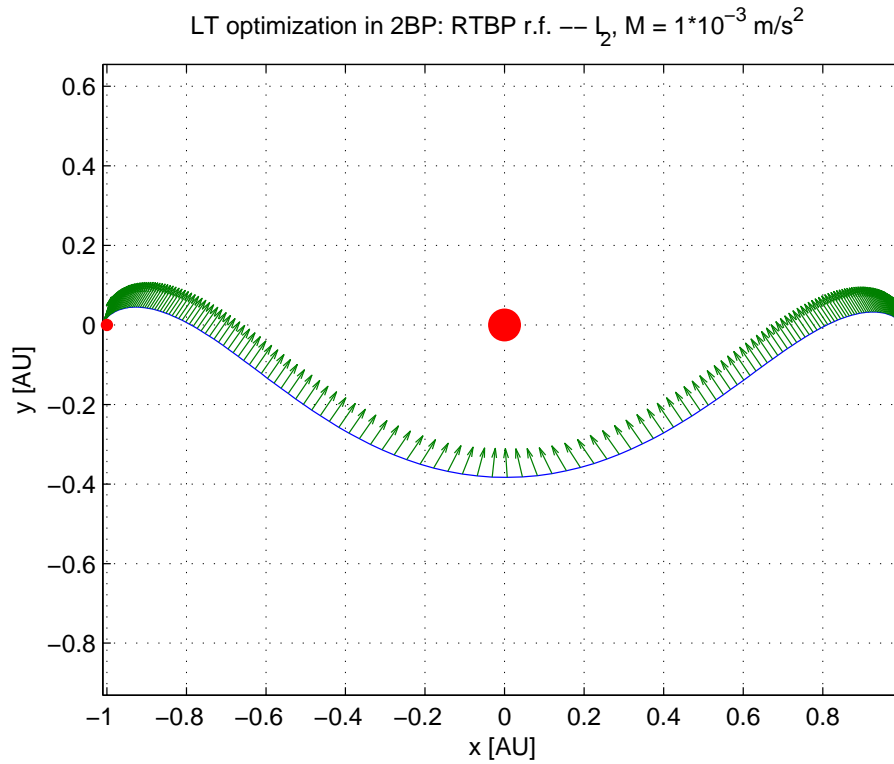


Figure 6.33 Integrating in RTBP the optimized results in 2BP, Trajectory: L_2 , integration in RTBP $M = 1 \cdot 10^{-3} \text{ m/s}^2$, $T_{final} = 282 \text{ d}$

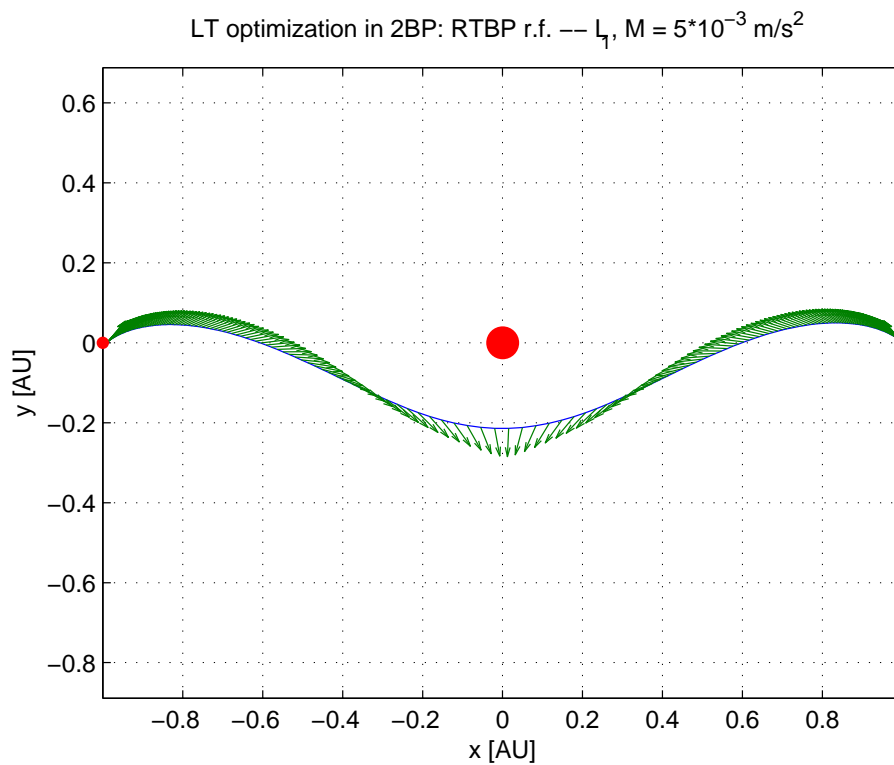


Figure 6.34 Integrating in RTBP the optimized results in 2BP, Trajectory: L_1 , integration in RTBP $M = 5 \cdot 10^{-3} \text{ m/s}^2$, $T_{final} = 143 \text{ d}$

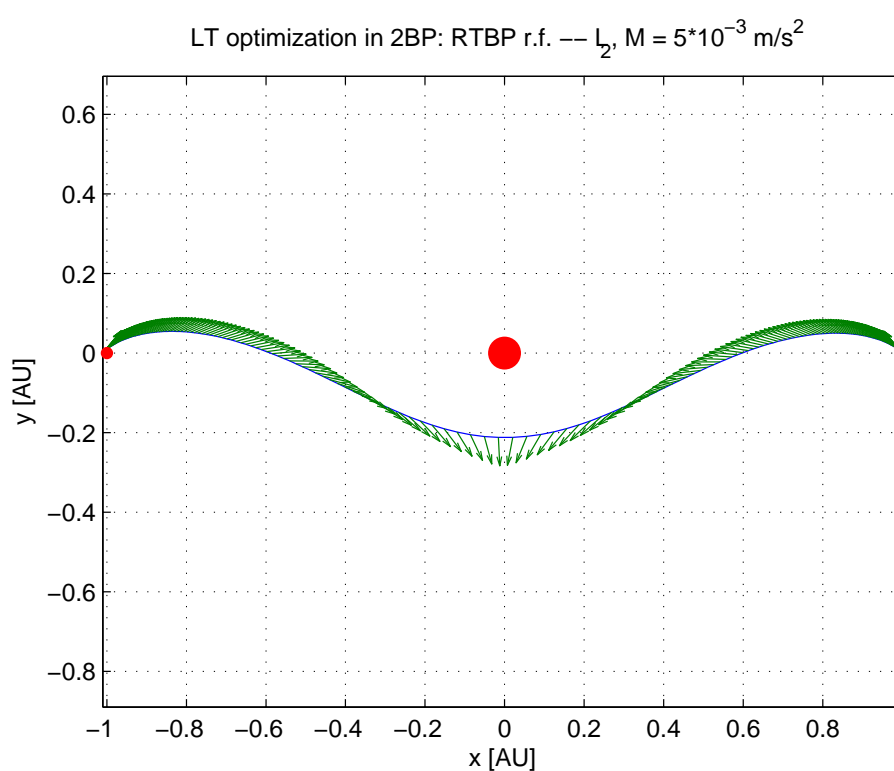


Figure 6.35 Integrating in RTBP the optimized results in 2BP, Trajectory: L_2 , integration in RTBP $M = 5 \cdot 10^{-3} \text{ m/s}^2$, $T_{final} = 146 \text{ d}$

6.5 Optimization in 2BP and integration in RTBP, taking into account the mass flow

So far the acceleration due to the thrust has always been considered constant in magnitude. However, this is not true, since the thrust is due to the mass consumed by the propulsion system.

Therefore, we decided to refine our model taking into account also Equations (6.5) and (6.6): this means that the acceleration varies with time, and in particular varies linearly with it.

For our simulations we chose the same values of thrust and I_{sp} provided by the Ion Propulsion engine on the Dawn spacecraft flown by NASA [Rayman, 2006]: $T = 90 \text{ mN}$ and $I_{sp} = 3100 \text{ s}$.

$m_0 = 500 \text{ kg}$ is the mass of the s/c at $t = 0$, being this value consistent with the arguments in the science section (small-medium weight spacecraft, part of a constellation).

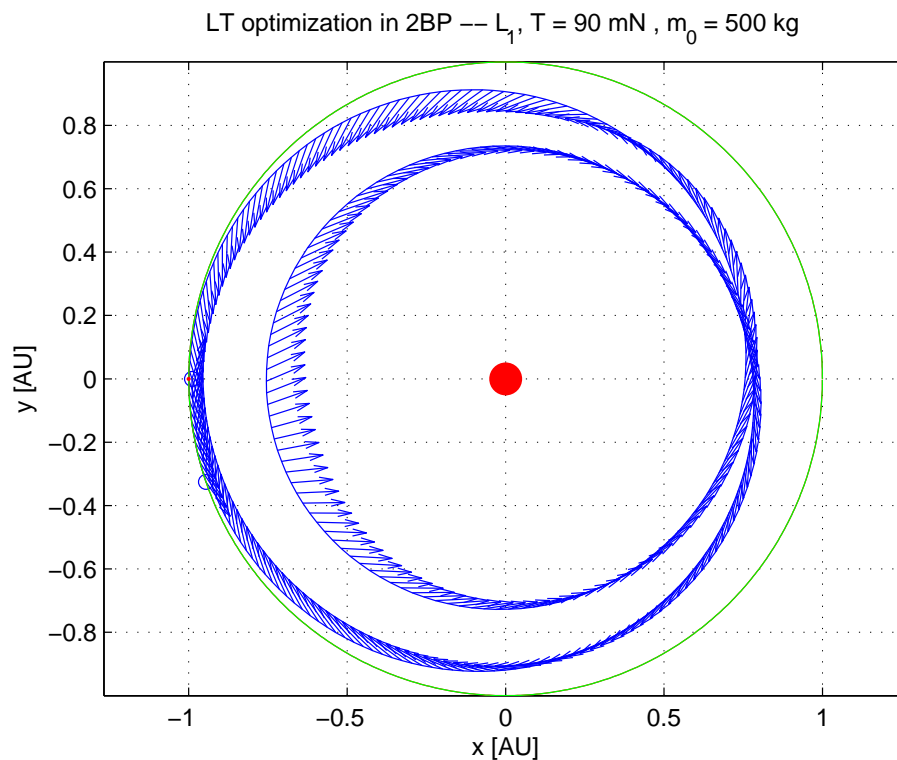


Figure 6.36 Optimization in 2BP, Trajectory: L_1 , $T = 90 \text{ mN}$, $I_{sp} = 3100 \text{ s}$, $m_0 = 500 \text{ kg}$, $m_{final} = 355 \text{ kg}$, $T_{final} = 1 \text{ y } 201 \text{ d}$

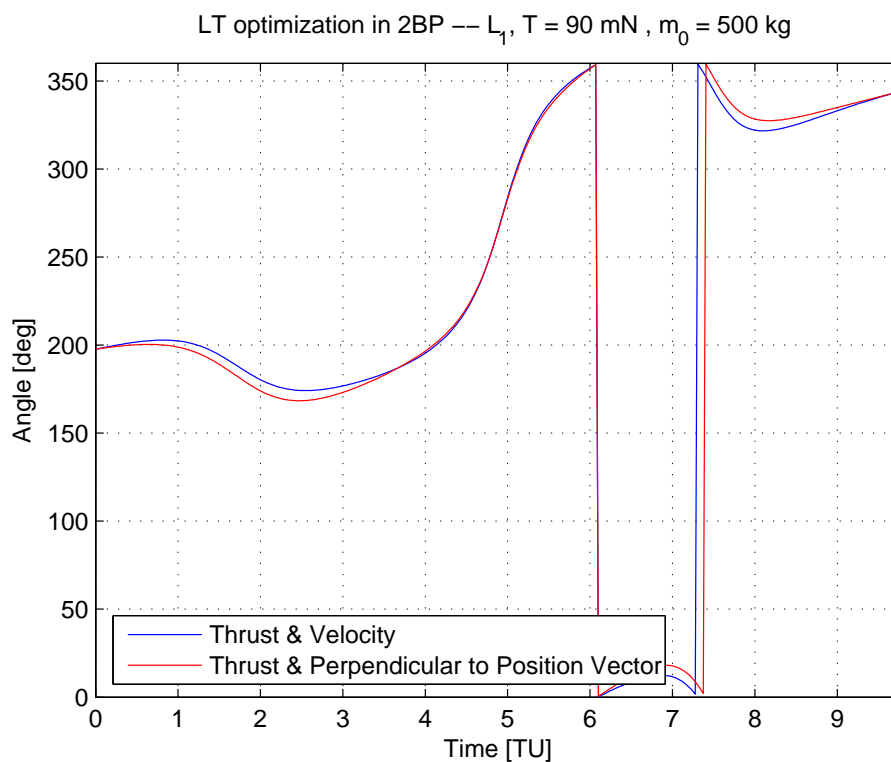


Figure 6.37 Optimization in 2BP, Angle: L_1 , $T = 90 \text{ mN}$, $I_{sp} = 3100 \text{ s}$, $m_0 = 500 \text{ kg}$, $m_{final} = 355 \text{ kg}$, $T_{final} = 1 \text{ y } 201 \text{ d}$

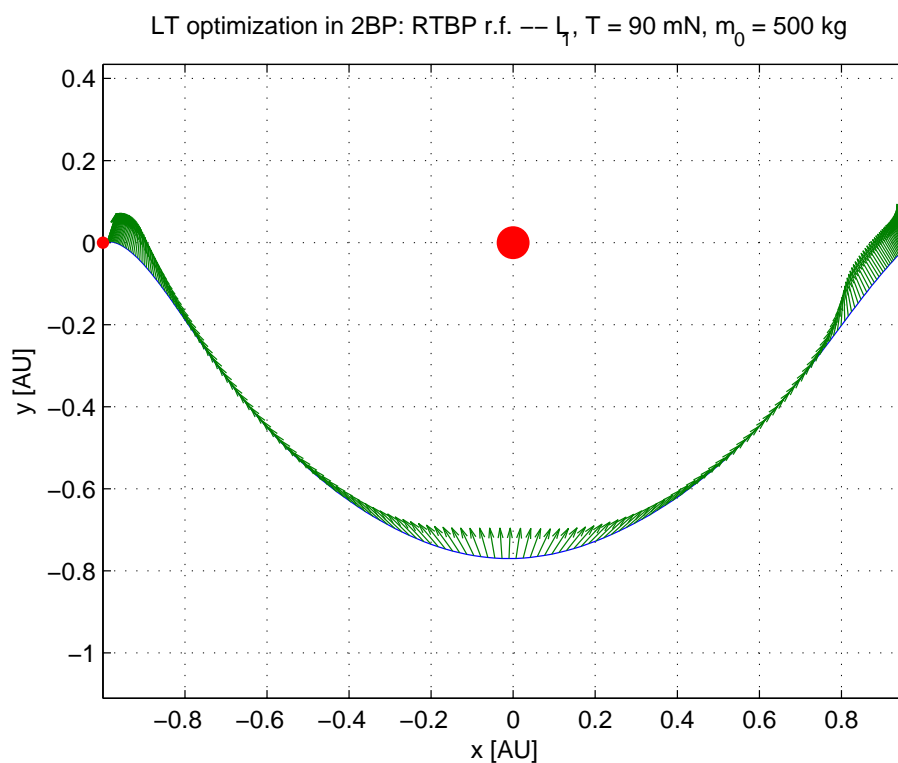


Figure 6.38 Integrating in RTBP the optimized results in 2BP, Trajectory: L_1 , integration in RTBP $T = 90 \text{ mN}$, $I_{sp} = 3100 \text{ s}$, $m_0 = 500 \text{ kg}$, $m_{final} = 355 \text{ kg}$, $T_{final} = 1 \text{ y } 201 \text{ d}$

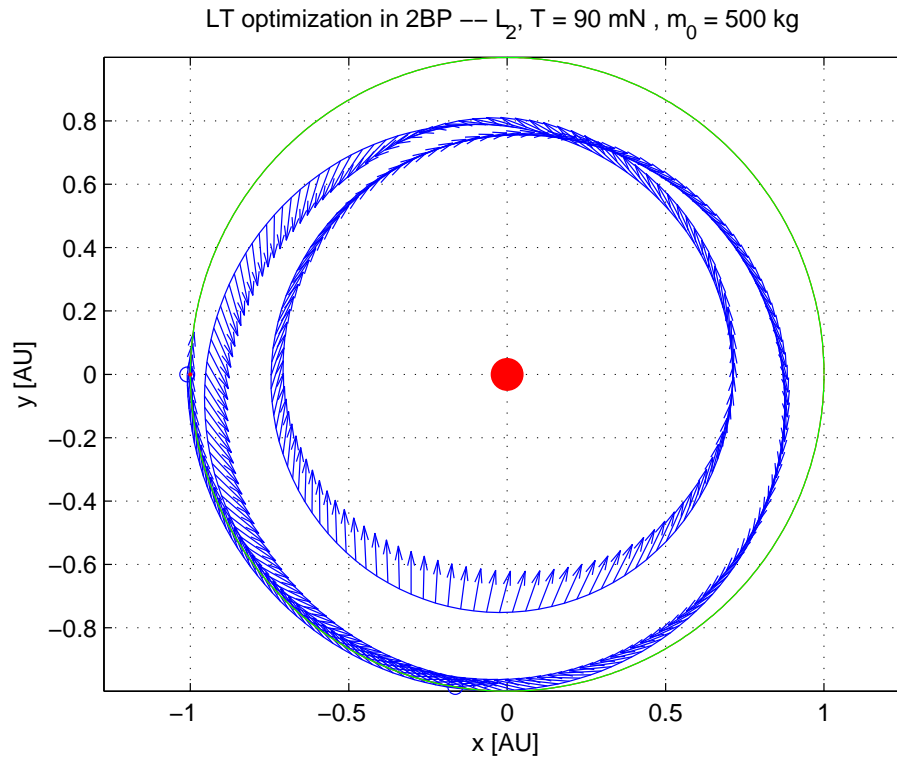


Figure 6.39 Optimization in 2BP, Trajectory: L_2 , $T = 90 \text{ mN}$, $I_{sp} = 3100 \text{ s}$, $m_0 = 500 \text{ kg}$, $m_{final} = 339 \text{ kg}$, $T_{final} = 1 \text{ y } 264 \text{ d}$

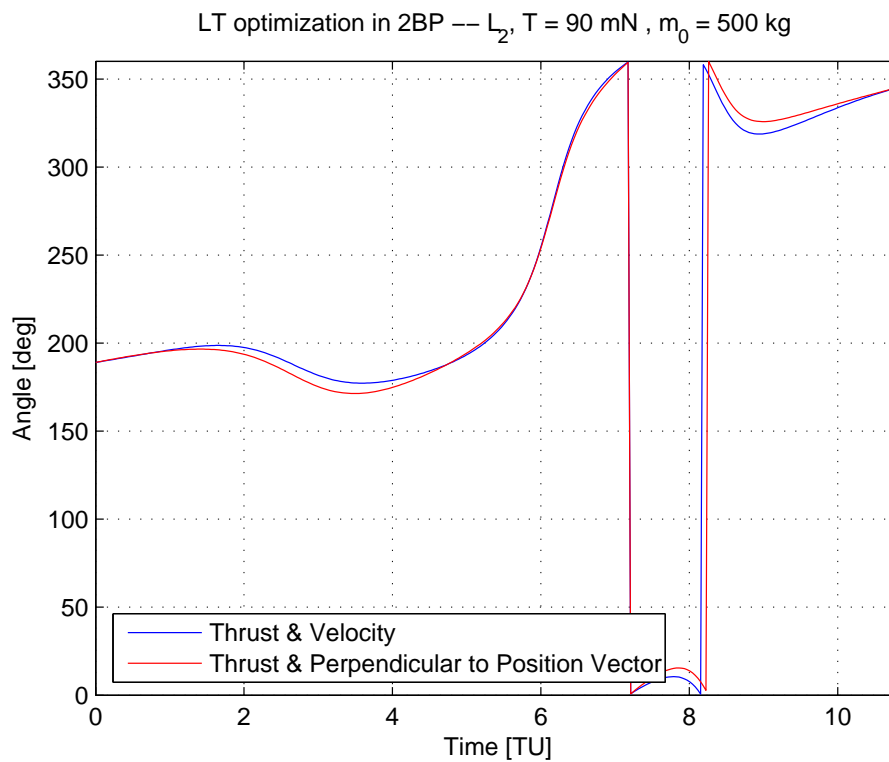


Figure 6.40 Optimization in 2BP, Angle: L_2 , $T = 90 \text{ mN}$, $I_{sp} = 3100 \text{ s}$, $m_0 = 500 \text{ kg}$, $m_{final} = 339 \text{ kg}$, $T_{final} = 1 \text{ y } 264 \text{ d}$

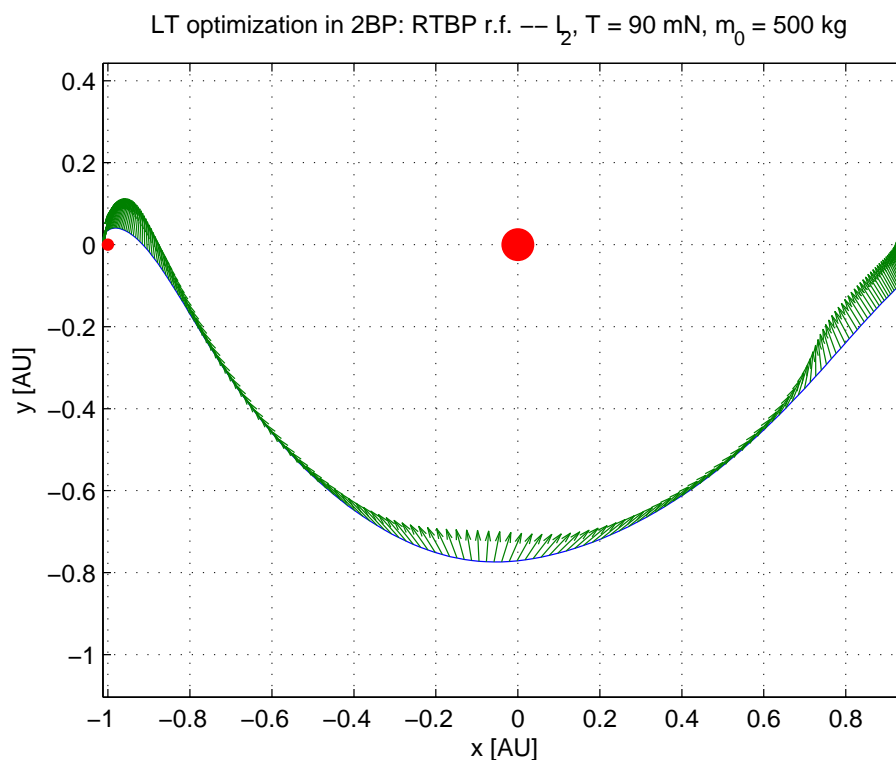


Figure 6.41 Integrating in RTBP the optimized results in 2BP, Trajectory: L_2 , integration in RTBP
 $T = 90 \text{ mN}$, $I_{sp} = 3100 \text{ s}$, $m_0 = 500 \text{ kg}$, $m_{final} = 339 \text{ kg}$, $T_{final} = 1 \text{ y } 264 \text{ d}$

Analysing the results, the mass consumption $(m_0 - m_{final})/m_0$ has the low value of 29 % (leaving from L_1) and 32 % (leaving from L_2), being the transfer time equal to 1 year and 201 days (L_1) and 1 year and 264 days (L_2).

However, in this case the optimization in 2BP is not precise enough to make the s/c reach the target L_3 in RTBP. This is due to the fact that the values of the varying acceleration are too low: even if the s/c is out of the SI of the Earth, the gravity field of the planet plays a role that should be taken into account.

Gravity Assisted Transfers

In this chapter a fourth (and last) strategy to reach the libration point L_3 of the Sun-Earth system will be explored, and in particular we will focus on Gravity Assisted Transfers.

We will first introduce the problem and explain the assumptions made, then give the equations for the unpowered and powered swing-by [*Broucke, 1988*] and conclude showing the results.

A priori, if we consider a single Gravity Assist (GA) with a planet that is not the Earth, we could already state that for this kind of transfer (leaving at 1 AU from the Sun and come back at the same distance) the cheapest solution should be a single GA with Mars: the results will confirm it. However, we wanted to study and give a wider overview of the possible combinations of GA sequences to reach L_3 . Therefore, Mercury, Venus, Mars and the Earth have been considered, combining then up to multiple GA with three planets.

The Venus-Venus-Earth GA sequence will look slightly more expensive in terms of ΔV_{Tot} with respect to the single GA with Mars, but for a much longer transfer time.

Even if a single GA with the Earth might seem the cheapest strategy, however, the very low (< 0.5 km/s) incoming and outgoing relative velocities at the surface of the Earth's sphere of influence could make this solution unrealistic and unusable for practical applications unless appropriately modified.

7.1 Definition of the problem: assumptions and procedure

A classic 3D patched conics method has been applied: each trajectory segment is modeled as 2BP governed by the respective central body. During the heliocentric cruise segments, the Sun is the central body and during the GA encounter the flyby planet is the central body.

When the s/c leaves the Earth at $t = 0$ it is considered to have the same position and velocity of the Earth and orbit about the Sun. The target L_3 is geometrically defined as an anti-Earth, that means L_3 has the same ephemerides of the Earth, except for the mean anomaly, that is the Earth's mean anomaly $+$ π . Moreover, L_3 is treated like an arrival planet, but with zero mass. No deep space manoeuvres and Low Thrust arcs have been considered.

The pattern can be summed up in the following legs:

1. a heliocentric elliptical orbit from the departure point to the flyby planet
2. a planetocentric hyperbola relative to the flyby planet
3. a heliocentric ellipse from the flyby planet to L_3 or the next flyby planet (in case of multiple GA)

A starting date and end date are given as initial guess (the date defines positions and velocities), as a sequence of planets to be encountered and the initial guess on the dates of encounters. For each leg a 3D Lambert problem is solved, thus the velocity change at departure (ΔV_d), the velocity change at the arrival at L_3 (ΔV_a) and the velocity change at each planetary encounter (ΔV_{Per}) are estimated. The swing-by parameters are computed as it will be shown in the next section, and the feasibility of the powered/unpowered swing-by is checked. In case a powered swing-by is requested, the velocity change (ΔV_{Per}) at the pericenter of the flyby planet is computed.

Each solution for the transfer is identified by $n + 2$ dates, n being the number of GAs. The problem becomes an optimization problem and the solution is the one that minimizes:

$$\Delta V_{Tot} = \Delta V_d + \Delta V_a + \sum_{i=0}^n \Delta V_{Per} \quad (7.1)$$

The sequence of GAs, their number and the planets involved are not variables of the optimization scheme. However, we introduced a set of nonlinear constraints, that is a minimum altitude for a given GA with a planet, in order to avoid impact trajectories. Therefore, the objective function (7.1) becomes:

$$\Delta V_{Tot} = \Delta V_d + \Delta V_a + \sum_{i=0}^n \left[\Delta V_{Per} + C \frac{(R_p + h - r_m)^2}{R_p^2} \right] \quad (7.2)$$

if $r_m < R_p + h$.

C is a weight, r_m the distance of the s/c from the GA planet at pericenter (as defined in Figures (7.1) and (7.2)), R_p the radius of the planet and h the

altitude of the s/c from the surface of the planet. This means that during the optimization procedure the results of the swing-by that have an altitude lower than the chosen one are not considered according to the weight. In our simulations we have chosen a value of the penalty C equal to 10 – 20 % during the Global optimization, and then lowered it to 10 % for the Local optimization. This is due to the fact that the optimum could be very close to the chosen constraints (for example, during a GA encounter, the flyby altitude that minimizes the objective function might be very close to the minimum altitude accepted, and if we do not relax the constraint chosen for the Global optimization, we might miss it).

The optimization scheme is as follows: a first optimization is done by a Global optimizer (for example, we used Genetic Algorithms or a grid search in a range of dates [*Goldberg, 1989*]). Then, these results are refined through a Local optimizer, and in particular we applied SQP algorithms.

As for the Global optimizer, we used a grid search when the dimension of the problem is small (1 or 2 swing-bys), otherwise we used Genetic Algorithms [*Izzo, 2007*]. The time step of the grid search has been taken in the range 5 days to one month, depending on the range of dates that had to be explored.

The initial guess on the initial date has been taken in 2009, while the initial guess on the final date has been taken such that each arc of the multiple GA transfer has enough time. Note that for single GA transfers, the dates found in the solutions can be extended in the future just shifting them by a time step equal to the synodic year.

At the end of this procedure the initial date, the final date, the encounter dates (with the flyby distance) and the ΔV_{sPer} (in case of powered swing-bys) that minimize the objective function are found.

7.2 Equations for the Gravity Assist

In this section the swing-by equations will be introduced.

First the procedure to compute the parameters that define an unpowered swing-by will be described. However, usually the opportunity for an unpowered swing-by is rare, and a powered GA encounter is needed. Thus, the classic method to determine the pericenter (r_m) of a powered swing-by will be shown.

7.2.1 Unpowered Swing-by

During a flyby the vector relationships between the incoming V-infinity vector $V_{\infty i}$, the outgoing V-infinity vector $V_{\infty o}$ and the two legs of the heliocentric transfer orbit

that "connect" at the flyby planet are as follows:

$$\bar{V}_{\infty i} = \bar{V}_i - \bar{V}_{Planet} \quad (7.3)$$

$$\bar{V}_{\infty o} = \bar{V}_o - \bar{V}_{Planet} \quad (7.4)$$

$$\sin 2\nu = \frac{|\bar{V}_{\infty o} \times \bar{V}_{\infty i}|}{V_{\infty}^2} \quad (7.5)$$

$$V_{\infty} = V_{\infty i} = V_{\infty o} = \sqrt{\frac{GM_{planet}}{-a}} \quad (7.6)$$

$$\cos(\nu + \pi) = -\frac{1}{e} \Rightarrow \csc \nu = e \quad (7.7)$$

$$r_m = \frac{a(1 - e^2)}{1 + e} = a(1 - e) = \frac{GM_{planet}}{V_{\infty}^2} (\csc \nu - 1) \quad (7.8)$$

where \bar{V}_{Planet} is the heliocentric velocity vector of the flyby planet at the flyby date, \bar{V}_i heliocentric velocity vector of the first transfer orbit at the flyby date, \bar{V}_o heliocentric velocity vector of the second transfer orbit at the flyby date, and r_m the periapsis radius of the flyby hyperbola.

The values of \bar{V}_i and \bar{V}_o depend on the solution of the Lambert's problem of the heliocentric elliptical orbit from the departure point to the flyby planet.

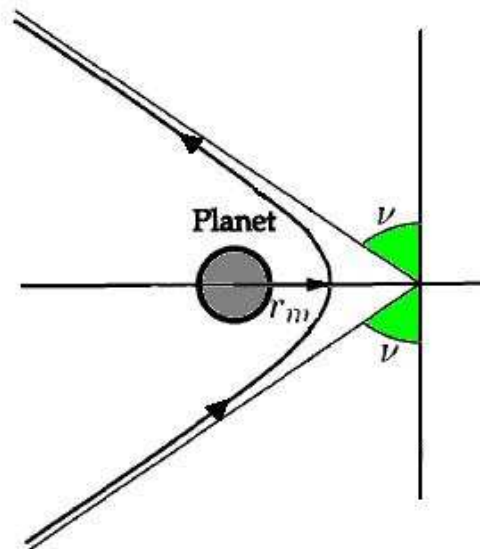


Figure 7.1 Scheme of the unpowered swing-by

7.2.2 Powered Swing-by

If $|\bar{V}_{\infty i}| \neq |\bar{V}_{\infty o}|$ a chemical additional impulse is required (see Figure (7.2)).

The solution is found constructing the two hyperbolas with the same pericenter, and then computing the chemical ΔV_{Per} supplied at this common pericenter.

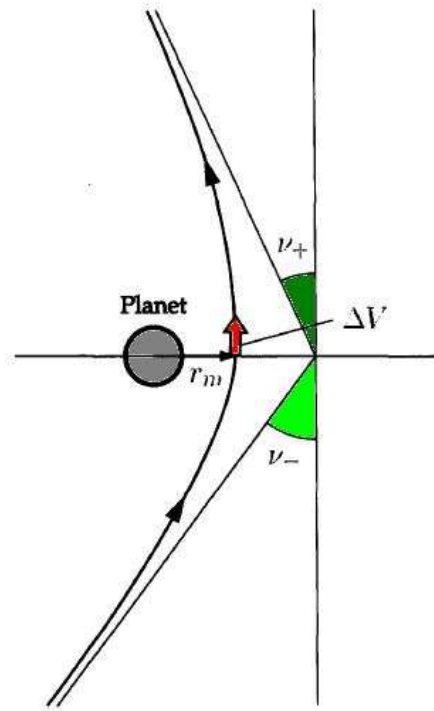


Figure 7.2 Scheme of the powered swing-by

The velocity difference at the pericenter of the two hyperbolas provides the ΔV to be applied is shown in Equation (7.11):

$$V_{m-} = \sqrt{GM_{Planet} \left(\frac{2}{r_m} - \frac{1}{a_-} \right)} = \sqrt{V_{\infty i}^2 + \frac{2GM_{Planet}}{r_m}} \quad (7.9)$$

$$V_{m+} = \sqrt{GM_{Planet} \left(\frac{2}{r_m} - \frac{1}{a_+} \right)} = \sqrt{V_{\infty o}^2 + \frac{2GM_{Planet}}{r_m}} \quad (7.10)$$

$$\Delta V_{Per} = |V_{m+} - V_{m-}| = \left| \sqrt{V_{\infty o}^2 + \frac{2GM_{Planet}}{r_m}} - \sqrt{V_{\infty i}^2 + \frac{2GM_{Planet}}{r_m}} \right| \quad (7.11)$$

To find r_m , the "twin equations" of the unpowered case are used, and the real common pericenter can be defined as:

$$\sin(\nu_- + \nu_+) = \frac{|\bar{V}_{\infty o} \times \bar{V}_{\infty i}|}{V_{\infty o} V_{\infty i}} \quad (7.12)$$

$$r_m = \frac{GM_{Planet}}{V_{\infty i}^2} (\csc \nu_- - 1) \quad (7.13)$$

$$\sin \nu_- = \frac{1}{1 + \frac{V_{\infty i}^2}{V_{om}^2}} \quad (7.14)$$

$$r_m = \frac{GM_{Planet}}{V_{\infty o}^2} (\csc \nu_+ - 1) \quad (7.15)$$

$$\sin \nu_+ = \frac{1}{1 + \frac{V_{\infty o}^2}{V_{om}^2}} \quad (7.16)$$

$$V_{om}^2 = \frac{GM_{Planet}}{r_m} \quad (7.17)$$

Therefore, combining Equations (7.12), (7.14) and (7.16), the non-linear equation for r_m is:

$$\sin^{-1} \left(\frac{|\bar{V}_{\infty o} \times \bar{V}_{\infty i}|}{V_{\infty o} V_{\infty i}} \right) = \sin^{-1} \left(\frac{1}{1 + \frac{V_{\infty i}^2}{V_{om}^2}} \right) + \sin^{-1} \left(\frac{1}{1 + \frac{V_{\infty o}^2}{V_{om}^2}} \right) \quad (7.18)$$

where the Equations (7.13), (7.15) and (7.17) should be substituted.

Equation (7.18) can be solved using a Newton-method.

7.3 Numerical results: Single and Multiple Gravity Assisted Transfers

In this section, results of single and multiple GA transfers will be given. All the sequences that have been explored are summed up in Table (7.4).

First, a transfer with no GA encounters has been investigated, and the plot of the trajectory is given in Figure (7.3).

This is the same case studied in the 2-burn single-revolution tangential transfer or 2-burn multi-revolution tangential transfer for $n = 3$ (flight time equal to one year and a half): there we found $\Delta V_{Tot} = 6.67$ km/s. Here, considering the ephemerides and thus not a circular orbit of the Earth about the Sun, $\Delta V_{Tot} = 6.57$ km/s.

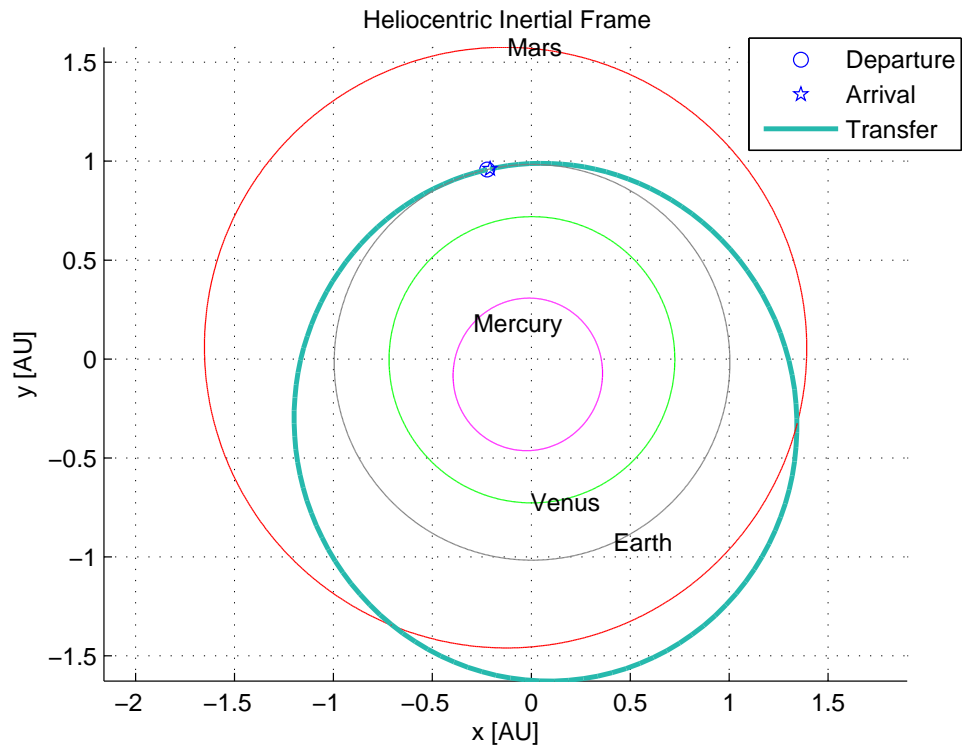


Figure 7.3 Results of direct transfer **Earth- L_3**

As a second case, a transfer trajectory with a single GA encounter with Mars has been explored. The optimum has been found for a time of flight equal to 1 year and 195 days, with $\Delta V_{Tot} = 6.26$ km/s. In Table (7.1) the results are given.

The single unpowered GA transfer with Mars is, in terms of ΔV_{Tot} , the best solution we have found for GA transfers, if the single powered GA transfer with the Earth turns out to be unrealistic and unusable (this solution is given later in this section).

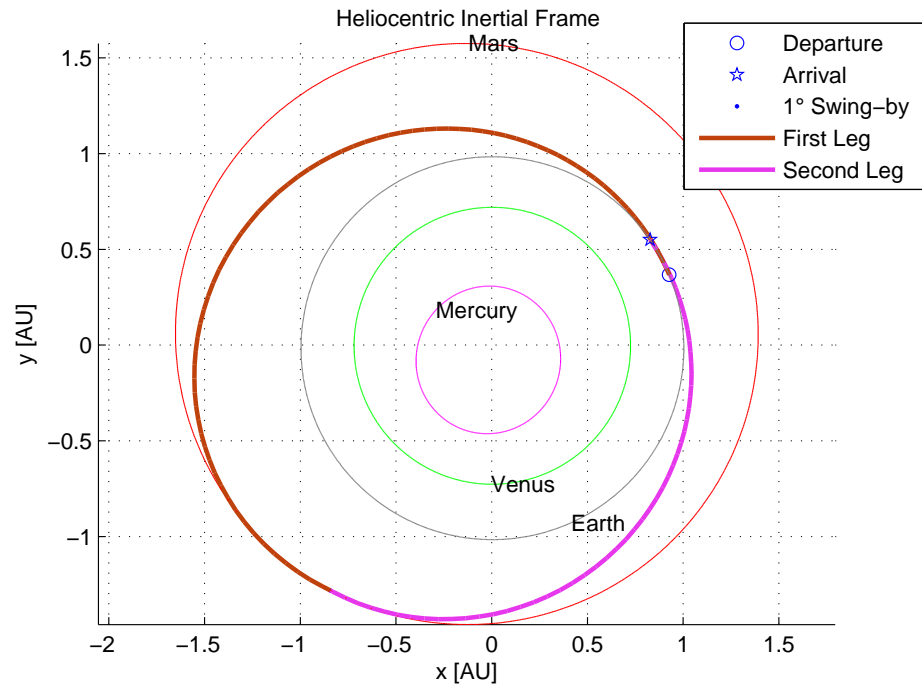


Figure 7.4 Results of the Gravity Assisted transfer trajectory **Earth-Mars- L_3**

Gravity Assist Sequence	Mars
Departure date [d-m-y]	15-10-2009
Arrival date [d-m-y]	28-04-2011
Encounter date [d-m-y]	21-09-2010
ΔV_d [km/s]	3.21809
ΔV_a [km/s]	3.04198
ΔV_{Per} [km/s]	0
Perigee altitude [km]	16016.5
Transfer time	1 y 195 d
ΔV_{Tot} [km/s]	6.26

Table 7.1 Overview of the transfer trajectory to Sun-Earth L_3 through Gravity Assist with Mars: data found through global and local optimization

Another sequence that has been investigated is a transfer trajectory with three GA encounters: Venus-Venus-Earth.

The trajectory is given in Figure (7.5).

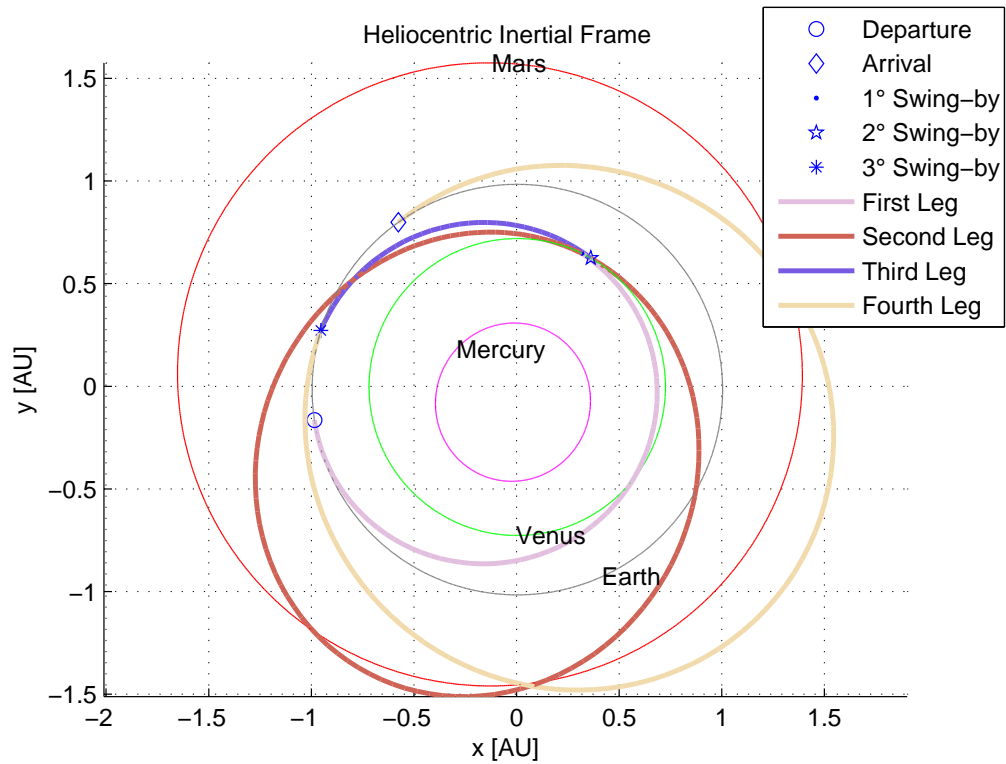


Figure 7.5 Results of the Gravity Assisted transfer trajectory **Earth-Venus-Venus-Earth- L_3**

This solution, as shown in Table (7.2), compared to the single GA with Mars has a slightly bigger ΔV_{Tot} (6.93 km/s), but a much longer flight time (3 years and 122 days).

Gravity Assist Sequence	Venus-Venus-Earth
Departure date [d-m-y]	29-03-2020
Arrival date [d-m-y]	29-07-2023
1 st Encounter date [d-m-y]	17-09-2020
2 nd Encounter date [d-m-y]	10-12-2021
3 rd Encounter date [d-m-y]	04-03-2022
ΔV_d [km/s]	3.00
ΔV_a [km/s]	3.73
1 st ΔV_{Per} [km/s]	0.07
1 st Perigee altitude [km]	995
2 nd ΔV_{Per} [km/s]	0.02
2 nd Perigee altitude [km]	995
3 rd ΔV_{Per} [km/s]	0.12
3 rd Perigee altitude [km]	994
Transfer time	3 y 122 d
ΔV_{Tot} [km/s]	6.93

Table 7.2 Overview of the transfer trajectory to Sun-Earth L_3 through multiple Gravity Assist with Venus-Venus-Earth: data found through global and local optimization

The transfer to L_3 with a GA encounter with the Earth has also been investigated.

We considered a GA with the Earth, without allowing multiple revolutions about the Sun after the GA encounter with the Earth. The trajectory is given in Figure (7.6) and the results in Table (7.3). The departure date is not important, since the eccentricity of Earth's orbit is almost zero, and thus the geometry of this transfer is the same any time of the year.

For a time of flight of 1 year and 221 days, $\Delta V_{tot} = 3.80$ km/s. This solution would look the best one found so far in this chapter.

However, this solution is characterized by very low (< 0.5 km/s) incoming and outgoing relative velocities at the surface of the Earth's sphere of influence, which cause the swing-by to be too slow to be instantaneous, contrary to what the model requires. This could make this solution unrealistic and unusable for practical applications unless appropriately modified, for example, by introducing deep space manoeuvres or allowing for resonant swing-bys with the Earth.

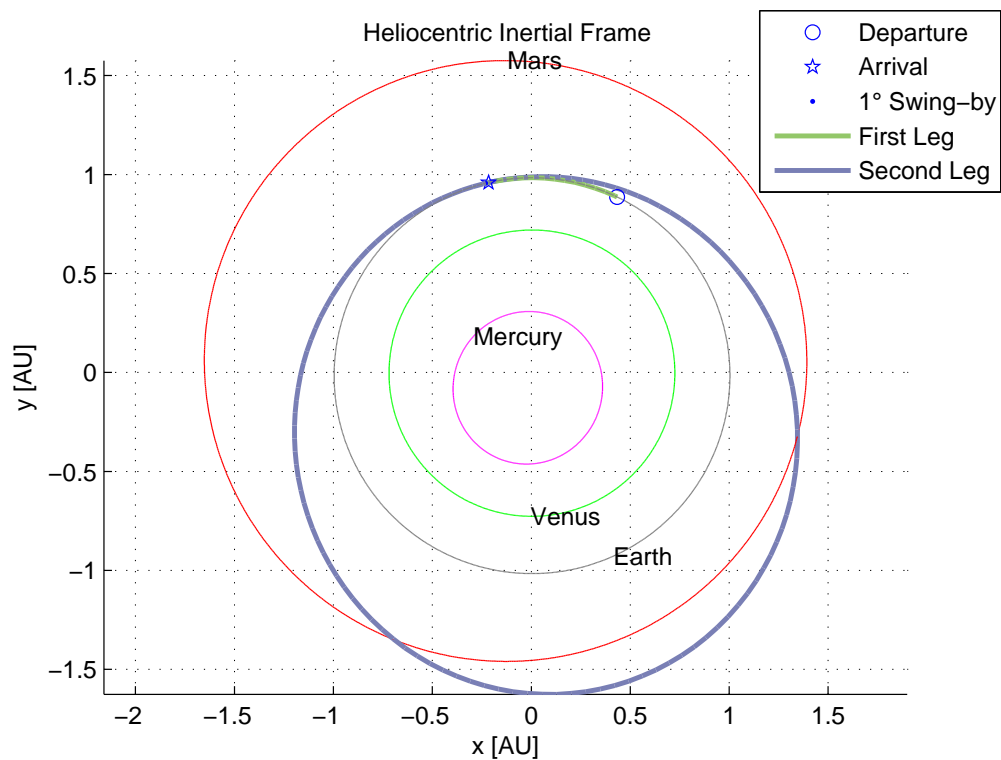


Figure 7.6 Results of the Gravity Assisted transfer trajectory **Earth-Earth- L_3**

An investigation of transfer trajectories that are resonant with the Earth and have a GA encounter with this planet could be a future development of this research.

Gravity Assist Sequence	Earth
Transfer time to the encounter	39 d
ΔV_d [km/s]	0.0014
ΔV_a [km/s]	3.2898
ΔV_{Per} [km/s]	0.5081
Perigee altitude [km]	998
Transfer time	1 y 221 d
ΔV_{Tot} [km/s]	3.80

Table 7.3 Overview of the transfer trajectory to Sun-Earth L_3 through Gravity Assist with Earth: data found through global and local optimization

Table (7.4) gives an overview of all the studied combinations of GA encounters:

Gravity Assist Sequence	ΔV_{Tot} [km/s]
Earth	3.80
Mars	6.26
Venus	16.00
Mercury	21.66
Mars-Earth	9.94
Mars-Venus	11.73
Venus-Earth	11.93
Venus-Mars	12.79
Venus-Venus	14.39
Mars-Earth-Venus	18.98
Venus-Venus-Earth	6.93
Venus-Earth-Venus	23.09
Venus-Mars-Venus	25.68
Venus-Earth-Mars	7.89

Table 7.4 Explored sequences of Gravity Assisted transfers trajectories to Sun-Earth L_3 : ΔV_{Tot} found through global and local optimization

Conclusions and possible future developments

In this research we wanted to explore different transfer strategies to reach the L_3 libration point of the Sun-Earth system, departing from the vicinity of the Earth.

The problem has been addressed and modeled with many different techniques, that can be summed up in four groups: High Thrust in the 2BP Sun-s/c, transfer in CR3BP through the manifolds, Low Thrust, and Gravity Assisted transfers.

In terms of transfer time, High Thrust and Low Thrust are equivalent (1.5 years for High Thrust, a bit more than 1.5 years for Low Thrust). However, the best solution in terms of final mass is provided by Low Thrust, the mass consumption being about 30%.

An interesting solution is provided by the 2-burn multi-revolution transfer (High Thrust in the 2BP Sun-s/c): ΔV decreases with increasing transfer time, and $\Delta V < 1$ km/s for a transfer time of 10.5 years or longer.

The transfer using the stable manifold of a Lyapunov orbit near L_3 turned out to be not feasible, since, even with an initial burn to put the s/c into the manifold (which has an horseshoe shape, and thus does not reach the Earth), it would take centuries.

However, interesting results have been found using the manifolds of Lyapunov orbits near L_1 or L_2 , and then intersecting Lyapunov orbits near L_3 . If the launcher injects the s/c directly into the stable manifold of the Lyapunov orbit near L_1 or L_2 , then the ΔV required on the s/c is in the range [0.5 km/s - 1.5 km/s], for a total transfer time in the range [5.7 years - 11.2 years].

Concerning Gravity-Assisted transfers, the best solution has been found for a single GA with Mars, for the quite high value $\Delta V = 6.26$ km/s, and transfer time a bit more than 1.5 years. A better solution was given by a GA encounter

with the Earth ($\Delta V = 3.80$ km/s and transfer time of 1 year and 221 days), but this result could be unrealistic and unusable for practical applications due to the too low value of the difference between the velocity of the s/c and the velocity of the Earth during the encounter.

As a future development of the research, resonant orbits with the Earth that have a GA encounter with it could be explored, and it is likely that this strategy would lead to lower ΔV s than the one found for a GA encounter with Mars. Moreover, deep space manoeuvres and arc of Low Thrust could be added in the model where Gravity Assisted transfers are studied.

The Low Thrust model could be extended to the bicircular model, considering Venus, and the thrust could be taken both ON and OFF. Indeed, as we said in *Chapter 1*, Venus comes within 0.3 AU of L_3 every 20 months: station-keeping near L_3 once an orbit near that libration point is reached could be also analysed.

Bibliography

- Alligood, K., T. Saur, and J. Yorke (1996), *CHAOS: An Introduction to Dynamical Systems*, Springer.
- Barrabés, E., and M. Ollé (2006), Invariant manifolds of L_3 and horseshoe motion in the restricted three-body problem, *Nonlinearity*, *9*, 2065–2090.
- Bertotti, B., L. Iess, and P. Tortora (2003), A test of general relativity using radio links with the Cassini spacecraft, *Nature*, (425), 374–376.
- Brisson, A. E. Jr., and Y. C. Ho (1969), *Applied optimal control*, Blaisdel Publishing Company.
- Broucke, R. A. (1988), The celestial mechanics of gravity assist, AAS/AIAA Astrodynamics Conference, Minneapolis, MN, Aug. 15-17, 1988.
- Canalias, E., G. Gomez, M. Marcote, and J. Masdemont (2004), Assessment of mission design including utilisation of libration points and weak stability boundaries, ESA - Ariadna.
- Connors, M., P. Chodas, S. Mikkola, P. Wiegert, C. Veillet, and K. Innanen (2002), Discovery of an asteroid and quasi-satellite in an earth-like horseshoe orbit, *Meteoritics and Planetary Science*, *37*, 1435–1441.
- Font, J. (1990), *The role of homoclinic and heteroclinic orbits in two-degrees of freedom Hamiltonian systems*, Ph.D. dissertation, Departament de Matemàtica Aplicada i Anàlisi, Universitat de Barcelona.
- Gao, Y. (2003), *Advances in Low Thrust Trajectories Optimization and Flight Mechanics*, Ph.D. dissertation, University of Missouri-Columbia.
- Gill, P. E., W. Murray, and M. A. Saunders (2002), SNOPT: An SQP algorithm for large-scale constrained optimization, *SIAM J. Optim.*, *12*, 979–1006.
- Goldberg, D. E. (1989), *Genetic Algorithms in Search, Optimization, and Machine Learning*, Addison-Wesley.
- Gomez, G., J. Llibre, R. Martinez, and C. Simó, *Dynamics and Mission Design near Libration Points, Volume 1: Fundamentals: The Case of Collinear Libration Points*.
- Gomez, G., A. Jorba, J. Masdemont, and C. Simó (1993), Study of the transfer from the Earth to a halo orbit around the equilibrium point L_1 , *Celestial Mechanics and Dynamical Astronomy*, *56*(4), 541–562.
- Gomez, G., J. Masdemont, and C. Simó (1997), Lissajous orbits around halo orbits, *Advances in the Astronautical Sciences*, *95*, 117–134.

- Gomez, G., A. Jorba, J. Masdemont, and C. Simó (1998a), Study of the transfer between halo orbits, *Acta Astronautica*, 43, 493–520.
- Gomez, G., J. Masdemont, and C. Simó (1998b), Quasihalo orbits associated with libration points, *The Journal of the Astronautical Sciences*, 46, 135–176.
- Gomez, G., W.S. Koon, M.W. Lo, J.E. Marsden, J. Masdemont, and S.D. Ross (2001), Invariant manifolds, the spatial three-body problem and space mission design, AAS/AIAA Astrodynamics Specialist Conference, Quebec City, Canada, 2001.
- Gomez, G., W.S. Koon, M.W. Lo, J.E. Marsden, J. Masdemont, and S.D. Ross (2004), Connecting orbits and invariant manifolds in the spatial restricted three-body problem, *Nonlinearity*, 17, 1571–1606.
- Gooding, R.H. (1990), A procedure for the solution of Lambert’s orbital boundary-value problem, *Celestial Mechanics and Dynamical Astronomy*, 48, 145–165.
- Hartman, P. (1964), *Ordinary Differential Equations*, John Wiley and Sons.
- Hechler, M. (2008), Launch windows for libration point missions, *Acta Astronautica*, 64, 139–151.
- Howell, K. C. (1984), Three dimensional, periodic, halo orbits, *Celestial Mechanics*, 32, 53–71.
- Izzo, D., V. M. Becerra, D. R. Myatt, S. J. Nasuto, and J. M. Bishop (2007), Search space pruning and global optimisation of multiple gravity assist spacecraft trajectories, *Journal of Global Optimization*, 38, 283–296.
- Kemble, R. (2006), *Interplanetary Mission Analysis And Design*, Springer Praxis.
- Kirk, D. (1998), *Optimal Control Theory*, Dover Publications.
- Koon, W.S., M. W. Lo, J. E. Marsden, and S. D. Ross (2000), Heteroclinic connections between periodic orbits and resonance transitions in celestial mechanics., *Chaos*, 10(2), 427–469.
- Koon, W.S., J.E. Marsden, and S.D. Ross (2002a), Constructing a low energy transfer between Jovian moons, *American Mathematical Society*, 292, 129–145.
- Koon, W.S., M.W. Lo, J.E. Marsden, and S.D. Ross (2002b), Low-energy transfer from near-earth to near-moon orbit, *NASA Tech Brief*, 26.
- Koon, W.S., M.W. Lo, J.E. Marsden, and S.D. Ross (2007), *Dynamical Systems, the Three-Body Problem and Space Mission Design*, Springer Praxis.
- Marsden, J.E., and S.D. Ross (2006), New methods in celestial mechanics and mission design, *Bull. Am. Math. Soc., New Ser.*, 43(1), 43–73.
- Parker, T., and L. Chua (1991), *Practical Numerical Algorithms for Chaotic Systems*, Springer.
- Perko, L. (2006), *Differential Equations and Dynamical Systems*, Springer.
- Rayman, M., T. Fraschetti, C. Raymond, and C. Russell (2006), Dawn: A mission in development for exploration of main belt asteroids Vesta and Ceres, *Acta Astronautica*, 58(11), 605–616.
- Richardson, D. (1980), Analytic construction of periodic orbits about the collinear points, *Celestial Mechanics*, 22, 241–253.
- Ross, S.D. (2006), The interplanetary transport network, *American Scientist*, 3, 230–237.

- Ross, S.D., and D.J. Scheeres (2007), Multiple gravity assists, capture, and escape in the restricted three-body problem, *SIAM J. Appl. Dyn. Syst.*, 6, 576–596.
- Serban, R., W.S. Koon, M.W. Lo, J.E. Marsden, L.R. Petzold, S.D. Ross, and R.S. Wilson (2002), Halo orbit mission correction maneuvers using optimal control, *Automatica*, 38(4), 571–583.
- Stokes, G. H., and the NASA Science Definition Team (2003), Study to determine the feasibility of extending the search for near-earth objects to smaller limiting diameters, NASA Office of Space Science, Solar System Exploration Division.
- Szebehely, V. (1967), *Theory of orbits*, Academic Press.
- Teodorescu, P. P. (2008), *Mechanical Systems, Classical Models: Volume 2: Mechanics of Discrete and Continuous Systems*, Springer.
- Vallado, D. (2007), *Fundamentals of Astrodynamics and Applications*, El Segundo: Microcosm Press.
- Wakker, K.F. (2005a), *Astrodynamics I*, TU Delft, Faculty of Aerospace Engineering, Lecture notes AE4-874.
- Wakker, K.F. (2005b), *Astrodynamics II*, TU Delft, Faculty of Aerospace Engineering, Lecture notes AE4-874 II.
- Wertz, J.R. (2001), *Mission Geometry & Orbit Constellation: Design and Management*, El Segundo: Microcosm Press.
- Wiggins, S. (2003), *Introduction to applied nonlinear dynamical systems and chaos*, Springer.

Appendix A

Family of Lyapunov Orbits near L_3

Initial Condition (x_0 and \dot{y}_0), Period and Jacobi constant for the family of Lyapunov orbits generated near the libration point L_3 of the Sun-Earth system ($\mu = 0.304042340000000E - 05$), in RTBP reference frame and units.

y_0 and \dot{x}_0 are always equal to zero, and have not been reported in order to make the table fit the page.

x_0 [AU]	\dot{y}_0 [AU/TU]	Period [TU]	C [AU^2/TU^2]
0.100010126666320E+01	-0.199995172821808E-03	0.628316862705193E+01	0.300000607083724E+01
0.100020026666295E+01	-0.397980902021089E-03	0.628316894396245E+01	0.300000604123580E+01
0.100030026666270E+01	-0.597956543021011E-03	0.628316865888153E+01	0.300000599143504E+01
0.100040026666244E+01	-0.797922192980152E-03	0.628316861259508E+01	0.300000592163396E+01
0.100050026666219E+01	-0.997877854896765E-03	0.628316860016211E+01	0.300000583183255E+01
0.100060026666194E+01	-0.119782353176684E-02	0.628316859574440E+01	0.300000572203082E+01
0.100070026666169E+01	-0.139775922658705E-02	0.628316859390384E+01	0.300000559222876E+01
0.100080026666143E+01	-0.159768494234936E-02	0.628316859297521E+01	0.300000544242636E+01
0.100090026666118E+01	-0.179760068204769E-02	0.628316859250817E+01	0.300000527262362E+01
0.100100026666093E+01	-0.199750644867682E-02	0.628316859221367E+01	0.300000508282055E+01
0.100200026665840E+01	-0.399601625374488E-02	0.628316859179084E+01	0.300000208476931E+01
0.100300026665588E+01	-0.599353203668550E-02	0.628316859181070E+01	0.299999708667364E+01
0.100400026665335E+01	-0.799005677516248E-02	0.628316859187302E+01	0.299999008851853E+01
0.100500026665083E+01	-0.998559343797442E-02	0.628316859196231E+01	0.299998109028299E+01
0.100600026664831E+01	-0.119801449850857E-01	0.628316859207000E+01	0.299997009193999E+01
0.100700026664578E+01	-0.139737143677007E-01	0.628316859220296E+01	0.299995709345652E+01
0.100800026664326E+01	-0.159663045282698E-01	0.628316859235155E+01	0.299994209479359E+01
0.100900026664073E+01	-0.179579184005681E-01	0.628316859252247E+01	0.299992509590616E+01
0.101000026663821E+01	-0.199485589097183E-01	0.628316859271174E+01	0.299990609674324E+01
0.101200026663316E+01	-0.239269314960862E-01	0.628316859315064E+01	0.299986209735680E+01
0.101400026662811E+01	-0.279014455170388E-01	0.628316859366956E+01	0.299981009610604E+01
0.101600026662306E+01	-0.318721240666380E-01	0.628316859427142E+01	0.299975009236665E+01
0.101800026661801E+01	-0.358389901046664E-01	0.628316859494994E+01	0.299968208541817E+01
0.102000026661296E+01	-0.398020664579913E-01	0.628316859571121E+01	0.299960607444394E+01
0.102200026660791E+01	-0.437613758218707E-01	0.628316859655145E+01	0.299952205853109E+01
0.102400026660286E+01	-0.477169407612722E-01	0.628316859747160E+01	0.299943003667044E+01
0.102600026659781E+01	-0.516687837121690E-01	0.628316859847071E+01	0.299933000775649E+01
0.102800026659276E+01	-0.556169269828405E-01	0.628316859955112E+01	0.299922197058728E+01
0.103000026658771E+01	-0.595613927551206E-01	0.628316860071117E+01	0.299910592386442E+01
0.103200026658266E+01	-0.635022030856921E-01	0.628316860195176E+01	0.299898186619289E+01
0.103400026657761E+01	-0.674393799073125E-01	0.628316860327154E+01	0.299884979608108E+01
0.103600026657256E+01	-0.713729450300661E-01	0.628316860467219E+01	0.299870971194059E+01
0.103800026656751E+01	-0.753029201425873E-01	0.628316860615280E+01	0.299856161208623E+01
0.104000026656246E+01	-0.792293268132794E-01	0.628316860771273E+01	0.299840549473583E+01
0.104200026655741E+01	-0.831521864915255E-01	0.628316860935395E+01	0.299824135801021E+01
0.104400026655236E+01	-0.870715205088683E-01	0.628316861107467E+01	0.299806919993302E+01
0.104600026654732E+01	-0.909873500802047E-01	0.628316861287581E+01	0.299788901843062E+01
0.104800026654227E+01	-0.948996963049604E-01	0.628316861475669E+01	0.299770081133199E+01
0.105000026653722E+01	-0.988085801682378E-01	0.628316861671788E+01	0.299750457636857E+01
0.105200026653217E+01	-0.102714022541992E+00	0.628316861875924E+01	0.299730031117412E+01
0.105400026652712E+01	-0.106616044186148E+00	0.628316862088128E+01	0.299708801328460E+01
0.105600026652207E+01	-0.110514665749740E+00	0.628316862308254E+01	0.299686768013800E+01
0.105800026651702E+01	-0.114409907772046E+00	0.628316862536462E+01	0.299663930907419E+01
0.106000026651197E+01	-0.118301790683681E+00	0.628316862772677E+01	0.299640289733476E+01
0.106200026650692E+01	-0.122190334807708E+00	0.628316863016950E+01	0.299615844206287E+01
0.106400026650187E+01	-0.126075560360723E+00	0.628316863269246E+01	0.299590594030304E+01
0.106600026649682E+01	-0.129957487453953E+00	0.628316863529529E+01	0.299564538900100E+01
0.106800026649177E+01	-0.133836136094316E+00	0.628316863797875E+01	0.299537678500351E+01
0.107000026648672E+01	-0.137711526185488E+00	0.628316864074287E+01	0.299510012505812E+01
0.107200026648167E+01	-0.141583677528962E+00	0.628316864358646E+01	0.299481540581303E+01
0.107400026647662E+01	-0.145452609825097E+00	0.628316864651081E+01	0.299452262381686E+01
0.107600026647157E+01	-0.149318342674138E+00	0.628316864951539E+01	0.299422177551842E+01
0.107800026646652E+01	-0.153180895577277E+00	0.628316865260116E+01	0.299391285726654E+01
0.108000026646147E+01	-0.157040287937641E+00	0.628316865576647E+01	0.299359586530980E+01
0.108200026645642E+01	-0.160896539061324E+00	0.628316865901252E+01	0.299327079579634E+01
0.108400026645137E+01	-0.164749668158388E+00	0.628316866233915E+01	0.299293764477359E+01
0.108600026644632E+01	-0.168599694343851E+00	0.628316866574664E+01	0.299259640818803E+01
0.108800026644128E+01	-0.172446636638688E+00	0.628316866923432E+01	0.299224708188499E+01
0.109000026643623E+01	-0.176290513970791E+00	0.628316867280237E+01	0.299188966160832E+01
0.109200026643118E+01	-0.180131345175971E+00	0.628316867645120E+01	0.299152414300019E+01
0.109400026642613E+01	-0.183969148998891E+00	0.628316868018040E+01	0.299115052160079E+01
0.109600026642108E+01	-0.187803944094041E+00	0.628316868399040E+01	0.299076879284806E+01
0.109800026641603E+01	-0.191635749026689E+00	0.628316868788119E+01	0.299037895207742E+01
0.110000026641098E+01	-0.195464582273812E+00	0.628316869185244E+01	0.298998099452146E+01
0.110200026640593E+01	-0.199290462225044E+00	0.628316869590494E+01	0.298957491530965E+01
0.110400026640088E+01	-0.203113407183582E+00	0.628316870003755E+01	0.298916070946809E+01
0.110600026639583E+01	-0.206933435367140E+00	0.628316870425104E+01	0.298873837191909E+01
0.110800026639078E+01	-0.210750564908836E+00	0.628316870854561E+01	0.298830789748098E+01
0.111000026638573E+01	-0.214564813858112E+00	0.628316871292106E+01	0.298786928086770E+01
0.111200026638068E+01	-0.218376200181630E+00	0.628316871737734E+01	0.298742251668848E+01
0.111400026637563E+01	-0.222184741764161E+00	0.628316872191440E+01	0.298696759944758E+01
0.111600026637058E+01	-0.225990456409493E+00	0.628316872653274E+01	0.298650452354382E+01
0.111800026636553E+01	-0.229793361841283E+00	0.628316873123152E+01	0.298603328327035E+01
0.112000026636048E+01	-0.233593475703957E+00	0.628316873601166E+01	0.298555387281421E+01

Table A.1 Initial Condition (x_0 and \dot{y}_0), Period and Jacobi constant for the family of Lyapunov orbits generated near the libration point L_3 of the Sun-Earth system

Appendix B

Runge-Kutta Methods for Integration

Consider the following initial-value problem:

$$\frac{dy}{dt} = f(t, y) \tag{B.1}$$

where $a \leq t \leq b$ and $y(a) = \alpha$.

The most common Runge-Kutta (RK) method is RK4, which is a fourth-order method. The integration scheme for the RK4 integrator is:

$$\begin{aligned} w_0 &= \alpha \\ k_1 &= hf(t_i, w_i) \\ k_2 &= hf\left(t_i + \frac{h}{2}, w_i + h\frac{k_1}{2}\right) \\ k_3 &= hf\left(t_i + \frac{h}{2}, w_i + h\frac{k_2}{2}\right) \\ k_4 &= hf(t_i + h, w_i + hk_3) \\ w_{i+1} &= w_i + \frac{1}{6}(k_1 + 2k_2 + 2k_3 + k_4) \end{aligned} \tag{B.2}$$

for each $i = 0, 1, \dots, (N - 1)$, where N is the number of mesh points and $h = \frac{b-a}{N}$. The mesh points are given by:

$$t_i = a + ih \tag{B.3}$$

where $i = 0, 1, \dots, N$. The local truncation error for this method is $O(h^4)$ under the condition that $y(t)$ has at least five continuous derivatives.

An adaptive scheme that varies the step size has the advantage that the local truncation error can be kept within a specified bound. An ideal different-equation method for approximating the solution $y(t)$ would have the property that, given a tolerance $\epsilon > 0$, the minimal number of mesh points would be used to ensure that the global truncation error does not exceed ϵ at any of these points. Generally, equal spacing between mesh points does not lead to error control and minimisation of the number of mesh points. Although the global truncation error of an integrator cannot be determined in general, a close link exists between local and global truncation error. By using methods of different order, the local truncation error can be estimated. Hence, the step size can be adjusted to ensure that the global truncation error remains within specified bounds.

The reader can refer to [*Burden, Faires, 2000*].

In the computations of the results presented in this thesis a higher order adaptive method has been used, Runge-KuttaFeldberg 7-8 (RK78), where the truncation error is $O(h^7)$ under the condition that $y(t)$ has at least eight continuous derivatives.

RK78 is a Runge-Kutta-Fehlberg method, where a Runge-Kutta method with local truncation error of order eight is used to estimate the local error in a Runge-Kutta method of order seven.